Effects of Flow Shielding and Channeling on Tsunami-Induced Loading of Coastal Structures

Andrew O. Winter

A dissertation
submitted in partial fulfillment of the
requirements for the degree of

Doctor of Philosophy

University of Washington

2019

Reading Committee:

Michael R. Motley, Chair

Marc O. Eberhard, Chair

Randall J. Leveque

Pedro Arduino

Program Authorized to Offer Degree:
Civil and Environmental Engineering

University of Washington

Abstract

Effects of Flow Shielding and Channeling on Tsunami-Induced Loading of Coastal Structures

Andrew O. Winter

Co-Chairs of the Supervisory Committee:
Professor Michael R. Motley
CEE

Professor Marc O. Eberhard
CEE

Prior efforts to numerically model the complex fluid-structure interactions that occur as tsunami inundations pass through coastal communities have failed to consistently reproduce experimentally-measured flow velocities and depths. These deficiencies have led to inaccurate estimates of the forces and pressures acting on individual structures due to shielding and channeling effects caused by neighboring structures, which tend to reduce and increase structural demands, respectively. To address these shortcomings, the primary goals of this dissertation were to produce an experimental data set for a range of neighboring structure configurations from which shielding and channeling effects on force demands were identified as well as to develop an experimentally-validated computational fluid dynamics model that was capable of accurately reproducing the observed effects. Additionally, a parametric study that varied neighboring structure locations was conducted using the validated CFD model in order to develop a streamwise force-prediction design equation, which improves upon the methods provided in the ASCE 7-16 design provisions used to estimate force amplifications due to neighboring structures.

TABLE OF CONTENTS

LIST OF FIGURES

LIST OF TABLES

Nomenclature

Chapter 4 - Experimental Methodology

$S_{\max}$	Maximum piston wavemaker stroke
SF	Wavemaker scale factor
t	Unscaled wavemaker time
t_0	Unscaled wavemaker time offset
t_{wm}	Wavemaker delay time
W	Unconstricted flume width
W_{C}	Constricted flume width
x_{wm}	Wavemaker paddle position
τ	Scaled wavemaker time
τ	Scaled wavemaker time offset

Chapter 5 - Experimental Results

BR	Blockage ratio
g	Acceleration magnitude due to Earth's gravity at its surface
$F_{\text{Case i}}$	Case i force
F_{h}	Horizontal force
F_{v}	Vertical force
F_{X0}	Max ensemble-averaged streamwise force for Case A
F_{XC}	Max ensemble-averaged streamwise force for Cases B - F
FIR	Force increase ratio

L Streamwise distance between MRE and test structure

$\hat{p}$ Normalized ensemble average of pressure maxima

p_{14} Ensemble-averaged pressure for back (i.e. onshore) face gauge

p_{B} Back face hydrostatic pressure surface

$\overline{p}_{\mathrm{Case\ i}}$ Case i ensemble-averaged pressure

p_{L} Bi-linear pressure surface

p_{Q} Bi-quadratic pressure surface

u_{X0} Max median streamwise velocity for Case A

u_{XC} Max median streamwise velocity for Cases B - F

VAF Velocity amplification factor

W Unconstricted flume width

W_{C} Constricted flume width

z_{14} Vertical coordinate of back (i.e. onshore) face pressure gauge

β Wake clearance angle

γ_{water} Unit weight of water

μ Static friction coefficient

ρ_{water} Density of water

$\hat{\sigma}$ Normalized standard deviation of pressure maxima

Chapter 6 - Numerical Methodology

A_{water} Cross-sectional area of flume water

B u^+-axis intercept for von Kármán's log-law

c_{air} Speed of sound in air

C_p Specific heat at constant pressure

C_S Smagorinsky coefficient

C_v	Specific heat at constant volume
C_μ	Normalized turbulent kinematic viscosity
$C_{\varepsilon 1}$	First ω transport equation coefficient
$C_{\varepsilon 2}$	Second ω transport equation coefficient
$C_{\omega 1}$	First ω transport equation coefficient
μ_{water}	Dynamic Viscosity of water
ν	Kinematic viscosity
ν_{air}	Kinematic viscosity of air
ν_r	LES eddy viscosity
ν_T	Turbulent kinematic viscosity
ν_{water}	Kinematic viscosty of water
ω	Turbulence frequency
ω_{Log}	Log-law turbulence frequency boundary value component
ω_{Vis}	Viscous sub-layer turbulence frequency boundary value component
Ω	Fluid domain
$C_{\omega 2}$	Second ω transport equation coefficient
ϕ	Arbitrary OpenFOAM field variable
Π_{ij}	Velocity-pressure-gradient tensor components
ρ	Density
ρ_{air}	Density of air
ρ_{water}	Density of water
σ	Surface tension coefficient
$\boldsymbol{\sigma}$	Cauchy stress tensor
σ_{ij}	Cauchy stress tensor components

τ_w	Boundary or wall shear stress
$\boldsymbol{\tau}$	Deviatoric stress tensor
d_{H}	Hydraulic diameter
τ_{ij}	Deviatoric stress components
τ_{ij}^r	Anisotropic residual or sub-grid scale stress components
$\boldsymbol{\tau}^r$	Anisotropic residual or sub-grid scale stress tensor
$\boldsymbol{e}_i$	i-direction unit basis vector
f	Arbitrary function being Reynolds-averaged (only in Section 6.3.3)
f_σ	Surface tension momentum equation term
$\boldsymbol{f}$	Flux vector
$\boldsymbol{F}$	Flux tensor
g	Acceleration magnitude due to Earth's gravity at its surface
g	Arbitrary function being Reynolds-averaged
$\boldsymbol{g}$	Gravity vector
g_i	Gravity vector component
$G(\boldsymbol{r})$	LES spatial filtering function
h_{SWL}	Still-water-level depth
$H(\cdot)$	Heaviside function
k	Turbulent kinetic energy (TKE)
K_{air}	Isentropic bulk modulus of air
ℓ_m	Turbulence length scale
ℓ_S	Smagorinsky length scale
L	Turbulence length scale
$\boldsymbol{I}$	Second-order identity tensor

M	Mach number
M_{air}	Molar mass of air
p	Total pressure
$\langle p \rangle$	Reynolds-averaged pressure
p'	Fluctuating pressure
p_0	Static pressure
p_{wet}	Wetted perimeter
$\mathcal{P}$	TKE production rate
$\mathcal{P}_{ij}$	TKE production tensor components
Pr_k	TKE Prandtl number
Pr_ε	TKE dissipation rate Prandtl number
Pr_ω	Turbulence frequency Prandtl number
q	Conserved scalar quantity
$\boldsymbol{q}$	Conserved vector quantity
$\boldsymbol{r}$	LES filtering position vector
R	Universal ideal gas constant
$\boldsymbol{R}$	Reynolds stress tensor
R_{ij}	Reynolds stress components
$\mathcal{R}_{ij}$	Pressure-rate-of-strain tensor components
Re_L	Turbulence Reynolds number
$\tilde{Re}_T$	Turbulent Reynolds number
Re_λ	Taylor length scale Reynolds number
s	Scalar source term
$\boldsymbol{s}$	Vector source term

S	Sutherland temperature
$\overline{\mathcal{S}}$	Characteristic filtered rate of strain
$\boldsymbol{S}$	Strain rate or rate of deformation tensor
S_{ij}	Strain rate or rate of deformation components
$\langle S_{ij} \rangle$	Mean strain rate or rate of deformation components
$\langle \boldsymbol{S} \rangle$	Mean strain rate or rate of deformation tensor
$\overline{\boldsymbol{S}}$	Filtered rate of strain or rate of deformation tensor
$\overline{S}_{ij}$	Filtered rate of strain or rate of deformation components
T	Temperature
T_0	Reference temperature for Sutherland's Law
T_{kij}	Reynolds stress flux tensor components
u^+	Normalized parallel-to-boundary velocity
u_τ	Friction velocity
$\boldsymbol{u}$	Total velocity vector
u_i	Total velocity component
u_i^{air}	Volume-of-Fluid air phase velocity component
u_i^{water}	Volume-of-Fluid water phase velocity component
$\langle \boldsymbol{u} \rangle$	Reynolds-averaged velocity vector
$\langle u_i \rangle$	Reynolds-averaged velocity component
$\boldsymbol{u}'$	Fluctuating velocity vector
u_i'	Fluctuating velocity component
$\overline{\boldsymbol{u}}$	Spatially-filtered velocity vector
$\overline{u}_i$	Spatially-filtered velocity component
$\boldsymbol{u}^r$	Residual or sub-grid scale velocity vector

u_i^r Residual or sub-grid scale velocity component

W_{F} Unconstricted flume width

$\boldsymbol{x}$ Coordinate position vector

x_i i-direction coordinate

y^+ Normalized normal-to-boundary position

y_c^+ Viscous sub-layer/log-law region intersection point

α Volume fraction

β^* Specific turbulence frequency coefficient

δ_{ij} Kronecker delta

Δ LES filter width

ε TKE dissipation rate

ε_{ij} Dissipation tensor components

η Kolmogorov length scale

γ Adiabatic index of an ideal diatomic gas

κ Bulk viscosity

κ Mean curvature of air-water interface (only in Equation 6.39)

κ von Kármán's constant (only in Section 6.5)

μ Dynamic or shear viscosity

μ_0 Reference dynamic viscosity for Sutherland's Law

μ_{air} Dynamic viscosity of air

μ_T Turbulent dynamic viscosity

Chapter 7 - Numerical Model Validation

F_x Streamwise force

k Turbulent kinetic energy (TKE)

p	Total pressure
p_{avg}	Ensemble-averaged pressure
R_{ij}	Reynolds stress components
$\langle S_{ij} \rangle$	Mean strain rate or rate of deformation components
$\langle u_i \rangle$	Reynolds-averaged velocity component
u_i'	Fluctuating velocity component
x_i	i-direction coordinate
δ_{ij}	Kronecker delta
ε	TKE dissipation rate
η	Free-surface elevation
μ_T	Turbulent dynamic viscosity
ω	Turbulence frequency
ρ	Density

Chapter 8 - Force-Prediction Design Equation Development

D_{DS}	Design structure width
D_{NS}	Neighboring structure width
D_{O}	Wake width overlap with design structure offshore face
d_{W}	Idealized wake width at design structure offshore face
D_{W}	Idealized wake width
E	Sum of squared errors for wake size optimization
F_{C}	Flow channeling factor
F_{M}	Momentum factor
F_{S}	Shielding factor
F_{X}	Streamwise force ratio

L_f^*	Normalized wake formation length as a function of Re
L_r^*	Normalized recirculation region length as a function of Re
L_{W}	Idealized wake length
W^*	Normalized wake width as a function of Re
W_{F}	Unconstricted flume width
R_{L}	Wake length ratio
R_{W}	Wake width ratio
Re	Neighboring structure Reynolds number
u_1	Streamwise velocity component
x	Streamwise separation between design and neighboring structures
y	Transverse separation between design and neighboring structures
ν	Kinematic viscosity of water
θ	Wake angle

ACKNOWLEDGMENTS

I would like to take this opportunity to thank all of the people who helped me get to the point of completing my Ph.D. research. First of all, I could not have completed this work without the advice, patience, and support of my two primary advisors, Michael Motley and Marc Eberhard. Thank you for giving me the opportunity to pursue my academic interests to their fullest throughout our time working together.

To the rest of my doctoral committee, namely Randy Leveque, Pedro Arduino, and Vasily Titov, thank you for your efforts in reviewing all of my work and taking the time to provide your useful insights and suggestions. Specifically, I would like to thank Randy for the excellent courses I took from you concerning numerical analysis of time-dependent equations and the finite volume method, both of which proved immensely useful while trying to improve my OpenFOAM numerical modeling results. Also, to Pedro, thank you for helping me with my Hyak and DesignSafe struggles as well as for your superb materials modeling course, which I have to thank for my current understanding of tensor-based continuum mechanics.

At the Hinsdale Wave Research Lab, I could not have completed the experimental portion of my research without the substantial assistance I received from my colleagues Krishnendu Shekhar, Xinsheng Qin, Mohammad Shafiqual Alam, Zeyad Al-Sayhood, and Victoria Johnson as well as from the superb lab staff, including Tim Maddux, Pedro Lomónaco, Andre Barbosa, Bret Bosma, and Dan Cox.

To Robert Breidenthal, Dana Dabiri, Antonino Ferrante, and James Riley, your excellent courses helped me attain a much clearer understanding of fluid dynamics and turbulent flows. Furthermore, thank you for your patience and time spent answering my research-related questions outside of class. Your intuitions and tips often proved invaluable when

things seemed to be going so very wrong with processing experimental data and setting up numerical simulations.

To Hin Kei Wong, your tips and advice helped me avoid countless hours of suffering figuring out how to use OpenFOAM and helped to jump start my Ph.D. research. Without your contributions and insights I would not have mastered OpenFOAM fluid-structure interaction modeling and high-performance computing. To Cassie Gills, it was a pleasure to work with you developing and improving our OpenFOAM models of the wave flume experiments. Your doggedness and smarts not only helped you finish your masters thesis in record time, but helped work out the initial kinks in our models and significantly accelerate the development of my final OpenFOAM models. Also, thanks to Xinsheng for OpenFOAM advice and to Nasser Marafi and Andy Sen for your tips on using Hyak and Stampede2.

For your continued friendship and support as well as for inviting Ryan Ganey and myself to be an extended part of the "Core Crew", thank you to Kristina Tsvetanova, Tianye (Andrew) Yang, and Ashley Heid; I will always remember our time together fondly. To Kamal Ahmed, Rouzbeh Davoudi, and Nasser Marafi, thank you for being the best of Ph.D. qualifying exam study buddies and friends besides. Even though you did not directly contribute to my academic endeavors, I would like to thank my sister Emily as well as Brian Clavadetscher, Jason Ciummo, Jeff White, Ian and Paul Rummell, and Eric Allan for being devoted friends who helped me to relax and remember there is indeed an outside world to look forward to upon graduating. Above all though, I want to thank Kristina for always supporting me in everything and for being the most loving, devoted girlfriend I could ever wish for.

Concerning my research, this dissertation has been prepared in part as a component of a Natural Hazards Research Infrastructure (NHERI) research program aimed at studying tsunami-like wave and wave-borne debris impact forces on coastal structures as well as the University of Washington M9 Project, which aimed to mitigate the potential disaster con-

sequences of a future Cascadia Subduction Zone (CSZ) earthquake. The research efforts towards completing this document were directly funded by the National Science Foundation (NSF) through Grants CMMI-1344615, CMMI-1536198, and CMMI-1519679 and is based upon work supported by the NHERI Coastal Wave/Surge and Tsunami Experimental Facility (i.e. the Hinsdale Wave Research Lab) at Oregon State University, which is a major facility funded by the NSF. The numerical modeling completed during this work was facilitated through the use of the advanced computational, storage, and networking infrastructure provided by the Hyak high-performance computing (HPC) cluster, which is supported in part by the University of Washington eScience Institute, and the Stampede2 HPC cluster, which is operated by the Texas Advanced Computing Center (TACC) and funded by the NSF through grant ACI-1540931.

DEDICATION

To my mother Lynne, who is chiefly responsible for the person I grew up to be and who left this world far too soon.

Chapter 1

INTRODUCTION

Tsunamis present one of the most challenging physical phenomena to accurately model as well as one of the most difficult natural hazards for which to adequately design structures. This dissertation attempts to address these issues by demonstrating that fluid-structure interaction (FSI) of coastal structures during tsunami inundation events can be successfully modeled using three-dimensional computational fluid dynamics (CFD) methods to accurately reproduce both total and component-level wave-induced loads determined through experimentation. Furthermore, by expanding upon validated numerical models through parameter studies, improved force-prediction relations based upon the interaction of several structures in a coastal community were determined in order to allow for more accurate assessment of tsunami impact loading for future structural design and retrofit calculations.

1.1 Research Objectives

As is discussed in Chapter 3 - Prior Tsunami Impact Research, prior efforts aimed at predicting tsunami-like wave loading of coastal structures have focused primarily on resultant forces applied to such structures and have failed to precisely replicate experimental results in terms of structural demands. Thus, the principal aim of this dissertation was to extend this research through conducting an in-depth study of tsunami-induced loading of an elevated structure at both total and component levels, using three-dimensional computational fluid dynamics (CFD) methods to validate and extend experimental results. To this end, a series of numerical studies on an elevated rectangular building were conducted, following an experimental program. This work was carried out in two phases, namely a validation step, where the numerical models were calibrated to accurately simulate empirical results, and a param-

eter study step, where additional simulations extrapolating beyond the experimental cases were completed. The validation and extension of these results will allow future researchers and structural designers to better estimate both total and local demands on structural components during a tsunami event, demonstrating that the complex fluid-structure interactions that occur between multiple structures during an inundation can be accurately reproduced in terms of pressures and forces using CFD software.

Furthermore, this work attempts to address the fact that current engineering design provisions do not adequately account for the effects of structural geometries and neighboring structures. For instance, the AASHTO code for bridges focuses on wave impacts and surges due to coastal storms and does not address tsunami loading, whereas ASCE 7-16 for buildings has an entire chapter devoted to tsunami loading, yet does not sufficiently treat the influence of neighboring structures, providing force amplification factors for a limited range of applicability (AASHTO, 2008; ASCE, 2017). To improve upon the current ASCE 7-16 design provisions concerning the effects of neighboring structures on the demands for a design structure, numerical parametric study results for the streamwise force acting on the elevated structure model were utilized to develop an improved force amplification factor equation for the maximum tsunami-induced streamwise force acting on a design structure due to flow conditions resulting from the influence of neighboring structures.

1.2 Dissertation Outline

This dissertation is organized as follows:

Chapter 2 - Tsunamis: Causes, Effects, and Future Risks: provides background information on tsunamis explaining how they are generated, their propagation behavior, and the resulting effects of coastal inundations caused by them. Additionally, the risk of future tsunami events is discussed at length, focusing on subduction zone earthquake sources in the Ring of Fire surrounding the Pacific Ocean. In particular, the Cascadia Subduction Zone is highlighted as a key potential source of a future tsunami disaster.

Chapter 3 - Prior Tsunami Impact Research: introduces the broad range of tsunami engineering research topics including tsunami generation and inundation, tsunami impact forces on coastal structures, and tsunami-resilient design methods. However, the primary focus of this discussion was tsunami-induced forces on coastal structures and structural components. In particular, a strong emphasis was placed on shielding and flow channeling effects due to multi-structure arrays, where these effects were studied for a single structure within such configurations. Key observations are made concerning the two overall themes of this dissertation, particularly the experimental determination of shielding and flow channeling effects caused by neighboring structures as well as the development of a computational fluid dynamics model that is capable of accurately reproducing such effects.

Chapter 4 - Experimental Methodology: shows the experimental test configurations used during the elevated structure tests that were conducted at the Hinsdale Wave Research Lab in the Large Wave Flume (Higgins et al., 2017). The details discussed in this chapter include the types and locations of measurement devices, the wave types and their generation methods, the wave tank or flume experimental facilities, and the test structure on which wave impact demands were measured.

Chapter 5 - Experimental Results: presents an in-depth presentation and discussion of the elevated building test results, focusing on fluid velocities, pressures, and forces imparted on the design structure as well as free-surface elevation measurements. A particular emphasis is made on observations and measurements that demonstrate evidence of flow shielding and channeling phenomena.

Chapter 6 - Numerical Methodology: gives an explanation of how the OpenFOAM software package works and was used to simulate both bridge and building models (The OpenFOAM Foundation, 2019). This includes the governing equations, turbulence models, and numerical methods implemented in the software as well as how it was applied to setup up the models in terms of physical properties, boundary conditions, and mesh generation.

Chapter 7 - Numerical Model Validation: describes how the OpenFOAM numerical model

was validated against experimental data in terms of matching peak forces as well as the general trends of force time histories. Additionally, comparisons of free-surface elevation as well as local fluid pressures on the design structures were made.

Chapter 8 - Force-Prediction Design Equation Development: outlines the selected parameters and the ranges of values used for numerical parametric studies concerning resultant streamwise loading of an elevated rectangular structure. The position and number of neighboring structures were varied as well as the width of the numerical wave flume to assess the influence of these changes on both local and total structural demands. Furthermore this section lays out the development of a phenomenological model that estimates the maximum streamwise, horizontal force on a rectangular design structure due to the size and proximity of neighboring rectangular structures in terms of a normalized force ratio relative to the reference case without neighboring structures. Three key factors based on the geometric configuration of the structures as well as basic fluid mechanics, which determine the normalized force ratio when multiplied, were developed. Additionally, two coefficients relating to the size and shape of the wakes behind neighboring structures were incorporated into these factors, which were calibrated using the parametric study data to determine optimum values of these coefficients that are representative of the variations in wave impact loads for the entire set of building configurations.

Chapter 9 - Conclusions and Future Work: summarizes the main conclusions of the experimental and numerical work and highlights the principal contributions of this dissertation. Recommendations for future work concerning the improvement of tsunami impact force estimation methods are proposed.

Chapter 2

TSUNAMIS: CAUSES, EFFECTS, AND FUTURE RISKS

Before addressing tsunami modeling and force-prediction, it is important to understand the level of damage that tsunamis inflict, the risk of future tsunami events occurring, and what prior scholars have achieved towards improving tsunami inundation modeling and structural demand estimation. Assessment of the aftermath of tsunami inundations demonstrates how urgent it is that scientists improve upon the current state of the art in tsunami engineering, providing the motivation for the research presented in this dissertation. The urgency of the need for improved tsunami engineering methods is heightened further by tying it to the frequency of major tsunami events as well as where such events are likely to occur in the near future. Additionally, by conducting a thorough review of the state of the art in tsunami engineering, the areas of greatest need for improvement have been identified as: 1) how to successfully use CFD to reproduce experimental tsunami loading scenarios on a local scale and 2) how to use the results of such modeling to determine improved force estimation equations for a subset of structures in a coastal community. Each of these topics is dealt with at length in separate sections in this introduction, which is concluded by summaries of the overall research objectives of this dissertation and the contents of each subsequent dissertation chapter.

2.1 The Destructive Nature of Tsunamis

Tsunami inundation poses a serious risk to coastal communities, wreaking havoc around the globe. A tsunami, which translates as harbour wave from Japanese, consists of a series of waves known as a wave train, which have considerably longer wave lengths (100 to 500 km) than wind-driven ocean waves (30 to 40 m for normal sea states), even when compared

to hurricane-induced waves (up to 1 to 2 km). In deep ocean conditions where tsunamis are generated, their velocity can exceed 800 km/hr, which is comparable to that of a jet airplane; however, upon reaching coasts they reduce to 32 to 48 km/hr due to shoaling effects caused by shallow-water conditions. Conversely, tsunamis are often unnoticeable in the deep ocean since they commonly have amplitudes less than 1.0 m, but when they reach coastal regions, wave shoaling and focusing due to geometry of the continental shelf and coast results in amplitudes that typically range from 3 to 30 m. Such tall waves are unstable and soon break to form turbulent bores that rapidly flow over land, inundating large coastal regions and causing widespread devastation. During such events, the highest elevation a tsunami inundation reaches, the run-up elevation as shown in Figure 2.1, can range from 10 to 100 m for severe events depending on the local topography of the coastal region being inundated (Röbke and Vött, 2017; Koshimura, 2019; NTHMP, 2019).

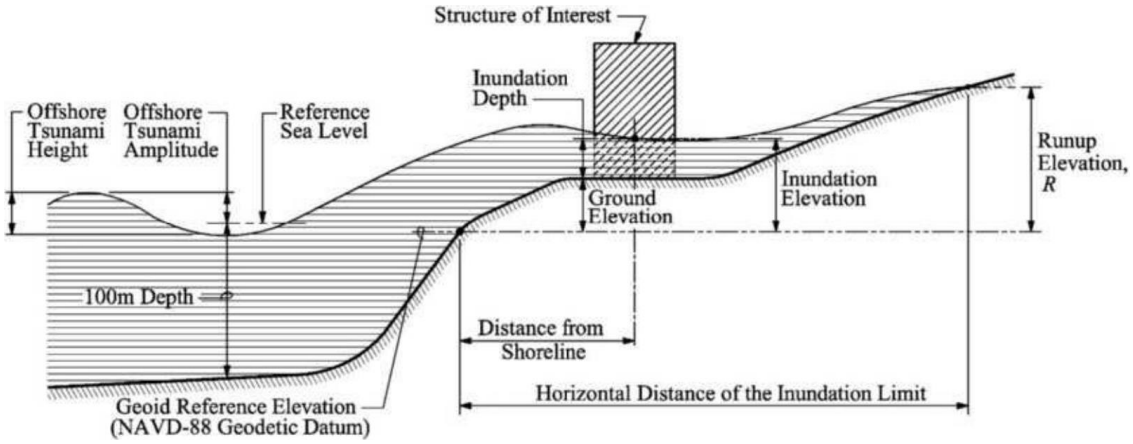

Figure 2.1: Tsunami Size and Inundation Terminology (ASCE, 2017)

The destructive nature of tsunamis is directly tied to wave shoaling, the physical phenomenon by which decreases in ocean depth as waves propagate towards a shoreline result in decreases in wave velocity and length, but increases in wave height and energy density. Assuming the wave train is moving in a single direction for the sake of brevity, the velocity is governed by the water wave dispersion relation, $\omega^2 = gk\tanh(kh)$, where $g = 9.81$ m/s^2 is the acceleration due to Earth's gravity at its surface, h is the ocean depth, $\omega = 2\pi/T = 2\pi f$ is the angular wave frequency, T is the wave period, f is the linear frequency, $k = 2\pi/\lambda$, is the

angular wave number, and λ is the wave length (Dean and Dalrymple, 1991). This relation may be derived using linear or Airy wave theory and is a direct consequence of the kinematic free-surface boundary condition for waves. The wave velocity or celerity, $c = \lambda/T = \omega/k$, can be determined from the angular frequency and wave number, which results in Equation 2.1 that tends to deep and shallow water limits.

$$c = \begin{cases} \sqrt{\dfrac{g\lambda}{2\pi}} & \text{for } \dfrac{h}{\lambda} > 0.5 \quad \text{(deep water)} \\ \sqrt{\dfrac{g\lambda}{2\pi}\tanh\left(\dfrac{2\pi h}{\lambda}\right)} & \text{for } 0.5 \leq \dfrac{h}{\lambda} \leq 0.5 \quad \text{(intermediate water)} \\ \sqrt{gh} & \text{for } \dfrac{h}{\lambda} < 0.05 \quad \text{(shallow water)} \end{cases} \tag{2.1}$$

Note that since tsunami wave lengths are so large relative to the depths of the Earth's oceans, the ratio h/λ falls within the shallow water range of wave behavior. For instance, the average depth of the Pacific ocean is about 4.3 km, whereas typical tsunami wave lengths range from 100 to 500 km, which gives $0.0086 < h/\lambda < 0.043$, demonstrating that tsunamis are indeed a shallow water phenomenon based on linear or Airy water wave theory. Assuming the same average ocean depth, the resulting deep ocean tsunami velocity would be about 205 m/s or 740 km/hr, whereas near the coast at a depth of 10 m the velocity would reduce to about 10 m/s or 36 km/hr as shown in Figure 2.2.

As a direct result of such velocity decreases, the wave length, λ, must also decrease as depicted in Figure 2.2. This behavior is related to the fact that the number of wave crests is a conserved quantity, which imposes the requirement that the linear wave frequency, $f = c/\lambda$, and consequently the wave period, T must remain fixed too. Thus when reductions in ocean depth force the wave velocity to decrease, the wave length must also decrease to maintain a constant wave frequency (Dean and Dalrymple, 1991).

Similar to the wave length and velocity, the wave height is also influenced by decreasing ocean depth. Changes in wave height are dictated by the fact that waves must conserve their mean energy flux in the direction they propagate, $\overline{\mathcal{F}} = Ec$, which is per unit width

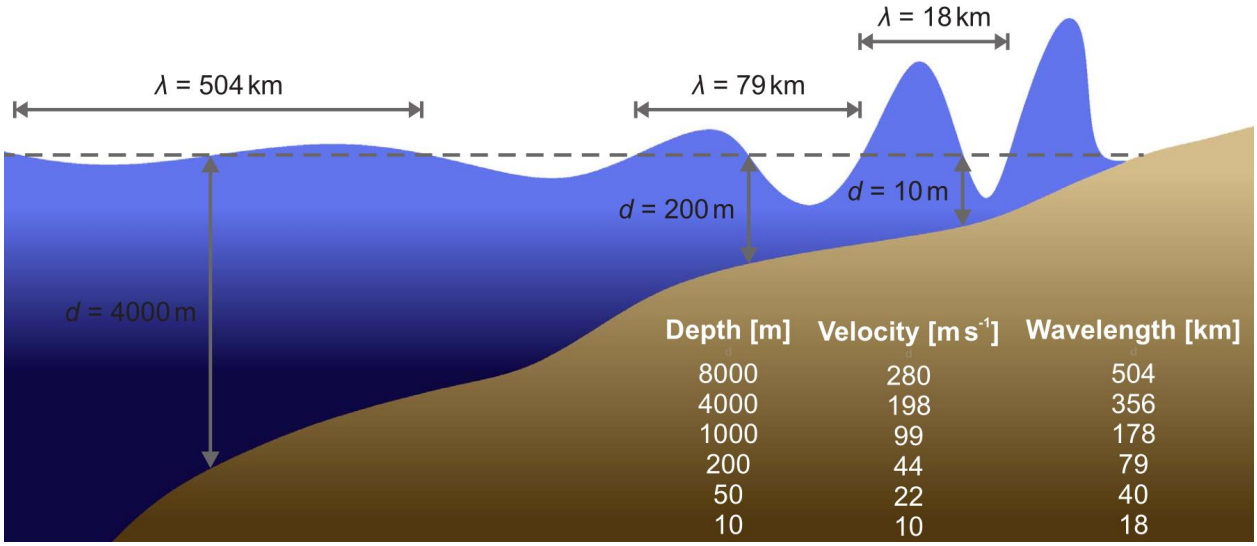

Figure 2.2: Variations in Tsunami Velocity and Wave Length due to Wave Shoaling Caused by Changes in Ocean Depth (T = 1800 s, Röbke and Vött 2017).

perpendicular to the wave propagation direction, where c is the wave velocity, $E = \frac{1}{8}\rho g H^2$ is the total wave energy density (i.e. energy per unit area beneath the wave) considering both potential and kinetic energy densities, ρ is the density of water, and H is the wave height. Since a tsunami must maintain a constant energy flux as it travels across an ocean, energy fluxes at different depths can be equated to give $E_o c_o b_o = Ecb$, which may be used to derive Green's Law, $H = H_o K_S = H_o \sqrt[4]{h_o/h}$, assuming that $b_o = b$ (i.e. $\theta_o = 0°$), where an o subscript indicates an initial deep ocean value, no subscript indicates a near shore value, b_o and b are the distances between adjacent wave rays perpendicular to the wave propagation direction as shown in Figure 2.3, and K_S is the shoaling coefficient for long waves, which determines the increase in wave height as tsunamis propagate from the deep ocean to shallow coastal waters (Green, 1838; Dean and Dalrymple, 1991).

In addition to shoaling effects, changes in wave height are also caused by water wave refraction, which occurs when waves approach a coast obliquely (i.e. $\theta_o > 0°$). Refraction is caused by reduced depths near coasts that result in waves being redirected toward propagating in the cross-shore direction (i.e. normal to the shoreline) the shallower the water gets, which consequently invalidates the Green's Law assumption of $b_o = b$. This behavior

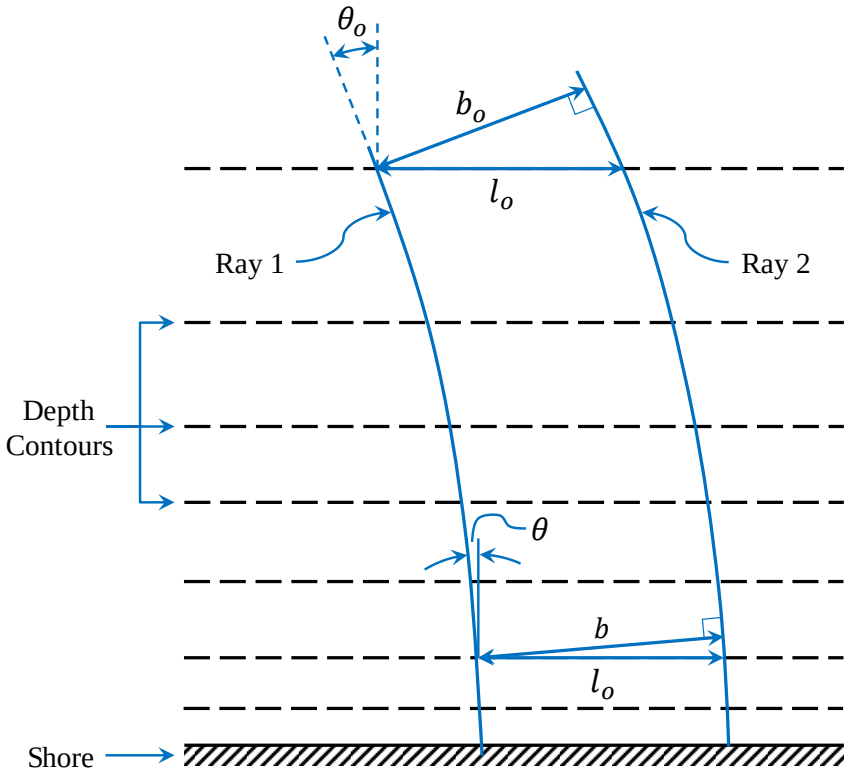

Figure 2.3: Water Wave Refraction due to Decreasing Ocean Depth as Waves Approach a Shoreline (Based on Dean and Dalrymple 1991).

is analogous to light passing through different media and having its path bent and as such it is also dictated by Snell's Law, $\sin(\theta_o)/c_o = \sin(\theta)/c$, where θ is the angle between the wave propagation direction and the cross-shore direction as shown in Figure 2.3. Using the geometry of Figure 2.3, an equation relating the distances between adjacent wave rays at different positions, $b_o/b = \cos(\theta_o)/\cos(\theta)$, can be used along with the fact that energy flux is conserved to derive the relation $H = H_o K_S K_R = H_o \sqrt[4]{h_o/h}\sqrt{\cos(\theta_o)/\cos(\theta)}$, where K_R is the wave refraction coefficient.

Comparing the shoaling and refraction coefficients shows that $K_S > 1$ always amplifies wave heights, whereas $K_R < 1$ always reduces wave heights. For instance, assuming an initial wave height of 1.0 m, an initial orientation of $\theta_o = 15°$, a final orientation of $\theta = 5°$, and

using the same wave example given earlier, where the initial depth was 4.3 km and the final depth was 10 m, results in $K_S = 4.55$, $K_R = 0.985$, and a near shore tsunami wave height of about 4.48 m. However, as demonstrated in this example and as was noted previously, shoaling and refraction alone cannot explain the size of past tsunamis that have been found to reach heights near 30 m, demonstrating that other factors such as wave focusing effects due to coastal bathymetries cause additional wave height amplifications.

Overall, the combined effects of velocity decreases, wave length shortening, and wave height increases in near shore regions result in massive tsunami waves that break at a critical point to form rushing bore-like walls of water. This occurs when the depth reaches a specific fraction of the wave height, which is dependent on the slope of the beach that the wave is approaching. For example, McCowan (1894) determined that this fraction $\kappa = H_b/h_b = 0.78$ for a flat beach, where H_b and h_b are the wave height and depth at the breaking point. The beach slope dependence of this ratio has also been investigated by many researchers such as Weggel (1972), who found that $\kappa = b(m) - a(m)H_b/(gT^2)$, where m is the beach slope, $a(m) = 43.8(1 - e^{-19m})$, and $b(m) = 1.56/(1 + e^{-19.5m})$ (Dean and Dalrymple, 1991; Robertson et al., 2013a). Furthermore, in order to maintain conservation of energy flux when the wave velocity diminishes with decreasing ocean depth, the energy density of the wave must increase accordingly to maintain a constant energy flux, which results in towering waves that deliver high-energy impact forces to coastal structures, causing widespread destruction of the built environment.

2.1.1 Earthquake-Induced Tsunamis

Such mighty waves require considerable energy input sources in order to generate the initial conditions necessary for tsunamis to propagate across oceans and inundate coasts. Tsunami wave trains are set in motion by a wide range of physical phenomena, including earthquakes, landslides, volcanic activities, and extreme meteorological conditions (Röbke and Vött, 2017; NTHMP, 2019). In the case of earthquake-induced tsunamis, sudden, upward

or downward shifts in seafloor elevation due to tectonic plate motions cause the water above to also displace vertically as shown in Figure 2.4, which results in waves that propagate away from the earthquake source perpendicular to it due to gravity (Röbke and Vött, 2017; Koshimura, 2019). The rate at which sea floor displacement occurs has been demonstrated to have a strong influence on the resulting wave profile at the ocean surface such that rapid, impulsive motions produce wave forms similar to the sea floor displacement profile, whereas slow, creeping motions produce waves that are qualitatively similar to the shape of the velocity time history of the sea floor motion (Hammack, 1973). Additionally, Hammack (1973) found that linear wave theory is applicable if the maximum sea floor displacement is small relative to the surrounding, uniform water depth, which was confirmed by Jamin et al. (2015). These effects are further complicated by the local shape of the sea floor and if inertial effects are considered too, then initial tsunami wave heights may exceed the maximum seabed displacement (Dalrymple and Derakhti, 2018). Lateral plate motions can also contribute to increasing the severity of a tsunami, but to a much lesser degree unless they occur along steep sea floor slopes and the horizontal displacement is large relative to the vertical displacement (Tanioka and Satake, 1996).

Throughout the last two decades, a number of catastrophic earthquake-generated tsunamis, particularly those that occurred in the Indian Ocean in 2004, Chile in 2010, and Japan in 2011, as well as many smaller-scale events (e.g., Peru in 2001, Sumatra in 2006, 2010, and 2018, the Solomon Islands in 2007, 2010, and 2013, and Samoa in 2009) have led to a significantly increased public awareness of how frequent and potentially devastating these natural disasters can be (Esteban et al., 2013). All told, these events resulted in losses that numbered in the hundreds of thousands in terms of lives lost and caused widespread destruction of the built environment and transportation infrastructure. For instance, the 2004 Indian Ocean tsunami, which was caused by an earthquake with a moment magnitude (M_W) of 9.1, resulted in estimated damages and relief aid costing roughly 15 billion USD (Athukorala and Resosudarmo, 2005; Bandara and Naranpanawa, 2005), left approximately 1.5 million inhabitants without homes, and resulted in a reported death toll of over 220,000 (Saatcioglu

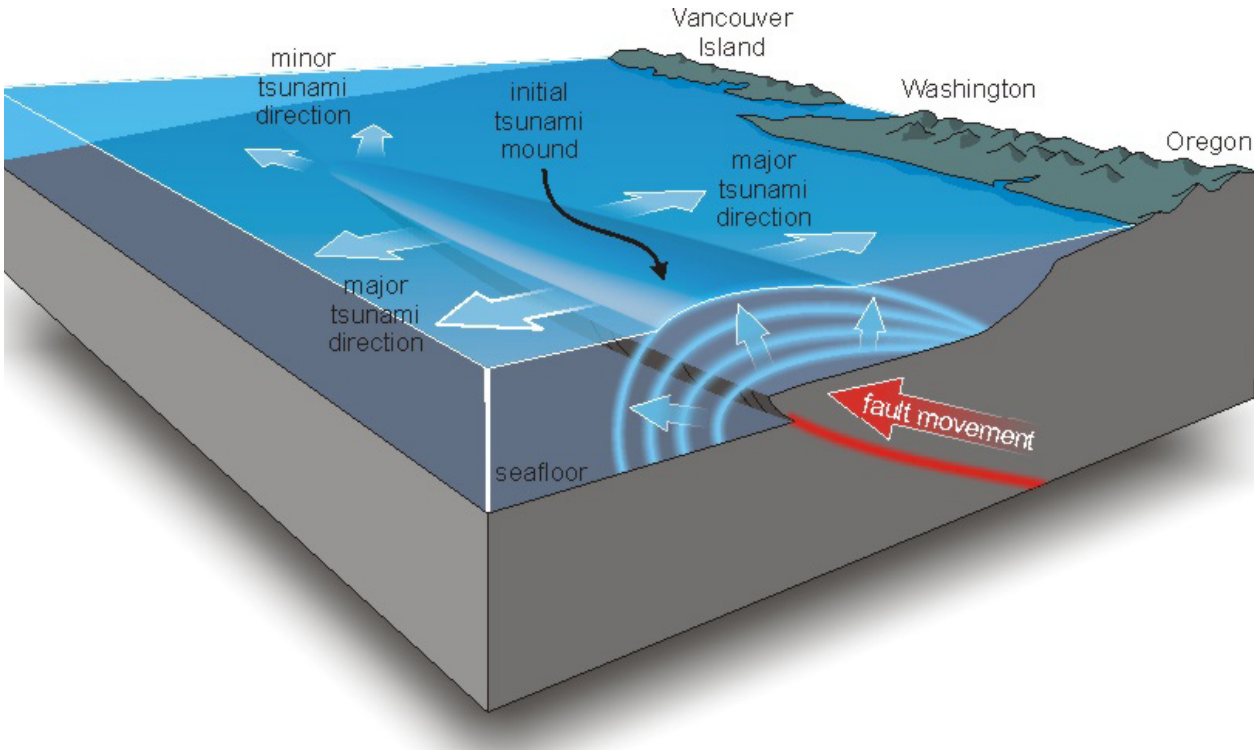

Figure 2.4: Earthquake-Induced Tsunami Generation and Propagation Normal to its Source Fault Shown at the Cascadia Subduction Zone (City of Richmond, 2017).

et al., 2005; Ghobarah et al., 2006; Yeh et al., 2007; Imamura, 2008; Suppasri et al., 2012c, 2013b,a; Shibayama et al., 2016). Similarly, the M_W 9.1 Great East Japan Earthquake in 2011 caused a tsunami that resulted in over 20,000 casualties and fully or partially destroyed 128,000 to 837,000 structures (Mimura et al., 2011; Kazama and Noda, 2012; Mori and Takahashi, 2012; Suppasri et al., 2012c,a,b; Foytong et al., 2013; Mase et al., 2013; Mori et al., 2013; Suppasri et al., 2013c; Leelawat et al., 2014; Naito et al., 2014), reaching estimated losses in the range of 195 to 305 billion USD (Nanto et al., 2011). Coastal devastation due to these events extended beyond the immediate impacts of monetary losses, lives lost, and structural damage to include long-term consequences such as significant erosion of coastlines, the washing away of both agricultural and natural forests and other vegetation, and residual flooding in low-lying regions as shown in Figure 2.5. The combination of these effects has led to significant delays in the recovery of coastal regions with poorer communities tradi-

tionally engaged in farming and aquaculture industries suffering most, resulting in livelihood changes for large proportions of surviving populations in affected areas due to lack of usable land, disparities in road reconstruction rates between communities, and reconstruction costs (Matsumaru et al., 2012; Daly et al., 2017; Ismail et al., 2018; Syamsidik et al., 2018; Adella et al., 2019).

(a) Near Banda Aceh, Indonesia (2004) (b) The Port of Onagawa, Japan (2011)

Figure 2.5: Before and After Comparison Showing Tsunami Damage in Coastal Communities: Deforestation, Erosion, Residual Flooding, Debris, and Loss of Buildings.

Such severe structural damage caused by the initial impact of tsunami waves and their subsequent inundation of inland regions is often compounded by widespread failure of transportation infrastructure components. These failures cut off escape, rescue, and recovery routes for those trapped in regions affected by tsunamis. For example, 81 of the 186 bridges along the only road connecting the major Indonesian cities of Banda Aceh and Meulaboh were either wiped out or damaged to the point of being unusable as a result of the 2004 Indian Ocean tsunami with 8 of the 42 major bridges in Banda Aceh suffering similar fates

as well (Iemura et al., 2005; Saatcioglu et al., 2005; Ghobarah et al., 2006; Unjoh and Endoh, 2006). Likewise, the tsunami induced by the 2011 Great East Japan Earthquake resulted in the loss of over 300 bridges out of approximately 3,200 surveyed bridges in the region affected by the tsunami (Hosoda and Maruyama, 2011; Aglipay et al., 2012; Akiyama et al., 2012; Kasano et al., 2012; Kawashima, 2012; Kazama and Noda, 2012; Maruyama et al., 2012; Unjoh, 2012; Akiyama et al., 2013; Fu et al., 2013; Maruyama et al., 2013; Zheng et al., 2013; Koon and Lau, 2015). Examples of such bridge failures are given in Figure 2.6, which shows bridge deck segments were uplifted or overturned without being destroyed during the 2011 Tohoku, Japan tsunami and a superstructure that collapsed due to the initial tsunami impact in the 2018 Palu, Indonesia tsunami.

(a) Utatsu Ohashi Bridge, Japan (2011) (b) Palu, Indonesia (2018)

Figure 2.6: Tsunami-Induced Bridge Damage

2.1.2 Landslide-Induced Tsunamis

Significant tsunami events of a similar magnitude as those caused by earthquakes have been caused by landslides too. Landslide-generated tsunamis are produced by either submarine landslides that displace the water above them similar to earthquake-generated tsunamis, or, subaerial landslides that generate massive waves when they impact bodies of water. The submarine variety of landslide-induced tsunami is most commonly caused by accompany-

ing earthquakes that dislodge unstable sections of shorelines and the seafloor as shown in Figure 2.7, which are commonly referred to as submarine mass failures or slumps. Prior to the 1998 Papua New Guinea Tsunami, during which waves reaching up to 15 m killed over 2100 people, the generation of tsunamis due to submarine landslides was considered a rare phenomenon and not considered a major tsunami hazard (Kawata et al., 1999; Tappin et al., 1999; Synolakis et al., 2002; Tappin et al., 2008). Initial modeling that only considered the coseismic seafloor displacement contributing towards the generation of the tsunami failed to reproduce the measured wave heights, giving run-up elevations of less than 2 m (Synolakis et al., 2002), which led researchers to search for evidence of an alternative or additional tsunami generation mechanism. During sea floor mapping investigations, it was discovered that 3.8 to 4.6 km^3 of a seafloor escarpment dropped 380 m as a result of the M_W 7.0 quake (Sweet and Silver, 2003). Further analysis utilizing both the coseismic seafloor displacement and landslide motion produced accurate tsunami run-up elevations, demonstrating the significance of submarine slides in the generation of tsunamis (Heinrich et al., 2001; Synolakis et al., 2002; Imamura and Hashi, 2003; Satake and Tanioka, 2003; Heidarzadeh and Satake, 2015). A similar scale earthquake of M_W 7.1 occurred more than half a century earlier on April 1, 1946 near Unimak, Alaska in the eastern Aleutian Islands that resulted in a massive, highly-directional tsunami, which reached a maximum run-up elevation of 42 m at Unimak Island, killed 167 people in Alaska, California, Hawaii, and the Marquesas Islands, and propagated roughly 15,000 km from its origin reaching Winter Island, Antarctica (Okal et al., 2002). Such strong directivity is a key characteristic of landslide-generated tsunamis with similar behavior having been observed during the 1896 Sanriku, 1929 Grand Banks of Newfoundland, 1983 Nihonkai-Chubu, 1992 Flores Island, 1993 Hokkaido Nansei-Oki tsunami events (Iwasaki, 1997). However, it wasn't until after the turn of the 21^{st} century and the 1998 Papua New Guinea Tsunami that investigations of seafloor bathymetry before and after the 1946 quake led to the discovery of a submarine landslide consisting of 200 - 300 km^3 of seafloor debris, which was determined to have been dislodged by the quake and triggered a tsunami that propagated parallel to the direction in which the slide occurred (Fryer et al.,

2004).

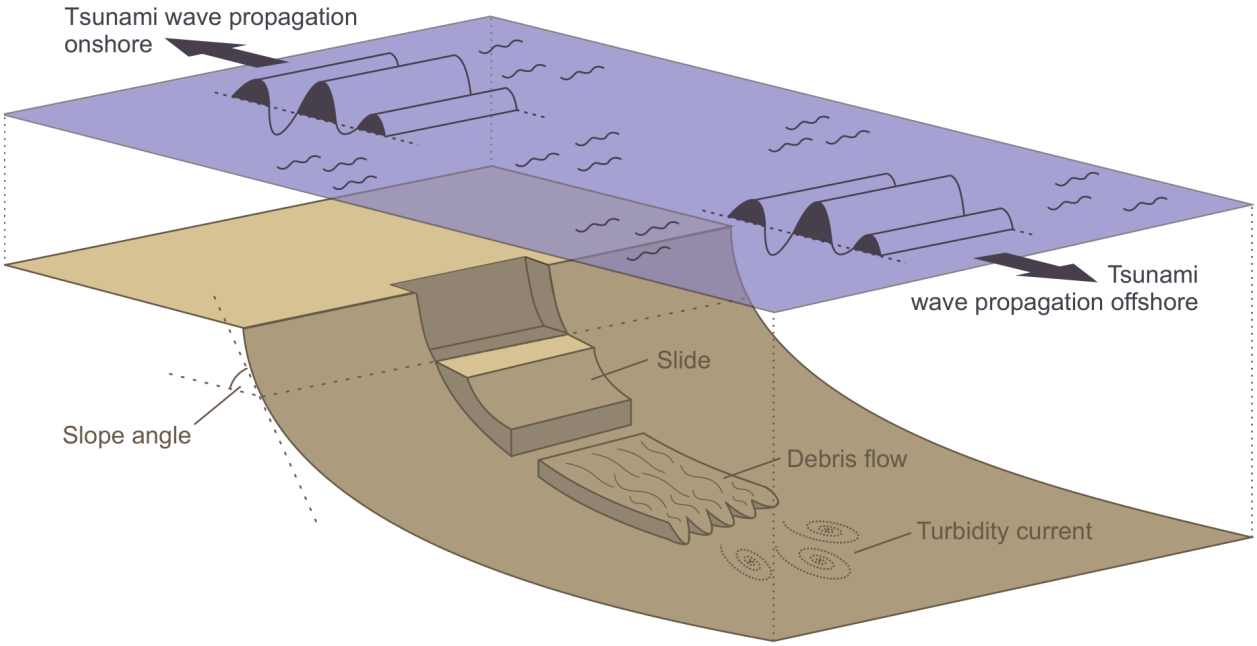

Figure 2.7: Submarine Landslide-Induced Tsunami Generation (Röbke and Vött, 2017).

Similar to the 1998 Papua New Guinea event, the 2010 Haitian earthquake, another M_W 7.0 event, induced a pair of twin tsunamis that were generated by submarine landslides. The worst damage occurred within the Bay of Grand Goâve near the earthquake epicenter, where about 400 m of the coastline failed due to the ground shaking and resulted in tsunami waves that exceeded 3 m (Fritz et al., 2013). The city of Jacmel also experienced tsunamis over 3 m high to the south on the opposite coast of Haiti, demonstrating how important the local bathymetry and geology are with respect to the generation of earthquake-induced, submarine landslides. Concerning the most recent instance of a notable submarine mass failure, a mysterious local tsunami that struck Palu, Indonesia in 2018 took the scientific community by surprise due to the M_W 7.5 earthquake that caused it having occurred along a strike-slip fault since they do not typically result in vertical tectonic plate motions significant enough to produce tsunamis. The tsunami, which reached run-up elevations of roughly 9.0 m, caused 2256 deaths, 4612 non-fatal injuries, the destruction of 5864 homes, and overall damages costing 912 million USD (NOAA, 2019). Through numerical modeling and

investigations of tidal gauge data, run-up elevation measurements, and the before-and-after bathymetry of Palu Bay, it was found that there was a high likelihood that the tsunami was primarily caused by or at the very least amplified by a combination of earthquake-induced submarine and coastal landslides within the Palu Bay through which the Palu-Koro fault runs in addition to any seafloor elevation changes that occurred due to the fault slip during the earthquake (Arikawa et al., 2018; Muhari et al., 2018; Heidarzadeh et al., 2019; Omira et al., 2019; Putra et al., 2019; Sassa and Takagawa, 2019; Takagi et al., 2019; Widiyanto et al., 2019).

When caused by subaerial landslides, these types of events often result in mega-tsunamis, which are named for the extreme wave run-up elevations caused by rapid land mass movements displacing large quantities of water. For example, the 1958 landslide in Lituya Bay, Alaska resulted in a wave that wiped out trees up to an altitude of 524 m on a mountainside as illustrated by Figure 2.8, but did not result in major damages with only 5 casualties having been recorded (Mader, 1999; Fritz et al., 2001; Mader and Gittings, 2002; Fritz et al., 2009; González-Vida et al., 2019). On the contrary, the 1963 landslide at the Vajont Dam in northeastern Italy sent roughly 270 million cubic meters of rock and soil into the reservoir, which caused a tsunami wave that initially destroyed the village of Casso on the opposing mountain slope due to a 260 m wave run-up before it over-topped the dam by up to 245 m, wiping out the villages of Longarone, Pirago, Villanova, Rivalta and Fae below and resulting in the loss of over 2500 lives (Kiersch, 1965; Kilburn and Petley, 2003). A year later in 1964, the Alaskan city of Valdez was obliterated by a series of tsunami waves, including a primary earthquake-induced tsunami due to the M_W 9.2 Great Alaskan or Good Friday Earthquake as well as roughly 20 further tsunami waves generated by both subaerial and submarine landslides, which were induced by the ground motion, that plunged into Prince William Sound (Hansen et al., 1969; Lander, 1996). All told the earthquake and tsunamis resulted in at least 129 deaths and 2.3 billion USD of damage to infrastructure and ships with the tsunamis inflicting damage in British Columbia, Washington, Oregon, California, Hawaii, and Japan and the shaking being registered in every U.S. state except Connecticut,

Delaware, and Rhode Island (Brocher et al., 2014; Parsons et al., 2014).

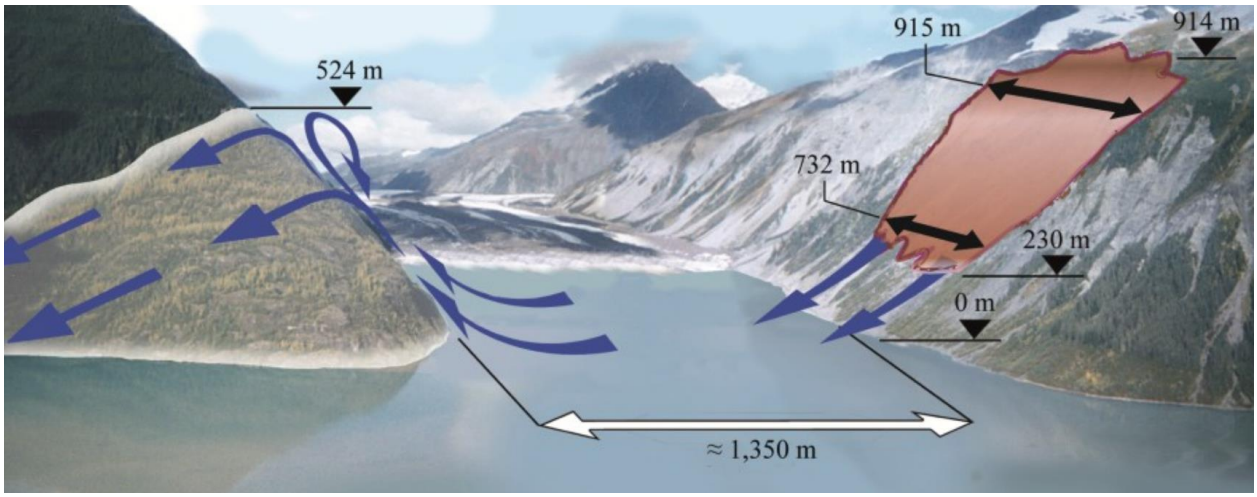

Figure 2.8: Subaerial Landslide-Induced Tsunami Generation in Lituya Bay, Alaska 1958 (Heller and Hager, 2014).

2.1.3 Volcanogenic Tsunamis

Volcanic eruptions, pyroclastic flows, landslides, and debris flows known as lahars may induce tsunami waves when they reach an ocean. For example, on December 30, 2002, subaerial and submarine landslides occurred on Stromboli Island, Italy, when the northwestern flank of the volcanic island known as the Sciara del Fuoco collapsed. The landslides sent roughly 10 million cubic meters of material into the Mediterranean Sea that resulted in a tsunami that caused 760,000 USD in damage to the villages of Stromboli and Ginostra as well as other surrounding Aeolian Islands, reaching the surrounding coasts of Campania, Calabria, and northern Sicily too (Willan, 2003; Tinti et al., 2005; Chiocci et al., 2008). In addition to Stromboli, which has a rich history of past tsunami events with five having occurred during the 20th century, the entire Aeolian archipelago is part of an arc of volcanic island that have also generated tsunamis in the past and risks for future volanigenic tsunamis (Maramai et al., 2005). More recently on December 22, 2018, the Indonesian volcano Anak Krakatau erupted and subsequently collapsed partially, which caused a submarine landslide-induced tsunami in the Sunda Strait that claimed 437 lives, non-fatally injured over 14,059 people,

and destroyed 2,752 homes and 510 ships (Associated Press Jakarta, 2018; The Star, 2018). Additionally, volcanoes have been known to cause tsunamis when lava domes collapse to form calderas, which results in large debris and pyroclastic flows that cause sudden changes in the local sea level that generate tsunami waves. The most notorious event of this type is the 1883 eruption of Krakatau during which roughly two-thirds of the island exploded and then collapsed into a caldera that is occupied by the aforementioned Anak Krakatau volcano today. Although the exact mechanism is widely disputed in the scientific literature, the combined effects of the eruption including air blasts, pyroclastic flows, and final caldera collapse generated a series of towering tsunami waves, which reached a maximum height of 46 m at the city of Merak, Indonesia, and resulted in 36,417 deaths according to Dutch East India Company authorities (Verbeek, 1884, 1886; Symons, 1888; Self and Rampino, 1981; Yokoyama, 1981; Camus and Vincent, 1983; Francis, 1985; Self, 1992; Mandeville et al., 1994; Carey et al., 1996; Choi et al., 2003; Pelinovsky et al., 2005; Mader and Gittings, 2006; Maeno and Imamura, 2011; Paris et al., 2014).

2.1.4 Meteotsunamis

Weather-induced tsunamis or meteotsunamis are produced when large, rapid changes in air pressure occur that lead to Proudman resonance, where the wind and wave velocities become equivalent, which amplifies initially very small waves that continue to grow further due to wave shoaling as depicted in Figure 2.10. The largest meteotsunami on record occurred in Vela Luka Bay, Croatia on June 21, 1978, when sudden, intense flooding due to 6 m waves, which were induced by intense small-scale air pressure disturbances, resulted in millions of dollars in damages. The incident lasted for several hours and came as a complete surprise since it did not coincide with preceding inclement weather conditions (NTHMP, 2019). Similar waves in the 3 to 6 m range have been recorded throughout the Mediterranean and Black Seas where the necessary atmospheric conditions are consistently generated with the most severely hit regions being Ciutadella Inlet on Menorca Island in Spain, Vela Luka Bay on

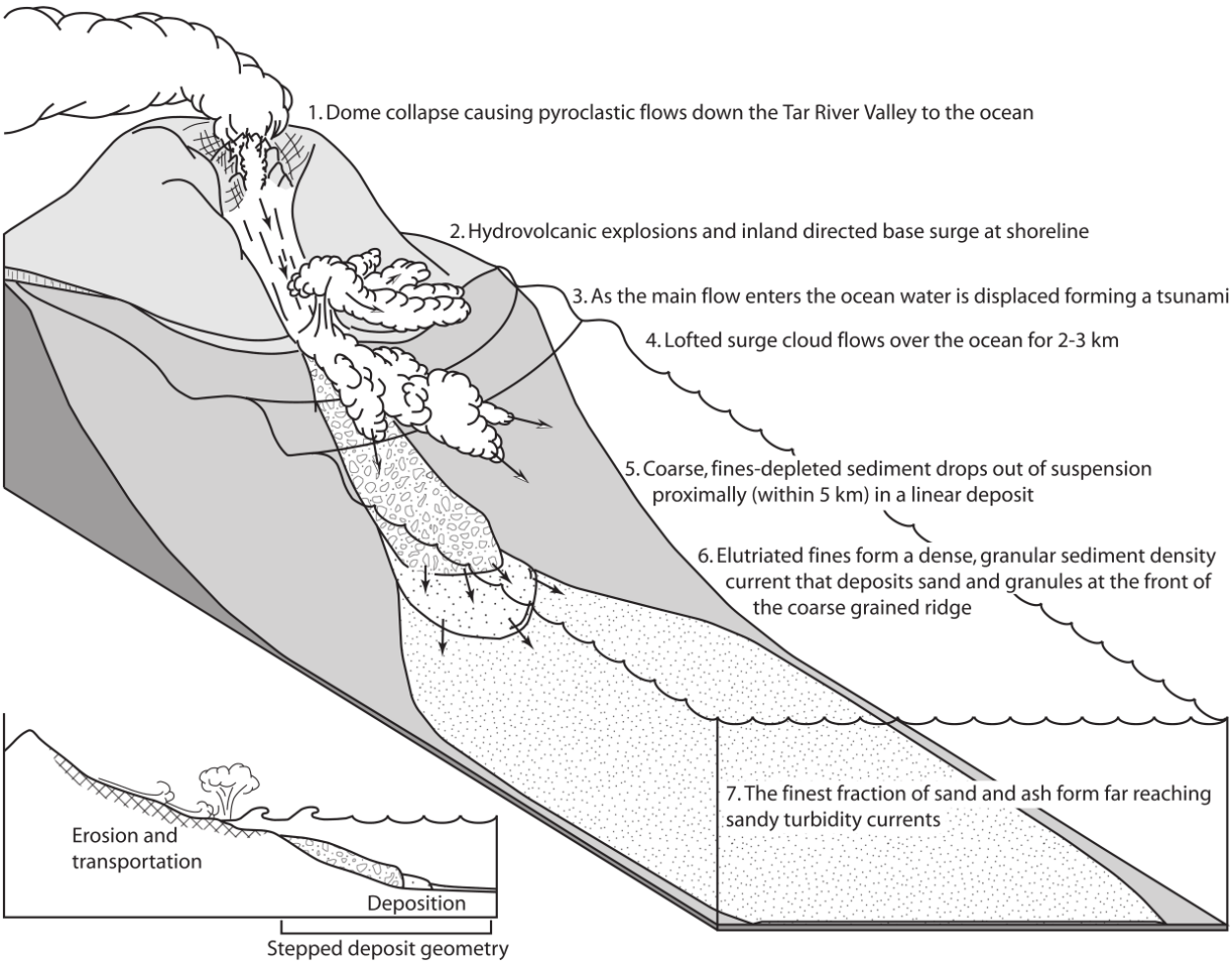

Figure 2.9: Volcanogenic Tsunami Development Stages Based on the 2003 Eruption of the Soufriére Hills Volcano, Montserrat (Trofimovs et al., 2008).

Korčula Island in Croatia, and Mazara del Vallo harbour on Sicily in Italy (Šepić et al., 2015). In contrast to these unexpected European events, meteotsunamis in the U.S. have been induced by squall lines consisting of high winds and thunderstorms that form ahead of cold fronts. For example, a 3 m wave produced by a squall line impacted the coast of Lake Michigan on June 26, 1954, which swept away eight people to their deaths near Chicago. Similarly on June 13, 2013 in Barnegat Inlet, New Jersey, a derecho, which is a more intense form of squall line with sustained winds instead of gusts, was responsible for generating a nearly 2 m wave that injured three people when it struck the jetty on which they stood

(NTHMP, 2019).

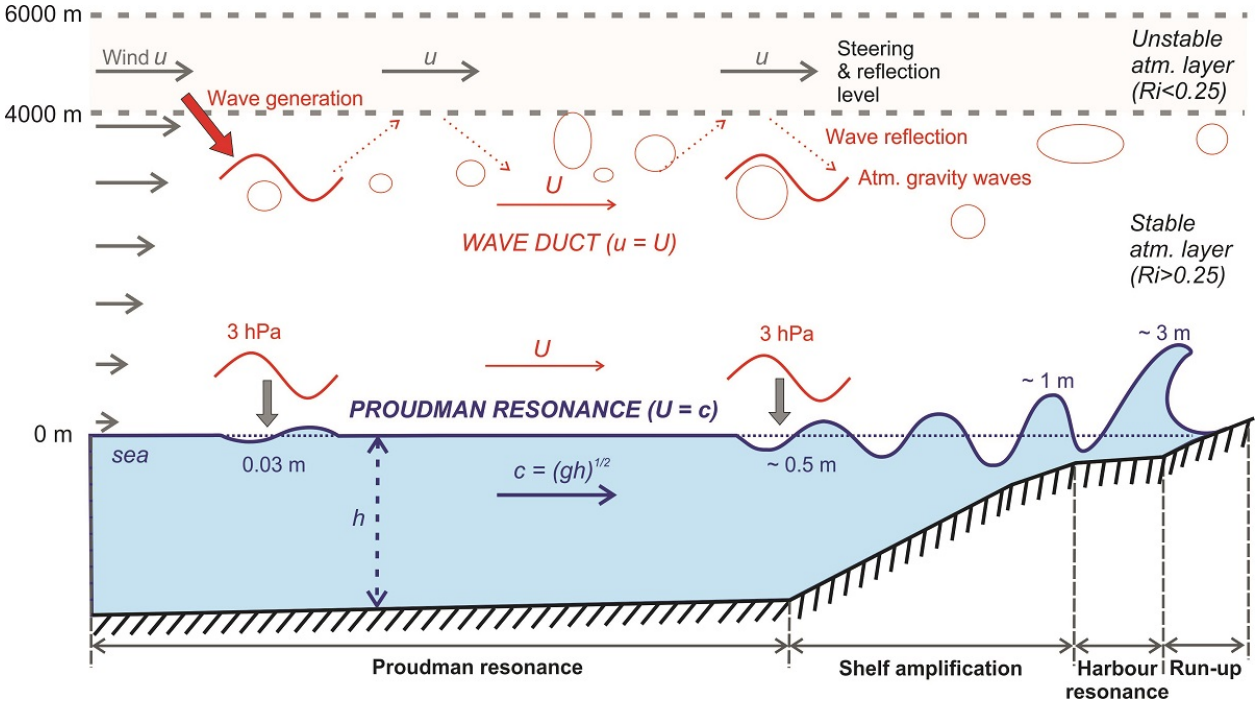

Figure 2.10: Meteotsunami Generation and Evolution (Šepić et al., 2015).

Regardless of the triggering mechanism that causes them it is clear that tsunamis present a serious risk to coastal communities as side effects of other dangerous geophysical and atmospheric conditions, making their impact as a secondary phenomenon that much more devastating. To be adequately prepared for such disasters in the future, the varying levels of risk of tsunamis around the globe must be recognized and understood. A thorough understanding of the primary causes and risks will allow cities to devise evacuation plans and implement improved tsunami detection systems as well as provide geophysicists and engineers with the necessary information to predict the severity of tsunami inundations and improve design provisions for tsunami impact loading.

2.2 The Threat of Future Tsunamis

Even though tsunamis generated by landslides, volcanic eruptions, and meteorological anomalies can result in the same degree of devastation as that of earthquake-induced

tsunamis, their frequency of occurrence is low, whereas tsunamis caused by earthquakes occur quite regularly as shown in Figure 2.11b. For instance, the majority of documented tsunamis, specifically 88% of the 811 tsunamis recorded since 1900 in the Global Historical Tsunami Database, have been of the earthquake-generated variety, making them the greatest source of risk for coastal cities (NTHMP, 2019). These tsunamis have largely occurred in the Pacific Ocean, which is home to the Ring of Fire, a roughly horseshoe-shaped region following the edges of the Pacific Ocean tectonic plate that is riddled with highly-active volcanoes and earthquake-generating faults in the Earth's lithosphere (i.e. the combination of the Earth's crust and the outermost, rigid section of its mantle, which are broken up into tectonic plates) as shown in Figure 2.12. Since tsunamis propagate radially away from their sources many countries surrounding the Pacific Ocean may be affected during each event. For instance, the United States coasts have been ravaged by over 500 tsunamis, which is over 60% of recorded tsunami events (Dunbar and Weaver, 2015).

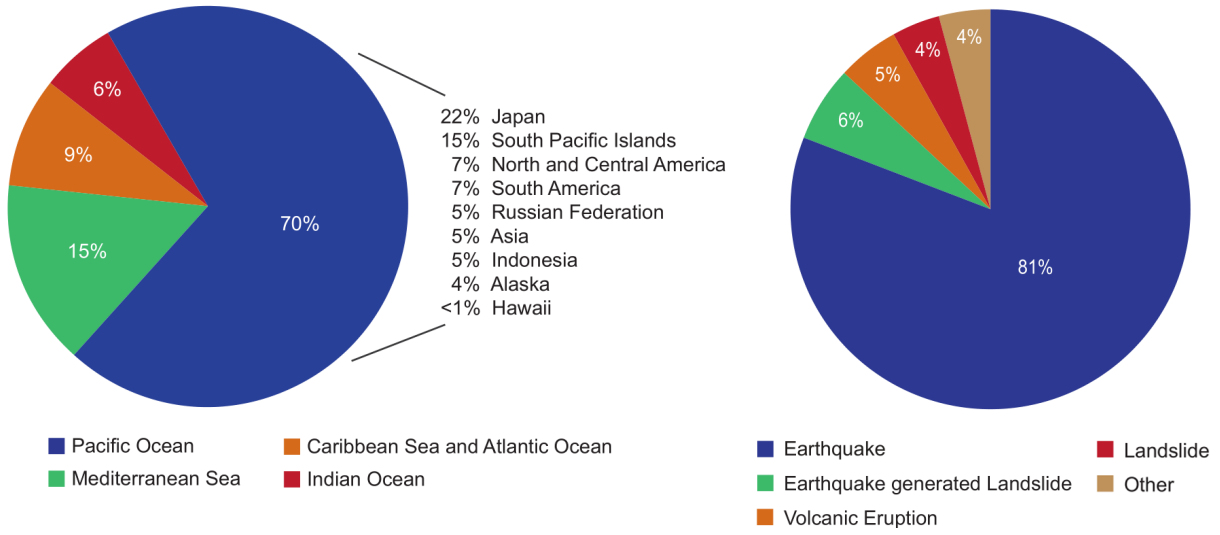

(a) Generation Locations

(b) Generation Mechanisms

Figure 2.11: Global Distributions of Tsunami Generation Locations and Mechanisms from 1610 to 2017 (Adapted from NOAA (2017))

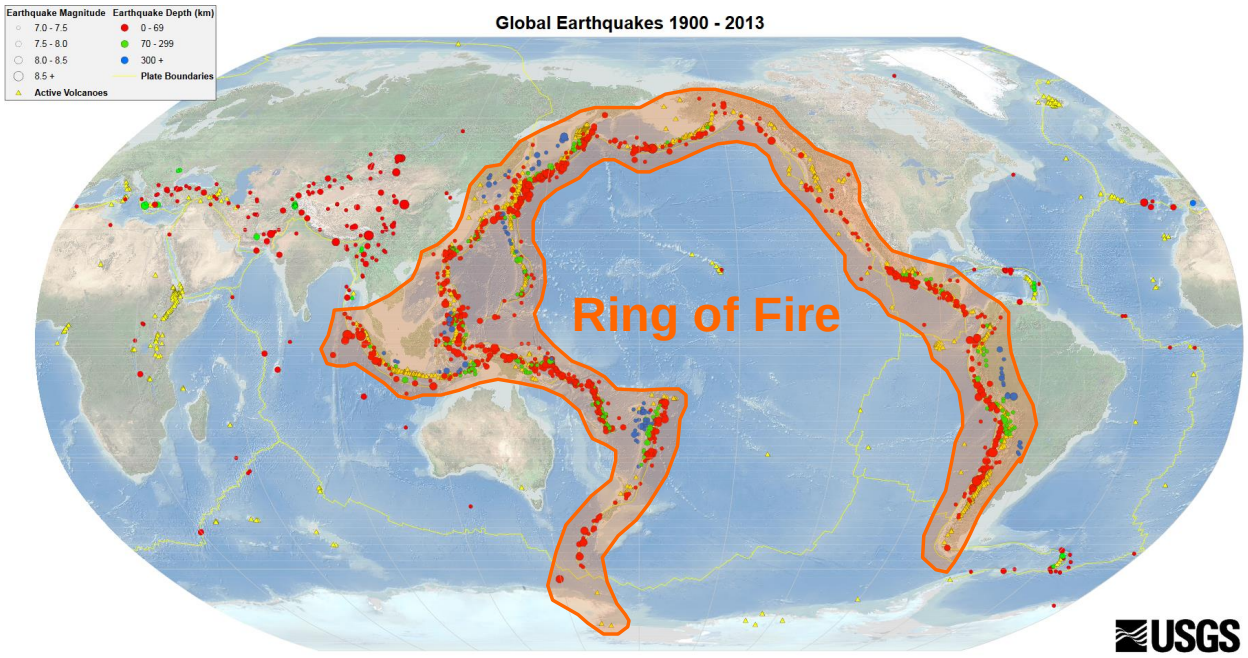

Figure 2.12: Earthquakes and Volcanoes in the Ring of Fire (Adapted from USGS 2013)

2.2.1 Subduction Zone Earthquake Tsunamigenesis

Focusing on tsunamis in the Pacific Ocean, the Ring of Fire has been the source of 78% of the logged in the Global Historial Tsunami Database (NTHMP, 2019), increasing from 70% just two years prior as shown in Figure 2.11a. The primary reason for this is the prevalence of subduction zone fault regions that surround the Pacific Ocean tectonic plate, where one tectonic plate of the earth subducts or descends beneath the other adjacent plate at a convergent plate boundary. During this geologic process, pairs of tectonic plates often become locked due to friction and interlocking of rough edges, which leads to a build up of stress in and deformation of the plates along the fault. Upon reaching a critical level of strain

energy stored in the plates due to deformation, the friction and interlocking forces between the plates are overcome causing the fault to rupture as the plates slip along their edges and the stress in them is released, which generates seismic waves that result in earthquakes. After such large fault slips, the end of the overriding plate above the subducting plate tends to rise up, whereas the overriding plate surface tends to subside above where the subducting plate plunges beneath it into the asthenosphere, which is the ductile portion of the Earth's mantle involved in the convection processes that cause tectonic plate motion. Sudden changes in seafloor elevation due to these plate motions cause large volumes of water to be displaced upward, which results in gravity-driven tsunami waves that propagate away from faults normal to them along their length and radially near their ends.

Earthquakes may occur along any of the three major fault types shown in Figure 2.13, which include reverse, normal, and strike-slip faults; however, tsunami-inducing subduction behavior only occurs for reverse faults along convergent tectonic plate boundaries where they become locked. Subduction zone earthquakes are commonly referred to as megathrust earthquakes due to producing the largest magnitude earthquakes, which can exceed 9.0 on the moment magnitude scale. Conversely, normal faults exist along divergent plate boundaries, where the plates are pulled away from each other due to convection of the Earth's mantle, such as along the mid-Atlantic Ocean ridge. Earthquakes caused by normal faults are among the lowest in magnitude, typically measuring lower than 7.0 on the moment magnitude scale, and the plate motions usually do not result in seafloor elevation changes that cause tsunamis. In the case of strike-slip or transform faults, pairs of tectonic plates displace parallel to their edges, which results in grinding of their edges and a potential for plate locking to occur in a similar fashion as with reverse faults. However, the earthquakes caused by strike-slip faults have smaller magnitudes than those caused by subduction at reverse faults, usually reaching up to about 8.0 on the moment magnitude scale, and do not typically result in tsunamis either. Other minor types of faults are also known to exist too such as oblique faults, which undergo combined reverse and strike-slip fault motions and may potentially generate tsunamis, or listric faults, which have curved fault planes and experience motions

similar to normal faults that would not result in a tsunami.

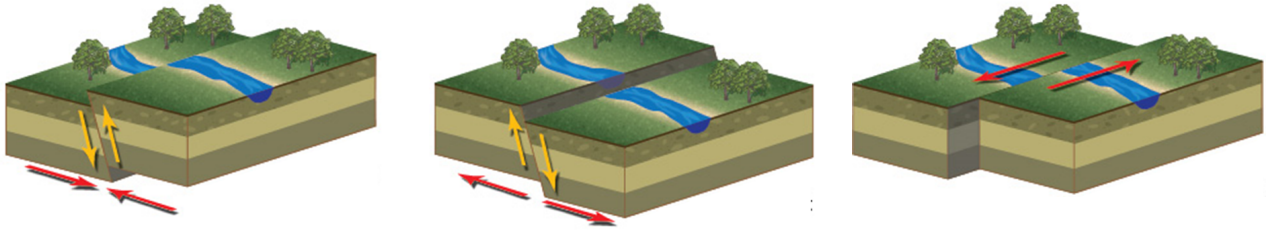

(a) Reverse Fault (b) Normal Fault (c) Strike-Slip Fault

Figure 2.13: Primary Lithospheric Fault Types (NWS, 2005)

Of the sixteen earthquakes with moment magnitudes (M_W) of 8.5 or greater that have occurred since 1900 listed in Table 2.1, thirteen have been megathrust subduction zone earthquakes that occurred at submarine reverse faults and resulted in tsunamis (USGS, 2016). The faults that caused these events are manifested at the seafloor as deep troughs, including the Aleutian, Japan, Kuril-Kamchatka, Peru-Chile, and Sunda Trenches. Other Pacific Ocean subduction zones that have experienced major earthquakes of magnitudes less than 8.5 within the last half century include the Bougainville, Izu Bonin, Kermadec, Marianas, Middle America, Philippine, Ryukyu, and Tonga Trenches. This summary of seismically active subduction zones accounts for all of the Pacific Plate subduction zones besides one, the Cascadia Subduction Zone (CSZ), which has lain dormant for an extended period and currently presents the greatest risk of a megathrust earthquake that may reach up to magnitude 9.0 and trigger massive tsunami inundations.

Table 2.1: Earthquakes since 1900 with $M_W \geq 8.5$

Year	**M_W**	**Earthquake Event**	**Location**	**Fault Type**	**Max Tsunami Height (m)**	**Deaths**	**Total Losses (USD)**
2012	8.6	Aceh	Sumatra, Indonesia	Strike-Slip	1	12	N.A.

2011	9.1	Great East Japan	Tohoku, Japan	Reverse	40.5	20896	360 billion
2010	8.8	Maule	Pelluhue, Chile	Reverse	2.6	525	15-30 billion
2005	8.6	Nias-Simeulue	Sumatra, Indonesia	Reverse	3	915-1314	N.A.
2004	9.1	Indian Ocean	Sumatra, Indonesia	Reverse	30	227898	15 billion
1965	8.7	Rat Islands	Alaska, USA	Reverse	10.7	0	10,000
1964	9.2	Great Alaskan	Alaska, USA	Reverse	67	131	2.3 billion
1963	8.5	Kuril Islands	Kuril Isl., Russia	Reverse	15	N.A.	N.A.
1960	9.5	Valdivia	Lumaco, Chile	Reverse	25	1000-7000	3.4-6.8 billion
1957	8.6	Andreanof Islands	Alaska, USA	Reverse	16	0	5 million
1952	9.0	Severo-Kurilsk	Kamchatka, Russia	Reverse	18	2336	N.A.
1950	9.0	Assam-Tibet	Medog, Tibet	Strike-Slip	N.A.	4800	N.A.
1946	8.6	Unimak Island	Alaska, USA	Reverse	42	167	N.A.
1938	8.5	Banda Sea	Indonesia	Oblique	1.5	N.A.	N.A.

1922	8.5	Vallenar	Atacama, Chile	Reverse	9	1000	5-25 million
1906	8.8	Ecuador-Colombia	Esmeraldas, Colombia	Reverse	5	500-1000	N.A.

2.2.2 Cascadia Subduction Zone

As shown in Figure 2.14, the Cascadia Subduction Zone stretches from northern Vancouver Island down to northern California and has not experienced a megathrust earthquake since the year 1700 based on comparisons of Japanese records of an orphan tsunami (i.e. a transoceanic tsunami inundation where the earthquake that generated it was locally undetectable due to how far away it occurred) and geological investigations (Atwater et al., 2015). The Cascadia Subduction Zone is comprised of a set of convergent plate boundaries where the Explorer, Juan de Fuca, and Gorda Plates sink beneath the continental North American Plate, which has been shown to have an extensive, recurring history of megathrust earthquake events. For example, Atwater and Hemphill-Haley 1997 compared prior work (e.g., Adams 1990; Atwater 1987, 1992; Clarke and Carver 1992; Darienzo and Peterson 1995; Meyers et al. 1996; Nelson 1992a,b; Nelson et al. 1996; Peterson and Darienzo 1996; Shennan et al. 1996) to their own investigation of Willapa Bay, Washington, demonstrating that seven major earthquakes with magnitudes that likely exceeded 8.0 occurred along the Cascadia Subduction Zone over a period of roughly 3500 years prior to the year 2000 with a mean recurrence interval in the range of 500 to 540 years. This range was determined by surveying outcrops along the Willapa and Niawiakum rivers where soil layers, marine diatom fossils, and radiocarbon dating were used to show that land that once existed as coastal marshes or forests had experienced tsunami inundations and subsided due to subduction zone earthquakes, becoming lower-lying estuarine wetlands or mudflats. Similar studies carried out by Witter et al. 2003 at the Coquille River estuary in southern Oregon revealed that

twelve major earthquake events took place over an approximately 6700 year period with an average recurrence interval ranging from 570 to 590 years. Further evidence of organic and sedimentary tsunami deposits have been found along the Oregon coast at Sixes River (Kelsey et al., 2002) and Bradley Lake (Kelsey et al., 2005), which showed thirteen major seismic events occurred about once every 500 years dating back over the last 7000 years after the last eruption of Mount Mazama in Oregon.

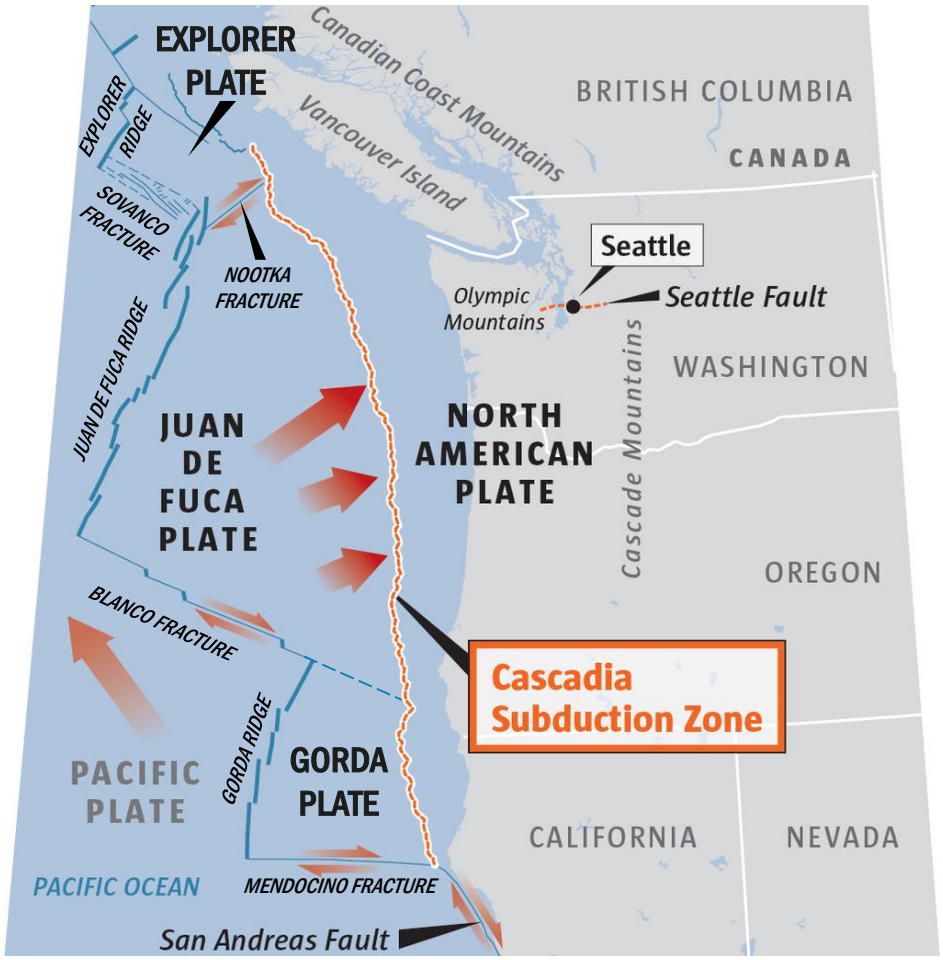

Figure 2.14: Cascadia Subduction Zone Plate Tectonics

Whereas the aforementioned investigations relied upon studying onshore conditions left behind by earthquakes and tsunamis, researchers such as Adams 1990, Goldfinger et al. 2003, Goldfinger et al. 2008, and Goldfinger et al. 2012 focused on analyzing seafloor turbidites, which are the sedimentary remnants of turbidity currents that consist of rapidly-flowing

mud or sand-laden water. These avalanche-like debris flows are set in motion by severe earthquakes and eventually settle on the abyssal planes of the ocean floor to form sedimentary rock. Adams 1990 found turbidite deposits in drilling cores at four sites spanning 580 km of the Washington and Oregon coasts, indicating that major earthquake events occurred thirteen times with a mean recurrence interval of 590 ± 170 years. Similarly, Goldfinger et al. 2003 collected a series of seafloor drilling cores along the entire Cascadia Subduction Zone in order to determine the frequency of strong ground motion events, which showed signs of eighteen major quakes. Goldfinger et al. 2012 conducted further analysis on the data gathered by Goldfinger et al. 2003 and Goldfinger et al. 2008, coming to the conclusion that during the last 10,000 years nineteen to twenty earthquakes occurred where the entire Cascadia Subduction Zone ruptured in addition to twenty-one to twenty-four partial rupture earthquakes where only portions of the subduction zone slipped.

In an attempt to combine all of the empirical data gathered to date while updating the United States National Seismic Hazard Maps, Petersen et al. 2014 arrived at a recurrence interval of 526 years for major Cascadia Subduction Zone earthquakes with moment magnitudes of 9.0 or more. However, it should be noted that in all of the sequences of major earthquake dates determined by the aforementioned researchers that there were large gaps of up to about 1000 years where no earthquakes occurred, but also that there were clusters of three to four earthquakes within 1000-year periods. Thus, even though the given recurrence interval was chosen to provide the best, average estimate based on all of the paleoseismic data gathered since the late 1980s, it must be viewed with caution since much shorter recurrence intervals have been observed to occur in clusters somewhat periodically in the past.

The scale of the impact that a magnitude 9.0 Cascadia Subduction Zone earthquake-induced tsunami would have on coastal communities would be of global proportions. Based on the aforementioned paleotsunami research as well as modern documentation of similar disasters, a tsunami of this magnitude would be capable of inundating the entire U.S. west coast, Hawaii, Alaska, Central and Southern America, Japan, Southeast Asian island nations, and possibly Oceania too. Hence, conducting further investigations of tsunami impacts on

coastal structures is of paramount importance.

Chapter 3

PRIOR TSUNAMI IMPACT RESEARCH

To mitigate losses of the magnitude that would be associated with a M_W 9.0 CSZ earthquake-induced tsunami, such as those for the 2004 Indian Ocean and 2011 Japanese tsunamis described in Section 2.1 - The Destructive Nature of Tsunamis, significant improvements in terms of structural design methods, particularly the determination of tsunami wave impact forces, are required. Owing to this need, considerable engineering research efforts have been dedicated in recent years towards improving structural load estimation methods for the design of new infrastructure and assessment of the existing built environment. These efforts have been focused on a range of tsunami engineering topics, including tsunami generation and propagation from ocean waters to coasts, tsunami run-up elevations resulting from inundation flows over land, tsunami wave impact loading on structures, wave transported debris impact loading (Nouri, 2008; Paczkowski et al., 2011; Naito et al., 2014), and design methods for tsunami-resistant structures (e.g., Yeh 2007; Riggs et al. 2011; Robertson 2014). The chief focus of this dissertation is upon tsunami wave loading of structures; however, in-depth knowledge of tsunami behavior in oceans, near coasts, and on land as well as the methods used by researchers to simulate these phenomena is essential to being able to conduct physically realistic experimental or numerical simulations of tsunami events.

3.1 Tsunami-like Wave Generation and Propagation

Tsunami generation as described in Section 2.1 - The Destructive Nature of Tsunamis, where vertical displacement of water due to vertical sea floor motions caused most commonly by earthquakes, volcanic activities, or landslides, has not been directly replicated in the vast majority of experimental and corresponding numerical model validation work that has been

conducted to date. Instead, tsunamis are commonly idealized either as single solitary waves generated by a piston-type wavemaker that are forced to shoal and break as they travel over sloped beach bathymetries, or, as dam-break generated waves, where a gate or valve confining a reservoir of water is suddenly released to flow under the influence of gravity alone, which results in a broken bore-like wave soon after the release due to the almost immediate shock that forms when a reservoir is released from rest. Neither approach produces waves that are truly tsunami-like since tsunamis are initiated as wave trains that consist of multiple solitary-like waves, which transform to broken, bore-like flows on land after shoaling and breaking. However, both approaches replicate specific aspects of tsunami behavior during tsunami events that they are intended to mimic.

For instance, solitary waves scaled to match tsunami proportions will accurately replicate shoaling, breaking and initial inundation behavior, but often result in lesser run-up elevations and shorter duration inundations due to wavemaker device limitations in terms of the water volumes they can displace. Such waves subject structures to both initial impulsive loading due to broken wave fronts and sustained, post-impact loading due to the initial lengths of such waves, albeit for a limited time compared to an actual tsunami, where multiple waves and larger water volumes maintain significant inundation depths (Simamora et al., 2007; Goseberg, 2013; Goseberg and Schlurmann, 2011, 2014). On the other hand, dam-break waves do not replicate the tsunami propagation and shoaling phases. Dam-break waves produce turbulent, broken bore-like wave fronts that are intended to be similar in nature to the initial tsunami impact phase of an inundation. This also results in highly-transient wave impact forces being imparted to structures, but without a sustained post-impact flow (Nouri et al., 2010; Moon et al., 2015). To achieve similar post-impact behavior with the dam-break method, very large initial reservoir volumes would be required to maintain a sustained inundation flow, which is typically not the case in such simulations. In an attempt to overcome inundation flow duration limitations due to wavemaker capacities, Tomiczek et al. (2016) and Tomiczek et al. (2017) devised an experimental setup that combined a shoaling, long, solitary wave generated by a piston-type wavemaker with a continuously pumped flow

to better capture the post-impact flow that was observed during the 2011 Tohoku, Japan tsunami.

The solitary wave and dam-break methods work well in both laboratory and numerical modeling settings, but they fail to produce tsunami travel time estimates or model tsunami propagation across oceans and the subsequent run-up process, which consists of wave shoaling and inundation flow. If a purely numerical approach is taken, sea floor displacement profiles due to earthquakes or other submarine tsunamigenic phenomena are used as initial conditions at the ocean surface above where they occur. The accuracy of such methods at simulating tsunami wave propagation and run-up largely depends on the characteristics of the numerical methods being employed and the assumptions that come with each method. For example, the Navier-Stokes equations as defined by Equations 6.8 and 6.9 provide a full 3D description of all possible incompressible, viscous fluid flows. However, except for use in modeling very localized regions of tsunami inundations, where Reynolds-Averaged Navier-Stokes, Large-Eddy Simulation and Smoothed-Particle Hydrodynamics models are often used, the Navier-Stokes equations and alternatives such as Lattice Boltzmann Methods are impractical to use as a basis for ocean scale tsunami propagation simulations due to their mathematical complexity and the computational resources required to accurately model tsunami behavior in 3D. The most common alternative approaches used in practice to model tsunamis are based upon varying forms of the non-linear shallow water equations (NLSWE), which are a 2D depth-integrated form of the Navier-Stokes equations assuming a hydrostatic pressure distribution, and the Boussinesq equations, which are another 2D depth-integrated form of the Navier-Stokes equations that include higher-order derivative terms to model non-hydrostatic pressure distributions. The Boussinesq equations work well for long waves in deep ocean waters (i.e. shallow water waves) and they model frequency dispersion effects too, which are not accounted for by the NLSWE; however, difficulties arise when waves reach dry land since the treatment of wetting and drying in the context of the Boussinesq equations requires the use of complicated moving shoreline algorithms. Some researchers have attempted to remedy this deficiency by devising hybrid methods that tran-

sition from using the Boussinesq equations to the NLSWE based on the local depth where waves are propagating such that the NLSWE are used both near shore and for over land inundations. On the other hand, researchers have attempted to improve the NLSWE through the development of non-hydrostatic models, which are augmented forms of the traditional NLSWE that include frequency dispersion.

A large number of software tools implementing these two sets of governing equations using a variety of numerical methods have been developed over the last several decades. For example, the Boussinesq equations were used as the basis of software packages including the finite volume method-based Celeris (Tavakkol and Lynett, 2017), the finite difference method-based FUNWAVE (Kirby et al., 1998; Shi et al., 2016), COULWAVE (Lynett et al., 2008), which allows the user to choose between high-order finite difference or finite volume methods, and many other similar codes (e.g., Wei and Kirby 1998; Tonelli and Petti 2013; Judge et al. 2018). Similarly, a significant number of NLSWE-based tools have been developed over the years as well, including the finite volume method-based GeoClaw, which is a subset of the Clawpack (Conservation Laws Package) geared towards solving geophysical problems such as tsunami propagation that uses adaptive mesh refinement (AMR) and parallelism to speed up computations in large domains (Mandli et al., 2016; Clawpack Development Team, 2019), the finite difference method-based MOST (Method of Splitting Tsunami), which is used by the National Oceanic and Atmospheric Administration (NOAA) for tsunami inundation simulations (Titov and Gonzalez, 1997; NOAA, 2006), the finite difference method-based, non-hydrostatic SWASH (Simulating WAves till SHore) (Zijlema et al., 2011), and a wide array of similar tools (e.g., Hu et al. 2000; Hubbard and Dodd 2002; Titov et al. 2011; Takabatake et al. 2019). Such models are commonly validated with benchmark experimental data sets (e.g., Synolakis 1987; Gedik et al. 2005; Charvet et al. 2013). For example, the solitary wave inundation of a circular island studied by Briggs et al. (1995) has been used to study the effectiveness of inundation modeling software in terms of run-up elevation and wave refraction behavior.

3.2 Tsunami-Induced Forces on Coastal Structures

Using these state-of-the-art methods to generate tsunami-like waves in laboratory and numerical models, a multitude of studies focusing on wave impact loads acting on coastal structures have been conducted. These studies have investigated the effects of tsunami inundations on both individual structural elements and entire structures. For instance, a large body of work has been dedicated towards characterizing and developing estimation methods for wave impact demands on single columns, walls, and decks. Similarly, wave impact demands have been investigated for full structures including commercial and residential buildings, bridges, wharves, jetties, breakwaters, dikes, seawalls. Due to the fact that the vast majority of the momentum transported by waves, but especially tsunamis, is directed horizontally, most of the studies aimed at analyzing wave loading have focused on horizontal forces and the effects they have on structures.

3.2.1 Horizontal Forces on Prismatic Structures and Components

Going back to the seminal papers of Bagnold (1939), Mitsuyasu (1966), and Cross (1967), who provided some of the first effective equations for estimating horizontal impact forces on walls due to breaking and bore-like wave fronts, a large body of work focused on wave impact forces acting on vertical wall structures has been carried out over the last century (e.g., Tsai and Jeng 1990; Hattori and Arami 1992; Ramsden 1993, 1996; Allsop and Calabrese; Arikawa 2009; Cuomo et al. 2010; Paczkowski et al. 2011; Robertson et al. 2011; Ramachandran et al. 2012; niga et al. 2013; Linton et al. 2013; Robertson et al. 2013b; Cunningham et al. 2014; Frandsen and Bérubé 2015; Tremblay and Frandsen 2015; Carratelli et al. 2016). Of particular interest is the work of Ramsden and Raichlen (1990), which expanded upon the fundamental developments of Cross (1967) by providing an improved force estimation equation. Additionally, Ramsden and Raichlen (1990) noted that the maximum wave force occurred after the maximum run-up elevation on a wall was reached and that the corresponding wave force magnitude was less than the hydrostatic force based on the run-up

elevation due to negative vertical flow acceleration. Others attempted to approach the problem of wave impact loading using analytical methods. For example, Cooker and Peregrine (1990) developed a successful method for determining breaking wave impact pressures based on Lagrange's theory of pressure impulse, which matched experimentally measured vertical pressure distributions closely over the entire wall height.

In addition to planar, wall-type structures, horizontal wave demands on slender vertical elements such as columns and piles have been investigated thoroughly too. Such studies are of key importance for analyzing tsunami loading of bridge piers, wharf piles, bottom story columns in washed-out buildings, and other elevated structure vertical supports. Experimental studies providing force estimates as well as necessary data for validation of numerical models have been conducted extensively (e.g., Tanimoto et al.; Chakrabarti et al. 1997; Árnason 2005; Nouri 2008; Árnason et al. 2009; Nouri et al. 2010; Santo and Robertson 2010; Al-Faesly et al. 2013; Nistor et al. 2011; Al-Faesly et al. 2012; Manawasekara et al. 2013; Palermo et al. 2013; Paulsen 2013; Cunningham et al. 2014; Shafiei et al. 2016).

Lateral wave impact demands on entire structures have been studied in-depth as well, where scaled-down, idealized models are typically employed (Asakura et al., 2000; Simamora et al., 2007; Fujima et al., 2009; Bridges, 2011; Bridges et al., 2013; Manawasekara et al., 2013; Nakamura et al., 2011; Sakakiyama, 2014; Bremm et al., 2015; Thomas et al., 2015; Johnson, 2016b; Pringgana, 2016; Tomiczek et al., 2016; Foster et al., 2017; Tomiczek et al., 2017; Baragmage et al., 2018; Chuang et al., 2018; Yang et al., 2018). Building tests have covered a wide range of realistic structure types too, including masonry (Shoji et al., 2014), reinforced concrete (Pacheco and Robertson, 2005; Macabuag et al., 2014; Yokoyama and Robertson, 2014; Petrone et al., 2017), steel frame (Cheung and Robertson, 2014), and timber buildings (Arikawa, 2009; van de Lindt et al., 2009; Linton et al., 2013) as well as buildings with openings (Lukkunaprasit et al., 2008; Mizutani et al., 2014; Wüthrich et al., 2018). Furthermore, coastal defense structures such as breakwaters, dikes, revetments, and seawalls have been investigated both separately (Marinski and Oumeraci, 1992; Mizutani and Imamura, 2001; Cuomo et al., 2011; Thomas and Cox, 2012; Tonelli and Petti, 2013; Trem-

blay and Frandsen, 2015; Oda et al., 2018) as well as in combination with other structures protected behind them (Sakakiyama, 2014).

3.2.2 Vertical Forces on Prismatic Structures and Components

Although horizontal tsunami-induced forces may be the most common source of structural demands during a tsunami event, the effects of vertical forces must also be considered as a significant source of structural demands. During tsunami inundations, buoyancy forces as well as hydrodynamic uplift forces have contributed significantly to failures of concrete floor slabs. When lateral support-providing concrete walls are not present, tsunami inundations knock out weak, non-structural walls and flow around the remaining columns. In such cases, hydrostatic buoyancy loading is the primary source of uplift. However, if concrete walls are present, then the possibility exists for walls to redirect the flow upward into floor slabs in corners where walls and slabs meet, which significantly increases the demand due to resulting hydrodynamic impact forces. Failures due to both types of behavior were noted by Saatcioglu et al. (2005) who investigated the aftermath of the 2004 Indian Ocean Tsunami. Similarly, large cracks and failures due to uplift forces were noted by Chock et al. (2013) in their review of structural performance during the 2011 Tohoku, Japan Tsunami. Based on the field evidence provided by such studies, the damaging effects of buoyancy forces alone or in combination with vertical hydrodynamic impact forces present a necessary topic for further investigation.

Prior studies that have investigated the effects of vertical loads on structures and attempted to quantify them are common for bridges, jetties, and other deck-type structures (e.g., Tirindelli et al. 2003; Cuomo et al. 2007; Liu et al. 2008; Cuomo et al. 2009; Sheppard and Marin 2009; Bradner et al. 2011a; Lau et al. 2011; Hayatdavoodi et al. 2014; Mazinani et al. 2014; Seiffert et al. 2014; Araki 2015; Azadbakht and Yim 2015b; Motley et al. 2016; Crowley et al. 2018; Winter et al. 2018); however, there is a limited quantity of investigations focusing on elevated building structures. For instance, Honda et al. (2014) conducted exper-

iments to measure forces on a Piloti-type structure supported above the ground by a central core at its base. Similar studies have been made for pile-supported elevated structures too (Wiebe et al., 2014; Park et al., 2017; Lomonaco et al., 2018; Alam et al., 2019). In addition to characterizing the horizontal and vertical wave loads acting on elevated structures, Goda's design equations for impulsive and non-impulsive pressures acting on a composite breakwater were adapted by Wiebe et al. (2014) for use in estimating wave forces acting on elevated structures to compare to their experimental data, which resulted in a good match between the augmented application of Goda's method and the experiments (Goda, 1973, 1974).

Some researchers have also attempted to directly model upward wave redirection into floor slabs and decks due to walls that suddenly arrest horizontal tsunami inundation flows. For instance, Robertson et al. (2008) experimentally investigated combined wall-slab structures, showing that the resulting uplift force on floor slabs is maximized when the incoming tsunami bore has a depth equivalent to the structure story height. Due to the highly-transient and complex nature of such impacts that involve the possibility of trapping air in the wall-slab corner and depend highly on the wave front shape and size, Chen et al. (2019) opted to develop a force estimation method based on measured impulse instead of force since impulse is much more consistently predictable quantity than peak forces.

3.2.3 Forces on Deck Type Structures

Similar to prior research that has focused on buildings and other vertical structural elements, the vast majority of researchers that have studied tsunami loading of bridges and other deck type structures focused on estimating total or resultant horizontal and vertical forces using long wave flumes with either a piston-driven paddle (e.g., Araki et al. 2011; Araki 2015; Bradner et al. 2011a,b; Chen et al. 2014; Cuomo et al. 2007; Guo et al. 2015; Iemura et al. 2007; Lomonaco et al. 2016; Martinelli et al. 2011; Mazinani et al. 2014; Scharnke and Hennig 2015; Toshimitsu 2014; Tirindelli et al. 2003, 2004) or a reservoir with a releasable gate (e.g., Shoji and Moriyama 2008; Lau et al. 2011; Shoji et al. 2011; Hoshikuma et al.

2012; Shoji et al. 2012; Hartana et al. 2013; Nakamura et al. 2013; Koon and Lau 2015; Wong 2015; Motley et al. 2016; Winter et al. 2018) to generate dam break type waves. A wide variety of bridge superstructure geometries have been assessed both experimentally and numerically. Prior studies have varied the superstructure super-elevation (e.g., Bricker and Nakayama 2014; Hayashi et al. 2014), the number of girders (e.g., Hoshikuma et al. 2012; Kerenyi et al. 2009; Nakao et al. 2013b), the deck width and thickness (e.g., Azadbakht and Yim 2015b; Hoshikuma et al. 2012; Nakao et al. 2013b), and the superstructure skew angle relative to the river or channel it spans (e.g., Wong 2015; Motley et al. 2016). Additionally, researchers have studied the effects of streamlining the superstructure by varying the deck shape, adding fairings, and perforating superstructure components (e.g., Abukawa et al. 2013; Kerenyi et al. 2009; Nakao et al. 2012; Rahman et al. 2014; Zhang et al. 2012).

As a part of the studies on the influence of girder spacing on bridge forces during a tsunami impact, the effects of trapped air between girders underneath bridge decks were studied. At low velocities (i.e. roughly 30% of the speed of sound in air), air behaves as a nearly incompressible fluid, meaning its volume will not change noticeably when compressed by an incoming tsunami wave that traps in between girders. Since its volume will not change notably, the trapped air will effectively increase the volume of water displaced by bridge superstructures, resulting in increased buoyancy forces. Due to this effect, it was observed that uplift forces increased significantly due to air trapped under bridges unless deck venting or end gaps were provided, which prevented the entrapment of air and reduced uplift forces (Cuomo et al., 2009; Bricker et al., 2012; Gaeta et al., 2012; Bricker and Nakayama, 2014; Hayatdavoodi et al., 2014; Salem et al., 2014; Araki, 2015; Seiffert et al., 2015; Azadbakht and Yim, 2016a; Xu et al., 2016, 2017).

3.3 Effects of Macro-scale Roughness

Although the large amount of research focused on individual structures and their components provides useful insights concerning tsunami impact loading effects, the primary focus of this study is on cases where multiple macro-scale roughness elements were included, re-

sulting in shielding and wave channeling effects not present for a single structure during the tsunami inundations being tested and modeled by researchers. Within this branch of research, adjacent or neighboring structures are commonly referred to as macroscale roughness elements (MREs). These types of studies emphasize the effects of neighboring structures on a specific test or design structure in terms of how they shield a design structure by redirecting incoming tsunami waves away from the design structure or how they focus waves into constricted channels aligned with a design structure. Due to local variations in inundation depth and flow velocity caused by adjacent structures, shielding and channeling effects result in decreased and increased structural demands, respectively.

3.3.1 Shielding Effects

Shielding effects in general result in decreased structural loads, but the degree to which loads are decreased depends highly on the distance between adjacent structures and a design structure. For instance, Simamora et al. (2007) experimentally investigated tsunami-like wave loading of six symmetric configurations of 1 to 12 box-shaped MREs, where the spacing of the MREs was varied. Their results demonstrated that a fully-shielded design structure experiences less streamwise load the closer the neighboring structure is to it in the wave propagation direction. These tests were numerically simulated by Nakamura et al. (2011), providing accurate inundation depth predictions, but inconsistent peak wave forces, which highlights one of the main difficulties in numerical modeling of complex fluid-structure interactions of a wave with multiple structures. Similarly, Bridges (2011), Bridges et al. (2013), and Yang et al. (2018) demonstrated that streamwise forces increase with increasing distance between a fully-shielded structure and an MRE causing the shielding by conducting tests on a broad range of macro-roughness element configurations utilizing box-like structures.

A further example of shielding effects was provided by Moon et al. (2015) who generated dam-break waves to investigate tsunami loading of two groups of cube-like macro-roughness elements, where one and two rows of MREs were used. They observed that the presence

of a second row drastically reduced the pressure on the offshore faces of the structures in the second, onshore row, demonstrating a clear shielding effect. What was more striking though, was that the close proximity of the two rows of MREs resulted in an increased pressure on the shoreward faces of the structures in the first, offshore row, which reduced the total streamwise forces acting on these MREs. This phenomenon is a result of increases in free-surface elevation between the two rows of MREs, where the flow is choked and redirected.

In addition to reducing forces on individual structures, shielding effects due to macro-roughness elements in the form of buildings help to reduce maximum tsunami run-up elevations. Buildings redirect tsunami waves diagonally from their edges, which results in an increase of alongshore wave momentum and a reduction in shoreward wave momentum. Such shoreward momentum losses prevent tsunami waves from traveling as far inland since their velocity in that direction is reduced. When considering a large community of coastal structures, multiple interactions of this sort occur in rapid succession that cause redirected waves to interfere with one another, resulting in further losses of shoreward momentum.

For example, Tomita and Honda (2007) numerically simulated the 2004 Indian Ocean tsunami inundation of Galle City, Sri Lanka, demonstrating that tsunami inundation models considering houses and other structures as obstacles result in significant reductions of maximum run-up. Similarly, Goseberg and Schlurmann (2011) elaborated upon the work of Goseberg (2011) who conducted tsunami-like wave inundation experiments on configurations cube-like MREs, where the MREs were either oriented parallel to or 45° away from the incident tsunami wave direction, demonstrating that the MREs significantly reduced the wave run-up elevation compared to when no MREs were present. Additionally, Goseberg (2013) expanded further upon the results of Goseberg and Schlurmann (2011) to produce nomographs for determining the reduction in wave run-up elevation depending on offshore wave amplitude and length, beach slope, and both cross- and alongshore blockage ratios of the MRE configuration.

Whereas all of the previously mentioned research on the influence of macro-roughness elements concentrated on small numbers of MREs, Cox et al. (2008) performed 1:50 scale

laboratory experiments of tsunami waves impacting a large segment of the city of Seaside, Oregon, which were numerically modeled by Park et al. (2013), Qin et al. (2018a), and Qin et al. (2018b). Comparisons of the recorded data showed that the experimental results exceeded the numerical results for free surface elevation and leading wave edge velocity during the initial impact phase of the wave loading. Agreement of flow velocities and inundation depths between experimental and numerical model results worsened as waves propagated onshore through the roughness elements, giving incorrect run-up elevations. These results corroborate those of Tomita and Honda (2007) and Goseberg and Schlurmann (2011) in showing that structures have a significant effect on tsunami inundations and further demonstrate that complex tsunami wave interactions with coastal structures on a community scale have not been captured well using CFD methods in the past as observed with the numerical results of Nakamura et al. (2011) too.

3.3.2 Flow Channeling Effects

On the contrary compared to shielding, channeling effects due to flow channel constrictions typically result in locally increased flow velocities and consequently increased forces due to the dynamic pressure of a flow being proportional to the square of the velocity. This behavior is analogous to the Venturi effect in steady flows, where decreased channel size results in increased velocity, but reduced total pressure. In heavily-developed, urban coastal communities where structures are closely-spaced, the gaps between pairs of structures can act as flow constrictions that produce increased forces on structures further onshore. However, as demonstrated by Simamora et al. (2007), increased forces acting on a design structure due to pairs of structures resulting in flow channeling only occur when such flow constrictions are aligned with the design structure so that the locally amplified flow velocity is directed at its offshore face. The results of Bridges (2011) and Bridges et al. (2013) also demonstrated this phenomenon. They observed that when pairs of MREs were placed so that the design structure was aligned between them, the flow was diverted away from the design structure for

large cross-shore distances between them, whereas for small distances a localized Venturi-like effect caused increased velocities between the MREs that resulted in higher forces acting on the design structure.

Expanding upon the analysis of Bridges (2011) and Bridges et al. (2013) for pairs of MREs, Thomas et al. (2015) focused on how the spacing between two macro-roughness elements influenced the force on a shore-ward test structure. For a pair of roughness elements, the design structure force increases with increased alongshore spacing up to a critical spacing for a given cross-shore distance between the design structure and the MREs. The farther away the MREs were placed offshore from the design structure the larger the critical alongshore spacing became (Bridges, 2011). Thomas et al. (2015) confirmed this behavior for a specific streamwise separation between the design structure and MREs, providing results that show how measured forces, wave run-up elevations, and flow velocities varied for increasing distances between the pair of roughness elements. They demonstrated that all three quantities followed similar trapezoid-like, tri-linear trends with respect to increasing alongshore spacing between the MRE pair, where the force initially increased linearly until it reached a constant plateau value and then linearly decreased.

In addition to conducting experiments with pairs of macro-roughness elements, Bridges (2011) also investigated the behavior of larger numbers of MREs. Of particular interest are the results for trios of MREs with the center MRE aligned with the test structure. Bridges (2011) demonstrated that the test structure force is maximized when the center MRE is moved in the offshore direction and minimized when the center MRE is moved in the onshore direction. This is because these configurations channel the flow toward and away from the test structure, respectively. Also, this effect held true regardless of the streamwise separation of the MREs and the test structure, but the largest forces occurred in the range $3 < x/a < 4$, where x is the streamwise separation between the MREs and test structure and a was the side length of the identical, square MREs and test structure.

Another key channeling effect is a strong dependence on the degree of flow obstruction that is caused by macro-roughness elements. The degree of flow obstruction is quantified

by the blockage ratio, which is defined as $BR = 1 - W_C/W$, where W_C and W refer to the constricted and unconstricted channel widths. When investigating the impact of dam-break generated, bore-like waves on rectangular and circular structures, Nouri (2008) observed that amplified forces due to increased flow velocities caused by flow shielding followed a bi-linear trend, where the force linearly increased from the unblocked channel force at $BR = 0$ until reaching a peak at BR of about 0.25, after which the force linearly decreased for increasing flow blockage. More specifically, Nouri et al. (2010) observed force increases of 25%, 40%, and 25% for blockage ratios of 0.125, 0.250 and 0.375, respectively, when compared to results from tests without flow constriction. These results are cited as the basis for one of the methods included in the ASCE 7-16 Chapter C6 commentary describing how to amplify design forces when channeling effects are present.

One of the major limitations to the vast majority of both experimental and numerical simulations of macro-roughness element effects is that the tsunami wave propagation direction is always perpendicular to the shoreline. During wave shoaling, the change in sea floor depth results in wave refraction that redirects waves to travel progressively more perpendicular to shoreline; however, tsunamis have been observed to arrive onshore flowing diagonally relative to the shoreline. In such cases, oblique wave impacts on structures can result in channeling in regions where orthogonal wave impacts would cause shielding.

In their studies of broken solitary wave impacts on groups of columns and walls, Robertson and Mohamed (2009) and Santo and Robertson (2010) discuss this effect in the context of columns and walls located at the bottom stories of buildings, where non-structural elements have been wiped out. They illustrate the fact that if tsunami inundations impact a structure obliquely, shielding of interior columns and walls is often reduced since the wave can propagate unhindered past exterior elements in a diagonal motion to directly impact interior elements. Significant increases in hydrodynamic forces were observed, particularly for flow blockage ratios exceeding 40%, when the interior columns were not aligned with the exterior columns parallel to the wave flow direction. Also, similar results occurred for obliquely approaching waves that were channeled between exterior columns. The opposite

effect was observed for cases where the columns were aligned with the wave flow direction, where notable decreases in forces were observed, demonstrating that shielding effectively reduces wave force demands.

Channeling effects can also be induced by natural bathymetric and topographic features too. For example, sea floor anomalies such as reefs can cause channeling effects similar to buildings where there are gaps in such features. This phenomenon was observed in the aftermath of the 2004 Indian Ocean Tsunami, where more severe damage was documented in regions between sea floor obstructions. However, when unbroken sea floor obstructions are present, wave run-up and inundation depths were reduced. Lynett (2007) numerically studied how such features reduce tsunami run-up and inundation depth, showing that as the obstruction width-to-height ratio increased so too did the run-up and inundation depth.

3.3.3 Identified Research Gaps

The most significant limitation to these prior studies of the influence of macro-roughness in terms of neighboring structures on resulting tsunami loads for a design structure is the minimal range of cases that have been experimentally tested and numerically modeled. In particular, the biggest void in the field of results is the lack of asymmetric arrangements of neighboring structures relative to a design structure. For instance, nearly all of the studies reviewed in this section used pairs of block-like structures as macro-roughness elements arranged in configurations where the midpoint between a pair of MREs was aligned with the structure being tested or modeled to measure force demands instead of using configurations with asymmetrically-positioned or misaligned MRE arrangements. Additionally, there is a lack of general force prediction methods or equations pertaining to the shielding and channeling effects of adjacent structures with the two most successful examples, Nouri et al. 2010 and Thomas et al. 2015, having only a limited range of applicability in terms of geometric configurations of structures as specified in the ASCE 7-16 Chapter 6 Commentary (ASCE, 2017). Thus expanding the range of applicable adjacent structure configurations as

well as generating a corresponding force prediction model present the most important topics to be investigated in this field of research, making it worthy of being the key focus of this dissertation. Finally, the biggest hurdle to overcome in achieving the goal of developing a widely-applicable force estimation equation based on a large array of MRE configurations is to develop a computational fluid dynamics model capable of accurately reproducing free-surface elevations, flow velocities, pressures, and total forces acting on or surrounding a design structure. As was demonstrated by the numerical modeling difficulties that Cox et al. (2008), Nakamura et al. (2011), Park et al. (2013), Qin et al. (2018a), and Qin et al. (2018b) experienced while trying to accurately reproduce localized experimental results when attempting to model entire communities at once, it is clear that more refined numerical methods are required to obtain consistent results between experiments and numerical models.

Chapter 4

EXPERIMENTAL METHODOLOGY

To evaluate the influence of macro-scale roughness in the form of neighboring structures on the loading of an elevated, coastal structure, tests of a reference case without adjacent structures as well as five adjacent structure configurations were conducted, subjecting the structure to unbroken and broken, tsunami-like wave impacts in the Large Wave Flume (LWF) at the Hinsdale Wave Research Lab (HWRL). To evaluate the effects of the constructed environment on tsunami-induced, structural forces, fluid velocities, free-surface elevation, and the pressures and forces exerted on an elevated structure were measured for the unbroken and broken wave types. The wave naming conventions of unbroken and broken refer to the state of the waves when they arrived at the test structure. For instance, the broken wave collapsed offshore as a spilling wave ahead of the test structure, whereas the unbroken wave propagated as a smooth solitary wave along the flume, breaking onshore past the test structure.

The use of an elevated test structure differs notably from the types of macro-roughness elements presented in Chapter 3 - Prior Tsunami Impact Research, where all of the elements were prismatic structures that rested on flume or wave basin bottoms. This choice of structure type presents the possibility of not only assessing pile-supported coastal structures, but also allows for loads to be measured on a structure as if a prior wave in a tsunami wave train had destroyed non-structural walls on the lower levels thereby reducing the demand since piles alone resist the force imparted by the toe of subsequent incoming tsunami bores. The following sections describe the wave flume, test structure, instrumentation, wave generation methods, and the macro-scale roughness conditions used in the experiments.

4.1 *Wave Flume*

The Large Wave Flume at the HWRL was used to generate the tsunami-like waves that impacted the test structure. The flume geometry and test structure position used for all experiments is shown in Figure 4.1. The coordinate system origin ($x = 0.0$ m, $y = 0.0$ m, $z = 0.0$ m) was set to be at the bottom of the flume in the center of the front face of the wave maker paddle at its rest position with the stream-wise, wave propagation direction denoted as the positive x-direction and the upward, vertical direction designated as the positive z-direction, leaving the positive y-direction to point toward the left flume wall for a Cartesian coordinate system. All dimensions are given in Figure 4.1 except for the floor slab thickness of 0.1524 m, which caused a sudden decrease in the flume depth at bay marker 2 since the first slab was lain on the flume bottom. Since the floor slabs were restrained both above and below to prevent any motion, the region beneath the floor slabs was not filled with soil or other fill material, allowing water to occupy the empty space..

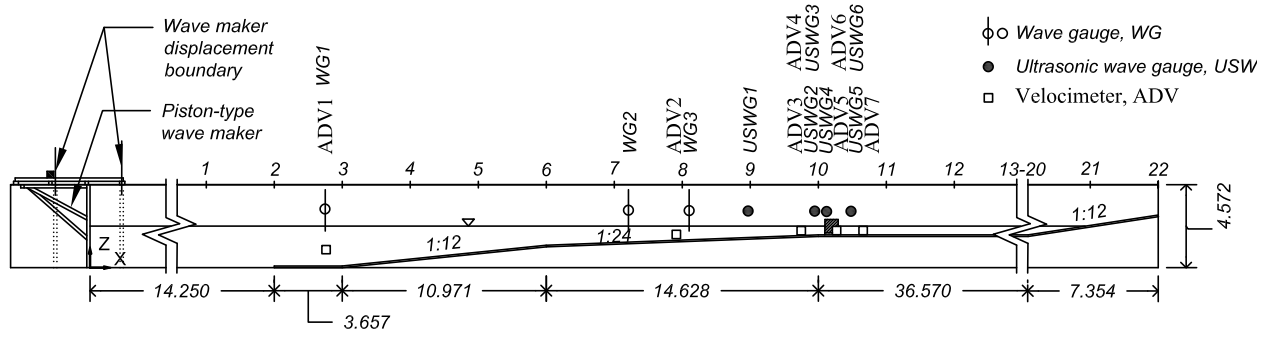

(a) Elevation View

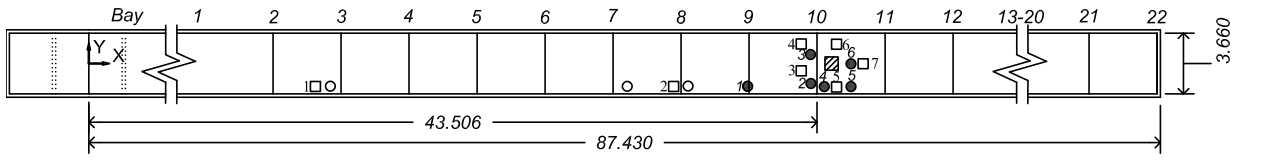

(b) Plan View

Figure 4.1: Large Wave Flume at the HWRL (Alam et al., 2019)

4.2 Test Structure

The test structure is shown along with its overhead, wall-mounted support frame that spanned the flume width in Figures 4.2a and 4.2b. Low-friction bearings that connected the test structure to the support frame allowed for free movement in the stream-wise (x) and transverse (y) directions. The test structure was a reinforced steel box suspended from the support frame that was 0.615 m tall with a 1.016 m square base elevated off of the flume bottom by 0.25 m long legs, beneath which was a 5 mm gap to prevent the legs from touching the flume bottom to avoid vertical forces being absorbed by the flume bottom. Internally, the test structure was supported by a welded frame of 0.0381 m square hollow steel sections. Along the offshore and onshore faces of the test structure, these sections were placed at three even spaces in the transverse direction (i.e. y-direction), whereas along the left and right alongshore faces of the test structure these sections were placed at two even spaces in the streamwise direction (i.e. x-direction). These sections were continued along the top and bottom faces to create closed loops as demonstrated in Figure 4.2c. The off- and onshore faces were reinforced more than the left and right alongshore faces due to needing to resist the full impact of the waves on the offshore face. The offshore or front face of the test structure was positioned at $x = 43.76$ m, the centerline of test structure in the stream-wise direction was set to be at $Y = 0.0$ m, and the bottom face of the test structure was placed at an elevation of $z = 2.0$ m.

Except for the addition of twelve columns beneath it, the test structure and flume configuration used in these experiments was identical to the one used by Park et al. (2017), where the elevated test structure was subjected to regular, irregular, and tsunami-like transient waves without any additional structures. Each column was 25 cm-long with a 5.08 cm by 5.08 cm hollow cross-section. Figure 4.3 provides more details in terms of the test structure and support frame dimensions as well as the instrument positions relative to the test structure.

(a) Front View

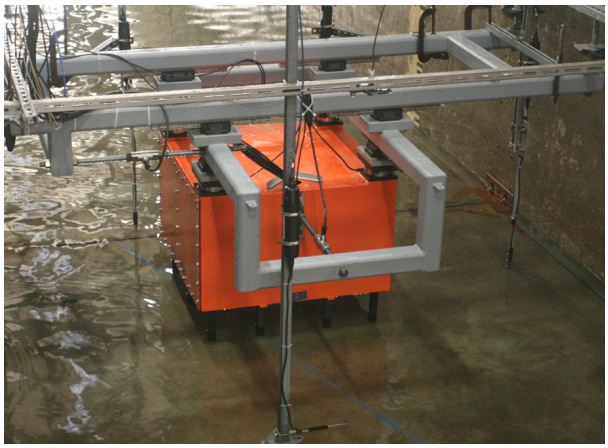

(b) Back View

(c) Internal View

Figure 4.2: Test Structure Assembly

4.3 Macro-scale Roughness Elements

To assess the influence of macro-scale roughness on the velocities, wave loads, and pressures, six testing configurations (Figure 4.4) were chosen to provide varying degrees of flow constriction and shielding of the test structure. For each case, the unobstructed channel width W and the constricted width W_c are shown to indicate the section of the flume that was considered when assessing flow constriction and shielding effects. These widths were selected according to the conventions laid out in ASCE 7-16 Chapter C6. The spacing and

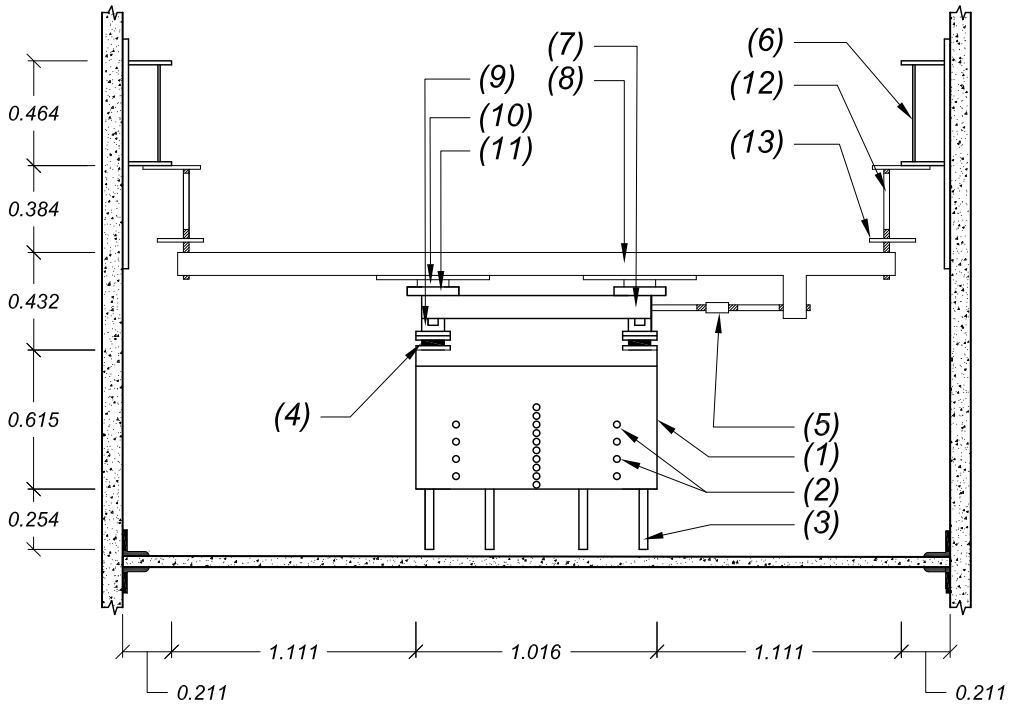

(a) Front View (Wave propagation direction is into the page)

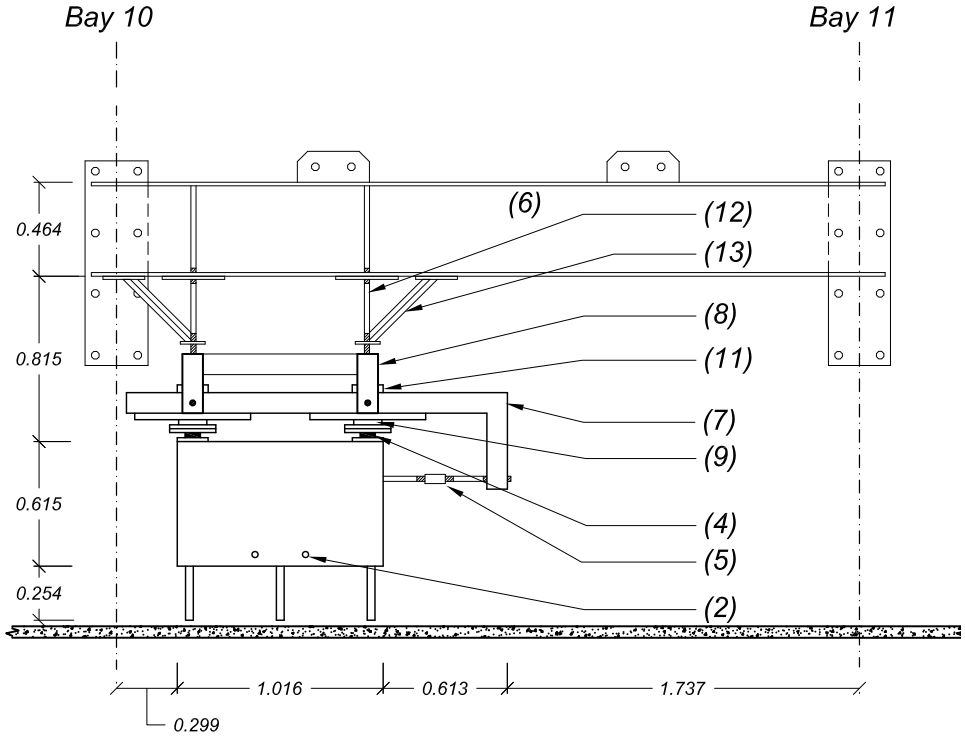

(b) Side View (Wave propagation direction is to the right)

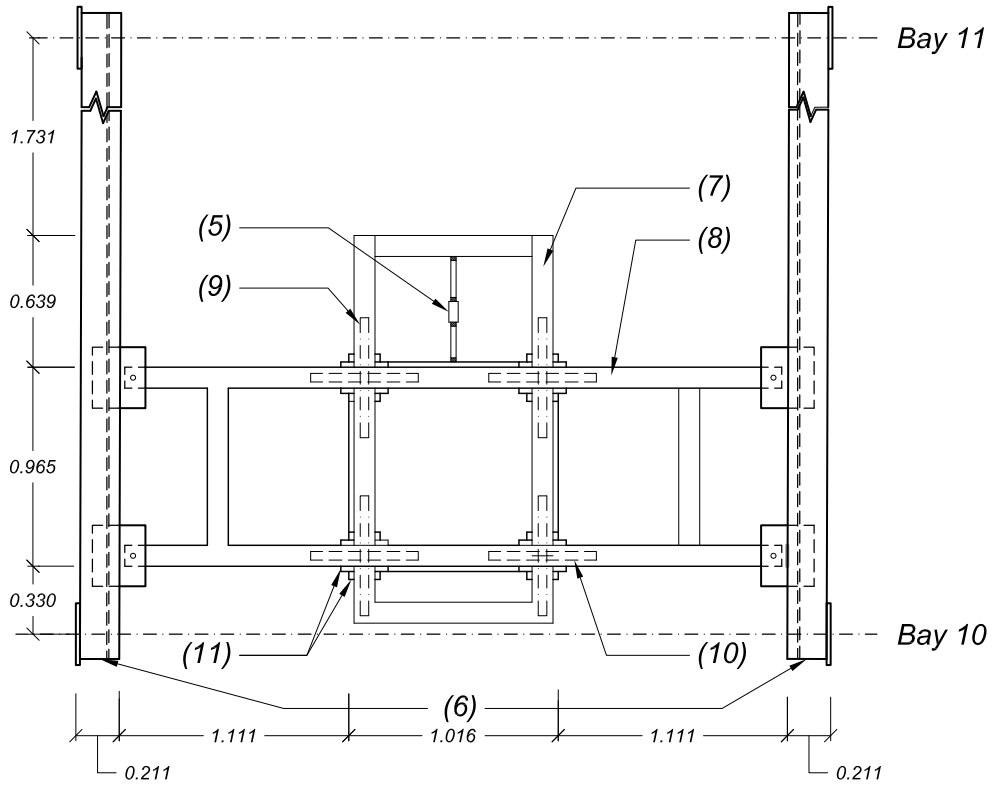

(c) Top View (Wave propagation direction is upward)

Figure 4.3: Elevated Structure and Instrumentation Plan and Elevation Views: (1) design structure body, (2) pressure gauge positions, (3) design structure legs, (4) pancake uni-directional load cell, (5) in-line load cell, (6) flume wall-mounted frame support beam, (7) streamwise support frame section, (8) transverse support frame section, (9) streamwise low-friction bearings, (10) transverse low-friction bearings, (11) bearing attachment block, (12) threaded-rod connections between the support frame and flume wall-mounted beams, (13) HSS stiffener braces (Alam et al., 2019).

sizes of the blocks were selected to be similar to streets and buildings found in coastal cities, such as Seaside, OR, where there are many waterfront hotels which would be less susceptible to being washed away by a tsunami inundation and would act as macro-roughness elements, channeling the flow towards structures farther inland.

The first configuration (Case A) had no roughness elements and served as the reference case for later use in normalizing the results of other cases relative to a case without adja-

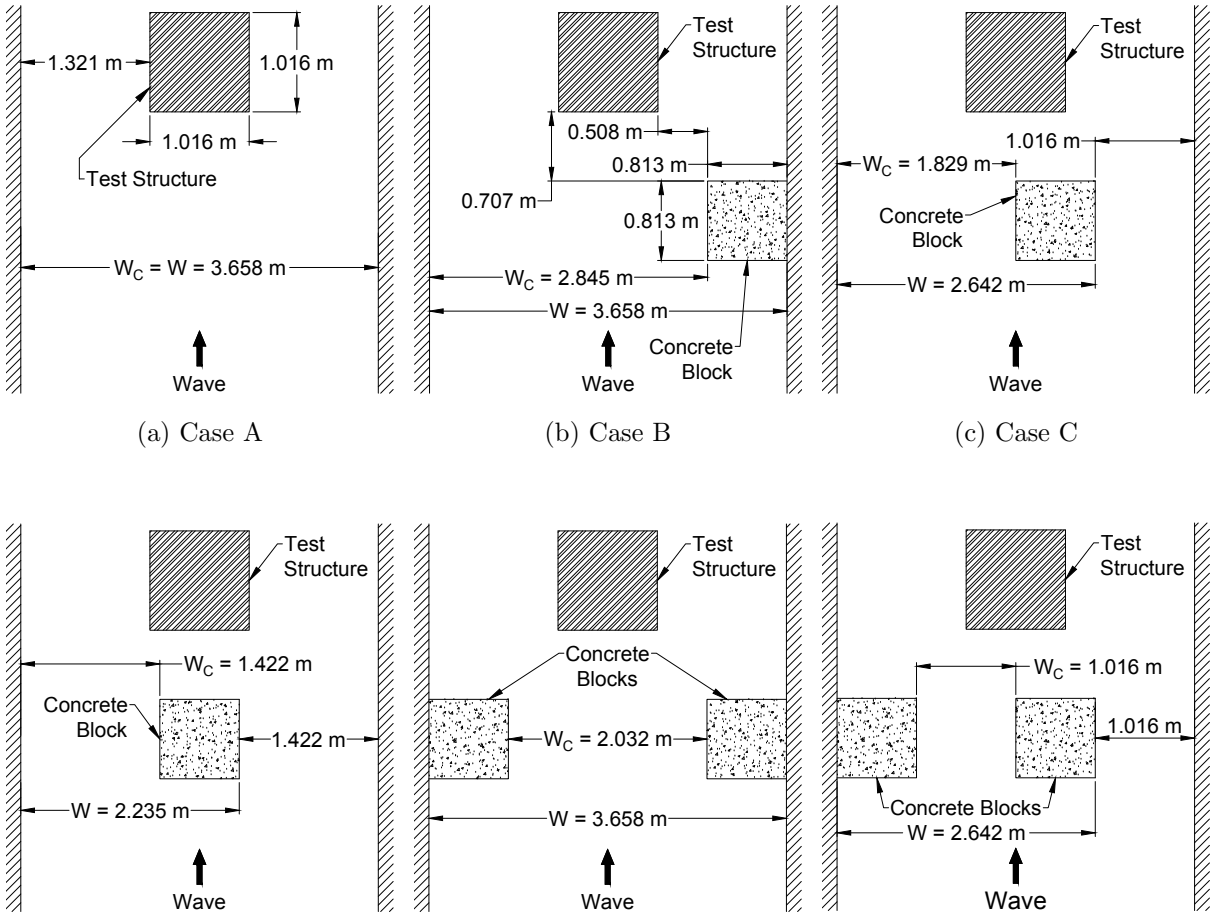

(a) Case A (b) Case B (c) Case C

(d) Case D (e) Case E (f) Case F

Figure 4.4: Macro-scale Roughness Element Configurations

cent structures obstructing the waves. The roughness elements used in the additional five configurations (Cases B-F) consisted of concrete blocks placed in alternating patterns, which were fixed to the channel. Each block was 1.1684 m tall and had square bases with 0.8128 m side lengths. The first three configurations (Cases B-D) made use of one concrete block, and last two configurations (Cases E and F) consisted of two concrete blocks, with symmetric and asymmetric configurations. All of the shielding blocks were placed at the center of the channel (Case D), at the channel edge (Cases B and E), or with their edge aligned with the midpoint of the test structure (Cases C and F).

It should be noted that Cases B, E, and F present configurations where stagnant flow

regions existed in the corners made by the flume walls and the offshore faces of the blocks touching the walls. This condition could hypothetically influence both the run-up elevation on the test structure faces and consequently the fluid pressures and forces acting on the test structure by directing the flow toward the flume center instead of allowing the flow to freely pass around the blocks. In effect, these situations present cases where the blocks touching the wall act as larger structures than they actually are in terms of how they influence the flow conditions as has been discussed by Goseberg (2011). For instance, a block touching a flume wall would act as a structure that is twice as wide in the transverse direction since by symmetry half of the flow would go to the left and half to the right of such a block with a stagnation region in the middle of the offshore face of the block.

However, instead of attempting to address this issue directly by using a block that is half as wide when placing a block against a flume wall, it was decided that in the interest of time and resource limitations that numerical modeling would be used to produce a validated model that could be used to compare cases with and without flume walls. For example, OpenFOAM computational fluid dynamics (CFD) simulation results for the one-MRE cases (Cases B, C, and D) using both an experimentally-validated model with the original flume width of 3.658 m and another model with a flume width twice as large have demonstrated that the walls have a minimal effect on the maximum total force imparted on the test structure by the broken wave as shown in Figure 4.5.

4.4 Wave Generation

Unbroken and broken tsunami-like waves were generated by the hydraulic piston of the Large Wave Flume at the HWRL. The piston was operated under displacement control, based on time histories of piston displacement specified by the research team. As shown in Figure 4.6, the displacement history of the unbroken wave was input as an error function, whereas the displacement history of the broken wave was derived from solitary wave theory.

The purpose of using an error function displacement history instead of other established

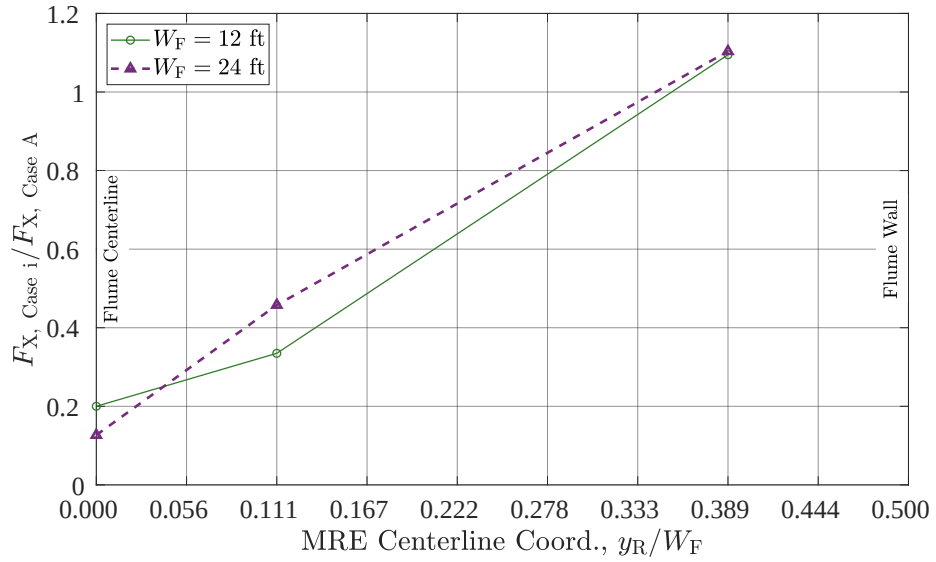

Figure 4.5: Comparison of Normalized Maximum Streamwise Forces for the One-MRE Cases (Cases B, C, and D) using 12 ft and 24 ft Flume Widths in OpenFOAM CFD Simulations of the Broken Wave, where y_R is the Distance between the Flume and MRE Centerlines and W_F is the Flume Width.

wave generation theories was to maximize the capabilities of the piston wavemaker in the Large Wave Flume. In particular, the wavemaker is limited to a maximum stroke of 4 m and maximum velocity of 4 m/s as noted previously. Wave generation schemes based upon shallow water wave theory and solitary wave theory result in piston displacement histories that reach the peak velocity before before the maximum stroke can be achieved, which would result in a smaller volume of water being displaced and consequently a lesser wave impact on the test structure. However, the error function approach allows the full piston stroke to be utilized while maintaining an allowable piston velocity.

The error function-based piston displacement history, $x_{wm}(t)$, was defined by Equation 4.1, where $S_{max} = 4$ m was the maximum piston stroke, $t_0 = 100\tau_0/SF + t_{wm} = 20.34$ s was the initial time offset, $SF = 360$ was a scaling factor used to stretch the displacement profile in time, $t_{wm} = 10$ s was the delay required for the wavemaker and data acquisition system to be readied, and τ_0 was the solution of $\text{erf}(\tau) + 1 = \text{tolerance} = 5(10^{-5})$, which

was an arbitrarily chosen starting point to ensure that the displacement remained near zero for an initial time period. Note that decreasing SF results in larger wave amplitudes and consequently larger wave velocities too, but the unbroken wave parameters were chosen to ensure that the waves generated using them broke after the test structure. The maximum piston velocity based on these parameters was 0.63 m/s, which was far below the limiting value for the wavemaker.

$$x_{\mathrm{wm}}(t) = \frac{S_{\max}}{2}\left[1 + \mathrm{erf}\left(\frac{100(t - t_0)}{SF}\right)\right] \tag{4.1}$$

For the unbroken wave, the still water level (SWL) was set to be 2.0 m near the wave maker, resulting in a SWL of 0.25 m at the test structure with no air gap beneath it. For the broken wave, the SWL was set to be 1.85 m near the wave maker, which resulted in a SWL of 0.1 m at the test structure with a 0.15 m air gap beneath it.

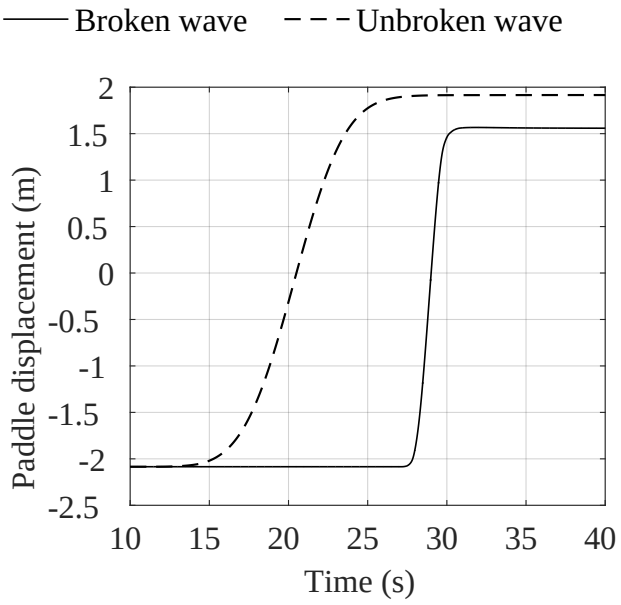

Figure 4.6: Wave Maker Displacement Time Histories

The advection of each wave form along the flume is depicted as a series of wave free-surface time histories in Figure 4.7 and Figure 4.8, where each time history represents the ensemble average over all of the tests conducted for each roughness element configuration.

In these figures, x is the distance from the wave paddle to the gauge. The results shown were recorded by *wmwg* located at $(x, y, z) = (0, 0, \text{N.A.})$, a wave gauge attached near the top of the piston wavemaker paddle, as well as by the resistance wire wave gauges *wg1* placed at $(x, y, z) = (14.169, -1.388, \text{N.A.})$, *wg2* placed at $(x, y, z) = (32.443, -1.379, \text{N.A.})$, and *wg3* placed at $(x, y, z) = (36.099, -1.368, \text{N.A.})$, which are shown in Figure 4.1. Note that the x-coordinate of *wmwg* changed with the motion of the wavemaker over time and the N.A. entries indicate the fact that the resistance wire gauges do not exist at a single point in the z-direction. The averaged time histories were nearly identical for all six test configurations during the initial wave impact on the test structure, demonstrating the consistency of the piston-type wavemaker in the Large Wave Flume. Noticeable differences in the waves began during the subsidence of the wave from the test structure after the peak wave height had been reached and when the waves returned after reflecting off of the end wall of the flume. The unbroken wave experienced minimal reduction of amplitude as it traveled down the flume, whereas the amplitude of the broken wave rapidly decayed as it approached the test structure. This difference is due to the significantly greater height and greater velocity of the initial form of the broken wave that resulted in the formation of a turbulent bore.

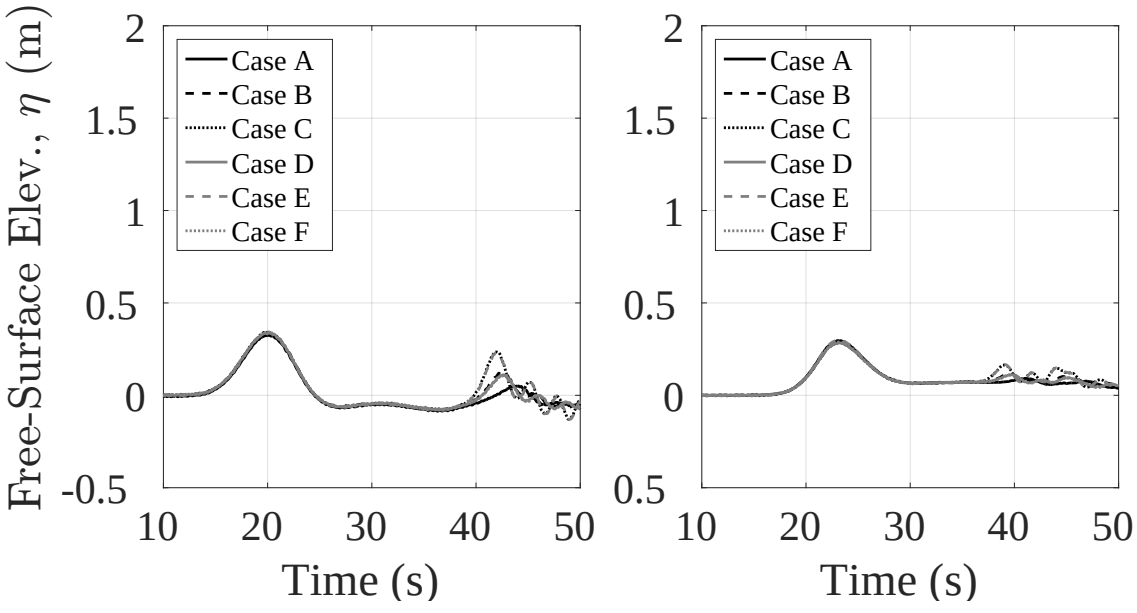

(a) *wmwg* (b) *wg1*

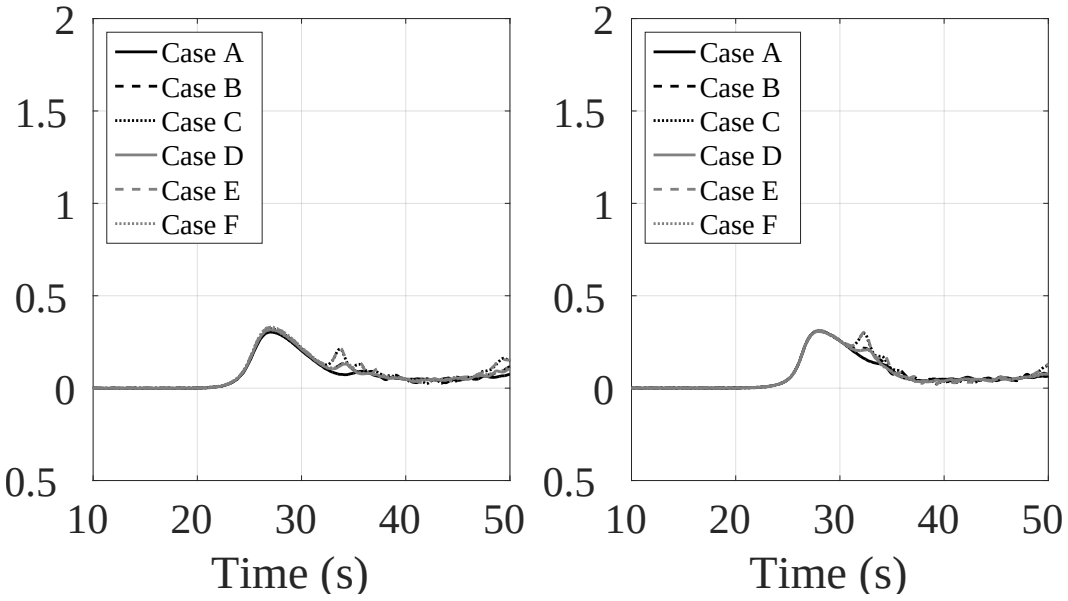

(c) *wg2* (d) *wg3*

Figure 4.7: Unbroken Wave Free-Surface Time Histories

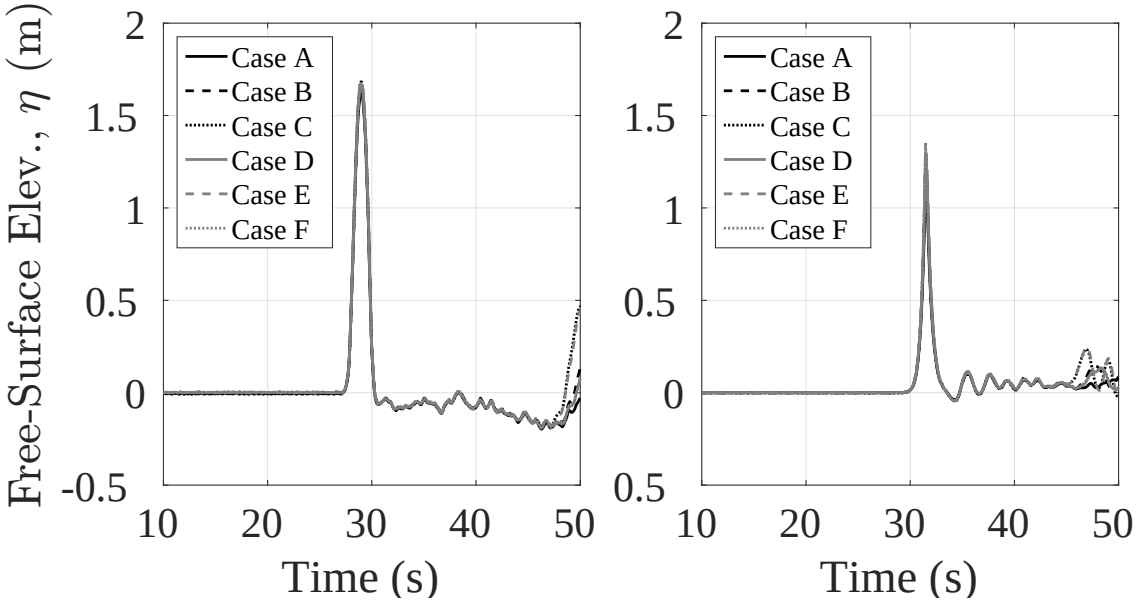

(a) *wmwg* (b) *wg1*

Concerning whether or not the waves used in this study were indeed tsunami-like, it may be observed in the engineering literature that solitary waves, which are forced to break

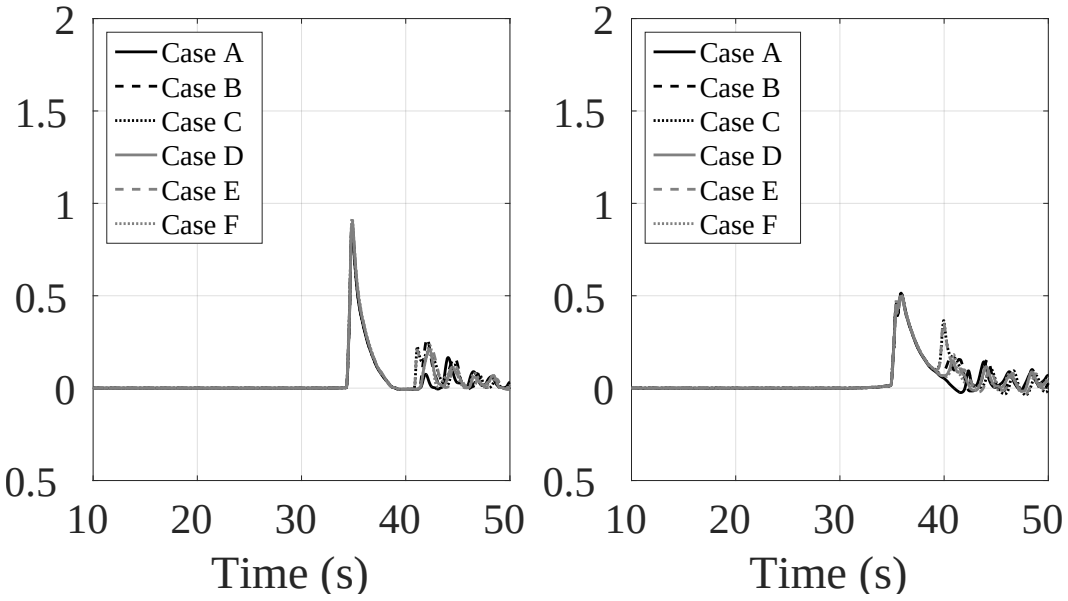

(c) *wg2* (d) *wg3*

Figure 4.8: Broken Wave Free-Surface Time Histories

and form turbulent bores as they propagate over sloped beds due to wave shoaling effects, are commonly used to generate similar conditions to those that occur during a tsunami inundation. For instance, a large number of researchers have used solitary waves as an initial condition for experimental investigations (Grilli et al., 1994; Briggs et al., 1995, 1996; Robertson and Mohamed, 2009; Swigler, 2009) as well as numerical simulations (Titov and Synolakis, 1995; Grilli et al., 1997; Lynett, 2009) of tsunami wave propagation. Additionally, continuous inundation flows were simulated experimentally using the same approach as described by Thomas and Cox (2012) to generate the unbroken wave, the duration of which was maximized through the use of the error function wave generation method that allows for use of the full wavemaker stroke. Due to the comparable nature of the waves used in this study to those used in past studies focusing on tsunami-like waves the terminology of tsunami-like has been used throughout to describe the unbroken and broken waves.

4.5 Instrumentation

The elevated test structure was fitted with an array of measurement devices including load cells, pressure gauges, acoustic Doppler velocimeters (ADVs), and two types of wave height gauges, wire resistance and ultrasonic gauges. Sample photos of these devices are shown in Figure 4.9.

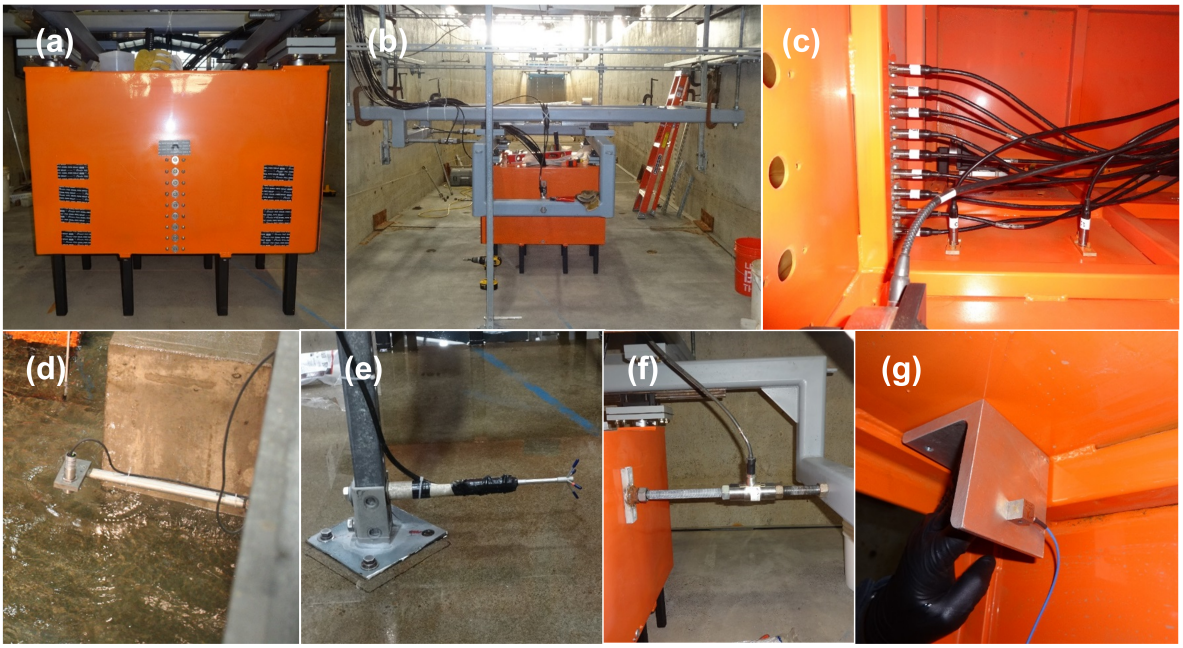

Figure 4.9: Elevated Structure Instrumentation Photos: (a) front face pressure gauge positions, (b) structure support frame, (c) internal pressure gauge attachment, (d) ultrasonic wave gauge, (e) acoustic Doppler velocimeter, (f) streamwise load cell, (g) internally-mounted accelerometer.

4.5.1 Load Cells

To measure the forces imparted on the test structure by the waves, nine load cells were used, including one stream-wise direction load cell (LC5), two transverse direction load cells (LC3 and LC4), four vertical direction load cells (LC6, LC7, LC8, and LC9), and two load cells connecting the front right and back left legs to the test structure. The two leg load

cell measurements are not discussed in this article, leaving the seven load cells shown in Figure 4.10.

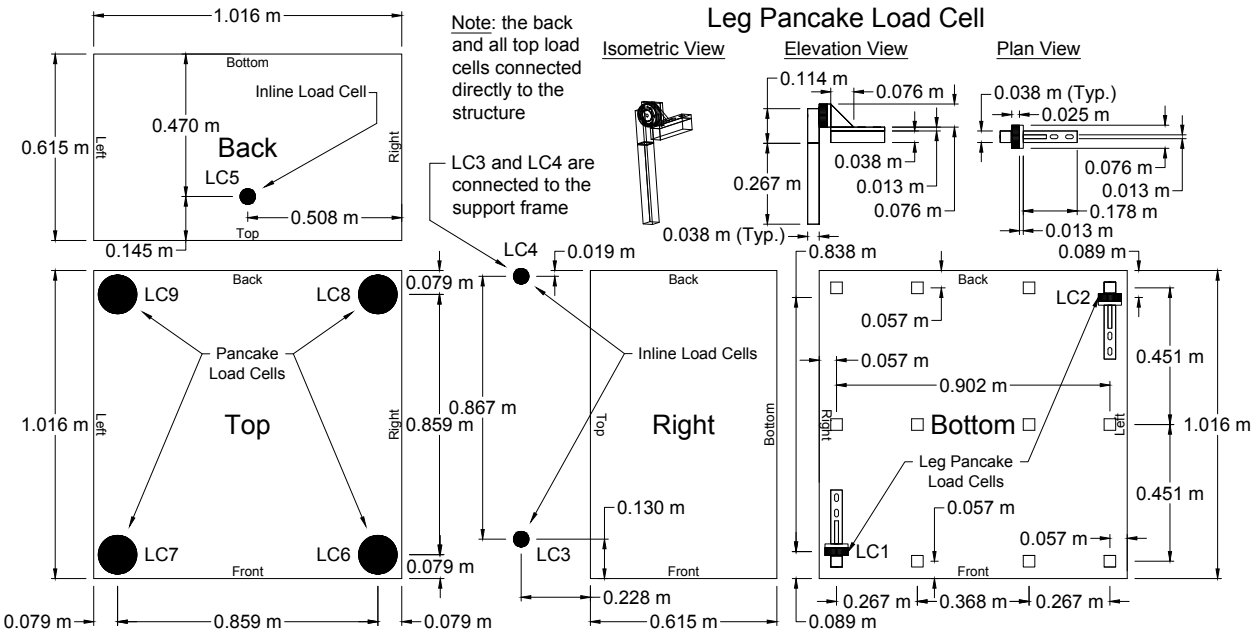

Figure 4.10: Load Cell Layout: B (Back), RF (Right Front), RB (Right Back), TFR (Top Front Right), TFL (Top Front Left), TBR (Top Back Right), TBL (Top Back Left)

4.5.2 Pressure Gauges

Fourteen pressure gauges were used to characterize the pressure distributions on the test structure. As shown in Figure 4.11, these gauges were utilized in three configurations to achieve a higher resolution pressure field in terms of the number of positions at which pressures were measured during the experiments. Note that the gauges are labeled PG1 - PG14, but the faces on which these labels appear is not always consistent.

Pressure gauge layout 1 was devised to determine the pressure distribution along the centerline of the test structure on the front, bottom, and back faces as shown in Figure 4.11a. The locations shown in Figure 4.11b for pressure gauge layout 2 were selected to capture the pressure distribution near the left and right edges of the test structure's front face and measure the pressure field over the bottom face of the test structure. To provide a good

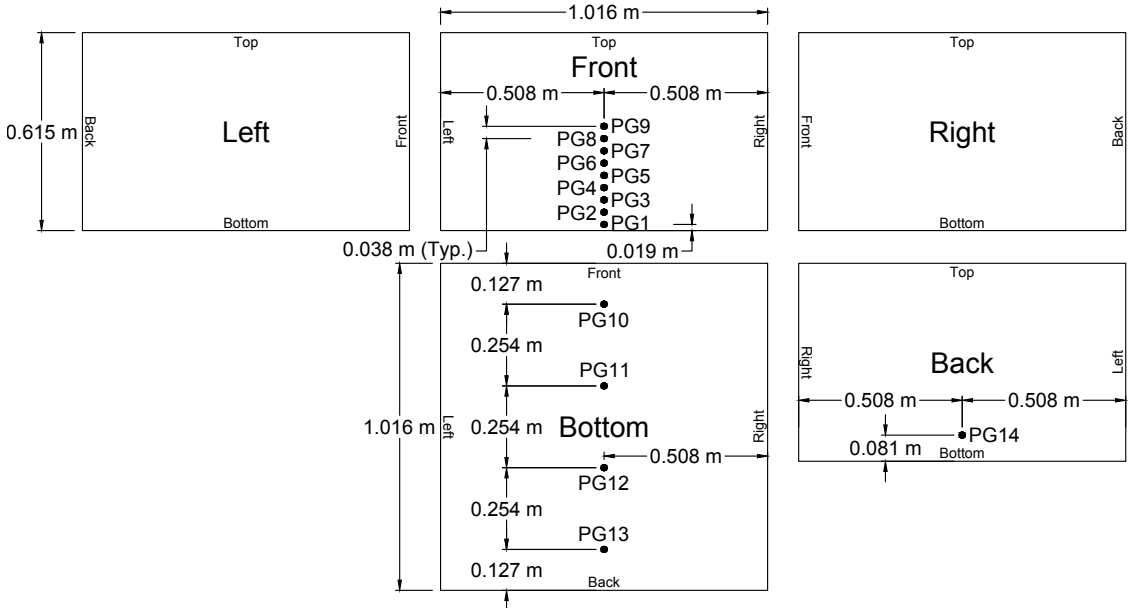

(a) Layout 1

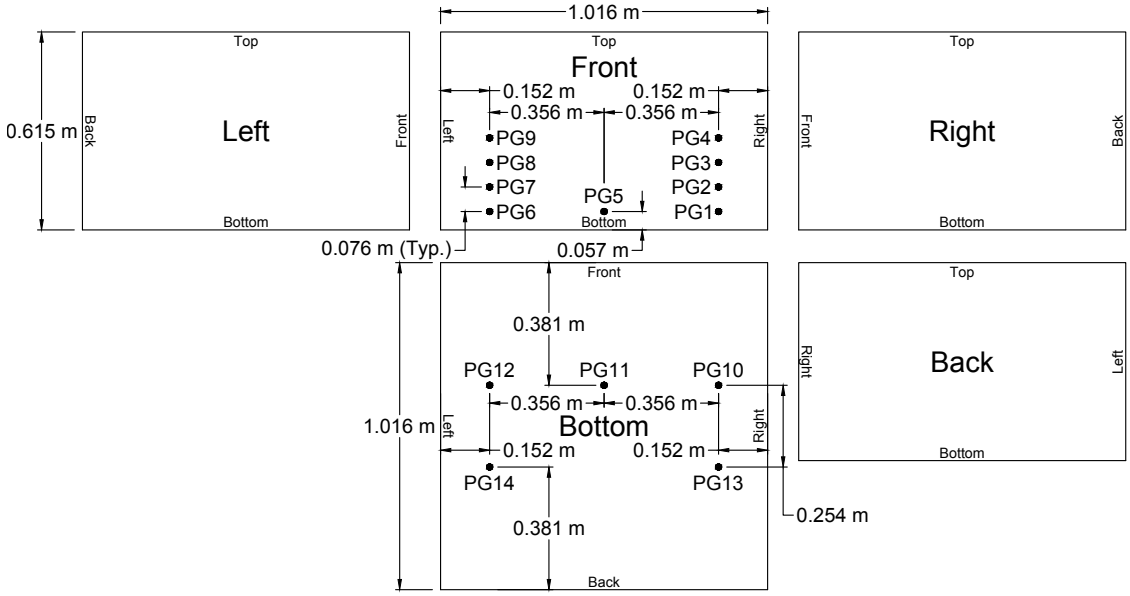

(b) Layout 2

overall characterization of the pressure distribution acting on the entire test structure, the pressure gauge layout 3 positions shown in Figure 4.11c were chosen. Furthermore, layout 3 provides the only assessment of the pressure distribution along the left and right faces of the test structure, which were placed at the same elevation at a large enough spacing in the

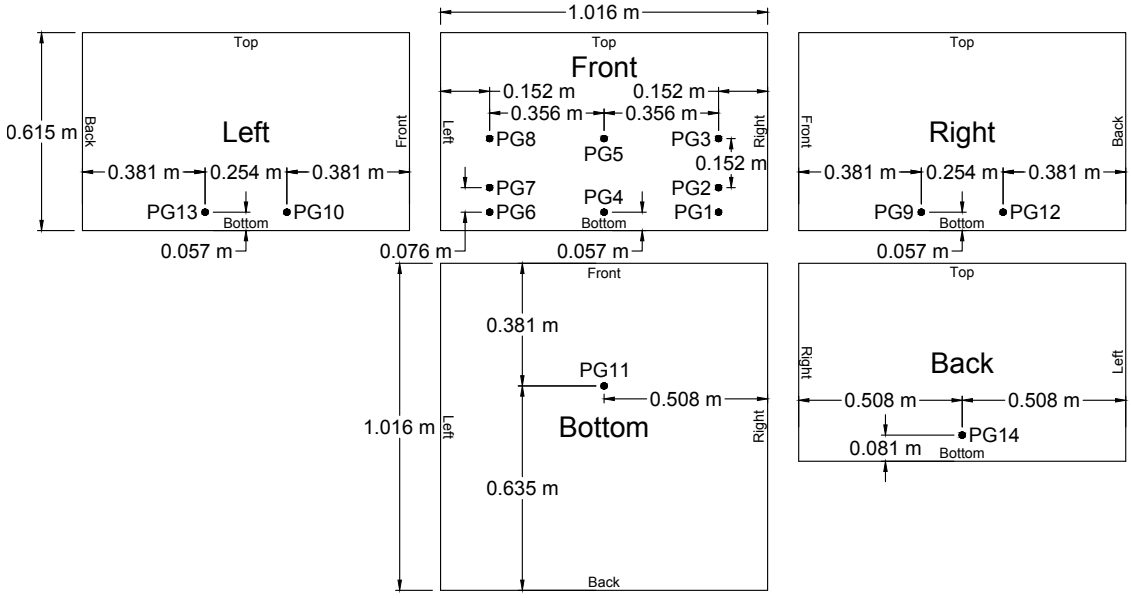

(c) Layout 3

Figure 4.11: Test Structure Pressure Gauge Layouts

streamwise direction to be able to assess if the test structure twisted during wave impact loading.

4.5.3 Acoustic Doppler Velocimeters

To study local velocity variations during the experiments, seven acoustic Doppler velocimeters (ADVs) were installed as shown in Figure 4.12. These gauges measured three-dimensional velocities surrounding the test structure, which was necessary for detecting flow direction variations as well as velocity amplifications. To ensure that the ADV measurements were not corrupted by noise resulting from entrained air in either wave case, they were submerged well below the still water level in both wave cases. Furthermore, to avoid skewed results due to erroneous spikes in the ADV time histories when computing ensemble velocities considering all of the experimental trials, median velocities were calculated instead of the mean velocities since the mean is highly susceptible to outliers, whereas the median is much more robust.

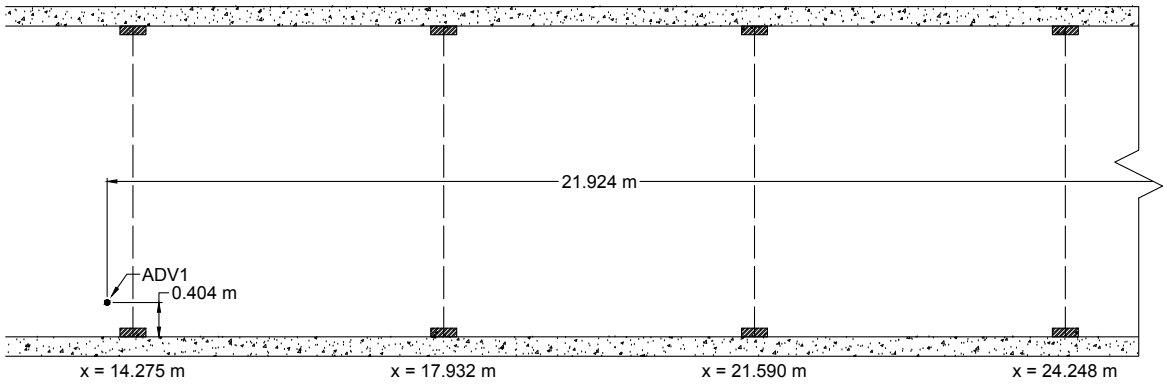

(a) ADVs near the Wavemaker

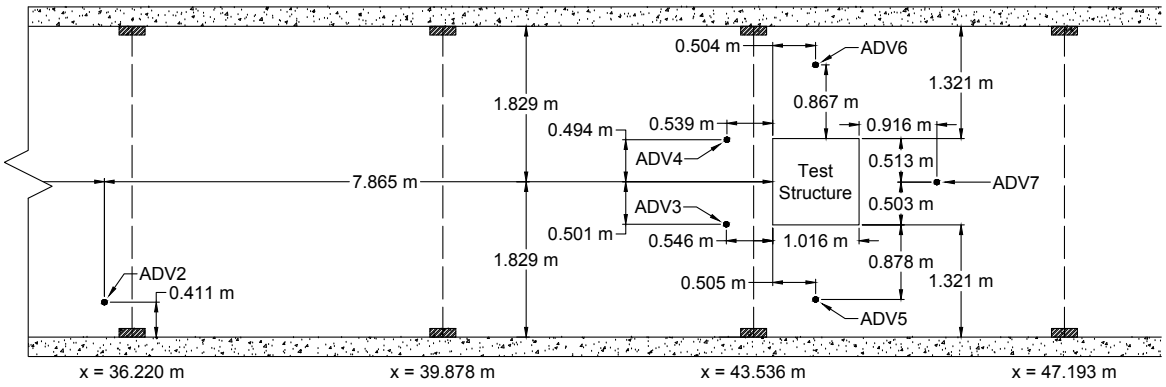

(b) ADVs near the Test Structure

Figure 4.12: Acoustic Doppler Velocimeter (ADV) Layout

4.5.4 Ultrasonic and Wire Wave Gauges

Wave heights were measured along the flume in front of the test structure at four locations using resistance wire gauges. The global locations of these gauges are shown in the flume plan and elevation views of Figure 4.1. Additionally, six ultrasonic wave gauges, which are also shown in Figure 4.1, were placed surrounding the elevated test structure. These gauges are also shown in Figure 4.13 in order to provide specific details concerning the exact positions of these wave gauges relative to the test structure.

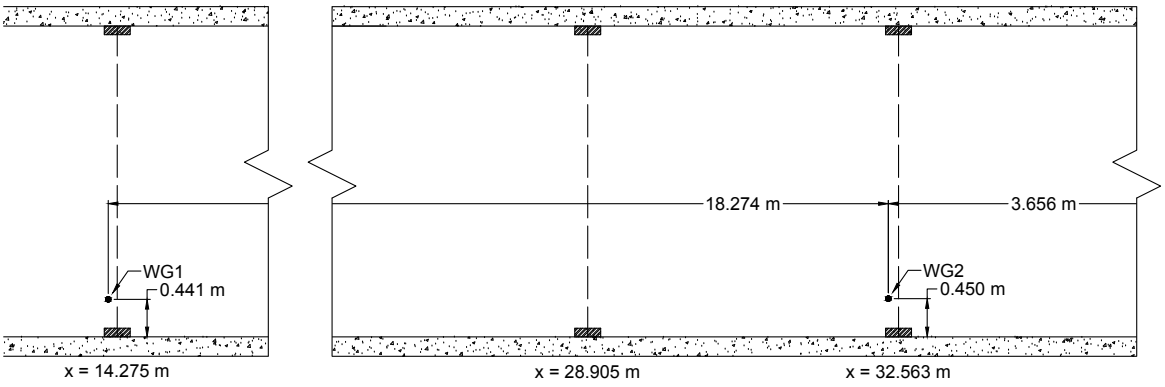

(a) Wave Gauges near the Wavemaker

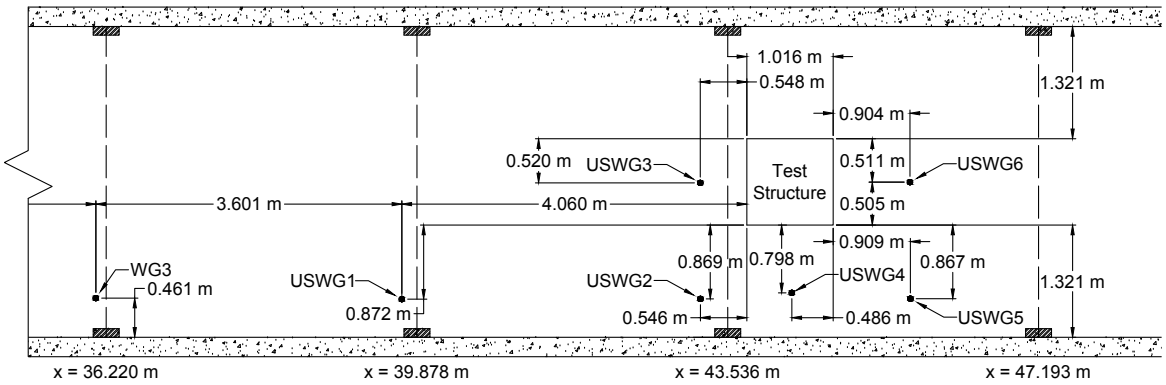

(b) Wave Gauges near the Test Structure

Figure 4.13: Wave Gauge Positions

4.6 Experimental Conditions Summary

The combination of six experimental test configurations with three pressure gauge layouts and three wave types resulted in a large number of unique configurations that were tested at the HWRL. Additionally, in order to gather enough data in order to capture the variability in the physical processes of wave impact loading as well as variability due to any component of the entire test apparatus comprised of the wave maker, test structure, and instrumentation, numbers of trials were chosen based on the wave type being tested. For the broken wave, 10 trials were settled upon after initial testing and likewise 5 trials were used for the breaking and unbroken waves.

These conditions are summarized in Table 4.1, which shows the test configuration and

the number of trials that were carried out for each configuration. A total of 246 tests were conducted, where the first 91 tests were executed with an unstiffened test structure support frame, whereas the remaining 155 were completed using a stiffened support frame. The frame was stiffened after visibly noticeable vibration of the frame was documented during the more violent broken and breaking wave type tests. In places where more tests than the typical amounts of 5, 10, or 15 are shown in Table 4.1, one of two situations arose during the tests, where either the test count was incorrectly recorded during the testing and found to be larger than planned after the fact or an issue with the test configuration was found and additional tests were conducted to account for them. For example, when using the stiffened test structure support frame, pressure gauge (PG) layout 3, and test configuration Case A for the breaking wave, the unrestrained concrete block used to represent a neighboring structure rotated about the vertical axis and was displaced away from the flume wall due to the repeated, severe wave impacts during the first three trials using these conditions. Once the issue was noticed, a steel support frame spanning the width of the flume was constructed to keep the concrete block(s) from displacing during further tests.

Table 4.1: Test Matrix

Frame Stiffness	**PG Layout**	**Test Config.**	**Wave Type**	**Trials**	**SWL (m)**
Unstiffened	Layout 1	Case A	Unbroken	15	2.00
Unstiffened	Layout 1	Case A	Breaking	15	2.00
Unstiffened	Layout 1	Case A	Broken	15	1.85
Unstiffened	Layout 2	Case A	Unbroken	5	2.00
Unstiffened	Layout 2	Case A	Breaking	5	2.00
Unstiffened	Layout 2	Case A	Broken	6	1.85
Unstiffened	Layout 3	Case A	Breaking	10	2.00
Unstiffened	Layout 3	Case A	Unbroken	10	2.00
Unstiffened	Layout 3	Case A	Broken	10	1.85
Stiffened	Layout 3	Case A	Unbroken	7	2.00

Stiffened	Layout 3	Case A	Breaking	10	2.00
Stiffened	Layout 3	Case A	Broken	10	1.85
Stiffened	Layout 2	Case A	Unbroken	5	2.00
Stiffened	Layout 2	Case A	Breaking	10	2.00
Stiffened	Layout 2	Case A	Broken	10	1.85
Stiffened	Layout 3	Case B	Unbroken	5	2.00
Stiffened	Layout 3	Case B	Breaking	8	2.00
Stiffened	Layout 3	Case B	Broken	10	1.85
Stiffened	Layout 3	Case C	Unbroken	5	2.00
Stiffened	Layout 3	Case C	Breaking	5	2.00
Stiffened	Layout 3	Case C	Broken	10	1.85
Stiffened	Layout 3	Case D	Unbroken	5	2.00
Stiffened	Layout 3	Case D	Breaking	5	2.00
Stiffened	Layout 3	Case D	Broken	10	1.85
Stiffened	Layout 3	Case E	Unbroken	5	2.00
Stiffened	Layout 3	Case E	Breaking	5	2.00
Stiffened	Layout 3	Case E	Broken	10	1.85
Stiffened	Layout 3	Case F	Unbroken	5	2.00
Stiffened	Layout 3	Case F	Breaking	5	2.00
Stiffened	Layout 3	Case F	Broken	10	1.85

Chapter 5
EXPERIMENTAL RESULTS

The introduction of adjacent structures affected the incident tsunami wave by either focusing it toward the test structure or diverting it away from the test structure. When the waves were diverted away from the test structure by adjacent structures that shielded it, the pressures and net forces were drastically reduced. On the contrary, narrowing of the flow channel locally increased the flow velocity, which caused by increases in the dynamic pressure of the flow that resulted in larger pressures and net forces applied to the test structure. Locally-increased velocities and fluid pressures acting on the test structure have been used to demonstrate where flow channeling occurred. Similarly, locally diminished or redirected flow velocities and reduced pressures were used as identifiers of regions where shielding due to adjacent structures occurred. This chapter discusses examples of each effect individually as well as when they were found to act in combination. For instance, the MRE configurations of Cases B and E primarily produced flow channeling effects, Case D caused shielding-dominated behavior, and the remaining cases, Cases C and F, resulted in both shielding and flow channeling effects.

5.1 Effects of Macro-roughness on Flow Velocities

To provide insight into how the adjacent structures influenced the wave flow patterns between the structures, the XY-plane velocity vectors parallel to the flume bottom (i.e. neglecting the Z-direction components that were measured too) were determined for each ADV and block configuration at the point in time when the peak stream-wise velocity component for ADV4 was reached. This ADV position was selected since it was located just ahead of the test structure in the unobstructed path of the waves impacting the test structure for all

macro-roughness element configurations regardless of the degree to which the test structure was shielded by macro-roughness elements. Furthermore, ADV4 provided the only suitable location to measure local flow velocity amplification effects for all MRE configuration cases, whereas ADV3 was fully shielded by a MRE in Cases C and E. These results are shown for both the unbroken and broken waves in Figure 5.1, where the ensemble medians over all of the tests completed for each roughness element configuration were used to determine the vector components and which time corresponded to the maximum stream-wise velocity for ADV4.

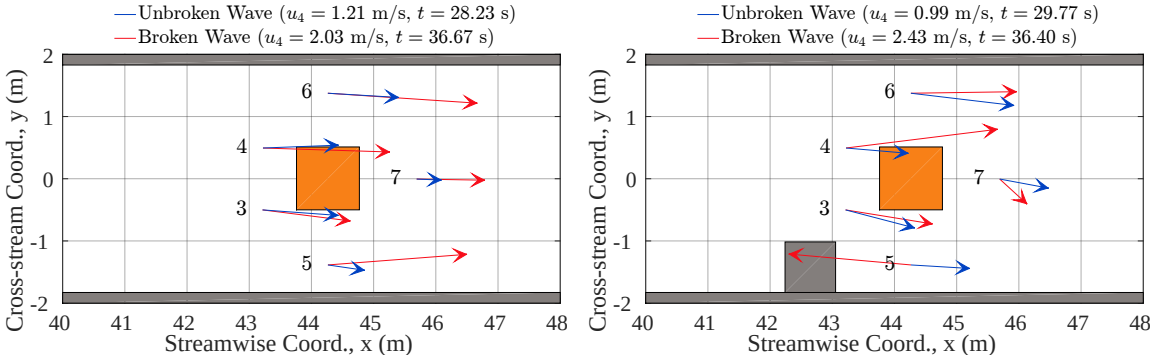

(a) Case A

(b) Case B

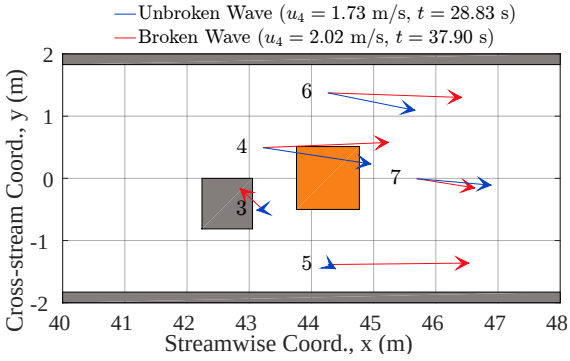

(c) Case C

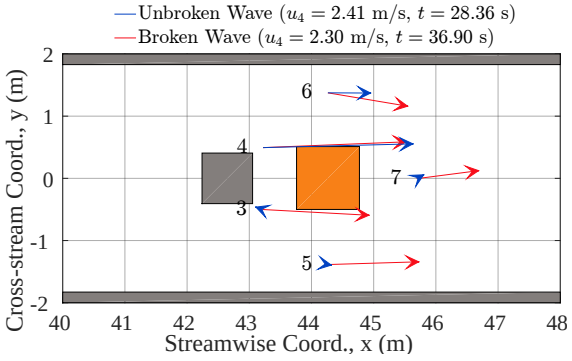

(d) Case D

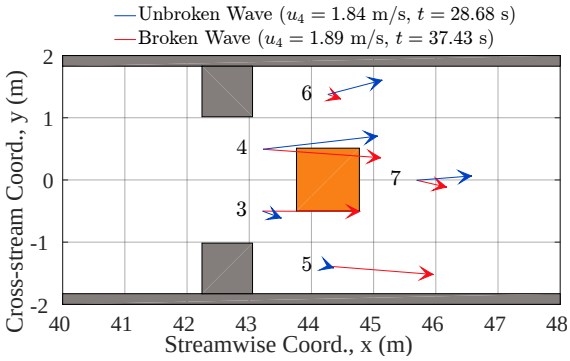

(e) Case E

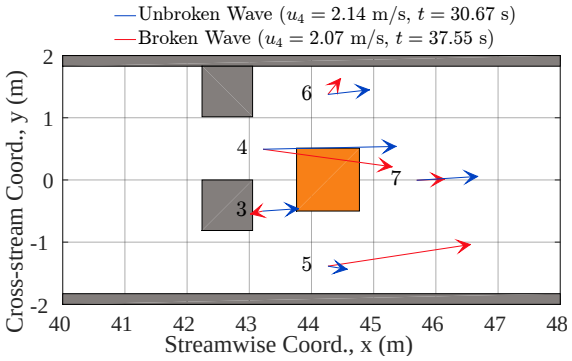

(f) Case F

Figure 5.1: ADV Velocity Vectors at the Time of Peak Stream-wise Velocity for ADV4

5.1.1 Flow Constriction Effects

As a measure of the degree of flow constriction for a specific case, the blockage ratio defined as $BR = 1 - W_c/W$, where W_c is the constricted width and W is the unobstructed width, was used for comparison purposes between cases. For Cases A through F, the blockage ratios were 0, 0.222, 0.308, 0.364, 0.444, 0.615, respectively. These values were determined using the W_c and W dimensions shown in Figure 4.4.

If the roughness element configurations are divided into two subsets, the one-block (Cases B, C, and D) and two-block (Cases E and F) scenarios, the maximum stream-wise velocity measured by ADV4 increased as the channel flow width decreased for the unbroken wave within these case subsets, particularly if the flow restriction was near that velocimeter. For the one-block cases, the maximum velocity recorded by ADV4 increased linearly with increasing blockage ratio from 0.99 m/s for Case B ($BR = 0.22$) to 2.41 m/s for Case D ($BR = 0.36$). Similarly for the two-block cases, the maximum ADV4 velocity increased from 1.84 m/s for Case E ($BR = 0.444$) to 2.14 m/s for Case F ($BR = 0.62$). The broken wave maximum ADV4 stream-wise velocities showed similar behavior for the one- and two-block cases; however, there does not appear to be an all-encompassing trend for either wave type.

The lack of an overall trend for both wave types shows that increasing the blockage ratio does not always cause an increase in flow velocity, particularly when the ratio is increased by adding an additional adjacent structure instead of changing the position of a single adjacent structure. Increasing the number of neighboring structures may redirect the flow in a much different manner than for less neighboring structures. For instance, when comparing Case A to Case B in Figure 5.1 for the unbroken wave, it may be observed that the maximum stream-wise velocity recorded by ADV4 dropped from 1.21 m/s to 0.99 m/s even though the blockage ratio increased from 0 to 0.222. The difference between Case A and Case B is that in Case B both ADV3 and ADV4 measured increased transverse velocities due to the addition of a concrete block, which accounts for part of the reduction in stream-wise velocity for Case B. Additionally, dissipative, turbulent flow behavior in the form of swirling eddies,

where the flow field was highly re-circulatory near the concrete block and test structure as shown in Figure 5.2a, caused the redirection of the flow and reduced the wave energy through turbulence.

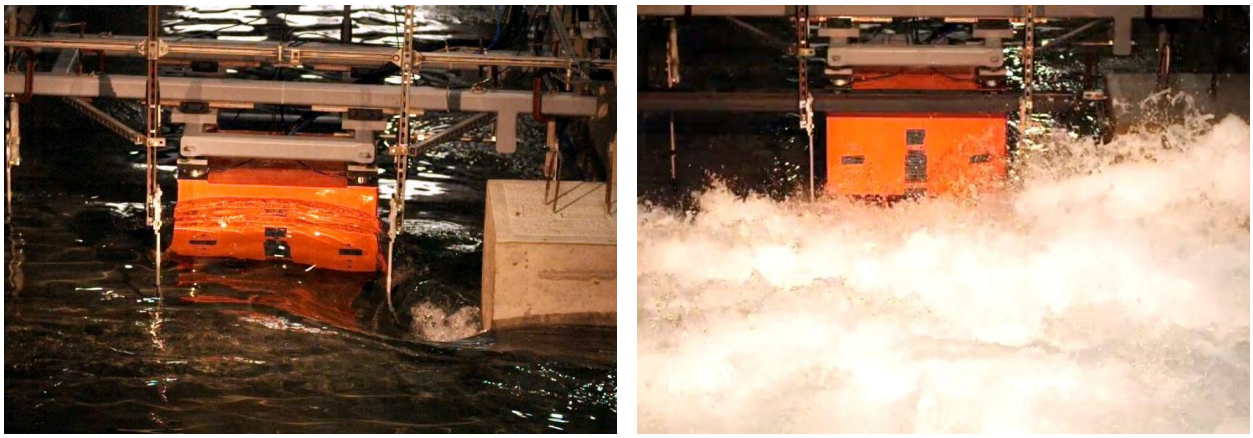

(a) Unbroken Wave: Large Eddies (b) Broken Wave: Fully-Formed Bore

Figure 5.2: Turbulent Flow Behavior

5.1.2 Flow Redirection Effects

The roughness elements led to a large degree of flow redirection, particularly for ADV3, which was most directly in the path of the eddies caused by the concrete blocks as well as behind one of the blocks in several scenarios. Redirection of the flow from being nearly perfectly stream-wise as it was in the base case (Case A) led to significant increases in the transverse direction velocity component, causing the wave to no longer directly impact the test structure.

For example, as shown for the broken wave in Figure 5.1, the transverse velocity measured by ADV3 increased in the negative y-axis direction for the asymmetrically-placed, 50%-blocked cases (Cases C and F), where the stream-wise velocity decreased with increasing shielding. Similarly, the largest reduction in stream-wise velocity at ADV3 for the broken wave occurred for the asymmetric two-block case (Case F) and simultaneously experienced the largest transverse velocity in the positive y-direction and a negative stream-wise velocity.

For the unbroken wave, the ADV3 velocity vectors were redirected in a similar manner as for the broken wave, where the transverse components increased for the cases with the concrete blocks placed along the flume walls (Cases B and E); however, they were no longer oriented in the same directions as the broken wave vectors, which is likely due to the highly transient, turbulent nature of the flow directly behind the concrete blocks being drastically different between the two wave types.

If comparisons of the flow redirections for ADV3 to those for ADV4 are made, significant differences in the vector directions as well as in the flow velocities for both wave types may be observed. What is striking about these differences is that they occurred for Cases A, D, and E, in which the test structure and macro-roughness element were arranged in symmetric configurations with respect to the centerline of the wave flume, where symmetric flow results were expected. The reason for the existence of these unexpected velocity vector magnitudes and orientations is the transient nature of the wave impacts, which are subject to strong temporal fluctuations in the flow field.

For the unbroken waves, temporal fluctuations in velocities at ADV3 were due to large eddies that formed near the corners of the macro-roughness elements as illustrated in Figure 5.2a, which led to recirculatory flows in these regions, where the velocity vectors constantly changed orientation and magnitude. For instance, when examining the velocity vectors for Case E, the unbroken wave results for ADV3 and ADV4 ought to be identical based on the symmetry of the macro-roughness element and test structure configuration. However, at the instant ADV4 reached its maximum streamwise velocity magnitude of 1.84 m/s as shown in Figure 5.1e, ADV3 recorded a much small velocity magnitude due to local flow fluctuations. However, the maximum velocity that ADV3 recorded during the unbroken wave impact in this case was 1.80 m/s. This demonstrates that flow symmetry due to configuration symmetry was satisfied over the entire duration of the wave impact, but not at each individual recorded instant due to flow fluctuations. On the other hand, the highly turbulent nature of the broken wave bores, which were extremely frothy and aerated in addition to being nonuniformly-shaped, led to similar temporary flow asymmetries too, even for cases

where the roughness elements were arranged in symmetric patterns with respect to the flume centerline.

5.2 Effects of Macro-roughness on Measured Forces

As was shown previously, constricting the channel flow width resulted in amplified flow velocities; however, these amplified velocities, which lead to higher dynamic pressures for the wave flow, were not always consistent with increases in the maximum stream-wise forces that were observed when the roughness element configuration was varied. As shown in Figure 5.3, this observation applied to both the unbroken and broken waves.

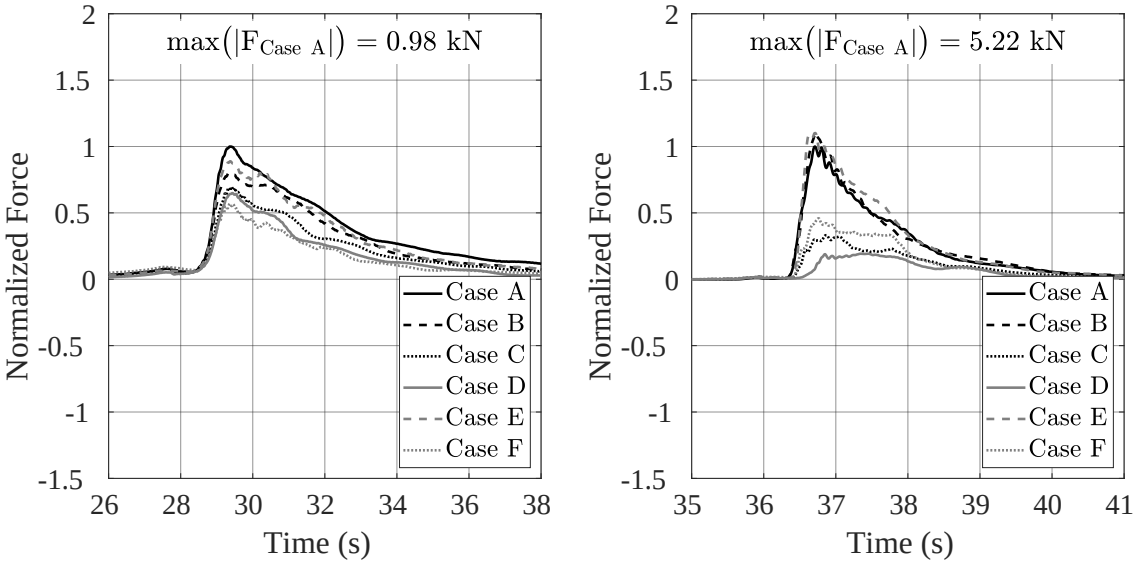

(a) Unbroken Wave

(b) Broken Wave

Figure 5.3: Stream-wise Load Cell (B) Force Histories Normalized by the Maximum Force of the Reference Case, $\max(|F_{CaseA}|)$

For example, consider the two cases (Cases B and E) where concrete blocks were not directly in front of the test structure. For these cases, the maximum stream-wise force increased by roughly 10% for the broken wave as shown in Figure 5.3. Consistent with the idea that increased flow velocities should result in greater wave forces, the maximum stream-wise flow velocity increased from 2.03 m/s for Case A to 2.43 m/s for Case B as shown in

Figure 5.1; however, the opposite occurred for Case E, where the flow velocity decreased to 1.89 m/s. For the unbroken wave, Cases B and E resulted in 20% and 10% force reductions, respectively. As is expected when the force decreases, the Case B flow velocity reduced to 0.99 m/s from 2.03 m/s for the reference case (Case A), but on the contrary Case E resulted in an increased velocity of 1.84 m/s. In these cases, the concrete block did not shield the test structure by directly blocking the wave from impacting the front face or significantly redirecting the flow path away from or around the test structure, whereas both of these effects were present for the remaining cases (Cases C, D, and F). For both wave types, the concrete blocks in Cases C, D, and F shielded either half (Cases C and F) or all (Case D) of the front face, resulting in significant stream-wise force reductions of 30% to 80% relative to the reference case even though the velocities either increased up to 2.41 m/s and 2.30 m/s for the unbroken and broken waves, respectively. These results demonstrate that large degrees of shielding reduced the net stream-wise force through the redirection of the flow away from the test structure.

In terms of the vertical forces, both wave types produced vertical load distributions that varied significantly as the degree of shielding varied near the offshore edge of the test structure. This may be seen by comparing the top front (LC6 and LC7) and back (LC8 and LC9) load cell force histories shown in Figure 5.4 and Figure 5.5. For the unbroken wave Figure 5.4a and Figure 5.4b show that there was minimal variation of the back vertical loads (LC8 and LC9) among the six macro-roughness configurations. In addition, the left (LC9) and right (LC8) load cells had nearly identical load histories, demonstrating that any overturning moment about the x-axis (i.e. stream-wise direction) was negligible.

In contrast, the top front load cell (LC6 and LC7) histories varied more on a case-by-case basis, as shown in Figure 5.4c and Figure 5.4d. For the unbroken wave, the peak forces measured by the front vertical load cell for Cases B to F varied from negative to positive with increasing shielding in terms of the percentage of the front face of the test structure that was directly obstructed by the concrete blocks. For example, the 0%-shielding configurations (Cases B and E) resulted in the lowest front vertical forces, which were followed by the 50%-

shielding (Cases C and F) and 100%-shielding (Case D) configurations. This progression from the minimum to the maximum front vertical force also coincides with decreasing maximum stream-wise force. As the maximum stream-wise force decreased with increased shielding, the overturning moment caused by the stream-wise force reduced as well, which corresponds to the increasing front vertical load cell forces.

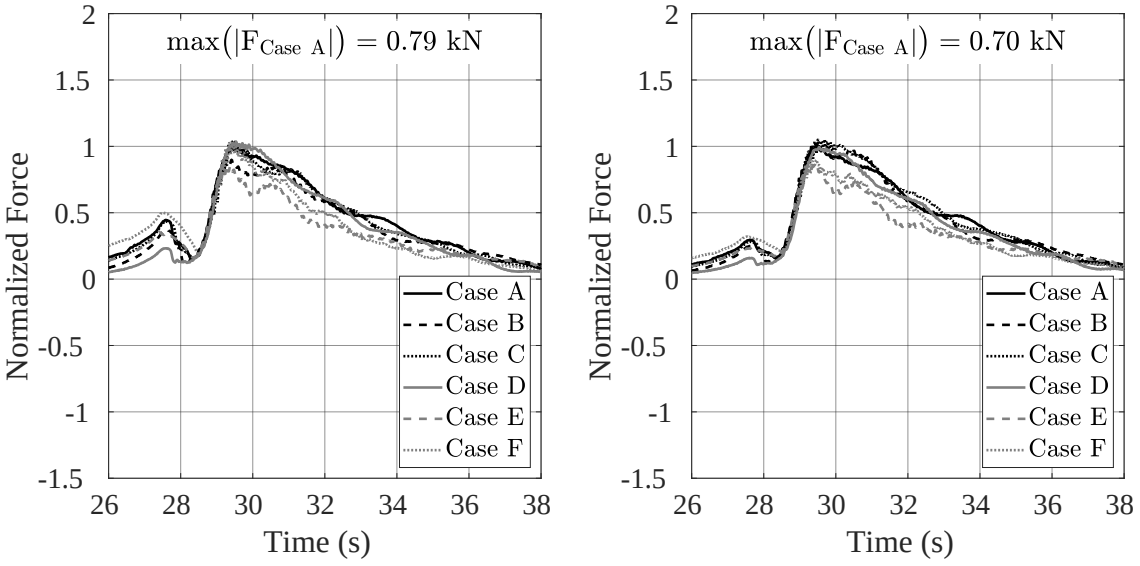

(a) Top Back Left (LC9)

(b) Top Back Right (LC8)

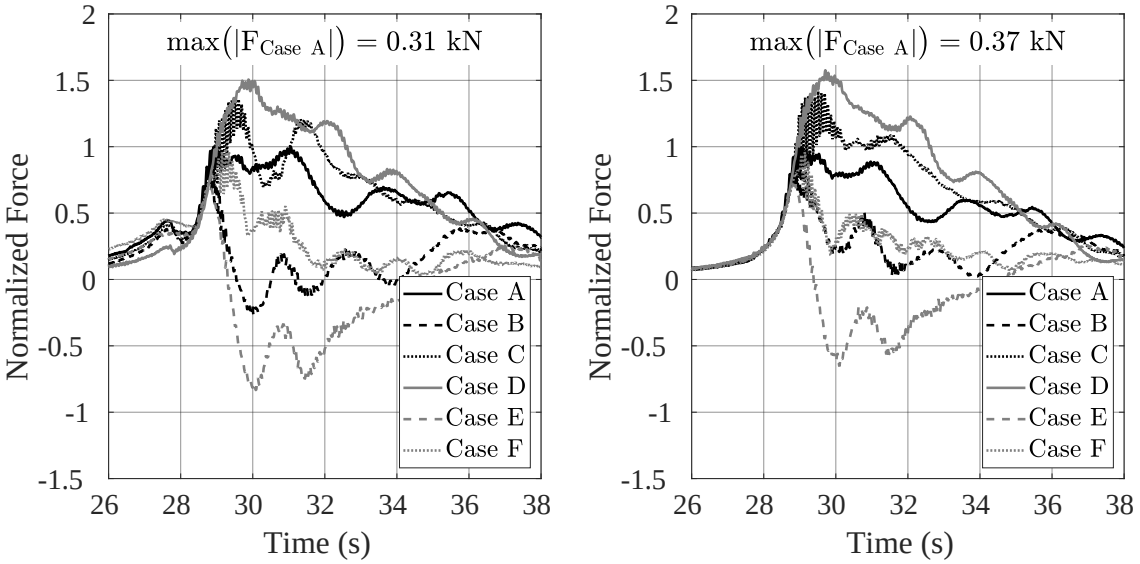

(c) Top Front Left (LC7)

(d) Top Front Right (LC6)

Figure 5.4: Unbroken Wave Vertical Load Cell Time Histories Normalized by the Maximum Force of the Reference Case, max($|F_{CaseA}|$)

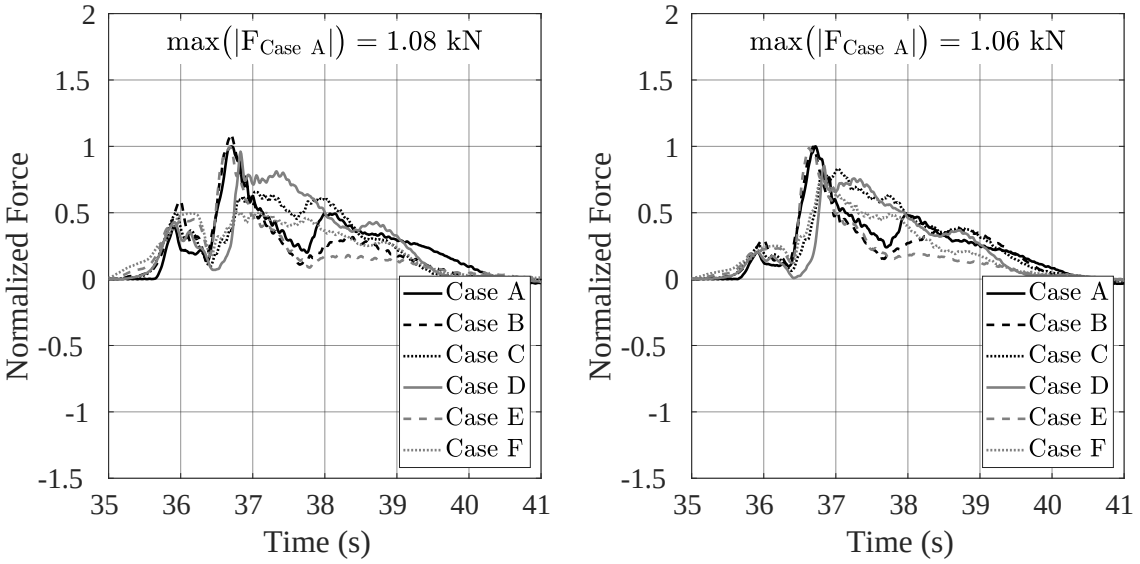

(a) Top Back Left (LC9)

(b) Top Back Right (LC8)

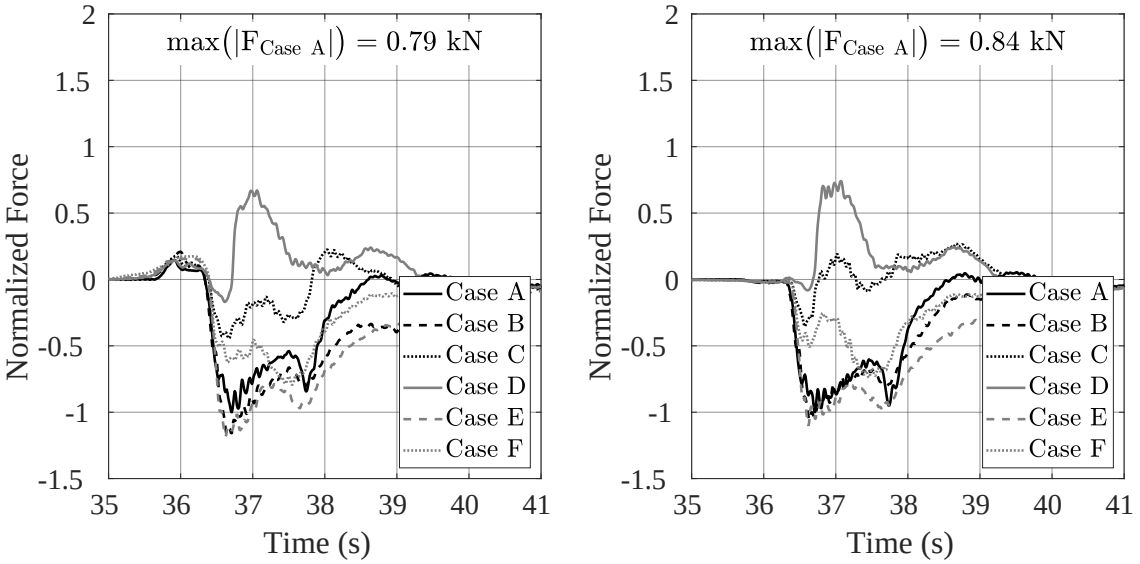

(c) Top Front Left (LC7)

(d) Top Front Right (LC6)

Figure 5.5: Broken Wave Vertical Load Cell Time Histories Normalized by the Max Reference Case Force, $\max(|F_{CaseA}|)$

As shown in Figure 5.5a and Figure 5.5b for the broken waves, the vertical forces measured by the top, back load cells (TBL and TBR) also were consistent for all of the configurations. The largest uplift forces measured by the back vertical load cells corresponded to the block configurations with 0%-shielding (Cases A, B, and F) of the test structure's front face. The remaining configurations with 50%- and 100%-shielding resulted in decreased maximum uplift forces. Additionally, as shown in Figure 5.5c and Figure 5.5d for the broken wave, the peak front vertical load cell force increased for increasing shielding and decreasing maximum stream-wise force, which follows the same trend as the unbroken wave data.

To better understand the relation between the stream-wise and vertical forces, time histories of the median vertical-to-horizontal force ratio are shown in Figure 5.6 and Figure 5.7 for both the unbroken and broken wave conditions, respectively. In these figures, the vertical-to-horizontal force ratios at the instants the peak stream-wise and vertical forces occurred are also noted. For this purpose, vertical force time histories were obtained by adding the time histories of all the vertical load cells.

For the unbroken wave, Figure 5.6 shows that the median vertical-to-horizontal force ratios are greater than unity, indicating that for all configurations, the vertical forces exceeded the stream-wise forces. Moreover, the median vertical-to-horizontal force ratio increased as the waves were diverted more with increasing shielding with the exception of Case E (see Figure 5.6b), where flow constriction results in increased stream-wise force relative to vertical force.

As shown in Figure 5.7, for the majority of the configurations, the median vertical-to-horizontal force ratios were below unity, which indicates that the stream-wise forces exceeded the vertical forces for the broken wave. This is consistent with the fact that an initial 0.15 m air gap present in the broken wave case compared to no air gap for unbroken wave resulted in lower buoyancy-induced uplift for the former compared to the later wave case. However, similar to the unbroken wave case, as the waves were diverted more with increased shielding (Case C and Case D), the median vertical-to-horizontal force ratios increased and exceeded unity. This was caused by decreases in the free-surface elevation on the front face of the test structure during the wave impact, which resulted from the flow being diverted away from the front face of the test structure by the concrete blocks, led to much smaller areas experiencing wave impact pressures, and reduced horizontal force demands. On the other hand, the roughness element configurations of Cases B and E focused the broken wave toward the test structure, which led to vertical-to-horizontal force ratios less than unity, indicating that the horizontal forces were increased in these cases due to channeling of the flow. As a result, similar trends in the vertical-to-horizontal force ratios were observed for these cases with respect to the reference case (Case A), yet always with lower values than those of the reference case.

Similarly, the significant changes in the front vertical loads shown in Figure 5.7 were due to the changing position in which the broken wave impacts the structure. Cases B and E diverted the broken wave the least and it still impacted the front face of the structure with a significant horizontal force compared to the vertical force. However, for Cases C, D, and F, the wave is blocked from directly impacting the front face of the test structure as well as

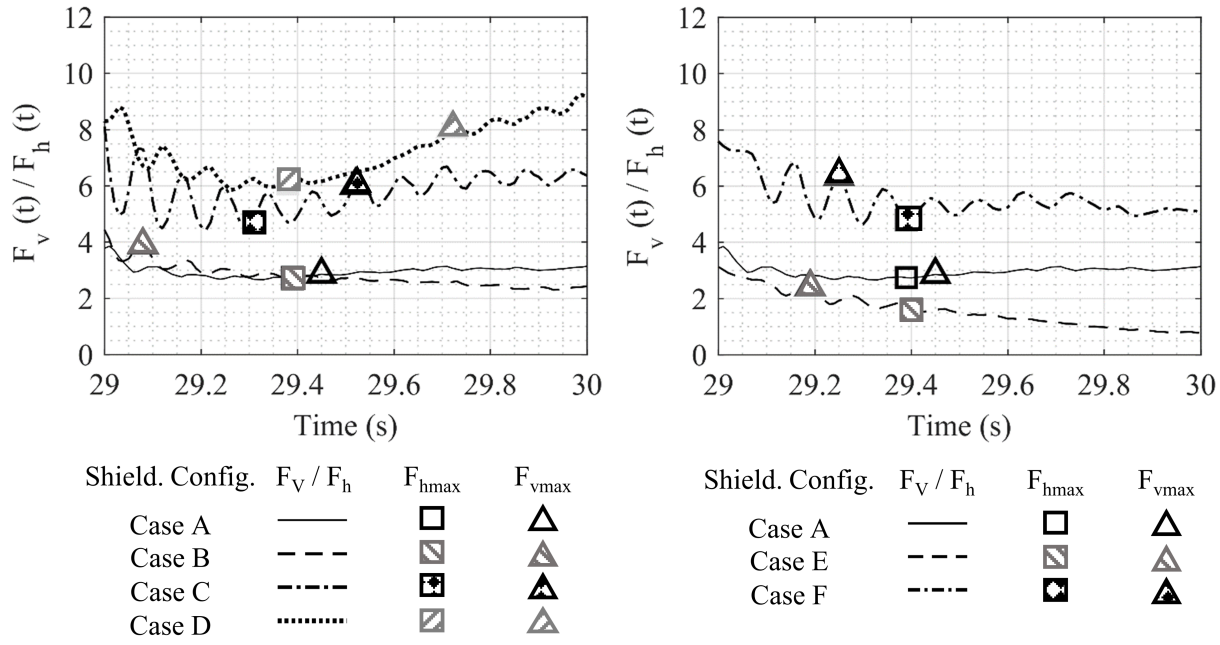

(a) Cases B, C, and D (One-block Cases) Compared to Case A

(b) Cases E and F (Two-block Cases) Compared to Case A

Figure 5.6: Vertical-to-Horizontal Force Ratio for the Unbroken Wave (Alam et al., 2019)

diverted sideways away from it, reducing the horizontal impact force on the front face of the structure and leading to increased uplift forces as the shortened broken wave impacted the underside of the front of the structure more than in Cases B and E.

5.3 Effects of Macro-roughness on Measured Pressures

The pressure distributions over the front face of the test structure were examined for each macro-roughness configuration. These results were compared to the reference case (Case A) without roughness elements by normalizing the pressures by the reference case pressures. Figure 5.8 and Figure 5.9 present pressure distributions for each configuration and both the unbroken and broken, tsunami-like wave types, respectively. The figures show the maxima of the ensemble-averaged pressures of the cases with roughness elements (Cases B to F) normalized by the maxima of the ensemble-averaged pressures of Case A ($\hat{p} = \max(\bar{p}_{\text{Case i}}) / \max(\bar{p}_{\text{Case A}})$, where i is any case from B to F. The figures also show the

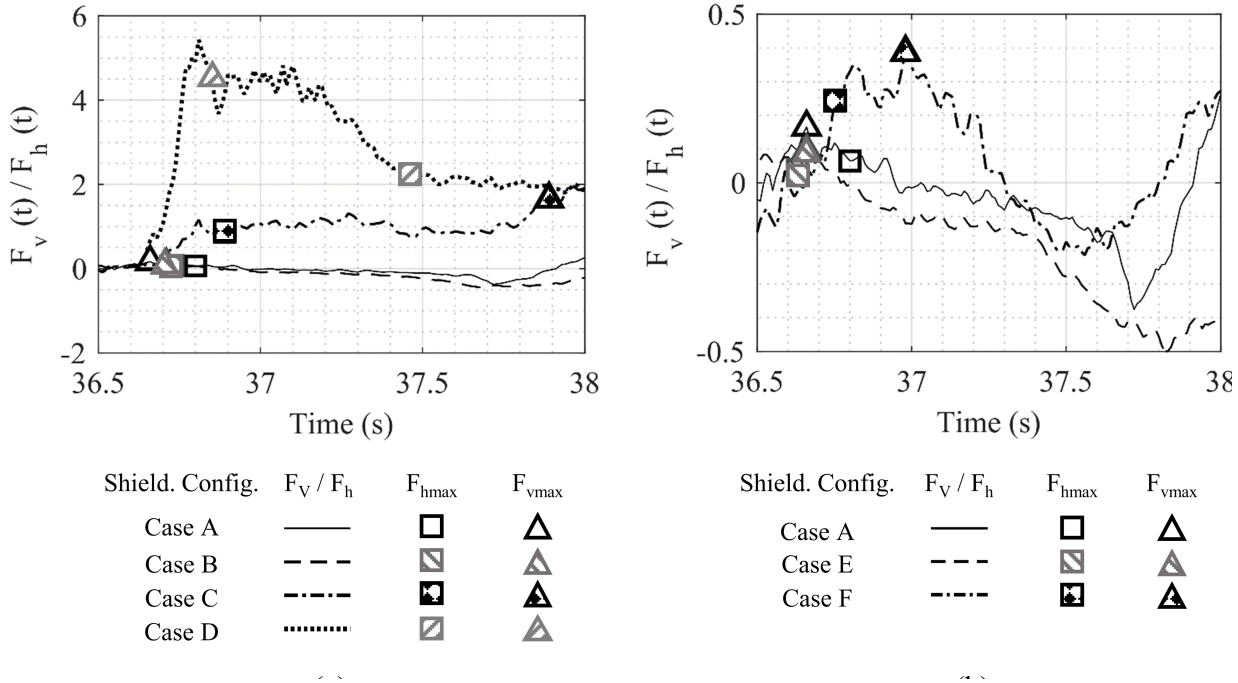

(a) Cases B, C, and D (One-block Cases) Compared to Case A

(b) Cases E and F (Two-block Cases) Compared to Case A

Figure 5.7: Vertical-to-Horizontal Force Ratio for the Broken Wave

ensemble standard deviations of the pressures calculated at the same point in time as the max ensemble-averaged pressures ($\hat{\sigma} = \sigma_{\text{Case i}} / \max(\bar{p}_{\text{Case A}})$), which were also normalized by the maxima of the ensemble-averaged pressures of Case A.

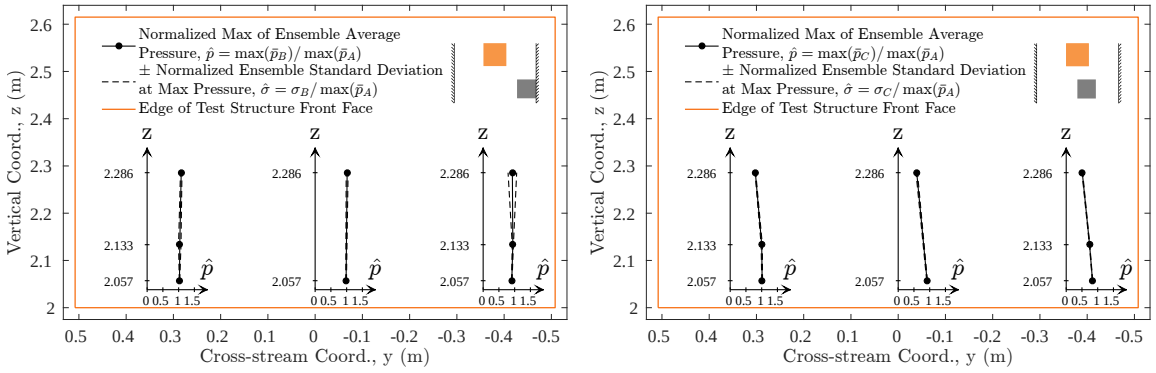

(a) Case B

(b) Case C

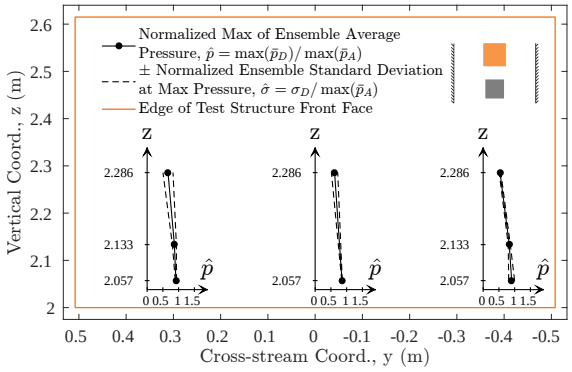

(c) Case D

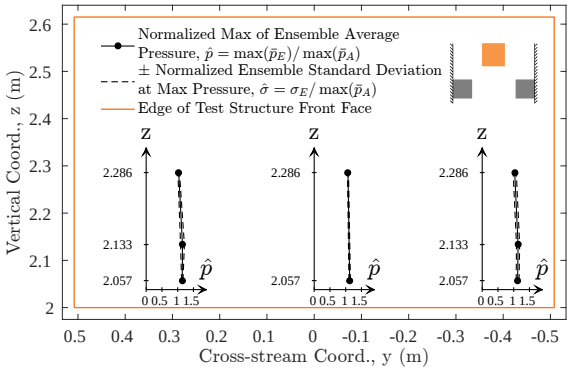

(d) Case E

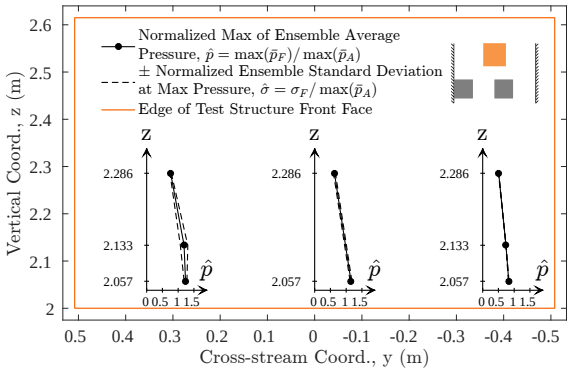

(e) Case F

Figure 5.8: Unbroken Wave - Effects of Macro-roughness Configurations on Front Face Pressures

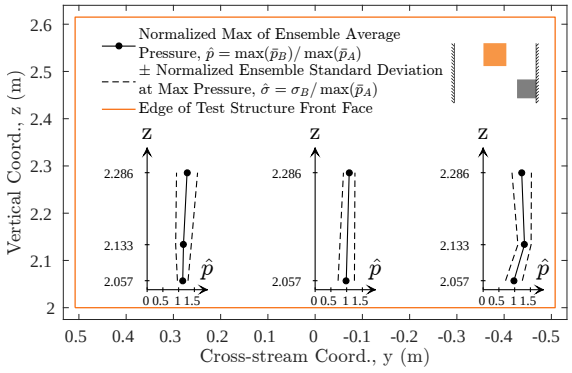

(a) Case B

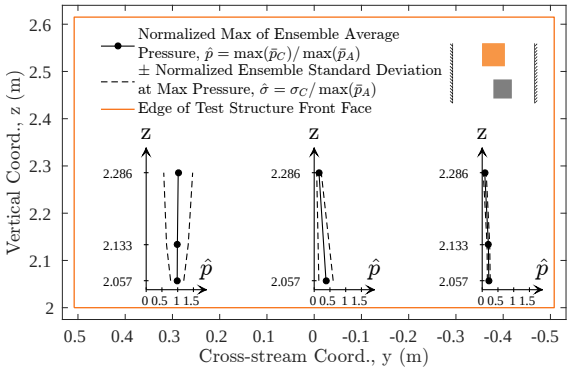

(b) Case C

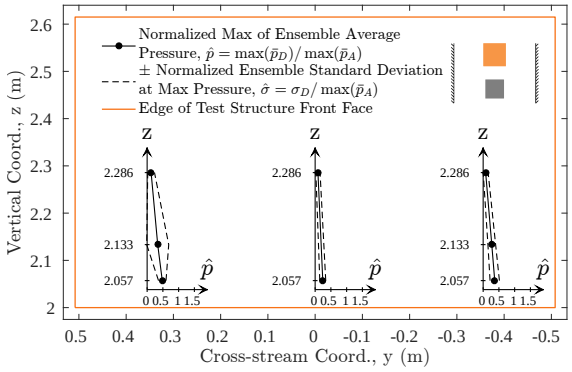

(c) Case D

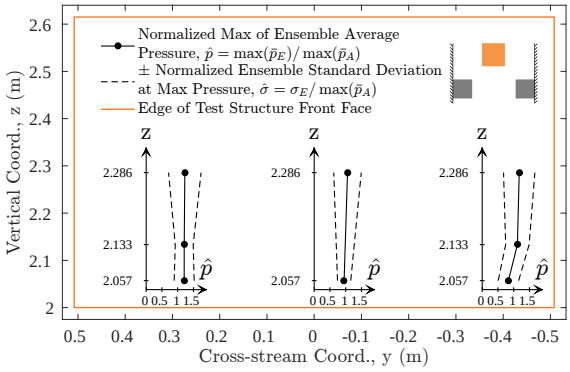

(d) Case E

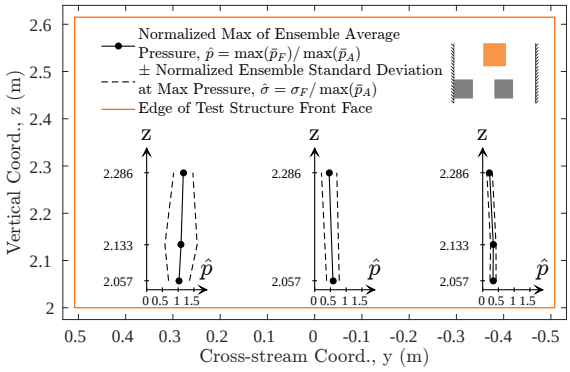

(e) Case F

Figure 5.9: Broken Wave - Effects of Macro-roughness Configurations on Front Face Pressures

By comparing the pressure distributions shown in Figure 5.8 and Figure 5.9 to the stream-wise forces in Figure 5.3, it may be observed that even though local pressures increased over the front face of the test structure for the Case E configuration, the overall stream-wise force measured by the load cells decreased by at least 50% for both unbroken and broken waves. This demonstrates that even though the entire structure was subjected to a smaller resultant stream-wise force for this configuration, local pressures on the front face increased, which would cause a larger force on a sub-region of that structural element, but not over the entire face.

5.3.1 Mean Pressures

In exposed regions of the front face of the test structure, local pressures increased for the Cases B and E and for the left column of pressure gauges for Cases C and F as demonstrated in Figure 5.8 and Figure 5.9. This further demonstrates how flow channel constriction results in the increased velocities, as shown in Figure 5.1, and consequently increased the local, total pressures due to an increase in the local, dynamic pressures.

Just behind the concrete blocks, in the most shielded regions of the front face of the test structure, significant decreases in pressure occurred for Cases C, D, and F with local pressure reductions reaching nearly 90% behind the blocks, as shown in Figure 5.9. For example, the middle and right pressure gauge columns of Cases C and F experienced the largest pressure reductions, ranging from 30% to 90%. Similarly, Case D resulted in pressure reductions of 45% to 90%, showing that increased shielding results in more severe local reductions in pressure behind upstream obstacles placed at distances similar to those between structures in an urban environment.

Another key difference between the unbroken and broken wave pressure distributions was the degree of variability as indicated by the locally large normalized standard deviations in max pressure. Looking at the broken wave results in Figure 5.9, these larger standard deviations occurred for un-shielded regions of the front face of the test structure. This is due to the much more turbulent nature of the broken bore-like wave as opposed to the smooth unbroken wave that was largely undisturbed by the roughness elements.

5.3.2 Pressure Distribution

The large reductions in pressure that occurred in shielded areas of the front face of the test structure for both wave types imply that the stream-wise forces on the test structure should have also decreased for increased shielding. Similarly, in exposed regions of the front face, local increases in pressure would cause increases in the stream-wise forces. To determine the net result of both of these local effects, the front and back face pressure gauge measurements

were compared to the stream-wise load cell (LC5) measurements.

In order to make a comparison between the load cell force measurements to the pressure gauge measurements, the pressure field was estimated over the entire front face of the test structure so the total stream-wise force due to the pressure field could be calculated by integrating it. The pressure fields were estimated for both the unbroken and broken waves using multi-linear regressions of the pressure gauge data at each point in time, which were then integrated using the trapezoidal method to determine the total force as well as the center of pressure, through which the total force acted. Also, in order to account for the pressure acting on the back face of the test structure, a hydrostatic pressure distribution was assumed and fit through the single back face pressure gauge measurement data point. Examples of the front and back face assumed pressure surfaces are shown in Figure 5.10.

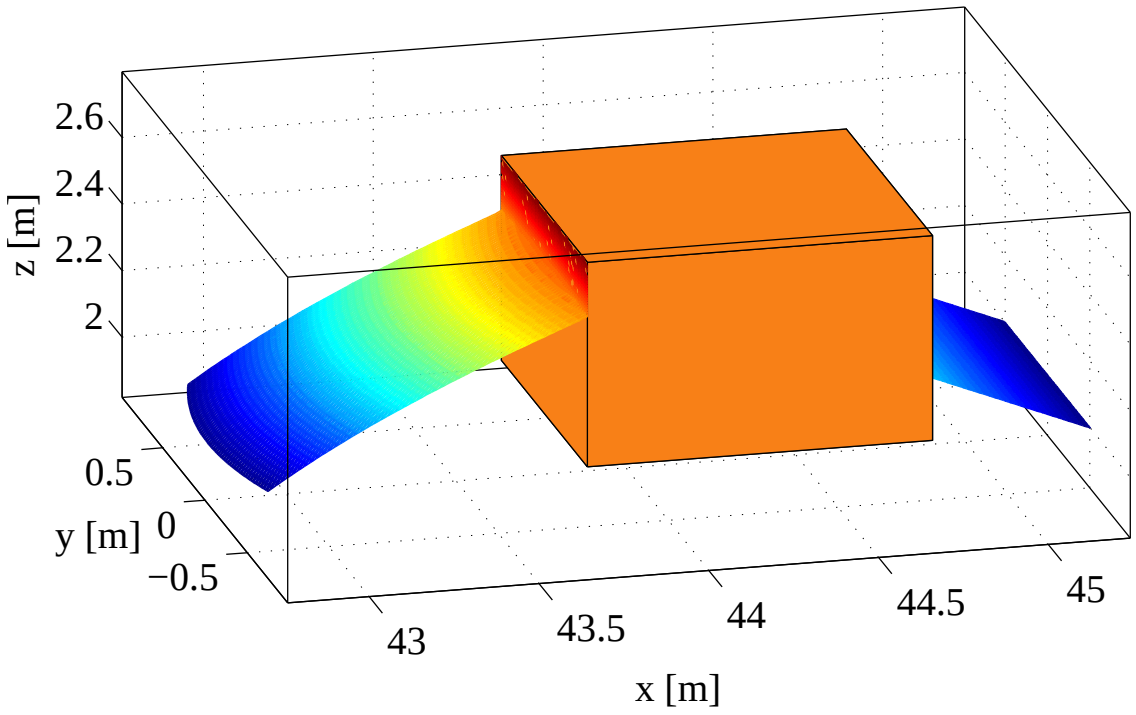

Figure 5.10: Assumed Pressure Field Profiles Acting on the Offshore and Onshore Test Structure Faces

For each point in time, a bi-quadratic surface as defined by Equation 5.1a was assumed and the polynomial coefficients were calculated to check if the surface gave a physically

realistic result. Note that the y- and z-coordinates given in the pressure field equation are the global coordinates of the wave flume shown in Figure 4.1). If $C_5 < 0$ in Equation 5.1a, then the surface was convex relative to the offshore face of the test structure and the result was kept. However, if $C_5 > 0$ in Equation 5.1a, then the surface was concave relative to the offshore face of the test structure, which resulted in aphysical, large pressure values near the top of the test structure, where they did not occur during the experiments since the waves impacted the test structure near its base before running up the offshore face. In these instances, a bi-linear surface as defined by Equation 5.1b was used instead, which avoided the over-prediction of pressures near the top of the test structure. The entire pressure integration process is outlined in detail by the flow chart provided in Figure 5.11.

$$p_{\mathrm{Q}}(y,z) = C_0 + C_1 y + C_2 z + C_3 yz + C_4 y^2 + C_5 z^2 \tag{5.1a}$$

$$p_{\mathrm{L}}(y,z) = L_0 + L_1 y + L_2 z + L_3 yz \tag{5.1b}$$

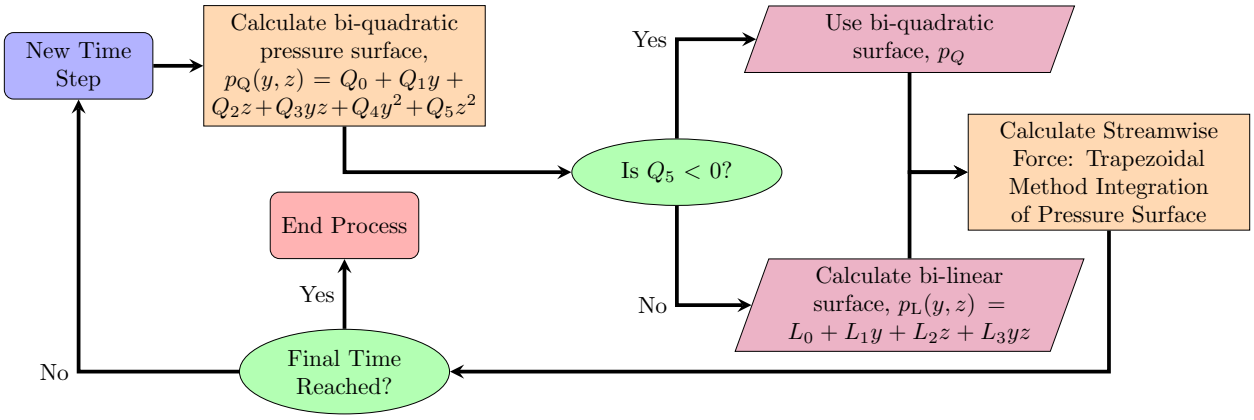

Figure 5.11: Pressure Integration Process Flow Chart

Additionally, the assumed hydrostatic pressure distribution acting on the onshore test structure face was determined and integrated. Using a slope of $\gamma_{\mathrm{water}} = g\rho_{\mathrm{water}}$, a linear surface was fit through the single pressure value measured on the onshore face of the test structure, assuming the distribution was uniform in the transverse or alongshore direction. The resulting linear surface is defined by Equation 5.2, where p_{14} is the onshore face pressure

gauge measurement and z_{14} is the vertical global coordinate location of the onshore face pressure gauge.

$$p_{\mathrm{B}} = -\gamma_{\mathrm{water}}(z - z_{14}) + p_{14} \tag{5.2}$$

Initial calculations showed there were notable discrepancies between the integrated pressure results and back load cell (LC5) force histories. This was caused by friction within the slider bearings mentioned previously in the experimental methodology section that allowed the test structure to translate in the stream-wise direction. To amend this issue, a suitable coefficient of friction ($\mu = 0.1$) was determined such that the maximum stream-wise load cell force added to the friction coefficient multiplied by the sum of the four vertical load cell forces (LC6, LC7, LC8, and LC9) at the same instant resulted in a close match for all of the roughness element configuration results and both wave types. All of the stream-wise load cell force histories presented in this manuscript were augmented in this manner.

For the unbroken wave, the near bi-linearity of the pressure fields is shown in Figure 5.12. The minimal variability of the unbroken wave data, regardless of which roughness element configuration was used, made the surface fits quite accurate with high coefficients of determination ($R^2 \geq 0.98$) even during the peak stream-wise load. The only notable variations in the pressure field due to increased shielding showed up in the bottom right corner of the front face of the test structure, which was directly behind one of the concrete blocks for Cases C and F. In these regions, the pressures locally decreased relative to the un-shielded pressure gauges. Particularly, Cases C and F showed the greatest degree of asymmetry in their pressure distributions, where significant decreases occurred on the right side of the front face of the test structure with minor decreases in the middle as was observed in Figure 5.9.

This difference is also evident when comparing the horizontal, box width coordinate (i.e. the y-axis of flume coordinate system) of the center of pressure from case A (0.0 m) to those of cases C and F (0.04 m). The changing centers of pressure for cases C and F show that the resultant stream-wise force due to the pressure field on the front face of the test structure

was shifted to the left of the center, indicating higher pressures were exerted over the left side of the front face than the right side. Case D also showed a notable reduction in the maximum inundation depth of the unbroken wave as well as reduced pressures over the entire front face of the test structure, which matches well with observations made from Figure 5.9.

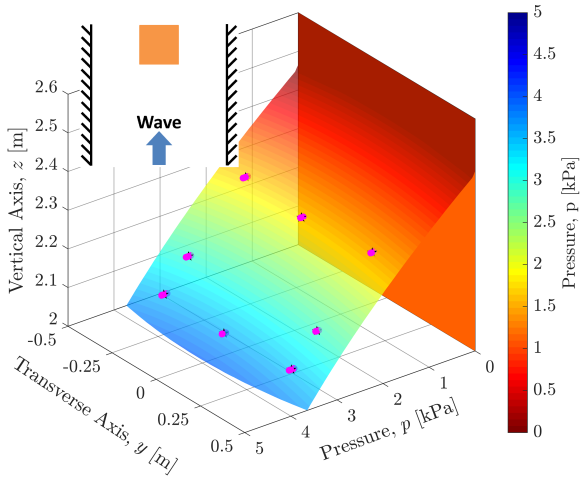

(a) Case A ($t = 29.36$ s)

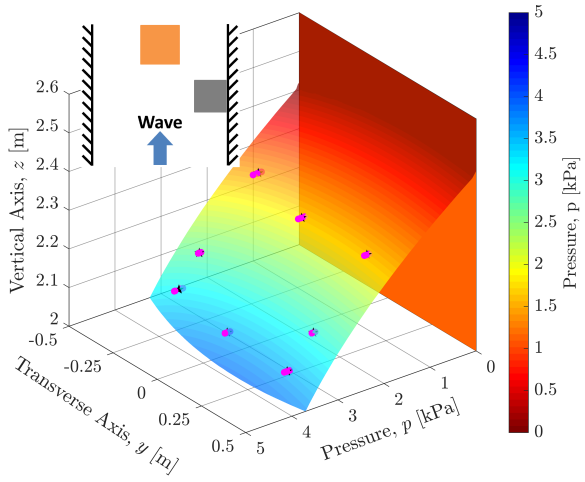

(b) Case B ($t = 29.41$ s)

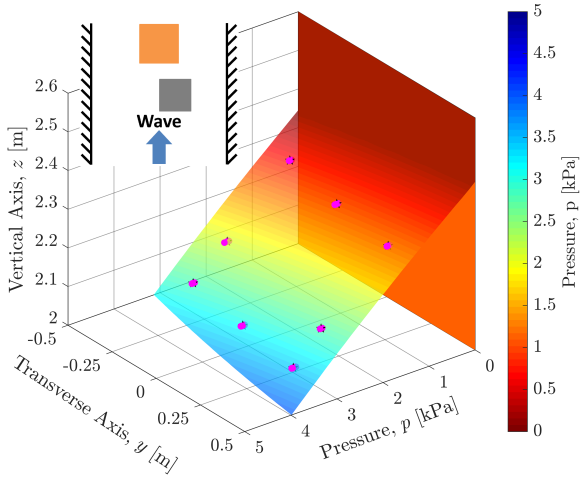

(c) Case C ($t = 29.41$ s)

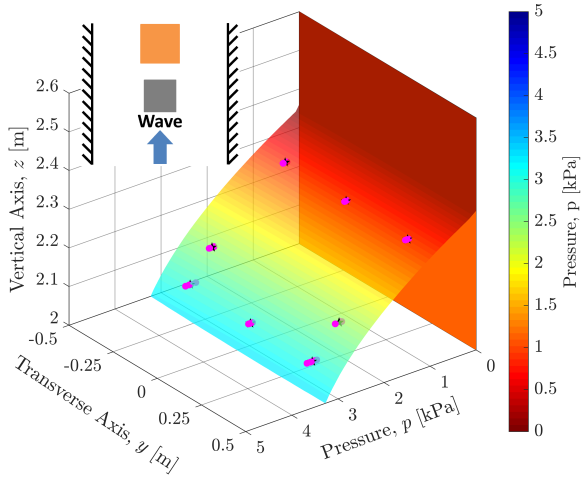

(d) Case D ($t = 29.44$ s)

The resulting integrations of these mean pressure field surface fits over time are shown in Figure 5.13, where they were compared to the mean stream-wise load cell time history

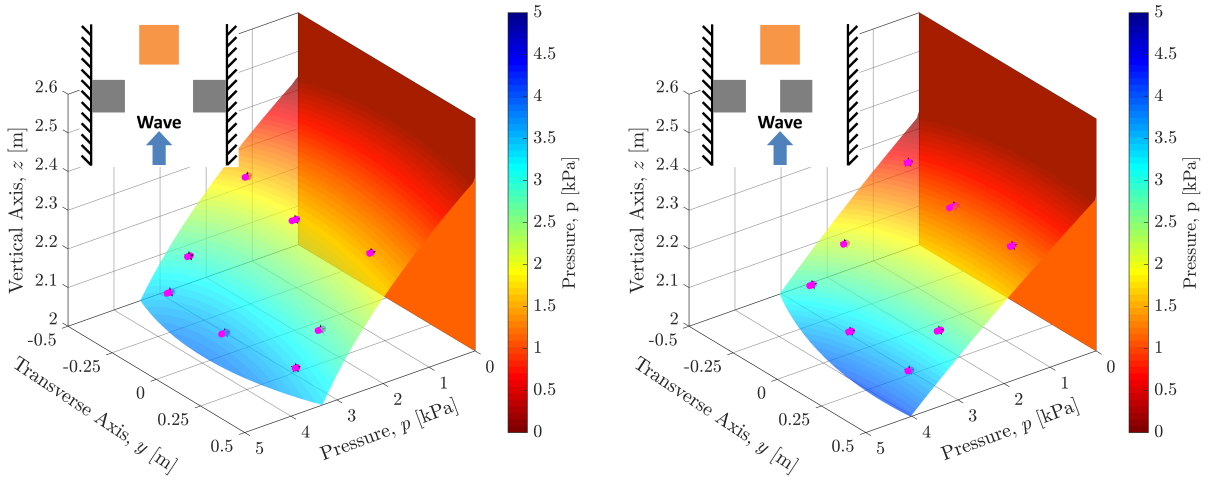

(e) Case E ($t = 29.37$ s)

(f) Case F ($t = 29.36$ s)

Figure 5.12: Unbroken Wave Pressure Surface Fit for Varying Macro-roughness at the Time of Max Streamwise Force

measurements. To demonstrate whether or not the integration results lie within the range experimental variability of the load cell measurements, each individual trial time history of the back load cell force was plotted as well. For Cases B and E, the peak forces of the integrated pressure fields match the load cell measurements very closely, whereas the remaining results for Cases A, C, D, and F did not match the load cell measurements as accurately, giving slightly underestimated peak forces, although the general trend and timing of the peak forces matched well. Additionally, the differences between the load cell and integrated pressure force histories are the larger during the post-peak decaying region of the force histories, where significant oscillations exist integrated pressure force histories, but not for the load cell force histories. These differences were caused by a combination of other loads not considered in the pressure integration, such as the overturning of the test structure, as well as any potential friction forces beyond the vertical force multiplied by the assumed friction factor of $\mu = 0.1$ that were sustained by the nominally friction-less bearings, which allowed the test structure to displace in the stream-wise and transverse directions.

Applying the same approach for the broken wave as with the unbroken wave produced

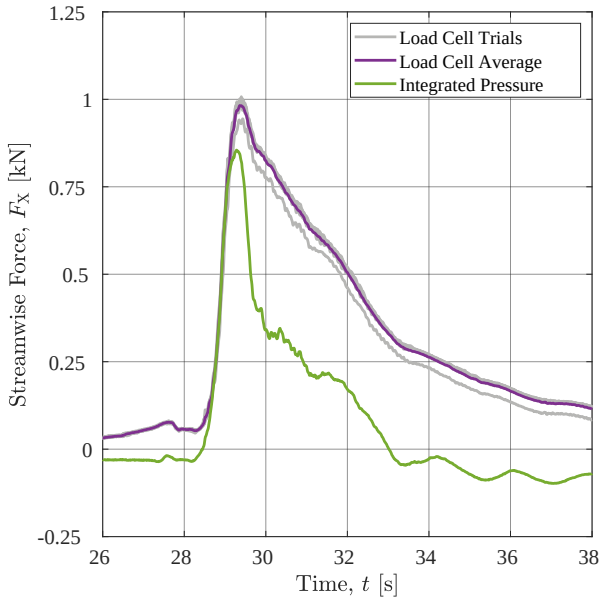

(a) Case A

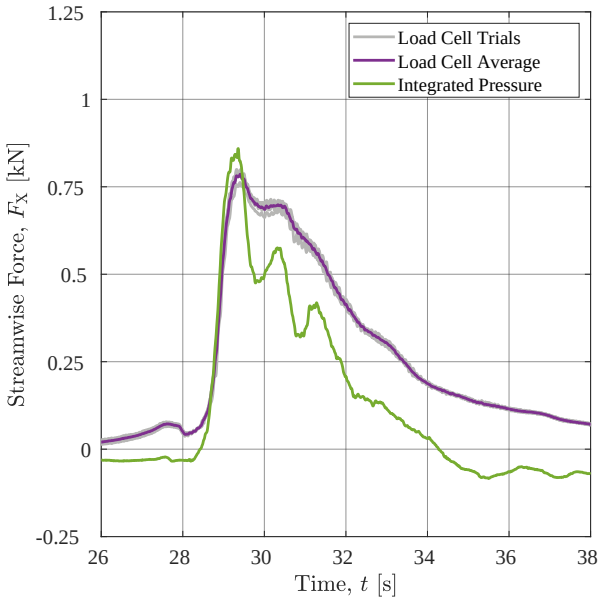

(b) Case B

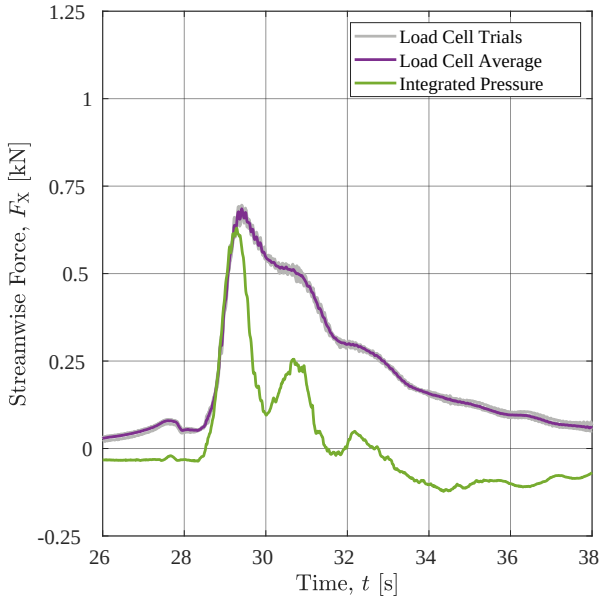

(c) Case C

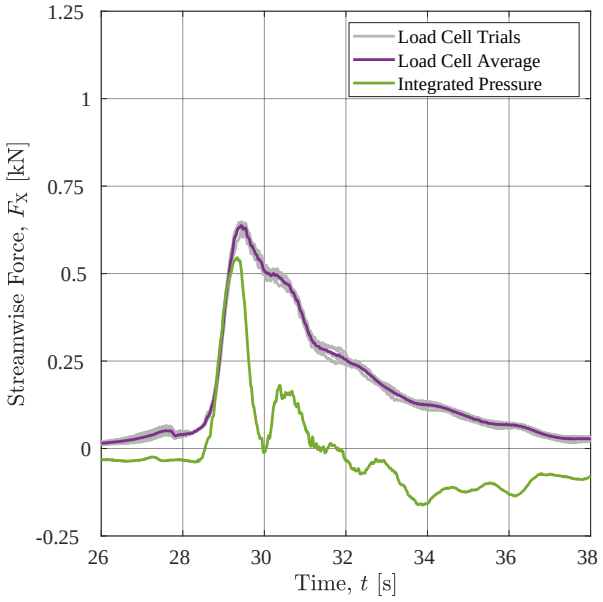

(d) Case D

much less accurate surface fit results due to the greater degree of variability in the measured peak pressure data as shown in Figure 5.14. As was shown previously in Figure 5.9, the Cases C, D, and F experienced pressure reductions over portions of the front face of the test structure, which led to large stream-wise force reductions relative to the reference case

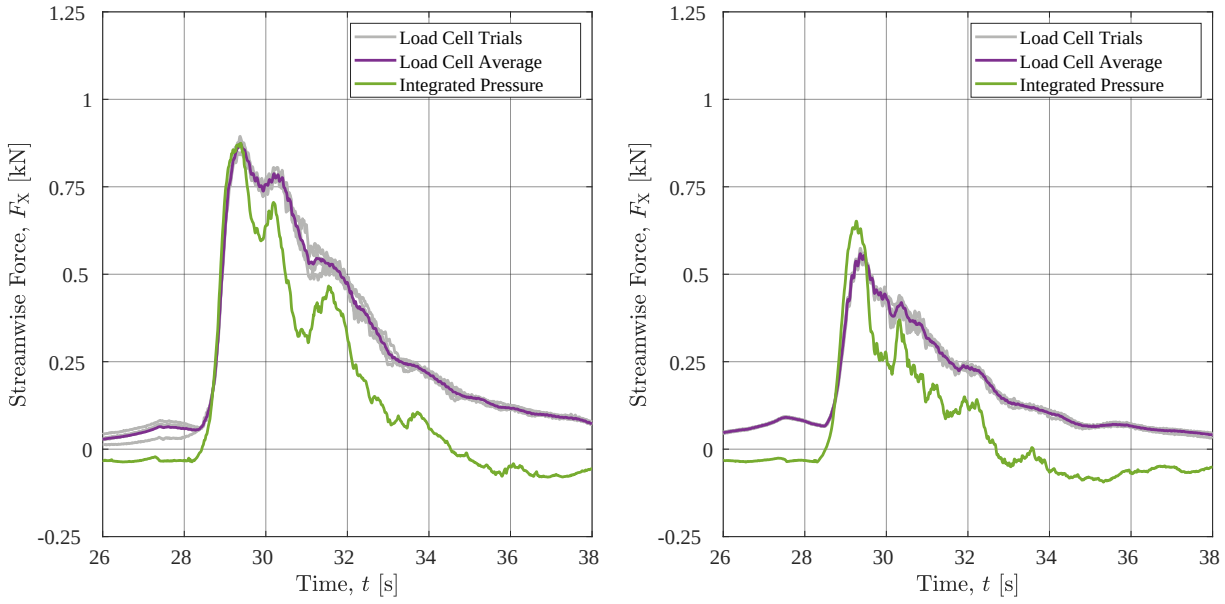

(e) Case E (f) Case F

Figure 5.13: Streamwise Force History Comparison between Load Cell (LC5) Measurements and Integrated Pressure Surface Fits for Varying Macro-roughness

(Case A) as shown in Figure 5.3. What was not immediately apparent was the fact that the estimated wave inundation depths would have decreased locally in the top right corners for Cases C and F and across the entire front face for Case D. Reductions in the inundation depth on the front face of the test structure reduced the areas over which the wave pressures acted, which accounts for the large force reductions along with the reduced pressures.

In a similar fashion to the unbroken wave results, the integrated pressure field forces matched the stream-wise load cell measurements very well in terms of the timing of peak forces for the broken wave as shown in Figure 5.15; however, the peak forces do not match as well as they did for the unbroken wave. For all of the roughness configurations except for Case D, where the impact is negated by the presence of the block fully shielding the structure, the peak integrated pressure force significantly exceeded the peak stream-wise load cell force. These sharp peaks are likely due to the highly impulsive nature of the bore-like, broken wave, which was more accurately captured by the highly sensitive pressure gauges than by

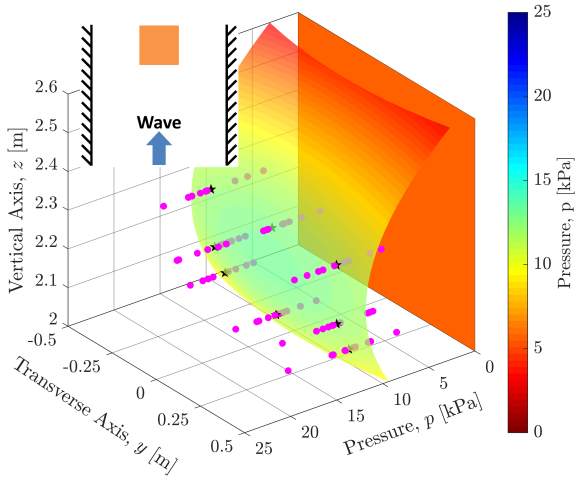

(a) Case A ($t = 36.71$ s)

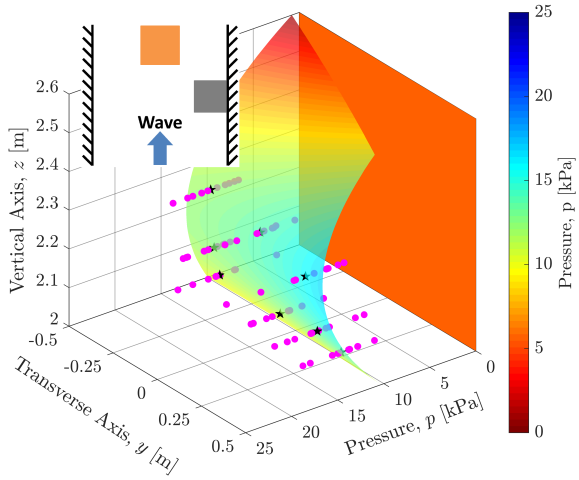

(b) Case B ($t = 36.72$ s)

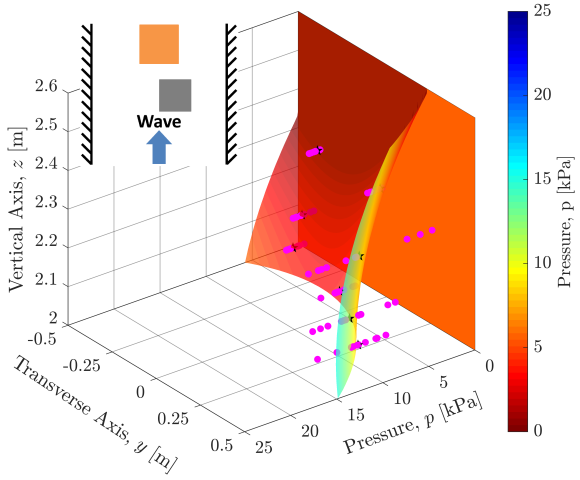

(c) Case C ($t = 36.86$ s)

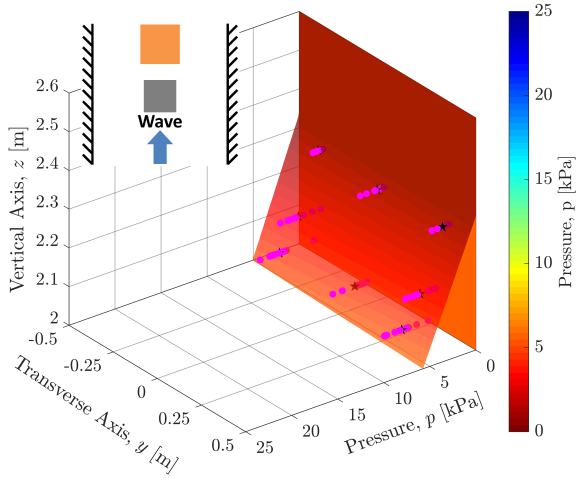

(d) Case D ($t = 37.45$ s)

the stream-wise load cell.

5.4 Comparison to Design Recommendations

To account for force increases due to velocity amplification in design practice, the ASCE 7-16 standard describes methods based on research by Nouri et al. (2010) and Thomas et al. (2015). Section C6.8.5 of ASCE 7-16 Chapter C6 presents the resulting force increase ratios

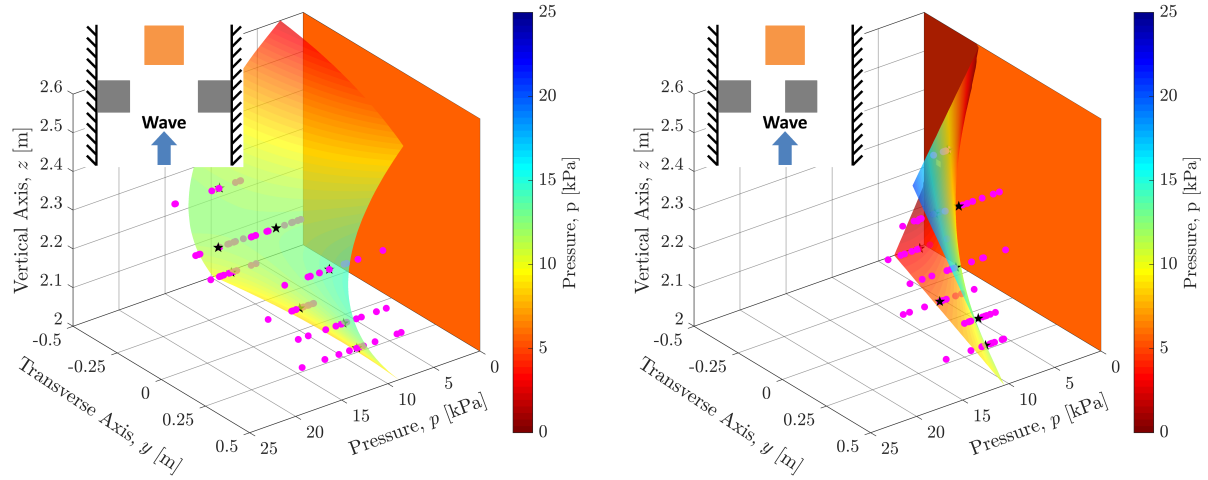

(e) Case E ($t = 36.71$ s)

(f) Case F ($t = 36.76$ s)

Figure 5.14: Broken Wave Pressure Surface Fit for Varying Macro-roughness at the Time of Max Streamwise Force

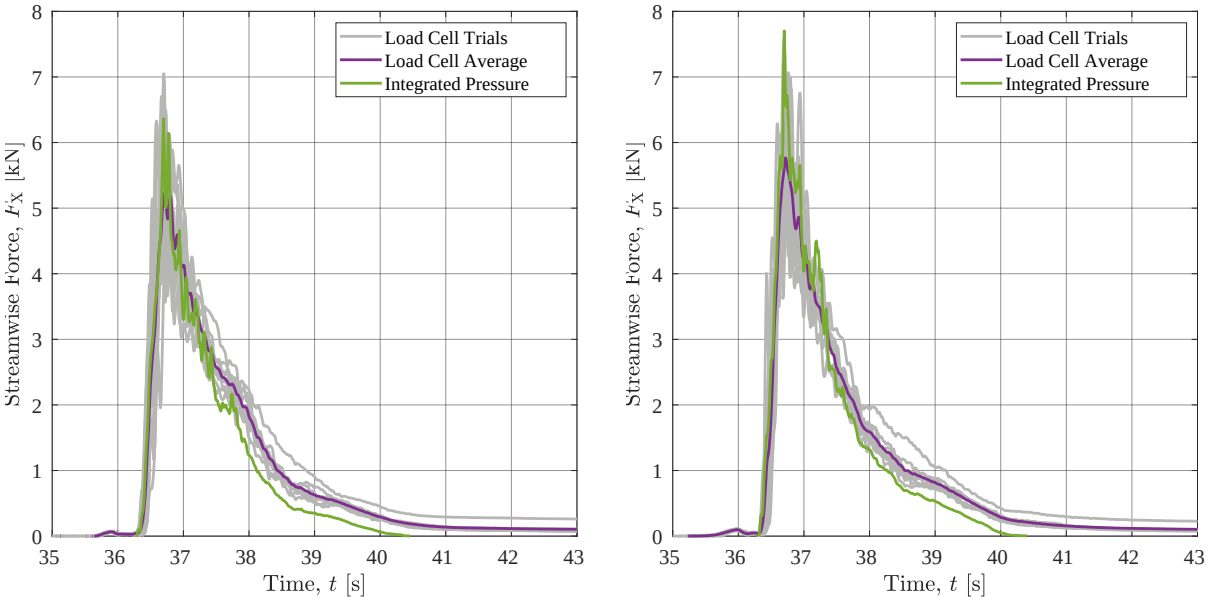

(a) Case A

(b) Case B

($FIR = F_{XC}/F_{X0}$) due to velocity amplification based on results reported by Nouri et al. (2010) and Thomas et al. (2015). Here, F_{XC} is the maximum stream-wise force of a given case and F_{X0} is the maximum force for the reference case. ASCE 7-16 Chapter C6 also specifies

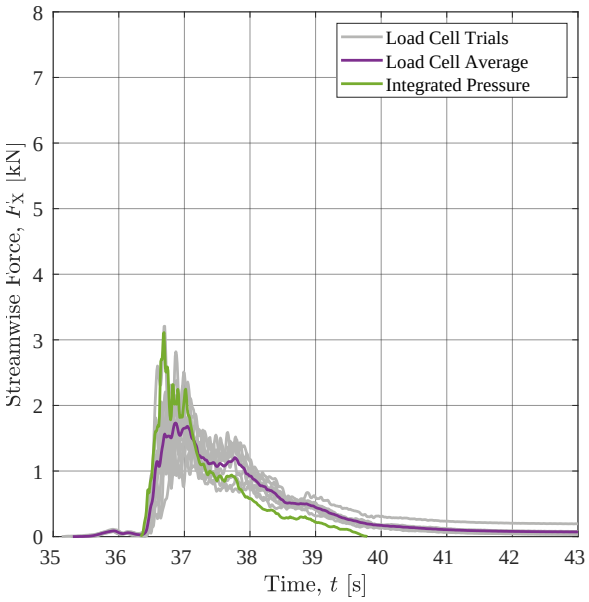

(c) Case C

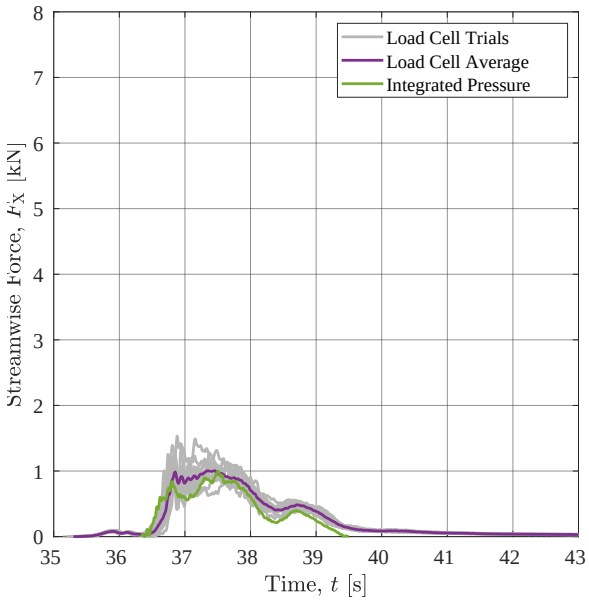

(d) Case D

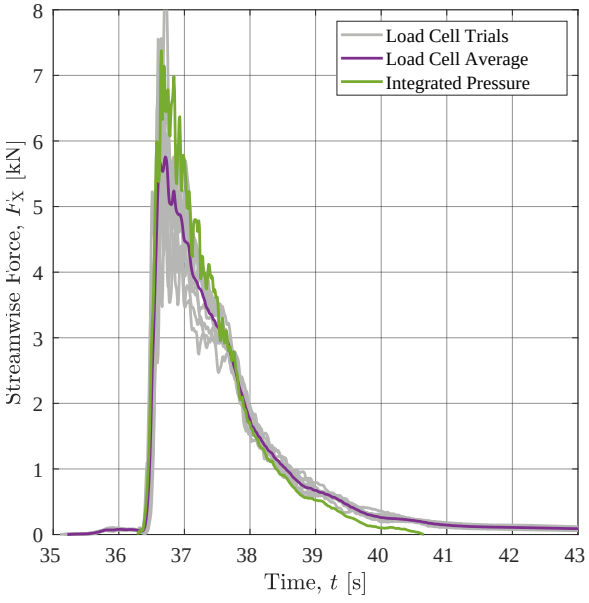

(e) Case E

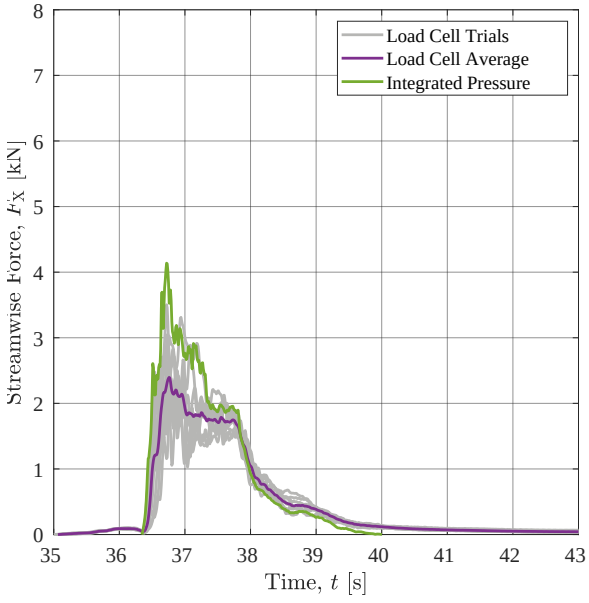

(f) Case F

Figure 5.15: Streamwise Force History Comparison between Load Cell (LC5) Measurements and Integrated Pressure Surface Fits for Varying Macro-roughness

restrictions for the usage of its method that employs the results of Nouri et al. (2010). The requirements are that $1 \leq L/W \leq 3$ and $0.6 \leq W_C/W \leq 0.8$ be satisfied, which rules out the application of the method for determining the force increase ratios when considering the experimental results presented in this paper since $L/W < 1$ for all of the roughness element configurations. Here, L is the distance between the upstream constriction and the design structure, W is the unobstructed flow width prior to the channel, and W_C is the constricted channel width as defined in ASCE 7-16 Chapter C6. Despite these limitations, the method was applied to determine whether or not it was suitable for a range of conditions outside the recommended limits.

To compare the experimental results of this paper to those of Nouri et al. (2010), they were overlaid on the same plot as shown in Figure 5.16. The most important difference between the two data sets is the fact that the data gathered by Nouri et al. (2010) only predicted increases in the maximum stream-wise force within the acceptable blockage ratio range (0.2 to 0.4), whereas both the unbroken and broken wave results show significant decreases in the maximum stream-wise force.

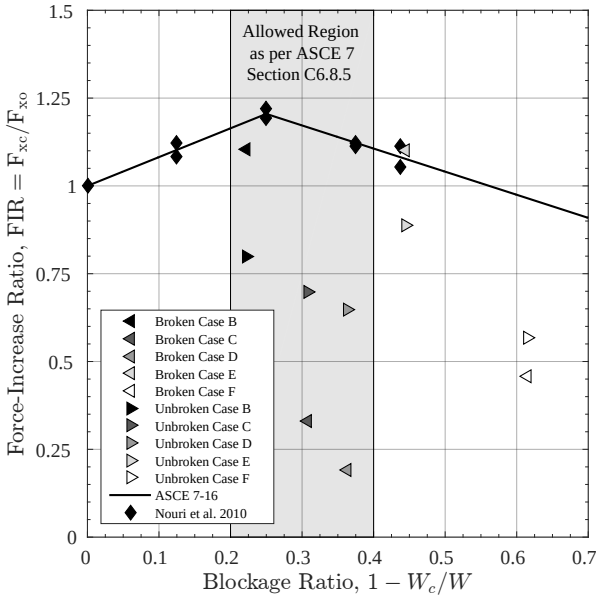

Figure 5.16: Force Increase Ratio Overlay of Experimental Results with Dam-break Test Data from Nouri et al. (2010)

With the exception of Case E, which amplified the maximum stream-wise force by channeling the wave toward the test structure, the maximum stream-wise force for the unbroken wave decreased in a roughly linear manner from the reference case point ($BR = 0,\ FIR = 1$) with increasing blockage ratio. This behavior matches the linear trend of the Nouri et al. (2010) data well for $BR \geq 0.25$ albeit at much lower force increase ratios, but with a similar slope. The primary reason so many of the force ratios are much lower than the results of Nouri et al. (2010) for both wave types is the fact that none of the tests conducted by Nouri et al. (2010) involved any form of shielding, but rather only flow channeling caused by symmetric channel width constrictions used to vary the blockage ratio and redirect the flow towards their test structure. The configurations with 0%-shielding (Cases B and E), which experienced much lower force reductions compared to the remaining cases, fit this category best out of Cases B to F. The best match with the Nouri et al. (2010) data occurred for Case E, which was the only case with symmetric constriction of the flume with the test structure perfectly aligned between the concrete blocks. This configuration channeled the wave toward the test structure, resulting in an amplified maximum force of about 10% for the broken wave as was noted previously. Even though there was not a perfectly symmetric reduction of the flume width for Case B, the resulting maximum stream-wise force increase of 10% matches the Nouri et al. (2010) data well for the broken wave too. All other configurations (Cases C, D, and F), which shielded $\geq$50% of the front face of the test structure, redirected the flow too much to produce similar results to those of Nouri et al. (2010) These cases resulted in the largest reductions in the maximum stream-wise force for both wave types.

Concerning the differences in the wave types being discussed, the broken wave is the most similar to the dam-break waves tested by Nouri et al. (2010), which became highly-turbulent, fully-formed bores prior to impacting the test structures. This is why the broken wave results match much better for Cases B and E where the roughness element configurations were similar to those used by Nouri et al. (2010) In contrast, the unbroken wave was still a smooth, solitary-like wave just prior to impacting the concrete blocks and test structure with lesser amplitude and velocity than the broken wave, which helps to explain the significantly

lower wave forces applied to the test structure by the unbroken wave.

These differences in behavior between the two wave types led to shielding of the test structure to be far less pronounced for the unbroken wave cases than for the broken wave cases. The initially smooth unbroken wave remained unbroken until approximately 6 m past the test structure, which allowed for the formation of large eddies near the macro-roughness elements and test structure due to flow separation occurring at their offshore corners, as shown in Figure 5.2a. This allowed the wave to impact the test structure across the entirety of its front face, but with altered flow directions due to the swirling, circular eddy motion. This circular motion led to lesser velocity components normal to the offshore face of the test structure as shown in Figure 5.1 and consequently lesser pressures as shown in Figure 5.9 and Figure 5.12, which ultimately resulted in the observed streamwise force reductions presented in Figure 5.16

On the contrary, the broken wave was already fully-broken by the time it reached the test structure as shown in Figure 5.2b. The high-velocity, turbulent flow did not result in a smooth flow pattern with swirling eddies near the MRE corners. Instead, the broken waves rushed past the MREs along more linear paths rather than being smoothly redirected along curved trajectories as was observed for the unbroken waves, which prevented the wave from significantly impacting the entire offshore face of the test structure. This behavior change was due the broken waves having a larger streamwise momentum than the unbroken waves near the test structure, which resulted in shielding of the test structure being much more effective for the broken wave than for the unbroken wave since the flow did not immediately reconnect behind the MREs.

The second method provided in ASCE 7-16 Chapter C6 uses the results of Thomas et al. (2015) to provide a means of estimating force increase ratios. Unlike with the Nouri et al. tests, where the test structure was placed in a wave flume filled with water, Thomas et al. subjected block configurations to slightly larger waves and placed their test structure and adjacent structures on a beach above the still water level. In order to develop a systematic method for comparing experimental results between the geometries of different MRE config-

urations, Thomas et al. (2015) established the wake clearance angle, β, as the angle between the design structure center-line parallel to the wave propagation direction (i.e. perpendicular to the shoreline) and the line created by connecting the center of the offshore face of the design structure with the offshore corner nearest to the design structure center-line of a macro-roughness element.

When using this approach, the seaward obstructions that make up the flow constriction being considered must be centered about the middle of the shore-ward design structure, be placed such that the wake clearance angle, β, falls in the range $10^\circ \leq \beta \leq 45^\circ$, and must be no more than 152.4 m (500 ft) offshore of the design structure, as illustrated in ASCE 7-16 Chapter C6. The only roughness element that complies with these restrictions is Case E. To compare the experimental results for Case E to those of Thomas et al. (2015), the data sets have been plotted together as shown in Figure 5.17.

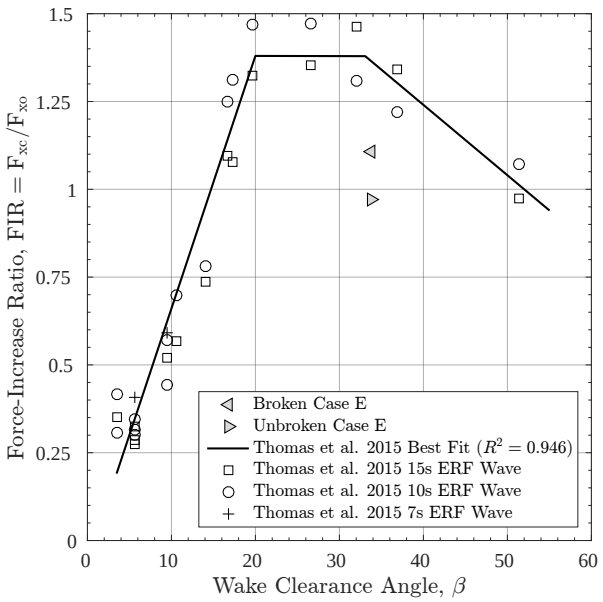

Figure 5.17: Force Increase Ratio Overlay of Experimental Results with Solitary-like Wave Test Data from Thomas et al. (2015)

Compared to the Nouri et al. (2010) results, those of Thomas et al. (2015) show slightly larger force increase ratios for wake clearance angles in the range $20^\circ < \beta < 35^\circ$ as well as

a trapezoidal distribution instead of a triangular one, indicating there is a wide range of wake clearance angles that cause maximum stream-wise forces of a similar magnitude. For wake clearance angles less than 20°, the space between the upstream obstacles was so small that the wave was mostly redirected around them instead of being focused between them toward the test structure, whereas for wake angles larger than 35° the channeling effect of the upstream obstacles reduced as the space between the upstream obstacles was increased. Bearing this general trend in mind, the Case E configuration falls on the upper limit of the constant force increase ratio range of wake clearance angles, which shows that Case E ought to have resulted in similar force increase ratios as the largest of the Thomas et al. (2015) results. However, both the unbroken and broken wave force increase ratios are much lower than the Thomas et al. (2015) data points, which is most likely due to the major differences in the experimental setup. Also, the stream-wise distances between the adjacent structures and the test structure that were used by Thomas et al. (2015) were proportionally much larger than for Case E.

In addition to comparing force increase ratios for both Nouri et al. (2010) and Thomas et al. (2015), the maximum stream-wise velocities were compared as velocity amplification factors ($VAF = u_{XC}/u_{X0}$). Here, u_{XC} is the maximum stream-wise velocity of a given case and u_{X0} is the maximum stream-wise velocity for the reference case. The velocity amplification factors for both Nouri et al. (2010) and Thomas et al. (2015) are shown in Figure 5.18 along with the experimental results of this paper.

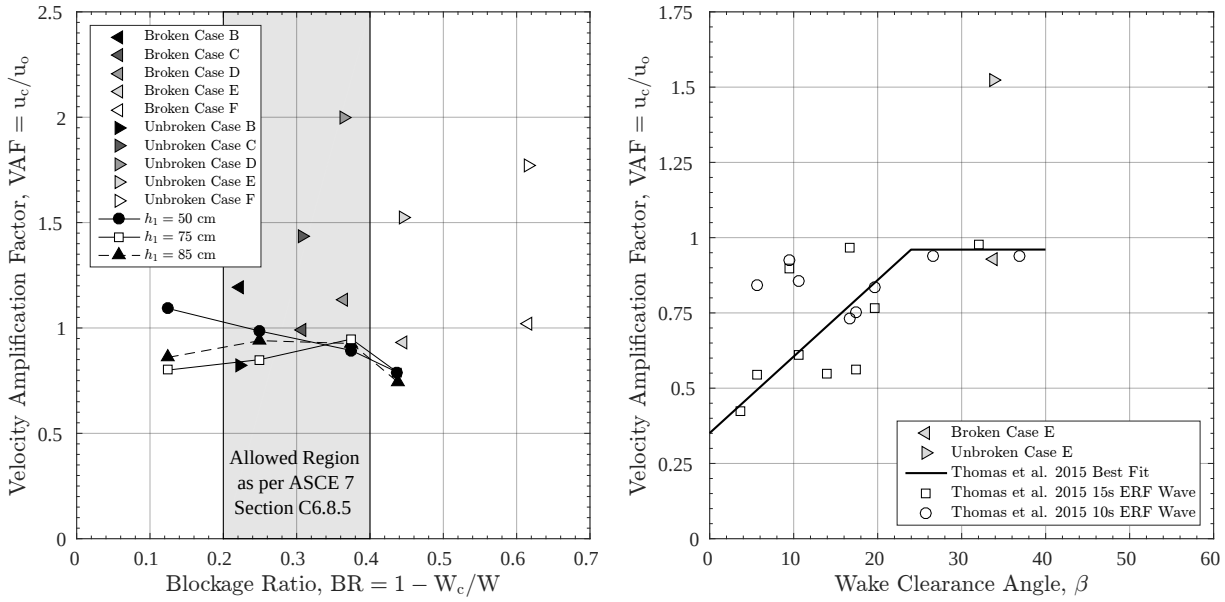

(a) Nouri et al. (2010) (b) Thomas et al. (2015)

Figure 5.18: Velocity Amplification Factor Overlay of Experimental Results with Test Data cited in ASCE 7-16 Chapter C6

Compared to the dam-break results of Nouri et al. (2010), which primarily show flow velocity decreases relative to their reference case, the solitary (broken) and solitary-like (unbroken) waves resulted in stream-wise flow velocities that were similar and significantly-increased, respectively, relative to Case A. Similarly, the unbroken wave result for Case E significantly exceeded the experimental results of Thomas et al. (2015), which were obtained for much larger distances between their test structure and adjacent structures, whereas the broken wave velocity amplification factor was much more similar in magnitude to the results of Thomas et al. (2015) This comparison provides evidence suggesting that the broken wave velocities are not significantly affected by the distance between upstream flow obstructions and the structure experiencing tsunami loads further onshore. Additionally, the fact that the velocity amplification factors were either much larger or roughly equivalent for the unbroken and broken waves compared to either the Nouri et al. (2010) or Thomas et al. (2015) data, yet the force increase ratios were smaller, indicates that the majority of cases were domi-

nated by shielding behavior that redirected the waves away from the test structure instead of channeling behavior that focused the waves toward the test structure causing velocity amplifications that resulted in increased forces.

5.5 Summary and Conclusions

Experiments were conducted to assess the influence of adjacent structures on local velocities, wave forces, and pressure distributions applied to an idealized, elevated, coastal structure considering a reference case without roughness. Two tsunami-like wave types, unbroken and broken waves, were generated to assess the influence of macro-scale roughness in the form of adjacent structures for varying wave conditions. Comparing the results of five different roughness element configurations to the reference case revealed that two key loading phenomena, shielding and wave channeling, are caused by adjacent structures.

Increased shielding of the front face of the test structure was found to outweigh the effects of velocity amplification, leading to a steady decrease in force increase ratios with increasing blockage ratios. It should be noted, however, that these force decreases came with localized pressure increases based on flow channelization as was discussed in Section 5.3, signifying that local structural components may be at increased risk even if the majority of a structure is shielded from the incoming flow.

More specifically, the degree of wave channeling was varied simultaneously with the degree of shielding as a result of moving the roughness elements to vary the percentage of the projected area that was blocked from a direct wave impact. Restrictions of the flume width resulted in local increases in fluid velocity. However, unless this rapid flow was channeled directly at the test structure, increased velocities did little to increase the forces and pressures acting in the stream-wise direction on the front face of the structure. In particular, Cases C, D, and F, which provided 50%-shielding to 100%-shielding, resulted in force reductions ranging from 30% to 45% for the unbroken wave and 55% to 80% for the broken wave. This finding demonstrates the effectiveness of neighboring structures to provide significant benefits

in mitigating tsunami forces with the exception of cases where the neighboring structures are positioned such that the channel between them is directly aligned with the test structure as was shown for Cases B and E, where the stream-wise pressures and forces increased when considering the structure as a whole. However, despite causing decreased net stream-wise forces, shielding also led to local force increases in exposed regions of the front face of the structure, increasing the risk to structural components in these regions.

Comparing these findings to those of both Nouri et al. (2010) and Thomas et al. (2015), which are cited in ASCE 7-16 Chapter C6 as valid approaches for determining force increase ratios, demonstrated that using the recommendations of ASCE 7-16 could significantly overestimate the force increase ratio for roughness element configurations dominated by shielding effects such as Cases C, D, and F, where the front face of the test structure was 50%- to 100%-shielded. In contrast, when the force increase ratios were controlled by channeling effects, which was true for Cases B and E, the force increase ratios presented in this paper matched the ASCE 7-16 recommended methods for the broken wave, but not the unbroken wave. The unbroken waves caused less severe impacts on the test structure, resulting in much lower force increase ratios compared to the broken wave results for the same roughness element configurations.

These observations demonstrate that the complex interaction of the two waves that were generated with the varying roughness configurations can be beneficial in terms of reducing the net wave forces applied to the test structure, but care must be taken to ensure that individual structure elements are structurally sound. Further, the nonuniform, local reductions and increases in pressures can lead to additional moments that a structure subjected to 100% of the wave impact would not experience, which could potentially require additional structural resistance.

5.6 Data Availability

Details concerning the test configuration and instrumentation as well as the recorded data sets for each wave type have been made publicly available via the NHERI DesignSafe Data Depot online repository (Motley et al. 2019, DesignSafe-CI, Dataset doi:10.17603/ds2-q2w5-0t48).

Chapter 6

NUMERICAL METHODOLOGY

This chapter provides an in-depth explanation of the OpenFOAM software including its inner workings in terms of the equations being solved and the numerical methods used to solve the system of equations. Additionally, problem-specific details in terms of fluid physical properties, boundary condition types, mesh generation techniques, and OpenFOAM case directory organization are discussed at length.

6.1 OpenFOAM Introduction

The numerical simulations performed during this study were carried out using version 5.0, of the Open Source Field Operation and Manipulation (OpenFOAM) software. OpenFOAM is a collection of C++ libraries that can be compiled to create individual applications, which are broadly categorized as either solvers or utilities. Each solver is geared toward simulating a specific physics phenomenon, and each utility allows the user to perform a specific operation on data associated with simulations (The OpenFOAM Foundation, 2019).

For multiphase fluid flows consisting of air and water, the most basic solver included in OpenFOAM is the `interFoam` solver, which is based on the Finite Volume Method and also relies on the Volume of Fluid Method of Hirt and Nichols (1981) for tracking the interface between the air and water phases as well as calculating interpolated fluid properties in regions where the fluids mix as discussed in the Section 6.4 section. The PIMPLE algorithm is used by this solver to couple pressure and velocity, which is a combination of the pressure-implicit split-operator (PISO) and semi-implicit methods pressure-linked equation (SIMPLE) algorithms (Patankar, 1980). However, this solver does not allow for use of moving boundaries and the default OpenFOAM-5.0 distribution does not include piston

wavemaker-type boundary conditions. To deal with these issues, the olaFlow add-on package of boundary conditions and solvers designed for coastal engineering purposes by Higuera (2017) was compiled too. In particular, the `olaDyMFlow` solver, which requires user-specified piston displacement and free-surface time histories, was used to mimic the piston wavemaker of the Large Wave Flume at the HWRL.

However, prior to explaining the input parameters and file structure for an OpenFOAM case using the `olaDyMFlow` solver, it is important to understand the basis on which this solver and other fluid solvers in OpenFOAM were developed. As such, the following four sections provide details on the Governing Equations, Turbulence Modeling, Volume of Fluid Method, and Boundary Conditions. Concluding these discussions, the OpenFOAM Case Structure, OpenFOAM Mesh Generation, OpenFOAM Case Execution sections describe in detail how OpenFOAM simulation cases were setup and run to model tsunami-like waves in a flume.

6.2 Governing Equations

The set of equations that describe the motion of a viscous fluid are the mass conservation or continuity equation and the momentum conservation equations, Equations 6.8 and 6.9, respectively, which are known collectively as the Navier-Stokes system of equations for incompressible, viscous fluids. This section presents how the fundamental forms of the continuity and momentum equations can be simplified to the incompressible fluid form used for modeling water as well as air at low velocities.

In general, continuity equations can be formed for a wide range of fields of physics, where the transport of a scalar quantity, q, is described in terms of its time rate of change, its flux vector, $\boldsymbol{f}$, as well as its production or destruction, s (i.e. either a source or sink). For example, this general framework applies directly to heat flow, energy transfer, electromagnetism, and probabilities in quantum mechanics in addition to fluid dynamics. The general, differential form of these relations is as shown in Equation 6.1.

$$\frac{\partial q}{\partial t} + \boldsymbol{\nabla} \cdot \boldsymbol{f} = s \tag{6.1}$$

For fluid flows, the scalar quantity of interest is the mass density, $q = \rho$, and its flux, $\boldsymbol{f} = \rho \boldsymbol{u}$, is its product with the fluid velocity vector, $\boldsymbol{u} = u_i \boldsymbol{e}_i$, where u_i is the velocity component magnitude acting in the $\boldsymbol{e}_i$ coordinate basis vector direction. For the equation to describe mass conservation in terms of density as the fluid flow evolves, the source term s must be zero, which results in Equation 6.2. This equation describes the conservation of mass for a system with a constant total mass.

$$\overbrace{\frac{\partial \rho}{\partial t} + \boldsymbol{\nabla} \cdot (\rho \boldsymbol{u}) = 0}^{\text{Coordinate–Free Form}} \quad \longrightarrow \quad \overbrace{\frac{\partial \rho}{\partial t} + \frac{\partial (\rho u_i)}{\partial x_i} = 0}^{\text{Cartesian Coordinates}} \tag{6.2}$$

Note that the Einstein summation convention has been assumed for the Cartesian coordinate representations of equations throughout this dissertation, where repeated indices are summed over from 1 to 3 to give scalar or zero-order tensor quantities and unique indices represent higher-order tensor type quantities. For example, x_i and u_i represent the x, y, or z coordinates and velocity components in the continuity equation, respectively, which appear in the flux divergence term. Since the index i is repeated in this term, it represents the following scalar sum.

$$\frac{\partial (\rho u_i)}{\partial x_i} = \frac{\partial (\rho u_1)}{\partial x_1} + \frac{\partial (\rho u_2)}{\partial x_2} + \frac{\partial (\rho u_3)}{\partial x_3}$$

To illustrate the effect of non-repeating indices, notice that the presence of a single unique component index, i, in each individual term of the momentum equation (Equation 6.4) indicates that it is really a set of three distinct equations due to momentum being a vector or first-order tensor quantity. Additionally, when assessing the tensor-order of a specific variable or term in an equation, the number of indices indicates its tensor order. For example, the Cauchy stress, σ_{ij}, is a second-order tensor that has two indices relating the direction in which a force is acting to the normal vector of the face over which the force is acting.

Moving from scalar transport of density to vector transport of momentum, the general relation that describes momentum transport is the Cauchy momentum equation, which is defined in terms of the momentum density vector, $\boldsymbol{q}$, the momentum density flux tensor, $\boldsymbol{F}$, and a source term vector, $\boldsymbol{s}$, that accounts for body forces. The differential form of this relation that describes transport of vector quantities is shown as Equation 6.3, which is the conservative form of the system of equations.

$$\frac{\partial \boldsymbol{q}}{\partial t} + \boldsymbol{\nabla} \cdot \boldsymbol{F} = \boldsymbol{s} \tag{6.3}$$

For the case of water-air fluid dynamics, the momentum density vector takes the form $\boldsymbol{q} = \rho \boldsymbol{u}$, the momentum density flux tensor, $\boldsymbol{F} = \rho \boldsymbol{u} \otimes \boldsymbol{u} - \boldsymbol{\sigma}$, is a measure of the kinetic and strain energies per unit volume of the fluid, and the body force vector, $\boldsymbol{s} = \rho \boldsymbol{g}$, is due to gravity alone. Note that $\boldsymbol{g} = g_i \boldsymbol{e}_i$ is the vector describing the direction in which gravitational acceleration acts and should have a magnitude of $\|\boldsymbol{g}\| = 9.81$ m/s. The resulting system of partial differential equations is given as Equation 6.4.

$$\overbrace{\frac{\partial(\rho \boldsymbol{u})}{\partial t} + \boldsymbol{\nabla} \cdot (\rho \boldsymbol{u} \otimes \boldsymbol{u} - \boldsymbol{\sigma}) = \rho \boldsymbol{g}}^{\text{Coordinate-Free Form}} \quad \longrightarrow \quad \overbrace{\frac{\partial(\rho u_i)}{\partial t} + \frac{\partial}{\partial x_j}\left(\rho u_i u_j - \sigma_{ij}\right) = \rho g_i}^{\text{Cartesian Coordinates}} \tag{6.4}$$

Here $\boldsymbol{\sigma}$ is the Cauchy stress tensor. The Cauchy stress may be decomposed according to the relation $\boldsymbol{\sigma} = \boldsymbol{\tau} - p\boldsymbol{I}$, where $\boldsymbol{\tau}$ is the deviatoric or shear stress tensor, p is the pressure or hydrostatic stress, and $\boldsymbol{I} = \delta_{ij} \boldsymbol{e}_i \otimes \boldsymbol{e}_j$ is the second-order identity tensor. Note that δ_{ij} is the Kronecker delta and $\boldsymbol{e}_i$ and $\boldsymbol{e}_j$ are coordinate basis vectors.

To fully define the Cauchy stress tensor, a fluid material material behavior model must be defined. Since water and air both behave like incompressible Newtonian fluids within the flow velocity regime used in all experiments and numerical models, viscous stresses were determined using a Newtonian fluid constitutive model. For instance, in all of the experiments and simulations conducted for this dissertation, the air flow velocity magnitude, $\|\boldsymbol{u}_{\text{air}}\|$, was below 10 m/s, which is a small fraction of the speed of sound in air near 20° C

according to the Newton-Laplace formula, $c_{\text{air}} = \sqrt{K_{\text{air}}/\rho_{\text{air}}} = \sqrt{\gamma p/\rho_{\text{air}}} = \sqrt{\gamma RT/M_{\text{air}}} = 343.2$ m/s. Here $K_{\text{air}} = \gamma p = 141.855$ kPa is the isentropic bulk modulus of air, $\gamma = C_p/C_v = 1.4$ is the adiabatic index for a diatomic, ideal gas such as air (roughly 78% Nitrogen, 21% oxygen, and 1% other elements), which is the ratio of the specific heat at constant pressure, C_p to the specific heat at constant volume, C_v, $\rho_{\text{air}} = 1.2041$ kg/m^3 is the density of air, $p = 1$ atm $= 101.325$ kPa is atmospheric air pressure near sea level, $R = 8.3145$ J $\cdot$ mol^{-1} $\cdot$ K^{-1} is the universal ideal gas constant, T is the air temperature in degrees Kelvin, and $M_{\text{air}} = 0.02896$ kg $\cdot$ mol^{-1} is the molar mass of air. This gives an approximate upper-bound Mach number of $M = \|\boldsymbol{u}_{\text{air}}\|/c_{\text{air}} = 0.03$ for all of the tests and simulations, which is far below $M = 0.3$, the Mach number at which air begins to transition from incompressible to compressible flow behavior (Johnson, 2016a). In fact, the flow velocity would have to reach roughly 100 m/s, which is approximately 220 mph, for significant compressible flow behavior to occur based on this criterion.

For Newtonian fluids, the shear stress tensor is a linear function of the strain rate or rate of deformation tensor, S_{ij}, which is defined in Equation 6.5, and its trace, $\text{tr}(\boldsymbol{S}) = \boldsymbol{S} : \boldsymbol{I} = S_{kk}$, which is identical to the divergence of the velocity field, $\boldsymbol{\nabla} \cdot \boldsymbol{u} = \partial u_k/\partial x_k$, as shown in Equation 6.6, which defines the shear stress tensor (Tadmor et al., 2012).

$$\overbrace{\boldsymbol{S} = \frac{1}{2}\left(\boldsymbol{\nabla u} + \boldsymbol{\nabla u}^T\right)}^{\text{Coordinate-Free Form}} \quad \longrightarrow \quad \overbrace{S_{ij} = \frac{1}{2}\left(\frac{\partial u_i}{\partial x_j} + \frac{\partial u_j}{\partial x_i}\right)}^{\text{Cartesian Coordinates}} \tag{6.5}$$

$$\begin{aligned} \overbrace{\boldsymbol{\tau} = 2\mu\boldsymbol{S} + \left(\kappa - \frac{2}{3}\mu\right)\text{tr}(\boldsymbol{S})\boldsymbol{I}}^{\text{Coordinate-Free Form}} \quad &\longrightarrow \quad \overbrace{\tau_{ij} = 2\mu S_{ij} + \left(\kappa - \frac{2}{3}\mu\right)S_{kk}\delta_{ij}}^{\text{Cartesian Coordinates}} \\ = 2\mu\boldsymbol{S} + \left(\kappa - \frac{2}{3}\mu\right)(\boldsymbol{\nabla} \cdot \boldsymbol{u})\boldsymbol{I} \quad &= \mu\left(\frac{\partial u_i}{\partial x_j} + \frac{\partial u_j}{\partial x_i}\right) + \left(\kappa - \frac{2}{3}\mu\right)\frac{\partial u_k}{\partial x_k}\delta_{ij} \end{aligned} \tag{6.6}$$

The proportionality constants μ and κ are the dynamic and bulk viscosities of the fluid, respectively, which are both functions of the fluid density and temperature. In the engineering literature, the dynamic viscosity is sometimes alternatively referred to as the shear

viscosity, whereas the bulk viscosity may also be referred to as the volume, dilation, or second viscosity. For an ideal gas such as air, μ is proportional to the square-root of temperature according to Sutherland's Law, $\mu(T) = \mu_0(T/T_0)^{3/2}(T_0 + S)/(T + S)$, where $\mu_0 = 1.716 \cdot 10^{-5}$ Pa $\cdot$ s is the reference viscosity, T is the temperature in degrees Kelvin, $T_0 = 273.15$ °K is the reference temperature, and $S = 110.4$ °K is the Sutherland temperature (Sutherland, 1893). For water, μ decreases exponentially with increasing temperature according to an Arrhenius-like equation, $\mu(T) = 2.414 \cdot 10^{-5} \cdot 10^{247.8/(T-140)}$, which has up to a 2.5% error within the range 0 °C to 370 °C, where T is temperature in degrees Kelvin and the dynamic viscosity is in Pa $\cdot$ s (Andrade, 1930; Raman, 1923). Since temperature variations were negligible for all experiments and analyses the dynamic viscosities of both air and water were assumed to be constant at $T = 20$ °C and taken to be $\mu_{\text{air}} = 1.8133(10)^{-5}$ Pa $\cdot$ s and $\mu_{\text{water}} = 1.0002(10)^{-3}$ Pa $\cdot$ s, respectively. These values correspond to densities of $\rho_{\text{air}} = 1.2041$ kg/m^3 and $\rho_{\text{water}} = 998.28$ kg/m^3 and kinematic viscosities of $\nu_{\text{air}} = \mu_{\text{air}}/\rho_{\text{air}} = 1.5060(10)^{-5}$ m^2/s and $\nu_{\text{water}} = \mu_{\text{water}}/\rho_{\text{water}} = 1.0035(10)^{-3}$ m^2/s at $T = 20$ °C.

According to Stokes' viscosity assumption, the bulk viscosity, divergence of the velocity field, or both are small or zero and as such the effect of bulk viscosity on determining shear stresses is neglected (Kundu et al., 2012). This assumption is true for incompressible fluids since they are divergence-free (i.e. $\boldsymbol{\nabla \cdot u} = 0$), causing the term in Equation 6.6 to vanish and making the specification of κ_{air} and κ_{water} unnecessary. Verification of this statement requires using the fact that incompressibility implies the density is constant and cannot vary over time in conjunction with the continuity equation. As demonstrated in Equation 6.7, the continuity equation may be rewritten by expanding the divergence term and then gathering terms to reduce the equation to the material derivative, $D(\cdot)/Dt = \partial(\cdot)/\partial t + \boldsymbol{u \cdot \nabla}(\cdot)$, of the density added to the product of the density and the divergence of the velocity. Since the density cannot vary over time, its material derivative, $D\rho/Dt$, must vanish, leaving $\rho(\boldsymbol{\nabla \cdot u}) = 0$ as the remaining equation. Furthermore, the density is non-zero and positive, proving that $\boldsymbol{\nabla \cdot u} = 0$ must be true to satisfy the simplified continuity equation for incompressible fluids.

$$\frac{\partial \rho}{\partial t} + \boldsymbol{\nabla} \cdot (\rho \boldsymbol{u}) = \frac{\partial \rho}{\partial t} + \boldsymbol{\nabla} \rho \cdot \boldsymbol{u} + \rho (\boldsymbol{\nabla} \cdot \boldsymbol{u}) = \frac{D \rho}{D t} + \rho (\boldsymbol{\nabla} \cdot \boldsymbol{u}) = 0 \tag{6.7}$$

Using the facts that incompressible fluids are divergence free and that air and water behave as Newtonian fluids, the mass and momentum conservation equations may be simplified by eliminating all terms including the divergence of the velocity field or derivatives of the density, factoring out the constant density and viscosity coefficients, and substituting the Cauchy stress for its decomposition, $\boldsymbol{\sigma} = \boldsymbol{\tau} - p\boldsymbol{I} = 2\mu \boldsymbol{S} - p\boldsymbol{I}$, where the term including divergence of the velocity in the shear stress tensor has been eliminated. The resulting, simplified equations are the incompressible Navier-Stokes equations defined by Equations 6.8 and 6.9. Note that the Laplacian operator, $\nabla^2(\cdot) = \boldsymbol{\nabla} \cdot \boldsymbol{\nabla}(\cdot) = \partial^2(\cdot)/\partial x_i^2$, has been used to simplify the viscous diffusion term.

$$\overbrace{\boldsymbol{\nabla} \cdot \boldsymbol{u} = 0}^{\text{Coordinate-Free Form}} \quad \longrightarrow \quad \overbrace{\frac{\partial u_i}{\partial x_i} = 0}^{\text{Cartesian Coordinates}} \tag{6.8}$$

$$\overbrace{\frac{\partial \boldsymbol{u}}{\partial t} + \boldsymbol{\nabla} \cdot (\boldsymbol{u} \otimes \boldsymbol{u}) = \nu \nabla^2 \boldsymbol{u} - \frac{\boldsymbol{\nabla} p}{\rho} + \boldsymbol{g}}^{\text{Coordinate-Free Form}} \quad \longrightarrow \quad \overbrace{\frac{\partial u_i}{\partial t} + \frac{\partial (u_i u_j)}{\partial x_j} = \nu \frac{\partial^2 u_i}{\partial x_j \partial x_j} - \frac{1}{\rho} \frac{\partial p}{\partial x_i} + g_i}^{\text{Cartesian Coordinates}} \tag{6.9}$$

Notice that Equations 6.8 and 6.9 have been divided by the fluid density in addition to having the Cauchy stress replaced by the Newtonian fluid stress model, when compared to Equations 6.2 and 6.4. The division by the density is motivated by the fact that the incompressible flow solvers provided in OpenFOAM assume that the governing equations have been divided by the density, resulting in a switch from using the dynamic viscosity, μ, to the kinematic viscosity, $\nu = \mu/\rho$, and from the pressure, p, to a modified pressure divided by the density. This means that post-processed pressure values need to be multiplied by the density in order to obtain physically meaningful results. Additionally, the Reynolds-averaged form of the governing equations were used in OpenFOAM to allow for the use of turbulence models that determine the Reynolds stress tensor, which is discussed in Section 6.3.3.

Concerning the implementation of turbulence models as discussed in Section 6.3, note that the divergence of the product of the total velocity components, $\partial(u_i u_j)/\partial x_j$, could have been simplified further if it were fully expanded since the divergence of the velocity would appear in one of the two resulting terms, the simplification of which would produce the non-conservative, convective form of the Navier-Stokes momentum equations. However, if this was done prior to substituting the total velocity components for either the mean and fluctuating velocity components for RANS turbulence models (i.e. $u_i = \langle u_i \rangle + u_i'$), or, the filtered and sub-grid scale velocity components for LES turbulence models (i.e. $u_i = \overline{u}_i + u_i^r$), then the term involving the fluctuating or sub-grid scale velocity components, $\partial\langle u_i' u_j' \rangle/\partial x_j$ or $\partial\langle u_i^r u_j^r \rangle/\partial x_j$, would have vanished, eliminating the so-called Reynolds or sub-grid stress tensor terms from the equations for RANS and LES models, respectively. Neglecting these terms would give an inaccurate representation of the true physical behavior since averages of products of the fluctuating velocity components are not necessarily equal to zero in shear flows (Kundu et al., 2012).

6.3 Turbulence Modeling

In and of themselves, the Navier-Stokes momentum equations and continuity equation fully describe all possible Newtonian fluid flows, in both turbulent and laminar flow regimes; however, when attempting to numerically model turbulent behavior using discretized forms of these governing equations, information is lost in the sense that the numerical mesh size governs the scale of turbulent eddies that can be resolved in a numerical solution. This inherent defect in numerical modeling of turbulent behavior led to the development of several, general classes of approaches that deal with the problem both directly and indirectly, including direct numerical simulation (DNS), large eddy simulation (LES), Reynolds-averaged Navier-Stokes (RANS) equation modeling, and RANS-LES hybrid modeling. Figure 6.1 provides a graphical comparison of the effectiveness of these approaches at resolving turbulent flow features.

Except for the first of the three approaches (DNS), either time-averaged (RANS) or

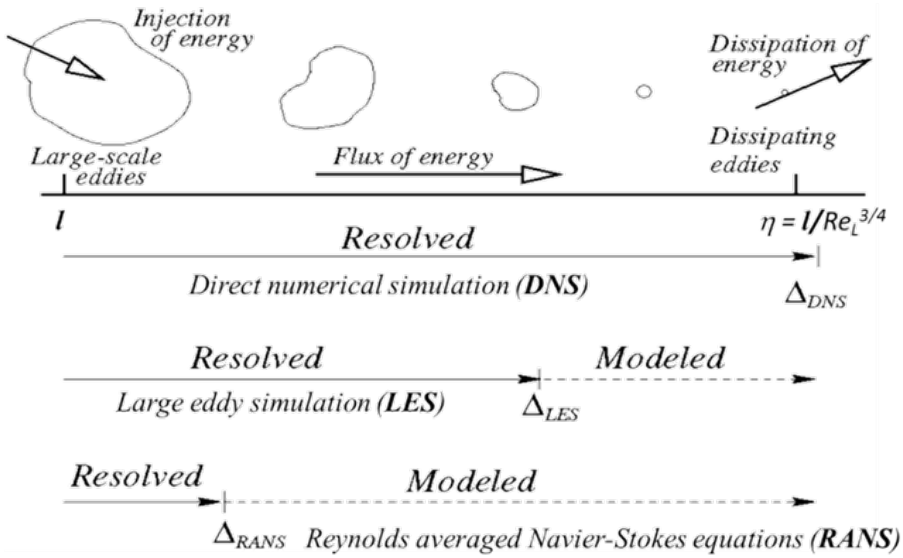

Figure 6.1: Comparison of DNS, LES, and RANS Turbulence Scale Resolutions (Bakker, 2006)

spatially-filtered (LES) forms of the governing equations as well as new model equations that describe turbulent energy dissipation processes are introduced. The necessity of turbulence model equations arises from the addition of new unknown variables in the modified forms of the governing equations, which result from the averaging and filtering processes and produce an ill-posed system of equations. To close the system of equations, turbulence models have been developed that relate the new unknown variables to known quantities such as the velocity gradient. In this manner, the so-called closure problem and resolution of turbulent phenomena are dealt with simultaneously.

It should be noted that the introduction of turbulence model equations generally results in increased complexity and computational cost of the overall fluid flow solution process. The degree to which this occurs depends on the type of turbulence model equations being implemented, which can be algebraic equations, ordinary differential equations (ODEs), or partial differential equations (PDEs) based on the assumptions made about the flow being modeled. For models defined by ODEs, but more so PDEs, numerical complications result from the numerical discretization and solution of the model equations in addition to the

augmented governing equations. However, without the addition of turbulence models that resolve turbulent behavior for large mesh sizes, computational fluid dynamics models that generate accurate representations of fluid flows would be restricted to laminar, low-Reynolds number flow regimes due to the exorbitant computational cost of using sufficiently small meshes to resolve turbulent behavior without a model as is discussed in Section 6.3.1.

When choosing the correct turbulence model for a specific application, there are several key factors to keep in mind. On one hand increased modeling accuracy in terms of resolving the true flow behavior is desired, whereas on the other reducing computational cost as much as possible is also a necessity. In order to produce a successful model in a reasonable amount of time, a balance of these two ideals must be achieved. For example, the primary goal of this dissertation was to provide accurate wave impact force estimates, which did not require extremely fine resolution of turbulent phenomena since the initial wave impact is an inertial force-dominated phenomenon as opposed to a viscous force-dominated phenomenon. This allowed for increased efficiency in terms of reduced computation times by relaxing the level to which turbulent behaviors were fully resolved. To assess the capability of various models to accurately predict wave impact forces, unbroken and broken waves were simulated using the geometry of Case A of Figure 4.4, the results of which are discussed in Chapter 7 and led to the selection of a RANS model, specifically the k-ω Shear Stress Transport model. For a general case, Figure 6.2 provides a flow chart of the questions that must be answered based on the specific problem being simulated when choosing a suitable turbulence model. Each additional level of approximation or lower order of model in the flow chart represents a further reduction in the capability of the model to capture the true turbulent flow characteristics.

6.3.1 Direct Numerical Simulation (DNS)

In the first of these approaches, the Navier-Stokes equations are solved exactly without any approximations or added modeling equations, but rather with restrictions on the mesh size of discrete numerical methods, such as the finite difference, finite element, and finite

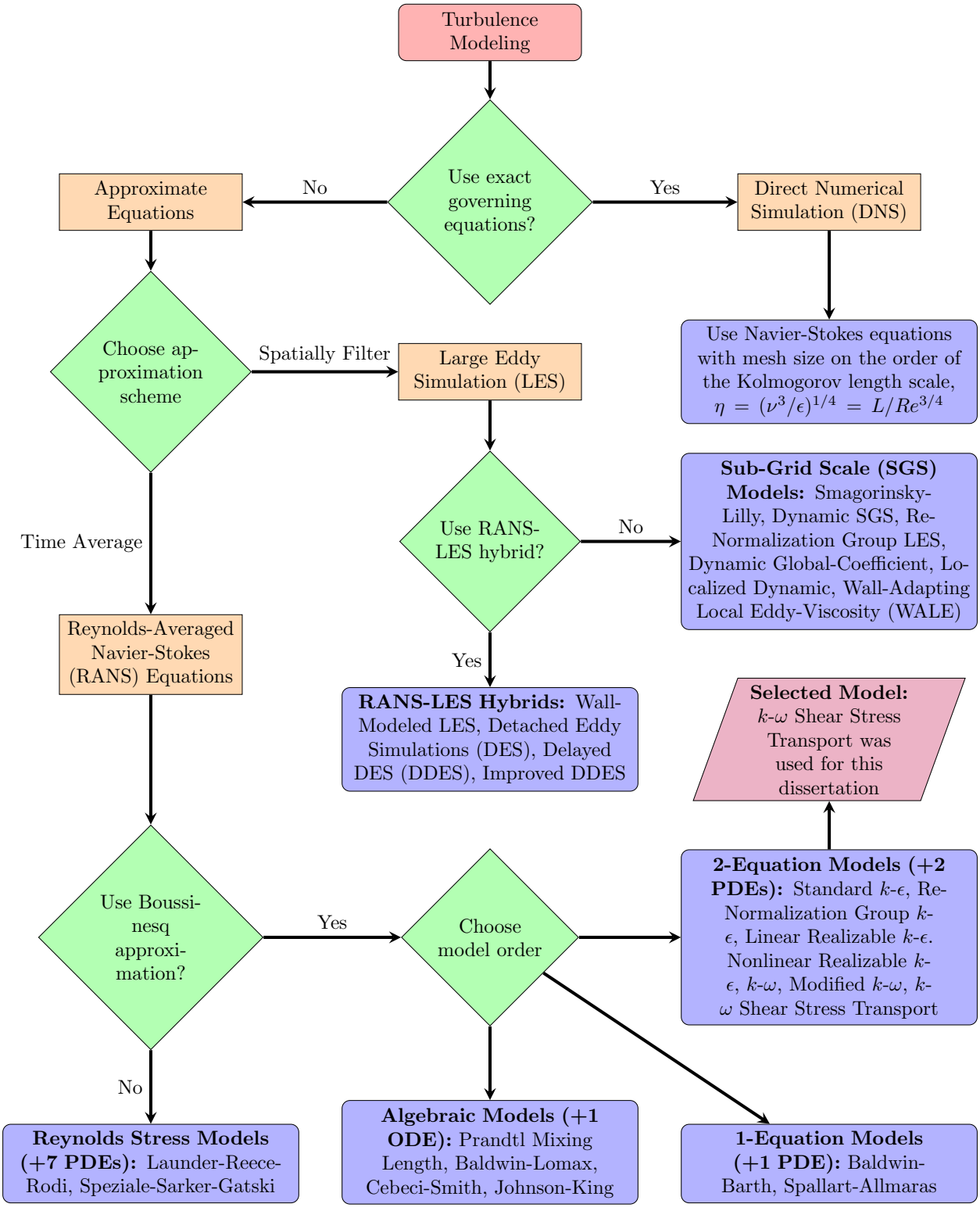

Figure 6.2: Turbulence Model Selection Flow Chart

volume methods, used to solve the governing equations. These restrictions are based on Andrey Kolmogorov's theoretical microscales, which describe the time, length, and velocity scales on which turbulent, viscous processes that dissipate energy into heat dominate fluid flow behavior. In his seminal 1941 paper on the subject, Kolmogorov proposed that these scales are universal parameters for all flow regimes that define the smallest scales of turbulent behavior, which consequently must be resolved for any numerical solution of a fluid flow to converge to the true physical behavior (Kolmogorov, 1941). To determine the adequate mesh size that will ensure the true turbulent behavior is simulated, the cell size must be on the order of the Kolmogorov length scale, η, defined by Equation 6.10, where ν is the kinematic viscosity, ε is the turbulent kinetic energy dissipation rate, $L = k^{3/2}/\varepsilon$ is the turbulence length scale for the problem being studied, k is the turbulent kinetic energy of the flow, and $Re_L = Lk^{1/2}/\nu$ is the turbulence Reynolds number of the flow, which is the ratio of inertial to viscous forces for the flow.

$$\eta = (\nu^3/\varepsilon)^{1/4} = L/Re_L^{3/4} \tag{6.10}$$

The most important observation that can be made from Equation 6.10 is that increases in the Reynolds number of a flow cause rapid decreases in the required cell size for a DNS numerical model. The fact that the mesh size restriction is Reynolds number-based limits the flow regimes that can be modeled from a practical standpoint in terms of the computational resources that would be necessary to conduct simulations with such large numbers of very small mesh cells. Even very modest Reynolds numbers necessitate extreme computation times since the required computation time in days is approximately $(Re_L/800)^3$ or $(Re_\lambda/70)^6$ assuming computations are carried out using a gigaflop machine according to Pope (2000), where Re_L and Re_λ are the turbulence and Taylor length scale Reynolds numbers, respectively, which are related according to $Re_\lambda = \sqrt{20/3 Re_L}$. For instance, modeling the atmospheric boundary layer, where $Re_\lambda \approx 10,000$ is typically the case, would require roughly $8.5 \cdot 10^{12}$ days for a gigaflop machine, which is far beyond current day computing

capabilities even when utilizing computing clusters such as the University of Washington's high-performance computing (HPC) cluster, Hyak, which is roughly capable of 200 teraflops. Thus, using DNS for practical applications with high Reynolds numbers is not feasible at present, including the experiments conducted for this dissertation. For example, during the broken wave tests $k = 0.0095$ m^2/s^2 and $\varepsilon = 0.0059$ m^2/s^3 were determined from measurements made using ADV1, which gives $Re_\lambda \approx 1010$ and consequently a rough estimate of $9 \cdot 10^6$ days of computation using Pope's upper bound estimate.

6.3.2 Large Eddy Simulation (LES)

The next best alternative to DNS in terms of accurately resolving small-scale turbulent flow features is large eddy simulation. In this approach, a low-pass filter is applied to the velocity field, which results in a decomposed velocity field, $\boldsymbol{u} = \overline{\boldsymbol{u}} + \boldsymbol{u}^r$, where $\overline{\boldsymbol{u}}$ is the filtered velocity vector and $\boldsymbol{u}^r$ is called the residual or sub-grid scale (SGS) velocity vector since it pertains to the scales of turbulence that are not directly resolved by this approach. The filtered velocity field is defined as a convolution integral of the total velocity field with a filter function, $G(\boldsymbol{r})$, over the entire fluid domain, Ω, as shown in Equation 6.11. The most common filters include the box function, $G(\boldsymbol{r}) = H(\Delta/2 - \|\boldsymbol{r}\|)/\Delta$, Gaussian function, $G(\boldsymbol{r}) = \sqrt{6/(\pi\Delta^2)}e^{-6\|\boldsymbol{r}\|^2/\Delta^2}$, and sharp spectral function, $G(\boldsymbol{r}) = \sin(\pi\|\boldsymbol{r}\|/\Delta)/(\pi\|\boldsymbol{r}\|)$, where H is the Heaviside step function and Δ is the range of influence called the filter width (Pope, 2000). Note that in the forms presented here the filter functions have uniform widths of influence in all three spatial coordinate directions; however, in some cases where it would prove beneficial to do so, different filter widths are used in different directions.

$$\overline{\boldsymbol{u}} = \iiint_\Omega G(\boldsymbol{r})\boldsymbol{u}(\boldsymbol{x} - \boldsymbol{r})d\boldsymbol{r} \tag{6.11}$$

Substituting the decomposed velocity field into the Navier-Stokes equations results in modified governing equations as defined by Equations 6.12 and 6.13 that end up with a new term dubbed the SGS or anisotropic residual stress tensor, $\boldsymbol{\tau}^r$, similar to how the Reynolds

stress tensor that appears in the RANS equations adds new terms that need to be modeled. To address the issue of adding the new unknowns of the SGS stress tensor into the system of equations, a filter and sub-grid scale model must be specified. For example, Smagorinsky devised the first SGS model shown in Equation 6.15, where $\overline{\boldsymbol{S}}$ is the filtered rate of strain or rate of deformation tensor as defined by Equation 6.14 and ν_r is the eddy viscosity, which is a linear eddy viscosity type of model similar to the Boussinesq approximation used to determine Reynolds stresses in RANS models.

$$\overbrace{\boldsymbol{\nabla}\cdot\overline{\boldsymbol{u}}=0}^{\text{Coordinate-Free Form}} \quad \longrightarrow \quad \overbrace{\frac{\partial\overline{u}_i}{\partial x_i}=0}^{\text{Cartesian Coordinates}} \tag{6.12}$$

$$\begin{aligned}
&\overbrace{\frac{\partial\overline{\boldsymbol{u}}}{\partial t}+\boldsymbol{\nabla}\cdot\left(\overline{\boldsymbol{u}}\otimes\overline{\boldsymbol{u}}\right)=\nu\nabla^2\overline{\boldsymbol{u}}-\boldsymbol{\nabla}\cdot\boldsymbol{\tau}^r-\frac{\boldsymbol{\nabla}\overline{p}}{\rho}+\boldsymbol{g}}^{\text{Coordinate-Free Form}}\\
&\overbrace{\frac{\partial\overline{u}_i}{\partial t}+\frac{\partial(\overline{u}_i\overline{u}_j)}{\partial x_j}=\frac{\partial}{\partial x_j}\left(\nu\frac{\partial\overline{u}_i}{\partial x_j}-\tau^r_{ij}\right)-\frac{1}{\rho}\frac{\partial\overline{p}}{\partial x_i}+g_i}^{\text{Cartesian Coordinates}}
\end{aligned} \tag{6.13}$$

$$\overbrace{\overline{\boldsymbol{S}}=\frac{1}{2}\left(\boldsymbol{\nabla}\overline{\boldsymbol{u}}+\boldsymbol{\nabla}\overline{\boldsymbol{u}}^T\right)}^{\text{Coordinate-Free Form}} \quad \longrightarrow \quad \overbrace{\overline{S}_{ij}=\frac{1}{2}\left(\frac{\partial\overline{u}_i}{\partial x_j}+\frac{\partial\overline{u}_j}{\partial x_i}\right)}^{\text{Cartesian Coordinates}} \tag{6.14}$$

$$\overbrace{\boldsymbol{\tau}^r=-2\nu_r\overline{\boldsymbol{S}}=-\nu_r\left(\boldsymbol{\nabla}\overline{\boldsymbol{u}}+\boldsymbol{\nabla}\overline{\boldsymbol{u}}^T\right)}^{\text{Coordinate-Free Form}} \quad \longrightarrow \quad \overbrace{\tau^r_{ij}=-2\nu_r\overline{S}_{ij}=-\nu_r\left(\frac{\partial\overline{u}_i}{\partial x_j}+\frac{\partial\overline{u}_j}{\partial x_i}\right)}^{\text{Cartesian Coordinates}} \tag{6.15}$$

Similar to Prandtl's mixing length concept (Prandtl, 1925, 1926a,b), Smagorinsky developed an additional equation to describe the eddy viscosity as defined by Equation 6.17 in terms of the characteristic filtered rate of strain, $\overline{\mathcal{S}}$ as defined by Equation 6.16, and the Smagorinsky length scale, ℓ_S. Smagorinksy assumed his length scale as defined within Equation 6.17 was proportional to the filter width Δ used in the filtering process applied to the velocity components. This proportionality assumption resulted in the need for the

determination of the Smagorinsky coefficient, C_S, which is the ratio of the length scale to the filter width.

$$\overline{\mathcal{S}} = \sqrt{2\overline{\boldsymbol{S}} : \overline{\boldsymbol{S}}} = \sqrt{2\overline{S}_{ij}\overline{S}_{ij}} \tag{6.16}$$

$$\nu_r = \ell_S^2 \overline{\mathcal{S}} = \left(C_S \Delta\right)^2 \overline{\mathcal{S}} \tag{6.17}$$

However, despite the benefits of LES in terms of resolving much finer turbulence length scales than the Reynolds-averaged approaches discussed in the following section, the method in general struggles to produce accurate results in regions near boundary walls, particularly for high-Reynolds number flows, without some special treatment in terms of wall-modeling add-ons or the use of hybrid methods that attempt to blend LES and RANS methods. Furthermore, LES turbulence models require greater computational resources than the simpler RANS turbulence models, making them the less attractive of the two approaches in terms of computational costs and performance. As such, RANS models were selected for the numerical modeling work completed in this dissertation due to the need for low computational cost to allow for a large parametric study of cases beyond the experimental configurations to be simulated as well as to better resolve near-wall region behavior of the high-Reynolds number tsunami flows of the experiments, providing sufficient mesh refinement was used.

6.3.3 Reynolds-Averaged Navier-Stokes (RANS) Modeling

The third class of turbulence models, which is typically the least effective at resolving turbulent flow characteristics, consists of closure models for the Reynolds-Averaged Navier-Stokes (RANS) equations. Reynolds averaging decomposes the total velocity and pressure variables, u_i and p, into mean components, $\langle u_i \rangle$ and $\langle p \rangle$, and fluctuating components, u_i' and p', according to $u_i = \langle u_i \rangle + u_i'$ and $p = \langle p \rangle + p'$ (Reynolds, 1895). If the density was not constant as it would be in a compressible flow, it would also be decomposed in this fashion.

The rules of Reynolds-averaging are as follows:

1. The average of the sum is the sum of the averages: $\langle f + g \rangle = \langle f \rangle + \langle g \rangle$.

2. Constants do not affect and are not affected by averaging: $\langle \alpha f \rangle = \alpha \langle f \rangle$, where α is constant.

3. The average of the time or space derivative of a quantity is equal to the corresponding derivative of the average: $\left\langle \frac{\partial f}{\partial s} \right\rangle = \frac{\partial \langle f \rangle}{\partial s}$, where s may be either x_i or t.

4. The average of the product of an average and an arbitrary function is equal to the product of the averages: $\big\langle \langle f \rangle g \big\rangle = \langle f \rangle \langle g \rangle$.

5. The averages of fluctuations vanish: $\langle f' \rangle = 0$.

Substitution of the dependent variable decompositions into the governing equations followed by averaging gives the incompressible, Reynolds-averaged continuity and momentum equations, Equations 6.18 and 6.19, respectively (Pope, 2000; Kundu et al., 2012).

Continuity Equation:

$$\frac{\partial u_i}{\partial x_i} = \frac{\partial (\langle u_i \rangle + u_i')}{\partial x_i} = 0$$

Reynolds-Averaged Continuity Equation:

$$\left\langle \frac{\partial (\langle u_i \rangle + u_i')}{\partial x_i} \right\rangle = \frac{\partial \big(\big\langle \langle u_i \rangle + u_i' \big\rangle\big)}{\partial x_i} = \frac{\partial \big(\big\langle \langle u_i \rangle \big\rangle + \cancelto{0}{\langle u_i' \rangle}\big)}{\partial x_i}$$

$$\overbrace{\boldsymbol{\nabla} \cdot \langle \boldsymbol{u} \rangle = 0}^{\text{Coordinate Free}} \quad \longrightarrow \quad \overbrace{\frac{\partial \langle u_i \rangle}{\partial x_i} = 0}^{\text{Cartesian Coordinates}} \tag{6.18}$$

Navier-Stokes Equations:

$$\frac{\partial u_i}{\partial t} + \frac{\partial (u_i u_j)}{\partial x_j} = \nu \frac{\partial^2 u_i}{\partial x_j \partial x_j} - \frac{1}{\rho} \frac{\partial p}{\partial x_i} + g_i$$

$$\frac{\partial (\langle u_i \rangle + u_i')}{\partial t} + \frac{\partial \big((\langle u_i \rangle + u_i')(\langle u_j \rangle + u_j') \big)}{\partial x_j} = \nu \frac{\partial^2 (\langle u_i \rangle + u_i')}{\partial x_j \partial x_j} - \frac{1}{\rho} \frac{\partial (\langle p \rangle + p')}{\partial x_i} + g_i$$

Reynolds-Averaged Navier-Stokes (RANS) Equations:

$$\left\langle \frac{\partial(\langle u_i\rangle + u_i')}{\partial t} \right\rangle + \left\langle \frac{\partial(\langle u_i\rangle\langle u_j\rangle + \langle u_i\rangle u_j' + u_i'\langle u_j\rangle + u_i'u_j')}{\partial x_j} \right\rangle = \left\langle \nu \frac{\partial^2(\langle u_i\rangle + u_i')}{\partial x_j \partial x_j} \right\rangle \ldots$$

$$\ldots - \left\langle \frac{1}{\rho}\frac{\partial(\langle p\rangle + p')}{\partial x_i} \right\rangle + \langle g_i\rangle$$

$$\frac{\partial(\langle\langle u_i\rangle + u_i'\rangle)}{\partial t} + \frac{\partial(\langle\langle u_i\rangle\langle u_j\rangle + \langle u_i\rangle u_j' + u_i'\langle u_j\rangle + u_i'u_j'\rangle)}{\partial x_j} = \nu \frac{\partial^2(\langle\langle u_i\rangle + u_i'\rangle)}{\partial x_j \partial x_j} \ldots$$

$$\ldots - \frac{1}{\rho}\frac{\partial(\langle\langle p\rangle + p'\rangle)}{\partial x_i} + g_i$$

$$\frac{\partial(\langle\langle u_i\rangle\rangle + \cancelto{0}{\langle u_i'\rangle})}{\partial t} + \frac{\partial(\langle\langle u_i\rangle\langle u_j\rangle\rangle + \cancelto{0}{\langle\langle u_i\rangle u_j'\rangle} + \cancelto{0}{\langle u_i'\langle u_j\rangle\rangle} + \langle u_i'u_j'\rangle)}{\partial x_j} = \nu \frac{\partial^2(\langle\langle u_i\rangle\rangle + \cancelto{0}{\langle u_i'\rangle})}{\partial x_j \partial x_j} \ldots$$

$$\ldots - \frac{1}{\rho}\frac{\partial(\langle\langle p\rangle\rangle + \cancelto{0}{\langle p'\rangle})}{\partial x_i} + g_i$$

$$\frac{\partial\langle u_i\rangle}{\partial t} + \frac{\partial\big(\langle u_i\rangle\langle u_j\rangle\big)}{\partial x_j} + \frac{\partial(\langle u_i'u_j'\rangle)}{\partial x_j} = \nu\frac{\partial^2\langle u_i\rangle}{\partial x_j\partial x_j} - \frac{1}{\rho}\frac{\partial\langle p\rangle}{\partial x_i} + g_i$$

$$\overbrace{\frac{\partial\langle \boldsymbol{u}\rangle}{\partial t} + \boldsymbol{\nabla}\cdot\big(\langle\boldsymbol{u}\rangle\otimes\langle\boldsymbol{u}\rangle\big) = \boldsymbol{\nabla}\cdot\big(\nu\boldsymbol{\nabla}\langle\boldsymbol{u}\rangle - \langle\boldsymbol{u}'\otimes\boldsymbol{u}'\rangle\big) - \frac{\boldsymbol{\nabla}\langle p\rangle}{\rho} + \boldsymbol{g}}^{\text{Coordinate-Free Form}}$$

$$\overbrace{\frac{\partial\langle u_i\rangle}{\partial t} + \frac{\partial\big(\langle u_i\rangle\langle u_j\rangle\big)}{\partial x_j} = \frac{\partial}{\partial x_j}\left(\nu\frac{\partial\langle u_i\rangle}{\partial x_j} - \langle u_i'u_j'\rangle\right) - \frac{1}{\rho}\frac{\partial\langle p\rangle}{\partial x_i} + g_i}^{\text{Cartesian Coordinates}} \tag{6.19}$$

Applying the Reynolds averaging process to the governing equations results in a set of equations with more unknowns than equations due to the presence of the fluctuating velocity components in Equation 6.19, where they appear in the term $\langle u_i'u_j'\rangle$. To solve this problem, closure models describing the turbulence of a flow in an average sense are introduced that relate the product of this term with the density, $\rho\langle u_i'u_j'\rangle$, to the mean strain rate tensor, $\langle S_{ij}\rangle$ as defined by Equation 6.20, following Boussinesq's eddy or turbulent viscosity hypothesis (Boussinesq, 1877). This additional term appearing in the Reynolds-averaged Navier-Stokes equations is referred to as the Reynolds stress tensor, $R_{ij} = -\rho\langle u_i'u_j'\rangle$. Defined by Equation 6.21, the Boussinesq hypothesis is used to determine the Reynolds stresses R_{ij} for all RANS turbulence models except for Reynolds Stress Models (RSM),

where the Reynolds stresses are modeled directly with transport PDEs.

$$\overbrace{\langle \boldsymbol{S} \rangle = \frac{1}{2}\Big(\boldsymbol{\nabla}\langle \boldsymbol{u} \rangle + \boldsymbol{\nabla}\langle \boldsymbol{u} \rangle^T\Big)}^{\text{Coordinate-Free Form}} \quad \longrightarrow \quad \overbrace{\langle S_{ij} \rangle = \frac{1}{2}\left(\frac{\partial \langle u_i \rangle}{\partial x_j} + \frac{\partial \langle u_j \rangle}{\partial x_i}\right)}^{\text{Cartesian Coordinates}} \tag{6.20}$$

$$\begin{aligned} \overbrace{\boldsymbol{R} = -\rho\langle \boldsymbol{u}_i' \otimes \boldsymbol{u}_j' \rangle}^{\text{Coordinate-Free Form}} &\quad \longrightarrow \quad \overbrace{R_{ij} = -\rho\langle u_i' u_j' \rangle}^{\text{Cartesian Coordinates}} \\ = 2\Big(\mu_T\langle \boldsymbol{S} \rangle - \frac{1}{3}\rho k \boldsymbol{I}\Big) &\qquad\qquad = 2\left(\mu_T\langle S_{ij} \rangle - \frac{1}{3}\rho k \delta_{ij}\right) \\ = \mu_T\Big(\boldsymbol{\nabla}\langle \boldsymbol{u} \rangle + \boldsymbol{\nabla}\langle \boldsymbol{u} \rangle^T\Big) - \frac{2}{3}\rho k \boldsymbol{I} &\qquad\qquad = \mu_T\left(\frac{\partial \langle u_i \rangle}{\partial x_j} + \frac{\partial \langle u_j \rangle}{\partial x_i}\right) - \frac{2}{3}\rho k \delta_{ij} \end{aligned} \tag{6.21}$$

Here k is the turbulent kinetic energy as defined by Equation 6.22, ε is the dissipation rate of the turbulent kinetic energy as defined by Equation 6.23, and μ_T is the eddy or turbulent viscosity as defined by Equation 6.24, which is a dynamic viscosity-like parameter. Additionally, the ratio of ε and k, is commonly used in turbulence modeling and due to the resulting physical units of this quantity, it is referred to as the turbulence frequency, ω, as defined in Equation 6.25.

$$k = \frac{1}{2}\langle \boldsymbol{u}' \cdot \boldsymbol{u}' \rangle = \frac{1}{2}\langle u_i' u_i' \rangle \tag{6.22}$$

$$\varepsilon = \frac{C_\mu^{3/4} k^{3/2}}{\ell_m} \tag{6.23}$$

$$\mu_T = \rho\nu_T = \rho C_\mu \frac{k^2}{\varepsilon} \tag{6.24}$$

$$\omega = \frac{\varepsilon}{k} = \frac{C_\mu^{3/4} k^{1/2}}{\ell_m} \tag{6.25}$$

Note that calculation of ε requires determining the characteristic turbulence length scale, ℓ_m, appropriate for the problem being simulated. Typically, ℓ_m is assumed to be some percentage of a typical dimension of the problem domain. Also, the turbulent eddy viscosity

depends on an empirically-determined coefficient, C_μ, which was taken to be 0.09 (Launder and Sharma, 1974; Pope, 2000). This coefficient is a normalized form of the turbulent viscosity, $\nu_T\varepsilon/k^2$, which has been shown to be nearly constant near walls for turbulent, channel flows as demonstrated in Figure 6.3.

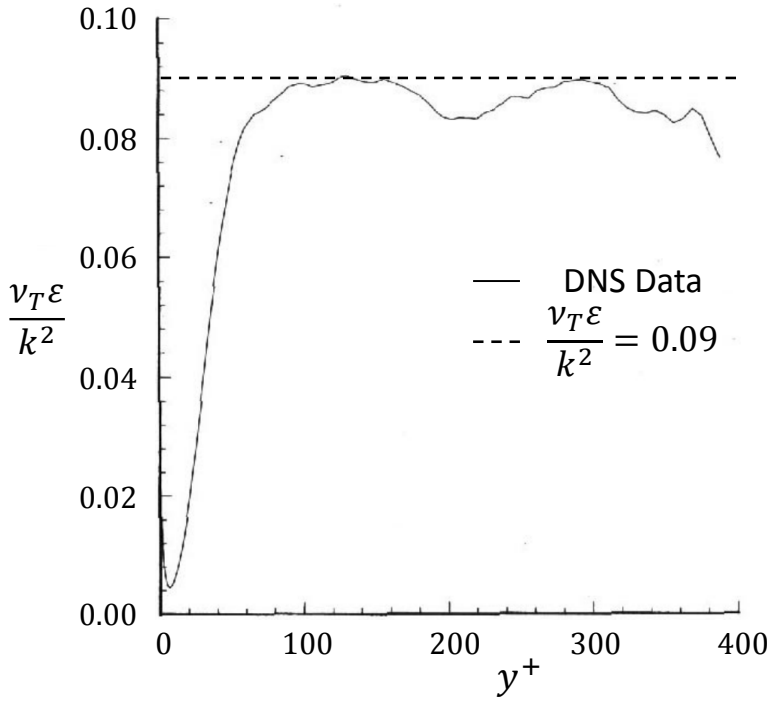

Figure 6.3: Normalized Turbulent Viscosity Profile from DNS of Channel Flow at $Re = 13,750$ (Adapted by Pope 2000 from Kim et al. 1987).

Concerning the choice of turbulence model to be used as a closure model for the RANS equations, there are two main categories, Reynolds stress models (RSM) and turbulent viscosity models, the second of which is split into several subcategories. In the first of these, model transport equations are developed for each of the individual Reynolds stresses, $R_{ij} = -\rho\langle u_i' u_j' \rangle$, which results in six partial differential equations (PDEs) as defined by Equation 6.26, and an additional transport PDE for either the turbulent kinetic energy dissipation rate, ε, as defined by Equation 6.27, or, for the turbulence frequency, ω, as defined by Equation 6.28, giving a total of seven additional PDEs to be solved simultaneously with the RANS equations.

$$\begin{aligned}\frac{\partial\langle u_i'u_j'\rangle}{\partial t}+\langle u_k\rangle\frac{\partial\langle u_i'u_j'\rangle}{\partial x_k}&=-\frac{\partial\langle u_i'u_j'u_k'\rangle}{\partial x_k}+\nu\nabla^2\langle u_i'u_j'\rangle+\mathcal{P}_{ij}+\Pi_{ij}-\varepsilon_{ij}\\&=-\frac{\partial T_{kij}}{\partial x_k}+\mathcal{P}_{ij}+\mathcal{R}_{ij}-\varepsilon_{ij}\end{aligned}\tag{6.26}$$

$$\frac{\partial\varepsilon}{\partial t}+\langle u_i\rangle\frac{\partial\varepsilon}{\partial x_i}=\frac{\partial}{\partial x_i}\left[\left(\nu+\frac{\nu_T}{\mathrm{Pr}_\varepsilon}\right)\frac{\partial\varepsilon}{\partial x_i}\right]+\left(C_{1\varepsilon}\mathcal{P}-C_{2\varepsilon}\varepsilon\right)\frac{\varepsilon}{k}\tag{6.27}$$

$$\frac{\partial\omega}{\partial t}+\langle u_i\rangle\frac{\partial\omega}{\partial x_i}=\frac{\partial}{\partial x_i}\left[\left(\nu+\frac{\nu_T}{\mathrm{Pr}_\omega}\right)\frac{\partial\omega}{\partial x_i}\right]+\left(C_{\omega1}\mathcal{P}-C_{\omega2}k\omega\right)\frac{\omega}{k}\tag{6.28}$$

The ε transport equation coefficients are typicially taken to be $\mathrm{Pr}_k = 1.00$, $\mathrm{Pr}_\varepsilon = 1.30$, $C_{1\varepsilon} = 1.44$, and $C_{2\varepsilon} = 1.92$ for all simulations as per the recommendations of Jones and Launder (1972) and Launder and Sharma (1974) for the standard $k-\varepsilon$ model. The first two coefficients, Pr_k and Pr_ε, are Prandtl numbers that represent the diffusion rates of the turbulent kinetic energy and its dissipation rate, respectively. Based on the work of Wilcox (1988), the ω transport equation coefficients are commonly taken to be $\mathrm{Pr}_\omega = 2$, $C_{\omega1} = 5/9$, and $C_{\omega2} = 3/40$. The remaining new term that appears in both of the ε and ω transport PDEs is referred to as the production of turbulent kinetic energy or often just as the production, $\mathcal{P}$, which is defined by Equation 6.29.

$$\mathcal{P}=-\langle u_i'u_j'\rangle\frac{\partial\langle u_i\rangle}{\partial x_j}\tag{6.29}$$

In Equation 6.26, $\mathcal{P}_{ij}$ is the production tensor of a turbulent flow as defined by Equation 6.30,

$$\mathcal{P}_{ij}=-\langle u_i'u_k'\rangle\frac{\partial\langle u_j\rangle}{\partial x_k}-\langle u_j'u_k'\rangle\frac{\partial\langle u_i\rangle}{\partial x_k}\tag{6.30}$$

Π_{ij} is the velocity-pressure-gradient tensor as defined by Equation 6.31,

$$\Pi_{ij}=-\frac{1}{\rho}\left\langle u_i'\frac{\partial p'}{\partial x_j}+u_j'\frac{\partial p'}{\partial x_i}\right\rangle=\mathcal{R}_{ij}-\frac{\partial T_{kij}^p}{\partial x_k}\tag{6.31}$$

ε_{ij} is the dissipation tensor defined by Equation 6.32,

$$\varepsilon_{ij} = 2\nu\left\langle \frac{\partial u_i'}{\partial x_k}\frac{\partial u_j'}{\partial x_k} \right\rangle \tag{6.32}$$

T_{kij} is the Reynolds stress flux tensor defined by Equation 6.33,

$$T_{kij} = \overbrace{\langle u_i' u_j' u_k' \rangle}^{T_{kij}^u} + \overbrace{\frac{1}{\rho}\Big(\langle u_i' p' \rangle \delta_{jk} + \langle u_j' p' \rangle \delta_{ik}\Big)}^{T_{kij}^p} \overbrace{-\nu \frac{\partial \langle u_i' u_j' \rangle}{\partial x_k}}^{T_{kij}^\nu} \tag{6.33}$$

and $\mathcal{R}_{ij}$ is the pressure-rate-of-strain tensor defined by Equation 6.34 (Pope, 2000).

$$\mathcal{R}_{ij} = \left\langle \frac{p'}{\rho}\left(\frac{\partial u_i'}{\partial x_j} + \frac{\partial u_j'}{\partial x_i}\right) \right\rangle \tag{6.34}$$

The above equations provide analytical descriptions of each term and their exact physical behavior; however, in practice the pressure-velocity-gradient and dissipation tensors, Π_{ij} and ε_{ij}, are modeled due to unknowns they introduce to the problem. Furthermore, the pressure-velocity-gradient tensor is typically broken down into the pressure-rate-of-strain tensor, $\mathcal{R}_{ij}$, and the pressure transport tensor, $\partial T_{kij}^p / \partial x_k$. Some examples of RSM models that use varying approaches to simulate these terms are the models of Rotta, Launder, Reece, and Rodi, who developed isotropization of production (LRR-IP) and quasi-isotropic (LRR-QI) models, Hanjalić and Launder (HL), Shih and Lumley (SL), Jones and Musonge (JM), Speziale, Sarkar, and Gatski (SSG), and Fu, Launder, and Tselepidakis (FLT) (Pope, 2000).

The second group of RANS turbulence models rely on far less equations, the number of which can range from a single ordinary differential equation (ODE) to two PDEs for the most widely-used models. For instance, the simplest class of turbulent viscosity turbulence models is referred to as algebraic models, which require the solution of an additional ordinary differential equation to describe the turbulence of the flow in addition to solving the RANS system of equations. Algebraic models either specify fixed turbulent viscosity for the entire flow or specify a turbulence mixing length, ℓ_m, on which the turbulent viscosity is dependent. For example, if the flow is horizontal in the x_1 direction with velocity u_1 over a wall boundary

in an x_2-x_3 plane, then the appropriate mixing length is defined by Equation 6.35. Examples of mixing-length models include those of Prandtl, Cebeci and Smith, and Baldwin and Lomax. The primary downside to algebraic models though is the need to specify ℓ_m for the entire flow, which is only possible for flows that have been extensively studied and measured experimentally such as attached boundary layer flows in aeronautical applications (Pope, 2000). Due to this issue, algebraic models are unsuitable for cases such as tsunami-like wave generation in flumes and as such were not implemented for this dissertation.

$$\nu_T = \ell_m^2 \left| \frac{\partial \langle u_1 \rangle}{\partial x_2} \right| \tag{6.35}$$

The next level of improvement in turbulent viscosity-based RANS turbulence models are the one-equation models, in which a single PDE transport equation for a chosen turbulence parameter is modeled. For example, the first one-equation model developed by Prandtl solves a transport equation for the turbulent kinetic energy, k, Spallart-Allmaras model makes use of a transport equation for the kinematic turbulent viscosity, ν_T, and the Baldwin-Barth model solves a transport equation for a turbulent Reynolds number, $\tilde{Re}_T$. These models also suffer downsides in that the mixing length must still be specified in addition to the turbulent viscosity, making them unsuitable for arbitrary flows without a well-defined knowledge of the mixing length throughout the flow.

However, the development of the transport equation for the turbulent kinetic energy, k, as defined by Equation 6.36 provides the basis of many two-equation turbulent viscosity-based RANS turbulence models (Anderson et al., 1997; Bardina et al., 1997; Pope, 2000; Kundu et al., 2012). The use of two transport equations for either k and ε or k and ω provides a complete description of turbulent flow behavior without the need to specify the mixing length definition for specific flow types. This is due to the fact that the mixing length may be defined in terms of either of these pairs of turbulence parameters as shown in Equation 6.23 and Equation 6.25.

$$\frac{\partial k}{\partial t} + \langle u_i \rangle \frac{\partial k}{\partial x_i} = \frac{\partial}{\partial x_j}\left[\left(\nu + \frac{\nu_T}{\mathrm{Pr}_k}\right)\frac{\partial k}{\partial x_j}\right] + \mathcal{P} - \varepsilon \tag{6.36}$$

A wide variety of k-ε and k-ω type models have been developed with various goals in mind for their use in modeling turbulent flows. For instance, the most popular k-ε models in use today are the Standard, Re-Normalization Group (RNG), Realizable Linear Eddy Viscosity, and the Realizable Non-linear Eddy Viscosity models. Similarly, the most prevalent k-ω models used in both industry and research are the Wilcox, Modified Wilcox, and Shear Stress Transport (SST) models. Each of these models rely on the basic transport equations for k, ε, and ω with modifications made in terms of coefficients being reformulated in terms of flow parameters with the goal of capturing specific physical phenomena better. For instance, the k-ω SST model has an inherent ability to capture strong flow separation behavior, whereas the standard Wilcox model does not.

As is discussed at length in Chapter 7 - Numerical Model Validation, each of the k-ε models mentioned herein as well as the k-ω SST and Launder-Reece-Rodi (LRR) Reynolds-stress models were tested to determine which model produced more accurate results in terms of the fluid forces and pressures acting on the test structure, when comparing OpenFOAM and experimental results. Based on the fact that the k-ω SST model was able to accurately replicate test structure demands for both unbroken and broken waves, it was selected as the model to be used when conducting the parametric study of macro-roughness element configurations discussed in Chapter 8 - Force-Prediction Design Equation Development. This may be attributed to its ability to simulate the effects of severe flow separation such as when the unbroken and broken waves impacted the concrete blocks followed by the test structure compared to the Standard k-ε model, which was developed for attached boundary layer flow over aerofoils and gave the most inconsistent results.

6.3.4 Estimation of Turbulence Parameters using Empirical Data

The turbulent kinetic energy (TKE) used for initializing all turbulence models was estimated using velocity component time histories measured by ADV1 at the location shown in Figure 4.12. To estimate the TKE, determining the ensemble average velocity component time histories, $\langle u_x(t)\rangle$, $\langle u_y(t)\rangle$, and $\langle u_z(t)\rangle$, was required, which was done by summing the x-, y-, and z-direction total velocity component histories (i.e. $u_x(t)$, $u_y(t)$, and $u_z(t)$) separately and dividing them by the number of trials that were measured. Typically this is done using all of the velocity components; however, the data measured for the vertical velocity, $u_z(t)$, was extremely noisy with large oscillations and as such was neglected when estimating the TKE.

The xy-plane fluctuating velocity component histories, $u'_x(t)$ and $u'_y(t)$, were calculated by taking the difference between trial velocity histories and the ensemble averaged velocity time histories. The median values of the fluctuating velocities at $t = 22.5$ s, the point in time the max value of $\langle u_x(t)\rangle$ occurred, were used to determine the TKE. The median fluctuating velocities were $u'_x = 0.0453$ m/s and $u'_y = 0.0125$ m/s for the unbroken wave, whereas they were $u'_x = 0.134$ m/s and $u'_y = 0.0325$ m/s for the broken wave. Based on these results, the TKE was estimated according to $k = \frac{1}{2}\langle \boldsymbol{u}' \cdot \boldsymbol{u}' \rangle = \frac{1}{2}\langle u'^2_x + u'^2_y + \cancelto{0}{u'^2_z} \rangle$, which gave $k = 1.44(10^{-3})$ m^2/s^2 and $k = 9.53(10^{-3})$ m^2/s^2 for the unbroken and broken waves, respectively.

In addition to the TKE, a turbulence length scale, ℓ_m, was needed to determine the TKE dissipation rate, $\varepsilon = C_\mu^{3/4} k^{2/3}/\ell_m$. As is commonly done in CFD practice, the turbulence length scale was estimated as 7% of the hydraulic diameter, d_{H}, at ADV1, where the velocity data was recorded. The hydraulic diameter was calculated as $d_{\mathrm{H}} = 4A_{\mathrm{water}}/p_{\mathrm{wet}} = 4W_{\mathrm{F}}h_{\mathrm{SWL}}/(W_{\mathrm{F}} + 2h_{\mathrm{SWL}})$, where A_{water} is the cross-sectional area of the water in the flume, p_{wet} is the wetted perimeter, W_{F} is the flume width, and h_{SWL} is the still water depth (2.0 m and 1.85 m for the unbroken and broken waves), which gave $d_{\mathrm{H}} = 3.821m$ and $\ell_m = 0.229$ m for the unbroken wave and $d_{\mathrm{H}} = 3.679m$ and $\ell_m = 0.258$ m for the broken wave.

Using these values, the TKE dissipation rates for the unbroken and broken waves were evaluated to be $\varepsilon = 3.934(10^{-5})$ m^2/s^3 and $\varepsilon = 5.940(10^{-4})$ m^2/s^3, respectively. Alos, determining the specific turbulence frequencies according to $\omega = \varepsilon/(\beta^* k)$, where $\beta^* = C_\mu = 0.09$, was required for the k-ω SST turbulence model, which resulted in $\omega = 0.303$ s^{-1} and $\omega = 0.692$ s^{-1}. Notice that this definition of ω is not quite identical to the one given by Equation 6.25; however, OpenFOAM is setup to work with the alternate definition given here, which is referred to as the specific turbulence frequency or dissipation rate. Furthermore, approximating the Reynolds stresses was necessary for the LRR turbulence model, which was done assuming an initially isotropic state where $R_{ii} = 2k/3$ and $R_{ij} = 0$ for $i \neq j$. Taking this approach gave $R_{ii} = 9.61(10^{-4})$ m^2/s^2 and $R_{ii} = 6.36(10^{-3})$ m^2/s^2 for the unbroken and broken waves, respectively.

6.4 Volume of Fluid Method

In a two-phase, incompressible fluid simulation using the finite volume method, the computational domain is discretized into a grid of polyhedral cells, which requires a method to keep track of the fluid properties of each cell. The volume of fluid method uses the volume fraction, α, to track the proportion of a cell filled with either water ($\alpha = 1$), air ($\alpha = 0$), or a mixture ($0 < \alpha < 1$) of the two fluids. Using this approach, the two fluids are modeled as a single effective fluid. The properties of this fluid are calculated as weighted averages of the individual fluid properties using the volume fraction. For example, the fluid density is calculated as a weighted average according to $\rho = \rho^{\text{water}}\alpha + \rho^{\text{air}}(1 - \alpha)$, where ρ^{water} is the density of water and ρ^{air} is the density of air (Dámian, 2009).

OpenFOAM uses a two-fluid Eulerian model to describe the flow, which requires solving for the water and air volume fractions separately according to the transport equations, Equations 6.37 and 6.38, respectively.

$$\frac{\partial \alpha}{\partial t} + \frac{\partial (\alpha u_i^{\text{water}})}{\partial x_i} = 0 \tag{6.37}$$

$$\frac{\partial(1-\alpha)}{\partial t} + \frac{\partial(u_i^{\text{air}}(1-\alpha))}{\partial x_i} = 0 \tag{6.38}$$

The velocity of the fluid in cells where water and air have mixed is also computed as a weighted average of their individual velocities, u_i^{water} and u_i^{air}, respectively, where $u_i = u_i^{\text{water}}\alpha + u_i^{\text{air}}(1-\alpha)$ is the net velocity of the effective fluid. The use of separate velocities adds an additional convective term to the transport equation, which results in a sharper interface between the water and air phases during a simulation (Dámian, 2009).

The effects of surface tension along the interface are also included using a continuum surface force model, where the surface tension forces are a function of the local curvature of the air-water interface and are accounted for by an additional term given in Equation 6.39 that is added to the right-hand side of the momentum equation, Equation 6.19.

$$f_\sigma = \sigma\kappa\frac{\partial\alpha}{\partial x_i}, \text{ where } \kappa = -\frac{\partial}{\partial x_i}\left(\frac{\partial\alpha}{\partial x_i}\Big/\sqrt{\frac{\partial\alpha}{\partial x_j}\frac{\partial\alpha}{\partial x_j}}\right) \tag{6.39}$$

Here σ is the surface tension coefficient, which has units of force per length, κ is the mean curvature of the air-water interface, and f_σ is the resulting term that gets added to the momentum equation to account for surface tension effects.

6.5 Boundary Conditions

Table 6.1 lists the boundary conditions (BCs) and wall functions used for each field variable, including the volume fraction, α (`alpha`), turbulent kinetic energy, k (`k`), turbulent kinetic energy dissipation rate, ε (epsilon), turbulence frequency, ω (`omega`), turbulent viscosity, ν_T (`nut`), total pressure sans the hydrostatic pressure, $p-\rho gh$ (`p_rgh`), velocity component vector components, u_i (U), and the boundary displacements (`pointDisplacement`), where the names in parentheses denote the C++ code names used in OpenFOAM for defining BCs. The boundary names given in Table 6.1 are general categories of boundaries that existed in the OpenFOAM wave flume models. For example, the term dynamic refers to boundaries that surrounded the region of the computational domain where the dynamic mesh motion

capabilities of the `olaDyMFlow` solver were used to generate the unbroken and broken waves described in Section 4.4 - Wave Generation. Similarly, the term fixed refers to boundaries of the mesh region past the dynamic, wave-generation mesh region that were static without mesh motion throughout all numerical simulations. Furthermore, the term walls refers to all flume walls including its bottom ($-z$ face), right ($-y$ face), left ($+y$ face), and end ($+x$ face) walls, whereas atmosphere ($+z$ face) refers to the upper cutoff point of the computational domain, which was set to be the top of the flume walls. The remaining terms refer to specific elements of the flume or experimental setup, where paddle ($-x$ face) is the piston wavemaker wall, test structure refers to the collection of boundaries defined by each of the six faces of the test structure, and concrete blocks refers to either one or two groups of six faces that define the concrete blocks used as macro-roughness elements.

Table 6.1: OpenFOAM Boundary Conditions used in Large Wave Flume Models

Boundary	**alpha**	**epsilon**	**k**	**nut**
paddle	zeroGradient	epsilonWallFunction	kqRWallFunction	nutkWallFunction
Dynamic Walls	zeroGradient	epsilonWallFunction	kqRWallFunction	nutkWallFunction
Dynamic Atmosphere	inletOutlet	inletOutlet	inletOutlet	calculated
Fixed Walls	zeroGradient	epsilonWallFunction	kqRWallFunction	nutkWallFunction
Fixed Atmosphere	inletOutlet	inletOutlet	inletOutlet	calculated
Test Structure	zeroGradient	epsilonWallFunction	kqRWallFunction	nutkWallFunction
Concrete Blocks	zeroGradient	epsilonWallFunction	kqRWallFunction	nutkWallFunction
Boundary	**omega**	**p_rgh**	**pointDisplacement**	**U**
paddle	omegaWallFunction	fixedFluxPressure	wavemakerMovement	movingWallVelocity
Dynamic Walls	omegaWallFunction	fixedFluxPressure	fixedNormalSlip	noSlip
Dynamic Atmosphere	inletOutlet	totalPressure	fixedNormalSlip	pressureInletOutletVelocity
Fixed Walls	omegaWallFunction	fixedFluxPressure	fixedValue	noSlip
Fixed Atmosphere	inletOutlet	totalPressure	fixedValue	pressureInletOutletVelocity
Test Structure	omegaWallFunction	fixedFluxPressure	fixedValue	noSlip
Concrete Blocks	omegaWallFunction	fixedFluxPressure	fixedValue	noSlip

Each of the boundary condition types listed in Table 6.1 has a specific definition in terms

of the physical conditions they represent and some of them can be used for both scalar and tensor quantities, whereas others are only used for one or the other. The following list describes each boundary condition assuming it is being defined for an arbitrary field variable, ϕ, when necessary.

1. *empty*: Specifically tailored for 2D or 1D analysis, this BC is assigned to boundaries whose unit normal vector points in the direction for which no solution of field equations is required.

2. *fixedValue*: A user-specified value of ϕ is assigned on a boundary.

3. *zeroGradient*: The normal gradient of ϕ is set equal to zero ($\nabla_n \phi = 0$) on a boundary whose unit normal vector is $\boldsymbol{n}$.

4. *inletOutlet*: For outflow, the *zeroGradient* condition is assigned to ϕ. For inflow, a user-specified *fixedValue* condition is assigned to ϕ.

5. *noSlip*: Used only for velocity BCs, a *fixedValue* velocity vector condition of (0,0,0) is assigned.

6. *totalPressure*: A user-specified, constant total pressure, p_0, is assigned on a boundary, which remains fixed such that variations in velocity cause corresponding variations in static pressure to keep the total pressure constant. For outflow, the static pressure equals the total pressure, $p = p_0$. For inflow, the static pressure is determined by the difference between the total and dynamic pressures, $p = p_0 - \frac{1}{2} u_i u_i$.

7. *pressureInletOutletVelocity*: The pressure must be specified at an inlet so that the velocity may be determined using the flux normal to the boundary. For outflow, the *zeroGradient* condition is assigned. For inflow, the velocity is set to be the component normal to the boundary of the fluid in the cell adjacent to the boundary. The velocity tangent to the boundary may be optionally set to a user-specified *fixedValue* condition.

8. *fixedFluxPressure*: The pressure gradient over a boundary is adjusted so that the boundary flux satisfies its velocity BC.

When defining the boundary conditions for k, ε, ν_T, and ω, it is necessary to know how the boundary condition changes with distance from the boundary. Figure 6.4 depicts the variation of the fluid velocity with distance from a boundary and depicts an inner region where boundary effects control and an outer region where the boundary conditions no longer apply and Equations 6.27 and 6.36 govern the behavior of k and ε, respectively (Anderson et al., 1997; Sondak, 1992).

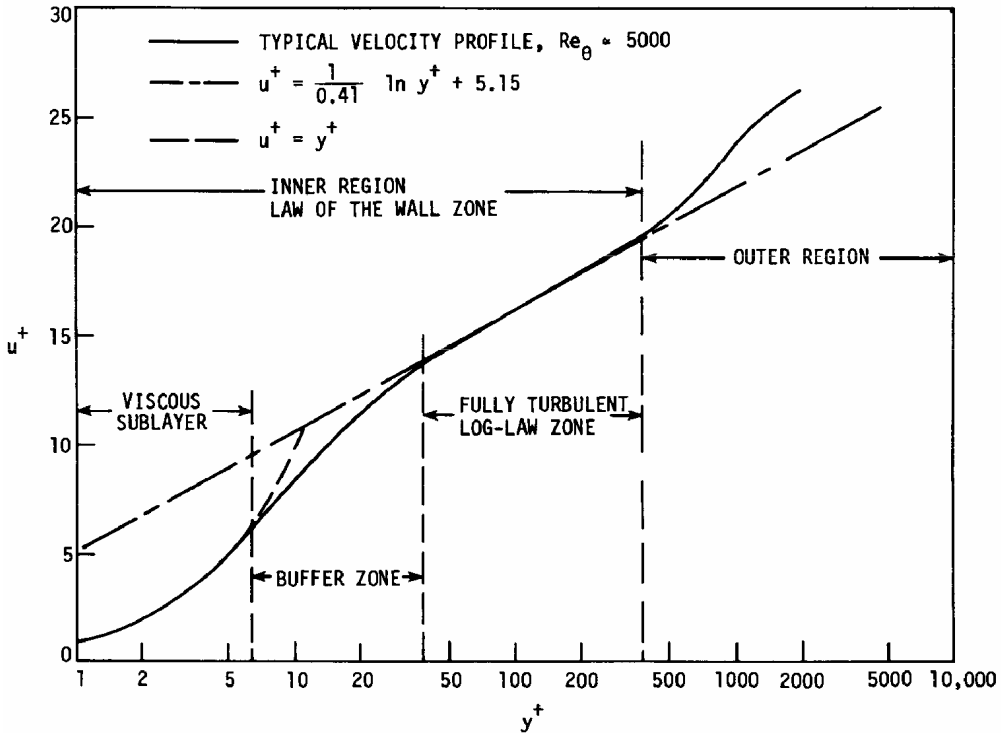

Figure 6.4: Law of the Wall Velocity Profile (Anderson et al., 1997)

Within the inner region the behavior transitions between the viscous sub-layer and fully turbulent region where von Kármán's log-law holds. These two behaviors are described by the relations defined in Equation 6.40.

$$u^+ = \begin{cases} y^+ & 0 < \mathrm{y}^+ < \mathrm{y}_\mathrm{c}^+ \\ \dfrac{1}{\kappa}\ln(y^+) + B = \dfrac{1}{\kappa}\ln(Ey^+) & \mathrm{y}_\mathrm{c}^+ < \mathrm{y}^+ \end{cases} \tag{6.40}$$

Here the position and velocity variables, y and u, have been normalized as $y^+ = u_\tau y/\nu$ and $u^+ = u/u_\tau$, respectively, where u_τ is the friction velocity. The friction velocity is related to the shear stress along the boundary, $\tau_w = \mu_T \partial u/\partial y$, according to $\tau_w = \rho u_\tau^2$. The coefficient $\kappa = 0.41$ is von Kármán's constant and $B = 5.15$ is the u^+-axis intercept. Additionally, E is a proportionality constant that depends on boundary roughness, which can be related to B using logarithmic identities. For example, $E = 9.8$ for smooth walls. Typically the buffer region where the behavior transitions is neglected and instead the viscous sub-layer and log region are connected at an intersection point, y_c^+, which is solved for using a Newton-Raphson iterative method. In addition to the velocity profile equations, the production and destruction of k can be related by $\tau_w \partial u/\partial y = \rho\varepsilon$ (Sondak, 1992; Anderson et al., 1997; **?**).

These relations can be used to derive the following wall functions that govern the behavior of k, ε, ν_T, and ω near boundaries.

1. *kqRWallFunction*:

$$k = \begin{cases} \dfrac{u_\tau^2}{\sqrt{C_\mu}} & \text{in the viscous sublayer } (0 < \mathrm{y}^+ < \mathrm{y}_\mathrm{c}^+) \\ \dfrac{u_\tau^2}{\sqrt{C_\mu}}\left(\dfrac{y^+}{y_c^+}\right)^2 & \text{in the log law region } (\mathrm{y}^+ > \mathrm{y}_\mathrm{c}^+) \end{cases} \tag{6.41}$$

2. *epsilonWallFunction*:

$$\varepsilon = \begin{cases} \dfrac{u_\tau^3}{\kappa y} & \text{in the viscous sublayer } (0 < \mathrm{y}^+ < \mathrm{y}_\mathrm{c}^+) \\ \dfrac{k^{3/2}}{\ell_m} & \text{in the log law region } (\mathrm{y}^+ > \mathrm{y}_\mathrm{c}^+) \end{cases} \tag{6.42}$$

3. *nutkWallFunction*

$$\nu_T = \begin{cases} \nu\left(\dfrac{\kappa y^+}{\ln(Ey^+)} - 1\right) & \text{in the viscous sublayer } (0 < \mathrm{y}^+ < \mathrm{y}_\mathrm{c}^+) \\ 0 & \text{in the log law region } (\mathrm{y}^+ > \mathrm{y}_\mathrm{c}^+) \end{cases} \tag{6.43}$$

4. *omegaWallFunction*

$$\begin{aligned} \omega_{\text{Vis}} &= \frac{6\nu}{\beta_1 y^2} \qquad \text{where } \beta_1 = 0.075 \\ \omega_{\text{Log}} &= \frac{k^{1/2}}{C_\mu^{1/4}\kappa y} \\ \omega &= \sqrt{\omega_{\text{Vis}}^2 + \omega_{\text{Log}}^2} \end{aligned} \tag{6.44}$$

Finally, example OpenFOAM C++ input scripts for the initial boundary conditions each field variable have been included in Appendix A. The example scripts provided there are for the reference case (Case A) of the six experimental configurations, which does not have any concrete blocks included as macro-roughness elements. Note that the exact name of each boundary is provided in these scripts as opposed to the general categories given in Table 6.1 into which these names fit. Also, the initial boundary values used for each of these quantities are provided within these scripts. All unnecessary, header-related comments displaying the OpenFOAM logo and version number were removed for the sake of brevity.

6.6 OpenFOAM Case Structure

Every OpenFOAM case shares the same basic structure of files and directories regardless of the physical problem being solved. In particular there are three key directories, `0.org`, `constant`, and `system` that must always be created prior to running an OpenFOAM case. This general file structure as well as the necessary contents of each directory are depicted in Figure 6.5, which applies to any of the MRE configuration cases.

Within the `0.org` directory, the initial boundary condition files are stored for each relevant field variable based on the physical problem being modeled and the numerical method being used to solve it. For the two-phase (i.e. water-air) `olaDyMFoam` solver utilizing the k-ω SST turbulence model, these variables were α (`alpha`), k (`k`), ε (`epsilon`), ω (`omega`), ν_T (`nut`), $p - \rho g h$ (`p_rgh`), $\boldsymbol{u}$ (`U`), and the boundary displacements (`pointDisplacement`), where the OpenFOAM file names have been provided in parentheses. Examples of each of these files are presented for a one-MRE case in Appendix A.

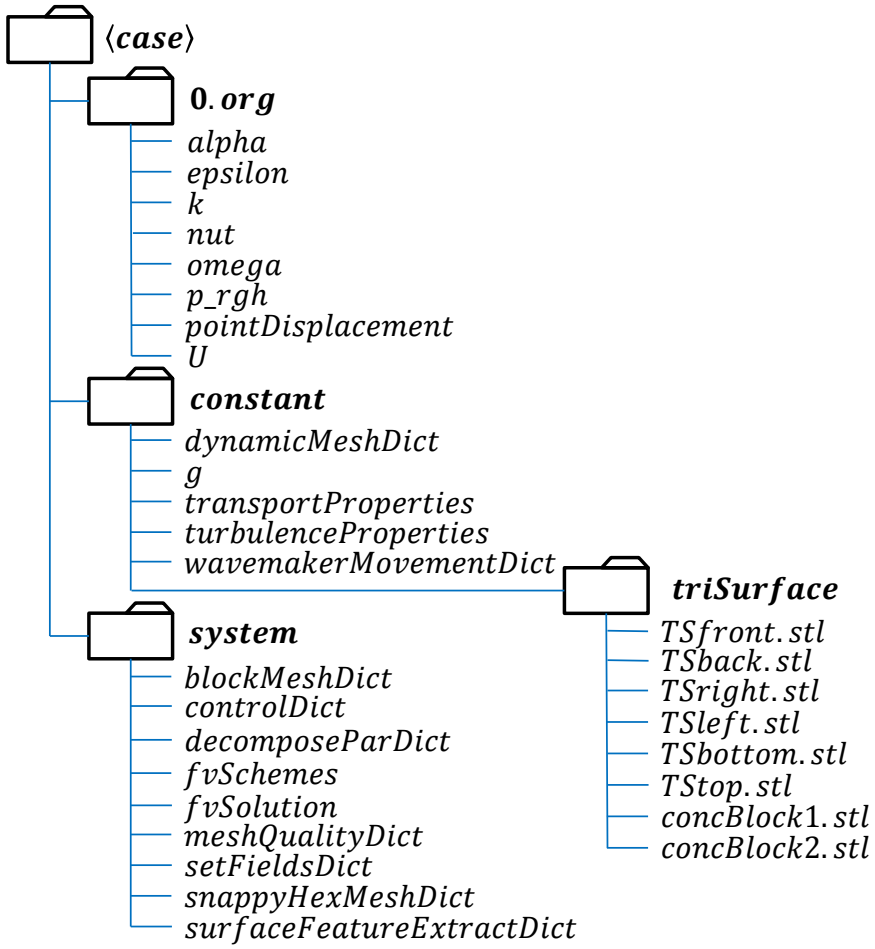

Figure 6.5: OpenFOAM Case Structure

In the `constant` directory, various fixed data is stored including global parameters such as gravity (`g`), geometry files used for meshing (.stl files stored in `triSurface`), mesh deformation controls (`dynamicMeshDict`), wavemaker displacement histories (`wavemakerMovementDict`), fluid properties (`transportProperties`), and turbulence model settings (`turbulenceProperties`). Similarly, the `system` directory stores assorted fixed parameters concerning meshing (`blockMeshDict`, `meshQualityDict`, `snappyHexMesh`, `surfaceFeatureExtractDict`), internal domain initial conditions (`setFieldsDict`), and solution algorithm setup and controls (`controlDict`, `decomposeParDict`, `fvSchemes`, `fvSolution`). Examples of each of these files are provided for a one-MRE case in Appendix B and Appendix C for the `constant` and `system` directories, respectively.

6.7 OpenFOAM Mesh Generation

For each simulation case, an initially uniform background mesh of nearly 4.39 million cells was generated using the actual Large Wave Flume width of 3.658 m and nearly 8.78 million cells for cases using a doubled flume width. The number of cells in different subdomains of the model were selected to result in cells with heights in the z-direction of 10 cm in regions far from the initial free-surface or still water level (SWL) that transitioned to 2.5 cm tall cells near the SWL using uniform cell grading. Similarly, cells far from the test structure and concrete block macro-roughness elements were assigned x-direction lengths of 10 cm, which reduced near the test configuration to 2.5 cm long cells. Transverse cell lengths in the y-direction were left constant at 5 cm for all simulations. The resulting mesh is shown in Figure 6.6, sections of which have been numbered according to the `hex` numbering written in the `blockMeshDict` file provided in Appendix C.

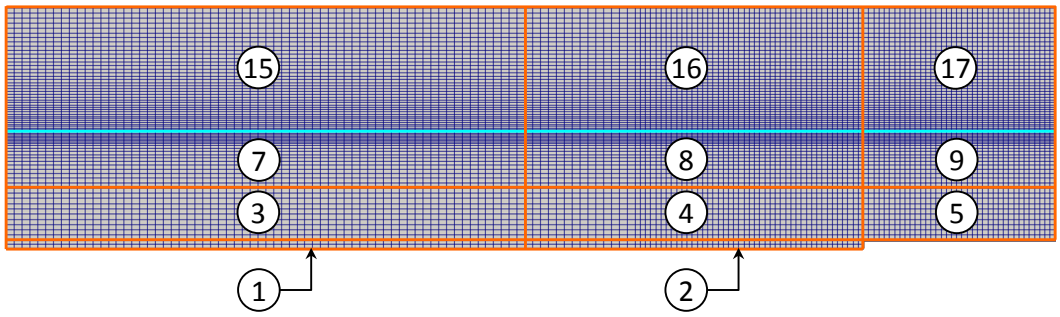

(a) Part 1 - Deformable Region to End of First Floor Slab

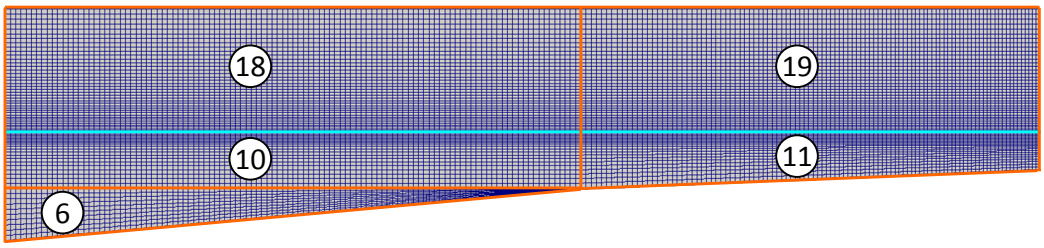

(b) Part 2 - Beach Slopes

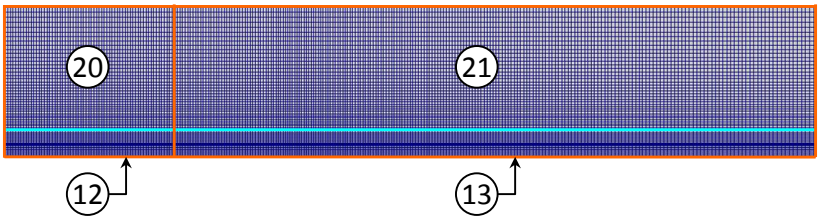

(c) Part3 - Test Structure Region

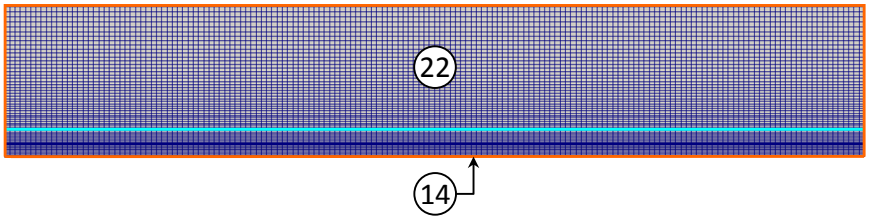

(d) Part 4 - Continuation to the Flume End

Figure 6.6: OpenFOAM Mesh Generation Results using the `blockMesh` Utility (Still Water Level is Indicated by the Cyan Lines)

The generation of the mesh shown in Figure 6.6 was completed in OpenFOAM using the `blockMesh` utility. This utility takes sets of points listed in an array called vertices, which are then used to construct hexes. For example, a single hex using just eight points that also shows the numbering convention for generating hexes is depicted in Figure 6.7. Additionally, a sample script showing the details of how this mesh was specified in the `blockMeshDict` file that was used as an input for the `blockMesh` command, is provided in Appendix C. Note that the specification of hex faces in the boundary section of the provided `blockMeshDict` requires that sets of four points be given that traverse the edges of faces following the right-hand-rule such that the normal vector formed by one's thumb would point outward.

The driving forces behind the choices of the hexes defined in the `blockMeshDict` file were the goals of eliminating non-orthogonality and skewness of the resulting mesh cells, examples of which are depicted in Figure 6.8. Considering only two cells to make the definition

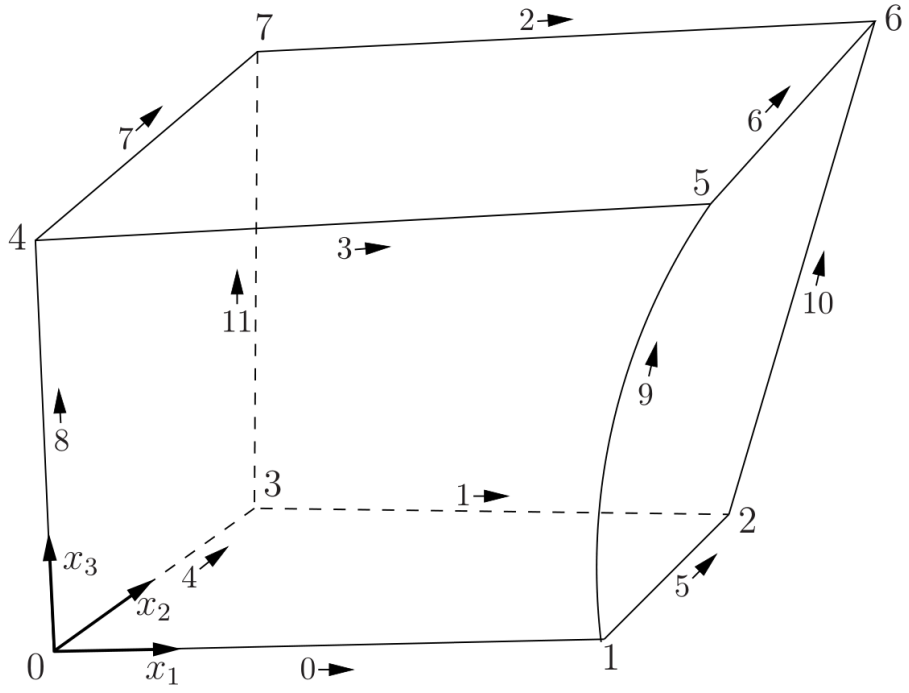

Figure 6.7: Hexahedral Block Convention Used by `blockMesh` (The OpenFOAM Foundation, 2019)

clearer, the degree of non-orthogonality in a mesh is defined as the difference of 90° and the angle between the adjacent cell faces and the line connecting the cell centers. Ideally non-orthogonality angles of 0° are desired; however, this cannot be achieved for the vast majority of real-world problems where angles and curves must be meshed. As such, a tolerable degree of non-orthogonality must be decided upon. For this study, a limiting value of 65° was selected, which can be found in the `meshQualityDict` file presented in Appendix C.

Once again considering a two-cell case, skewness is defined as the normalized distance between the midpoint of the adjacent cell faces and the point at which the line connecting cell centers intersects the adjacent cell faces. As with non-orthogonality, skewness ought to be minimized as much as possible in order to maintain the order of accuracy of the numerical methods employed in OpenFOAM and avoid numerical blow-up or unboundedness. As such, a max value of 2.0 was specified in the `meshQualityDict` file presented in Appendix C in order to achieve accurate and stable numerical results. The chosen non-orthogonality and

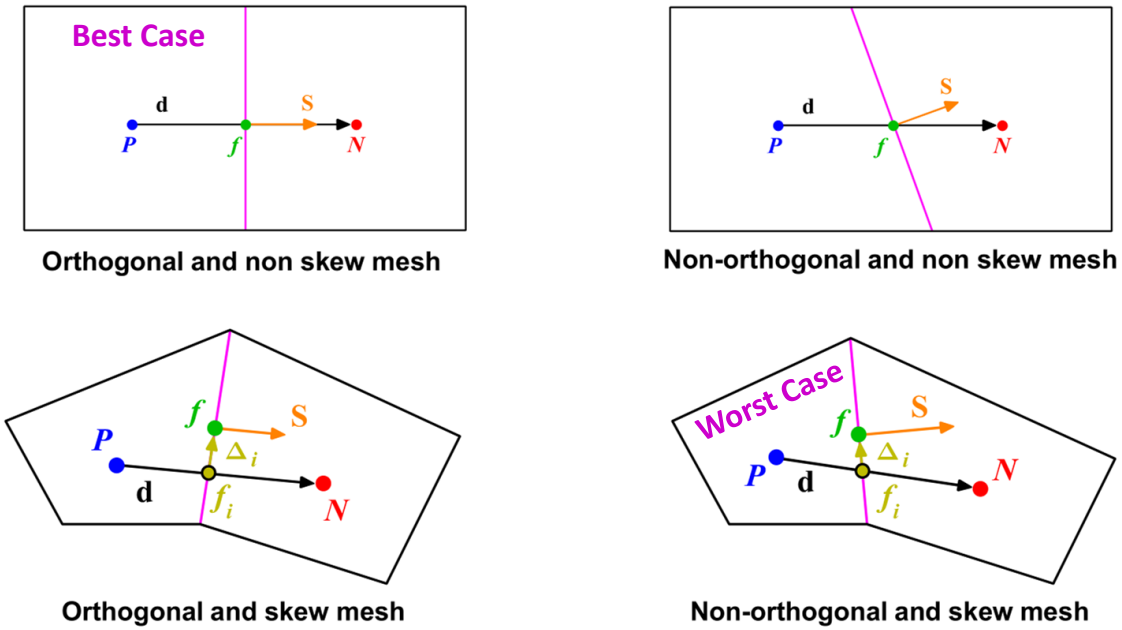

Figure 6.8: Mesh Criteria: Examples of High to Poor Quality Meshes (Guerrero, 2015)

skewness limits were used by `snappyHexMesh` when refining the mesh as well as by the `checkMesh` utility when assessing the overall quality of the mesh.

To incorporate the test structure and concrete blocks into the background mesh, the OpenFOAM utility `surfaceFeatureExtract` was used to import the surface geometry and then the `snappyHexMesh` utility was used to refine the mesh conforming to this geometry. The surface geometry was obtained from .stl files describing the surface of the superstructure, which were created by exporting CAD drawings of the bridge to data files written in the stereo-lithography (STL) format.

Instead of importing a single .stl file using `surfaceFeatureExtract`, the test structure was initially subdivided into individual faces for the purposes of measuring resultant forces and moments in addition to pressure distributions acting on specific faces. Furthermore, this splitting up of the test structure into components allowed for comparison of demands from face to face, which provides invaluable information in terms of being able to isolate specific regions subjected to extreme demands. The surface splitting process was completed using the open-source mesh generation software enGrid, which provides tools to manually select

individual or sets of surface components and export them as separate .stl files (Gloth, 2019). An example `surfaceFeatureExtractDict` script for the reference case (Case A) without concrete blocks has been provided in Appendix C to demonstrate the setup of this utility for extracting .stl surface data to be used by `snappyHexMesh`.

Once the surface data has been processed, mesh refinement around the imported surface files is completed in two stages using `snappyHexMesh`. The first stage refines the hexahedral mesh along the superstructure surfaces using a cell-splitting process and then removes cells inside the superstructure to create a new set of domain boundaries. It should be noted that the .stl files should describe closed surfaces without holes in order for the cell removal process to be completed correctly. If the net surface is not closed, a surface will be carved into the background mesh and mesh refinement will be performed around it, but the cells it surrounds will not be cut out of the domain.

The second stage snaps the sharp edges of the castellated mesh created during the first stage to lie along the superstructure surfaces. This is done by displacing vertices of the hexes lying along the boundary in an iterative procedure that attempts to reduce error and avoid creating cells with adverse geometric properties that do not satisfy user-specified mesh quality criteria. The setup of the castellated meshing plus snapping operations for the reference case (Case A) is demonstrated in the example `snappyHexMeshDict` script provided in Appendix C.

The variation in mesh resolution from the uniform region to the region near the superstructure boundaries resulting from these steps is demonstrated in Figure 6.9. After using `snappyHexMesh`, the resulting number of finite volume mesh cells was approximately 4.46 million, which is roughly a 1.5% increase relative to the initial, uniform background mesh of 4.39 million cells. This demonstrates that use of selective mesh refinement near the still water level and test configuration results in minimal cell count increase, but achieves the desired refinement level in these regions to improve the quality of the resulting numerical solution.

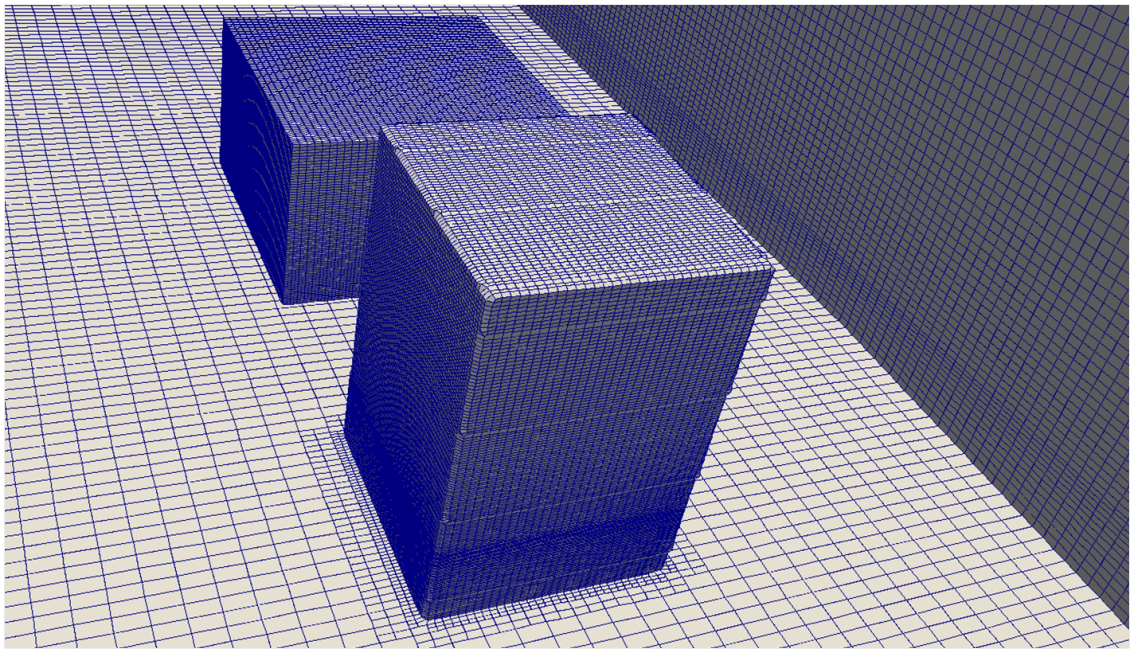

Figure 6.9: Comparison of Global and Test Configuration Mesh Sizes

6.8 OpenFOAM Case Execution

Prior to running OpenFOAM cases, the cases needed to be setup by completing meshing, setting initial conditions, and case decomposition so cases could be run in parallel. These operations were submitted as jobs to queues in the University of Washington high-performance computing (HPC) cluster, Hyak, using the `buildCase.sh` batch script presented in Appendix D. Once cases were setup they were submitted again as new jobs to Hyak queues in order to run the `olaDyMFlow` solver using the `runCase.sh` script provided in Appendix D. Note that all batch scripts presented in Appendix D were written to be used with the Slurm job scheduling software since Slurm is used in Hyak for job management. As such all batch scripts were submitted as jobs to a HPC queue using the command `sbatch <script name>`. Running the cases took roughly 2 to 4 days to complete the unbroken and broken wave cases using 4 nodes with 16 processors each to give a total of 64 processors per simulation. The variability in run times can be attributed largely to the stopping, waiting, and restarting process of using the checkpoint system of the Slurm scheduler, which allows for shared use of nodes that are not being used by their owners until the owners submit jobs to their nodes

again.

After cases completed running, they were reconstructed from the parallel decomposed format to the serial recomposed format using the `reconstructPar` OpenFOAM utility as demonstrated in the `reconstructCase.sh` batch script. Case reconstruction allows for much quicker post processing of 3D visuals of data such as the free-surface, velocity field, or pressure field using. For instance, the ParaView software, which is configured to read OpenFOAM case data, loaded case data and performed rendering operations much quicker when reconstructed cases were used instead of decomposed cases.

Once all visual post-processing was completed, individual time step data in terms of field variables and meshes were removed using the `cleanCaseAll.sh` script, which was executed in a Linux terminal as `bash cleanCaseAll.sh`. Cleaning cases was of critical importance due to the large number of files created by and storage space taken up by individual OpenFOAM simulations. However, if visual post-processing of cases is not necessary, which was the case during the simulations conducted for the MRE location parametric study discussed in Section 8.1 - Macro-Roughness Element Configurations, then the `purgeWrite` variable in the `controlDict` file should be set to a small integer value instead of 0, which is the default value that disables purging of time step data. The chosen value represents the number of the most recently solved time steps for which data will be saved.

Chapter 7

NUMERICAL MODEL VALIDATION

In order to develop a suitable numerical model for conducting a parametric study of shielding and channeling effects by varying macro-roughness element locations, a set of criteria must be met prior to further use. In the case of the unbroken and broken wave flume experiments, three key measurements, free-surface elevation, pressures on the test structure faces, and the total streamwise force acting on the test structure, were selected to be used for making comparisons between empirical and OpenFOAM results in order to validate the numerical model. This section provides these comparisons initially focusing on the reference case (Case A) alone during the Turbulence Model Selection Study, followed by a discussion of comparisons made between experimental and numerical streamwise force histories for the five remaining cases (Cases B through F) in the Validation of Macroscale Roughness Cases section, where only the selected turbulence model results are presented.

7.1 Turbulence Model Selection Study

When beginning the numerical model validation study, the initial goal was to develop a stable model that was capable of simulating tsunami-like wave propagation and wave-structure interaction. However, it soon became apparent that developing a high-quality mesh as well as choosing and properly configuring a turbulence model for modeling wave-structure interaction were the most critical elements of the validation process. Initially, the Standard k-ε model developed by Jones and Launder (1972) and improved by Launder and Sharma (1974) was selected as the turbulence model to be used for validation purposes. This choice was based upon the previous successes of the numerical modeling studies of Motley et al. (2016) and Winter et al. (2018) that focused on tsunami-like wave impact forces on bridges,

for which numerical model validation was performed by Wong (2015) using the Standard k-ε model in OpenFOAM and experimental data from dam-break tests presented during the 2014 Oregon State University tsunami modeling workshop (Cressman et al., 2014).

7.1.1 Total Streamwise Forces

When used to model the three-dimensional wave-structure interaction caused by tsunami-like long waves, initial numerical model results generated using the Standard k-ε model over-predicted the peak forces for both the unbroken and broken wave reference cases (Case A) as shown in Figure 7.1. Furthermore, the Standard k-ε model was found to give inconsistent results when the finite volume cell size was varied for the broken wave. When an attempt was made to improve the mesh quality by refining it, it was shown that increasing the number of cells in the y-direction (i.e. the transverse or alongshore direction) produced drastically different peak streamwise forces. For instance, when the y-direction cell size was changed from roughly 10 cm to 5 cm, the 5 cm cell case resulted in a larger peak force being measured on the test structure than for the 10 cm cell size case, demonstrating an unstable, divergent behavior as shown in Figure 7.2.

Based on the over-prediction of the peak streamwise force for both wave types and erratic results due to mesh size variations obtained for the broken wave using the Standard k-ε model, an investigation into the effects of different turbulence models was deemed necessary. To investigate the influence of the selected turbulence model on the force time history results, a set of four models were chosen to make comparisons with the results for the Standard k-ε model (`kEpsilon`)[1]. Two of the selected models were of the Reynolds-Averaged Navier-Stokes (RANS), two-equation type, specifically the Non-linear Realizable k-ε (`ShihQuadraticKE`) and k-ω Shear Stress Transport (`kOmegaSST`) models. Additionally, a Reynolds-Stress Model (RSM), the Launder-Reece-Rodi (`LRR`) model, was chosen to make a comparison between the RANS and RSM model types since the latter is supposed to more accurately simulate

[1]The OpenFOAM C++ code name of each turbulence model has been included in parentheses

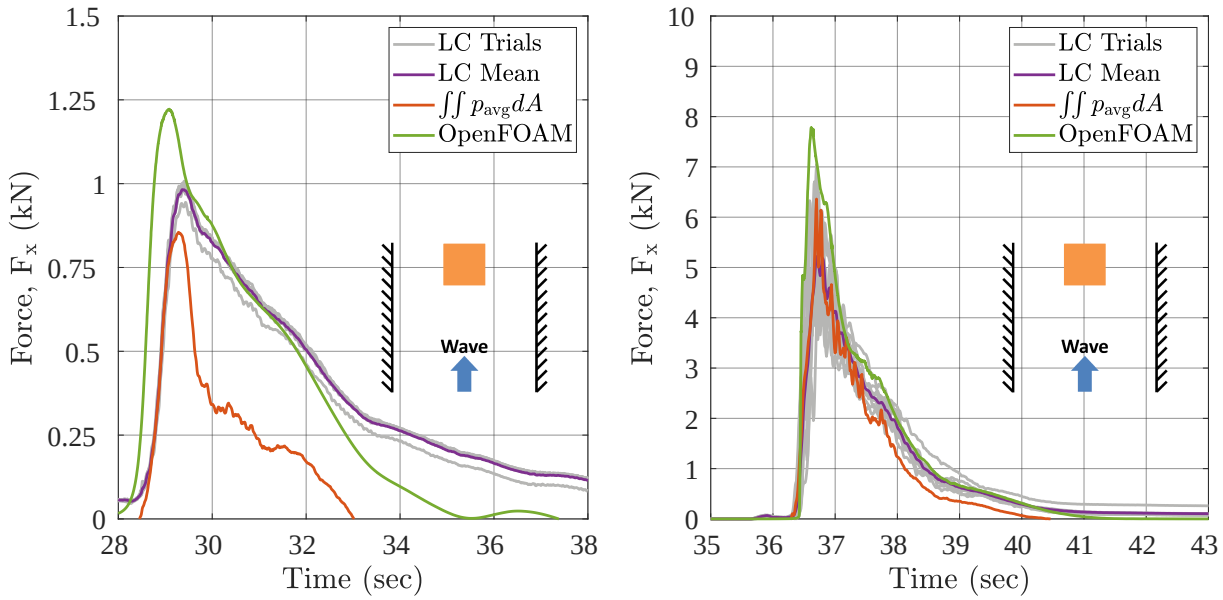

(a) Unbroken Wave

(b) Broken Wave

Figure 7.1: Streamwise Forces for Case A using the Standard k-ε Model with the Initial 10 cm Global Cell Size Mesh

turbulent flows, but at a greater computational cost. This comparison of model types was necessary in order to make an informed final model selection based upon trying to find a balance between accuracy of results and computational cost. Additionally, in order to allow for results to be comparable from model-to-model and wave-to-wave, the mesh with 5 cm size cells in the transverse direction was used for all simulations.

After running OpenFOAM simulations for both unbroken and broken wave types using each of the four selected turbulence models, it was found that the unbroken wave results varied little from model to model, whereas the broken wave results showed significant variability. As shown in Figure 7.3, the peak force for the unbroken wave was consistently over-predicted regardless of which turbulence model was used with the only notable improvement occurring for the Non-linear Realizable k-ε model. On the contrary, varying the turbulence model showed a clear improvement in the accuracy of the peak streamwise forces calculated using OpenFOAM for the broken wave simulations. In particular, the k-ω SST

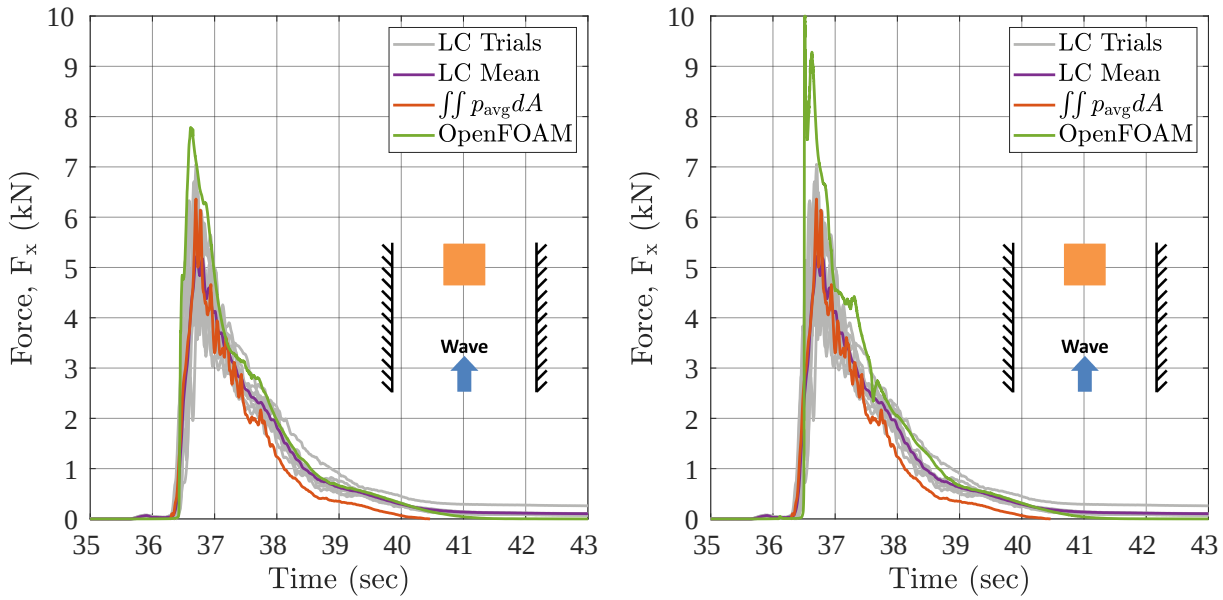

(a) Transverse Cell Size: 10 cm

(b) Transverse Cell Size: 5 cm

Figure 7.2: Effects of Decreasing the Transverse Cell Size on the Peak Streamwise Force for Case A due to the Broken Wave using the Standard k-ε Model.

model out-performed all other turbulence models, producing a near perfect match with experimental force histories based on load cell and pressure gauge measurements as shown in Figure 7.4. The Non-linear Realizable k-ε model predicted a similar peak force, but failed to match the timing of the experimental force histories, arriving roughly a quarter of a second early.

What is most striking about these results is the severe under-performance of the Launder-Reece-Rodi RSM model for the broken wave as shown in Figure 7.4d and the lack of improvement of the results for the unbroken wave as shown in Figure 7.3d despite the fact that RSM models directly model the behavior of each Reynolds stress term instead of using the simplified Boussinesq eddy viscosity hypothesis to determine the Reynolds stresses as functions of the turbulent kinetic energy and mean strain rate of the flow. However, even though the Reynolds stresses were modeled explicitly, the LRR model was initialized with data based on the Boussinesq hypothesis defined by Equation 6.21, which has been shown to be phys-

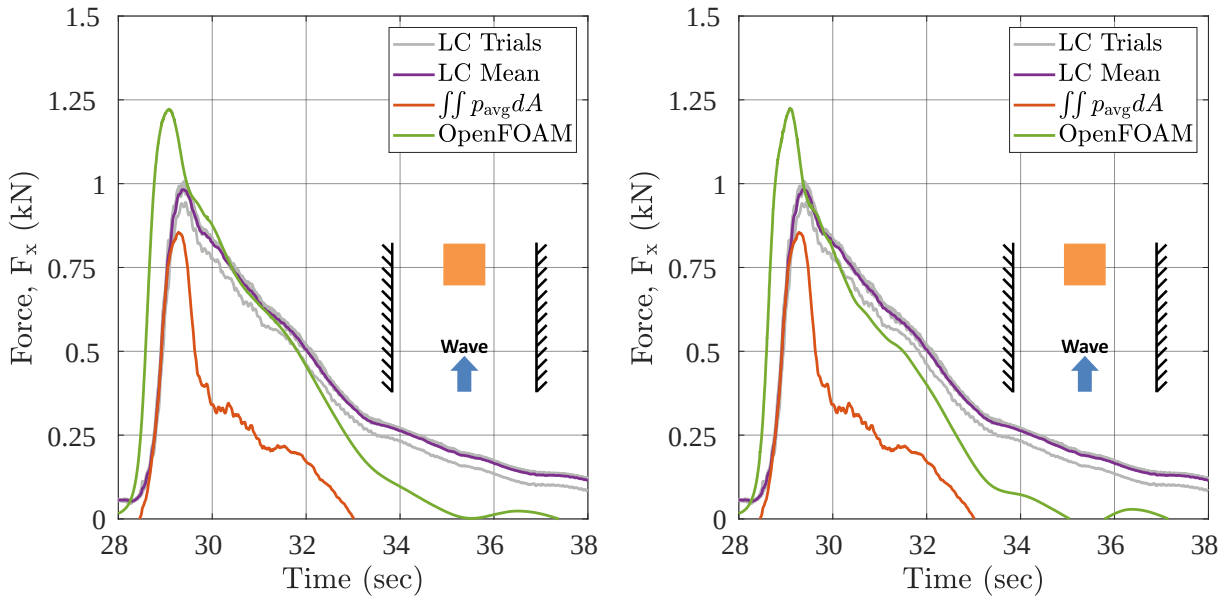

(a) Standard k-ε (`kEpsilon`)

(b) k-ω Shear Stress Transport (`kOmegaSST`)

(c) Non-linear Realizable k-ε (`ShihQuadraticKE`)

(d) Launder-Reece-Rodi (`LRR`)

Figure 7.3: Comparison of Streamwise Force Histories for Case A due to the Unbroken Wave

ically correct only in sub-regions of many turbulent flows (Schmitt, 2007). Since the fluid began at rest, the mean strain rate tensor, $\langle S_{ij} \rangle$, defined by Equation 6.20 vanishes, leaving the Reynolds stresses to be determined by the turbulent kinetic energy alone as shown in

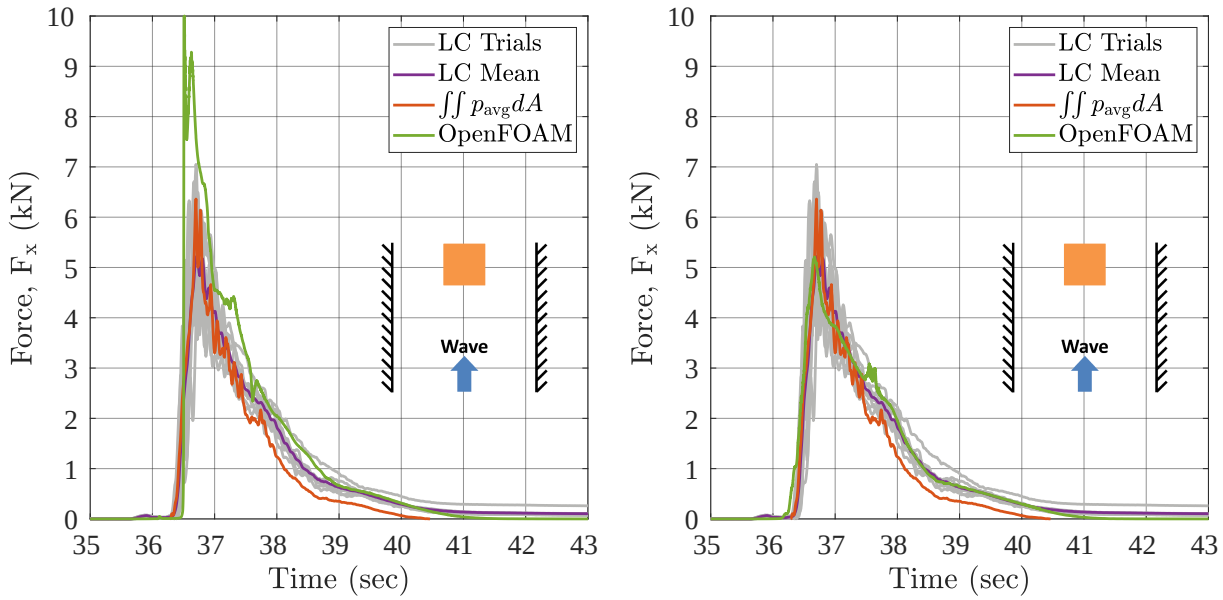

(a) Standard k-ε (`kEpsilon`)

(b) k-ω Shear Stress Transport (`kOmegaSST`)

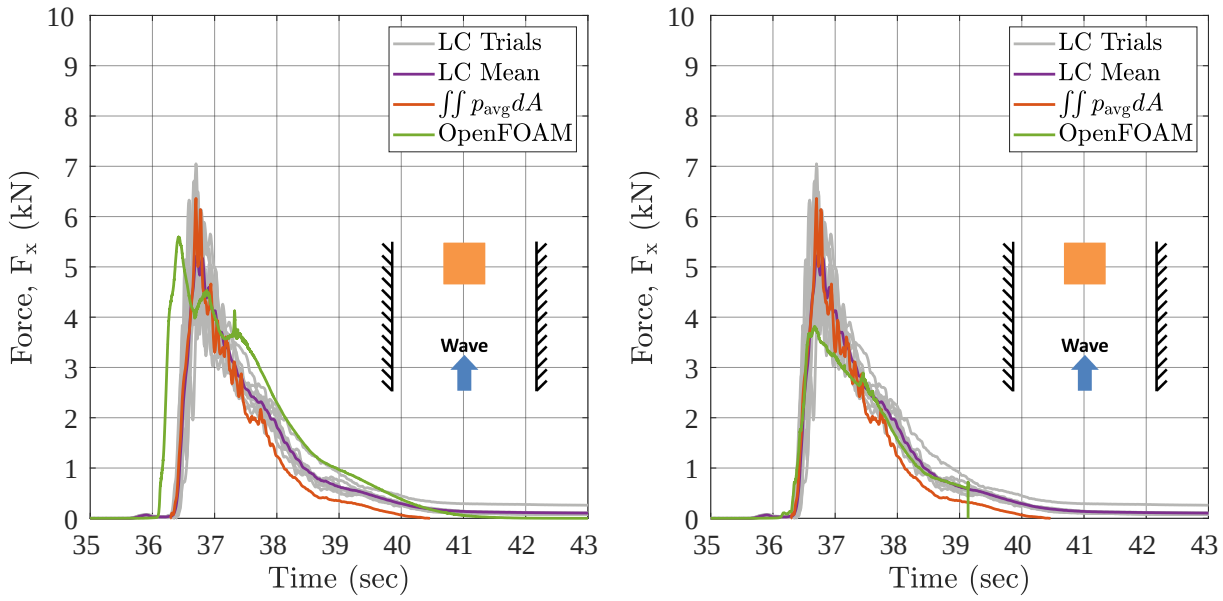

(c) Non-linear Realizable k-ε (`ShihQuadraticKE`)

(d) Launder-Reece-Rodi (`LRR`)

Figure 7.4: Comparison of Streamwise Force Histories for Case A due to the Broken Wave

Equation 7.1. To be consistent with the rest of the simulations, the initial Reynolds stresses were determined using experimentally-determined values for k based velocity measurements taken by ADV1, which was nearest to the wavemaker and best represented the initial state

of turbulence associated with the unbroken and broken tsunami-like long waves that were tested. Thus, multiple sources of error including experimental sources such as measurement device tolerances, noise, and post-processing methods as well as the theoretical assumption of Boussinesq led to the possibility of a poor initial setup for the LRR model that could explain its underwhelming performance, particularly in the case of the broken wave simulation for Case A.

$$R_{ij} = -\rho\langle u_i' u_j' \rangle = 2\mu_T \left[\frac{1}{2} \left(\cancelto{0}{\frac{\partial \langle u_i \rangle}{\partial x_j}} + \cancelto{0}{\frac{\partial \langle u_j \rangle}{\partial x_i}} \right) - \frac{1}{3} k \delta_{ij} \right] = -\frac{2}{3} \mu_T k \delta_{ij} \tag{7.1}$$

7.1.2 Pressures on the Offshore Face of the Test Structure

In order to better understand the variations in the forces that were observed for each turbulence model simulation, the pressures measured on the offshore face of the test structure were recorded in OpenFOAM too. As shown in Figure 4.11c, there were eight measurement locations used during the macroscale roughness element tests (Cases B through F). The pressure time histories for the unbroken and broken waves using the same 5 cm transverse cell size mesh are shown for the k-ε model in Figures 7.5 and 7.6, the k-ω SST model in Figures 7.7 and 7.8, the Non-linear Realizable k-ε model in Figures 7.9 and 7.10, and the Launder-Reece-Rodi model in Figures 7.11 and 7.12, where the percent error in the peak pressure relative to the empirical data are shown to demonstrate the accuracy of the numerical results for each pressure gauge.

For the unbroken wave, all of the turbulence models resulted in over-predicted peak pressures, early wave arrivals, and sustained loading durations that lasted approximately 1 second longer than the experimental time histories. With peak pressure percent errors falling in the ranges of 14.8% to 31%, 12.3% to 28.6%, and 13.4% to 31.7%, the Standard k-ε, k-ω SST, and LRR models were roughly twice as inaccurate as the Non-linear Realizable k-ε model, which gave peak pressure percent errors in the range of 6.8% to 16.4%. Despite this improved performance in terms of peak pressures for the Non-linear Realizable k-ε model,

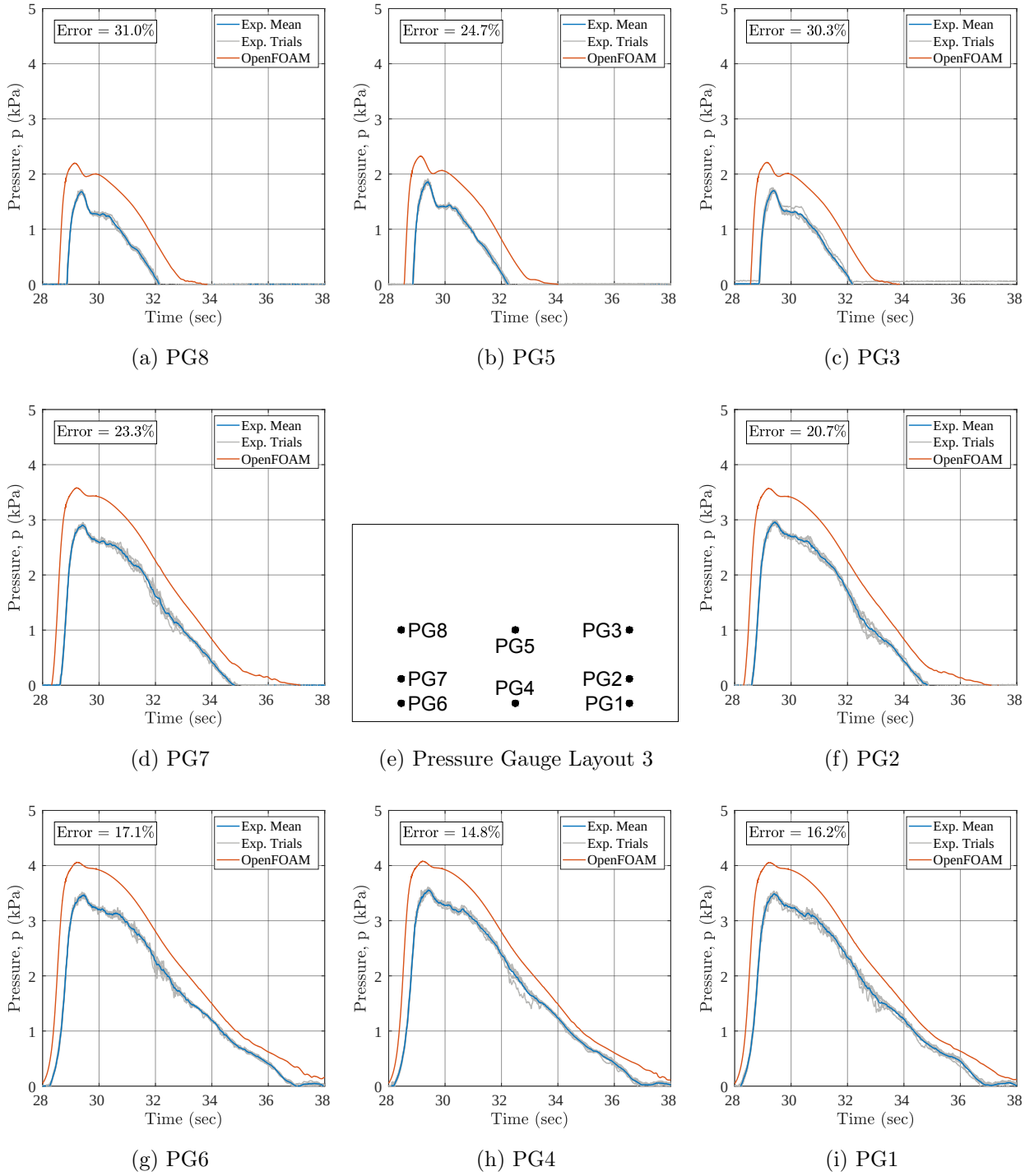

(a) PG8 (b) PG5 (c) PG3

(d) PG7 (e) Pressure Gauge Layout 3 (f) PG2

(g) PG6 (h) PG4 (i) PG1

Figure 7.5: Pressure Gauge Measurements Versus OpenFOAM Time Histories on the Offshore Test Structure Face for the Unbroken Wave using the Standard k-ε Model

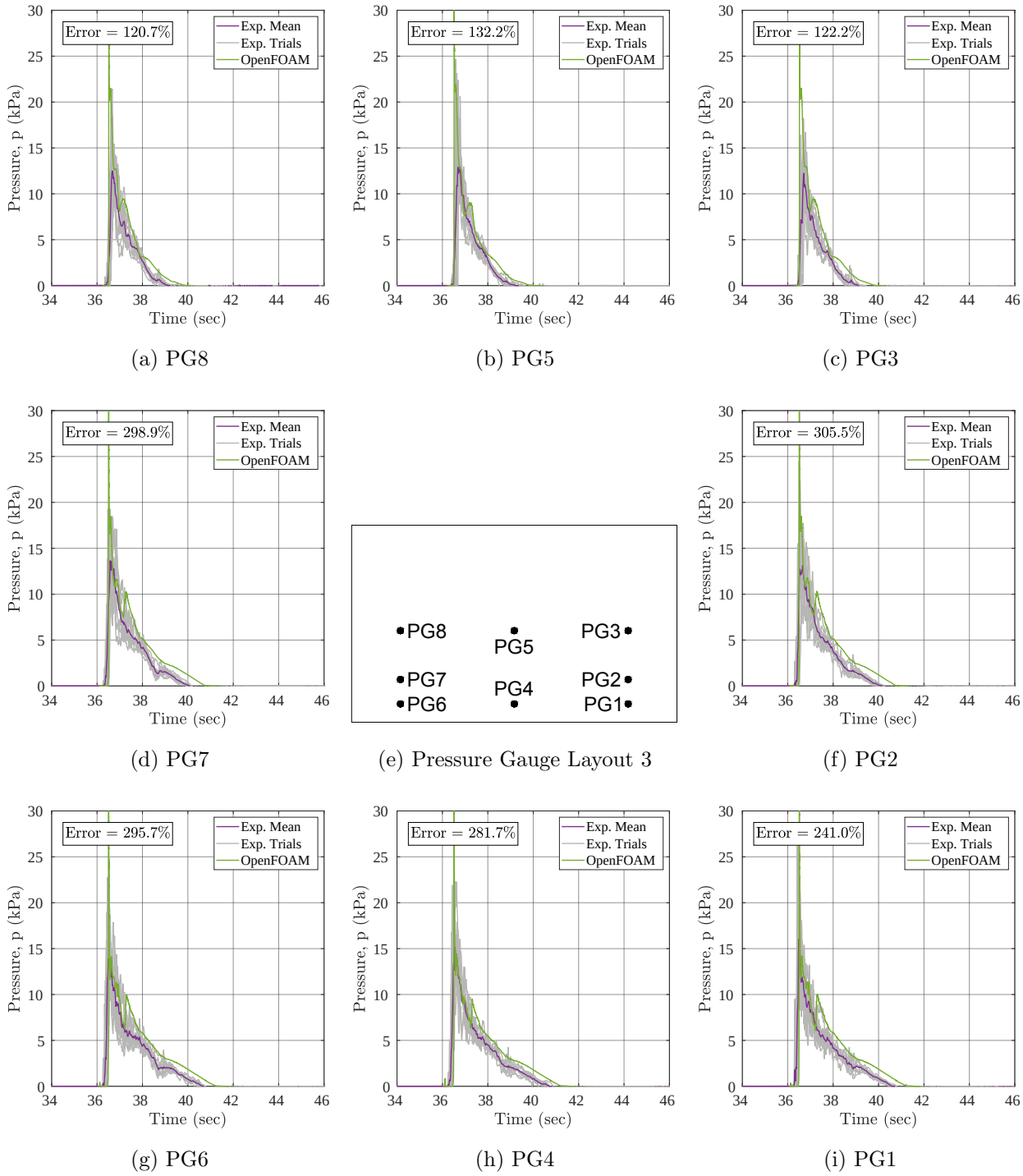

Figure 7.6: Pressure Gauge Measurements Versus OpenFOAM Time Histories on the Offshore Test Structure Face for the Broken Wave using the Standard k-ε Model

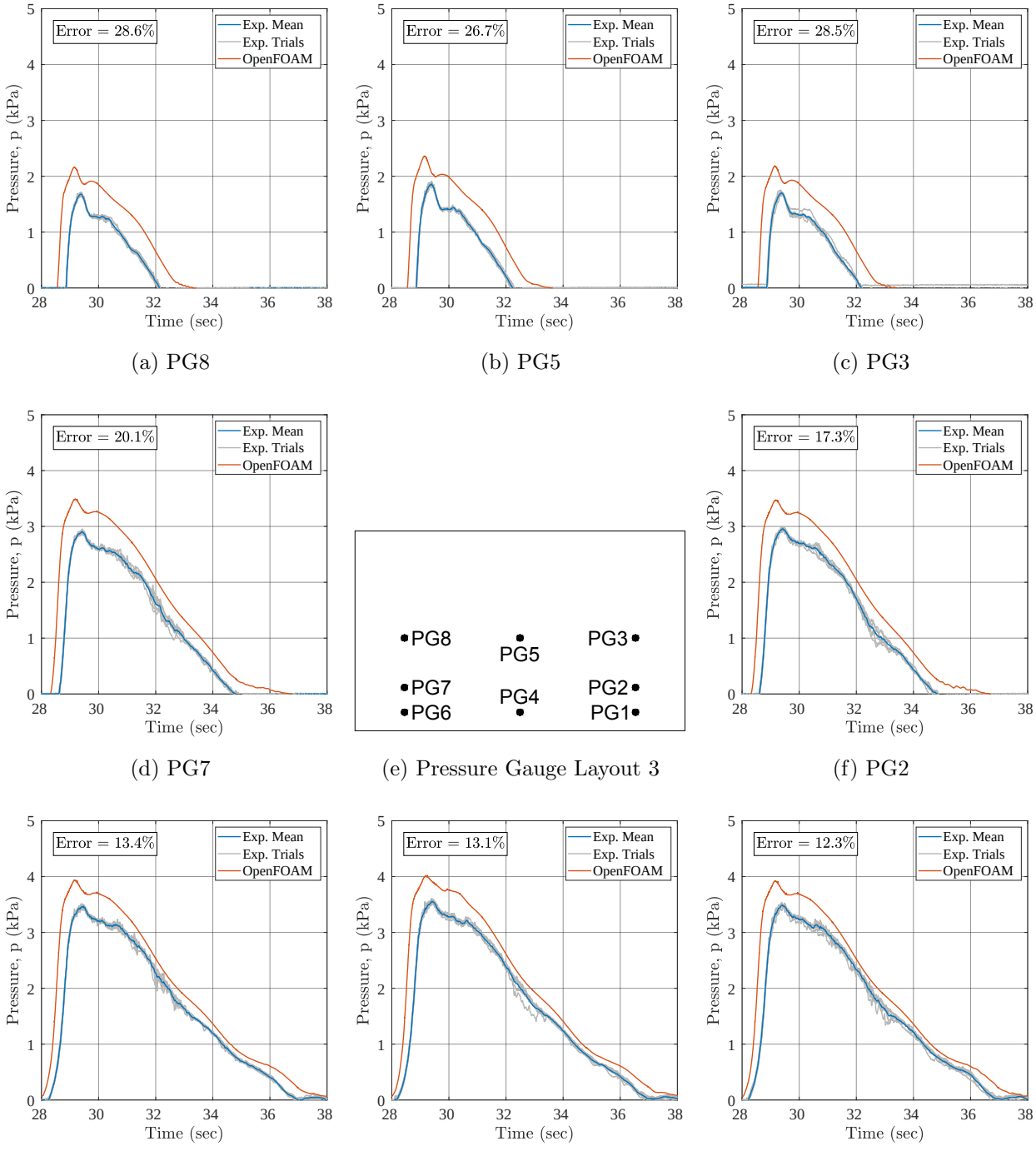

(a) PG8 (b) PG5 (c) PG3

(d) PG7 (e) Pressure Gauge Layout 3 (f) PG2

(g) PG6 (h) PG4 (i) PG1

Figure 7.7: Pressure Gauge Measurements Versus OpenFOAM Time Histories on the Offshore Test Structure Face for the Unbroken Wave using the k-ω SST Model

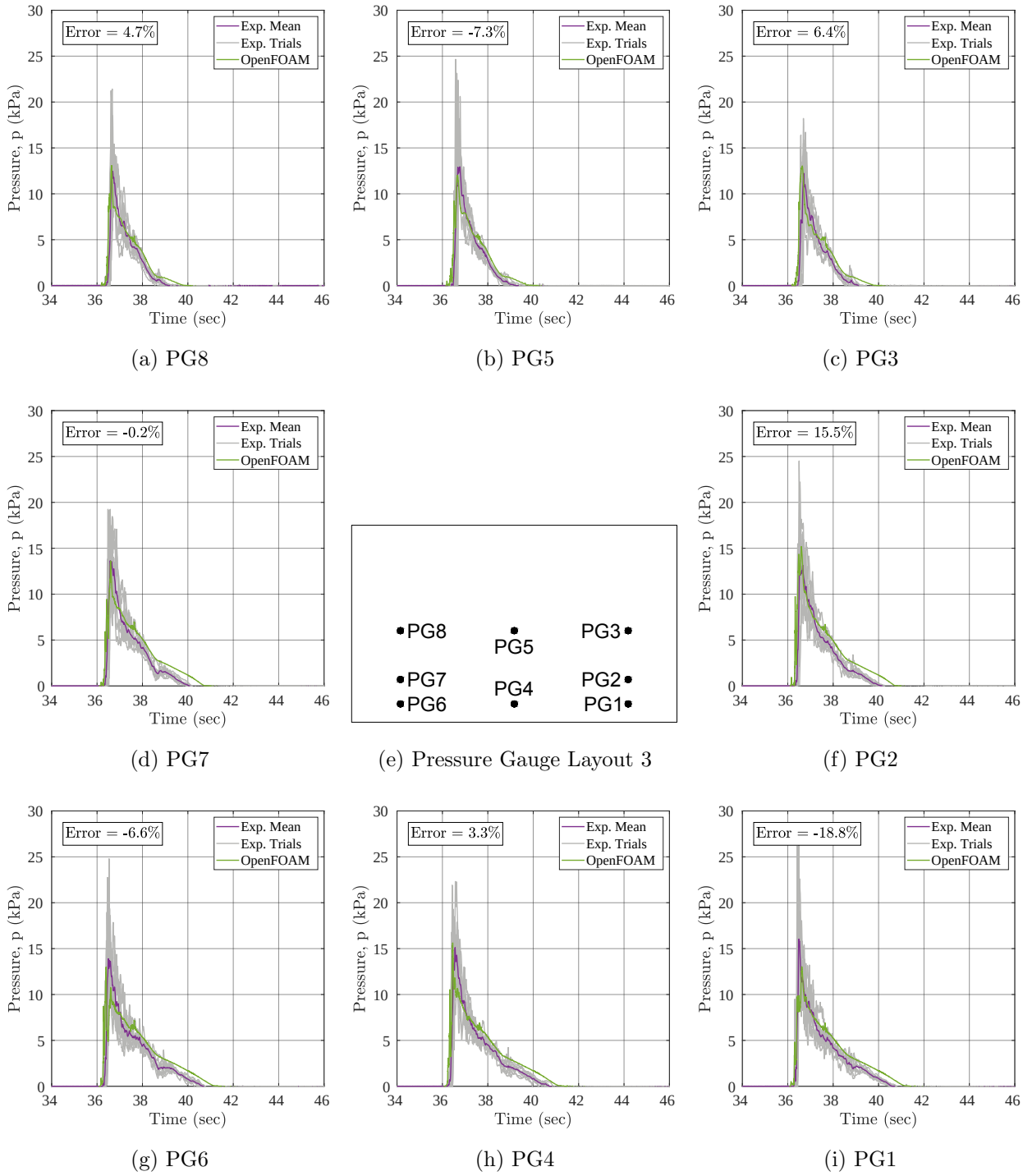

(a) PG8 (b) PG5 (c) PG3

(d) PG7 (e) Pressure Gauge Layout 3 (f) PG2

(g) PG6 (h) PG4 (i) PG1

Figure 7.8: Pressure Gauge Measurements Versus OpenFOAM Time Histories on the Offshore Test Structure Face for the Broken Wave using the k-ω SST Model

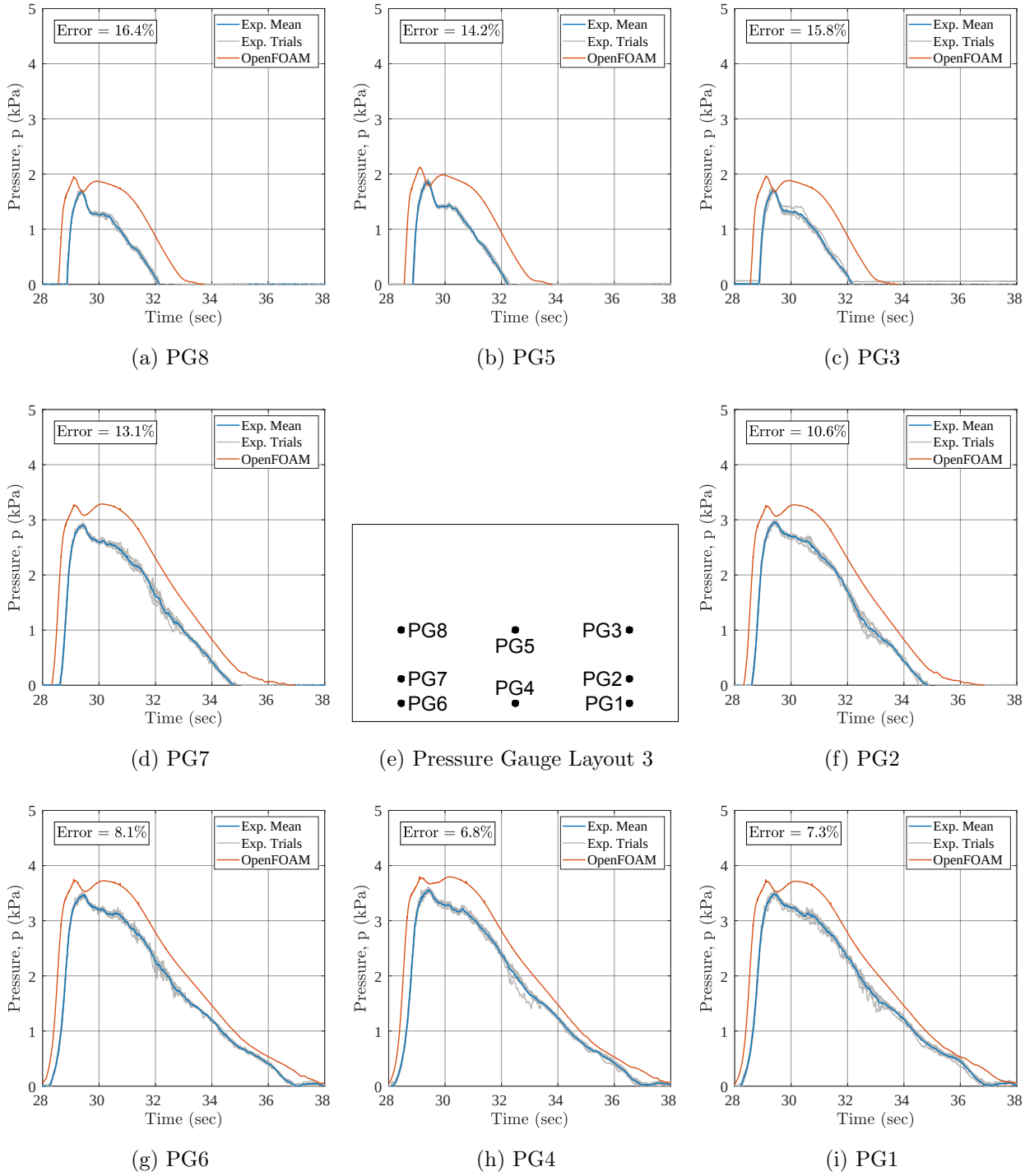

Figure 7.9: Pressure Gauge Measurements Versus OpenFOAM Time Histories on the Offshore Test Structure Face for the Unbroken Wave using the Non-linear Realizable k-ε Model

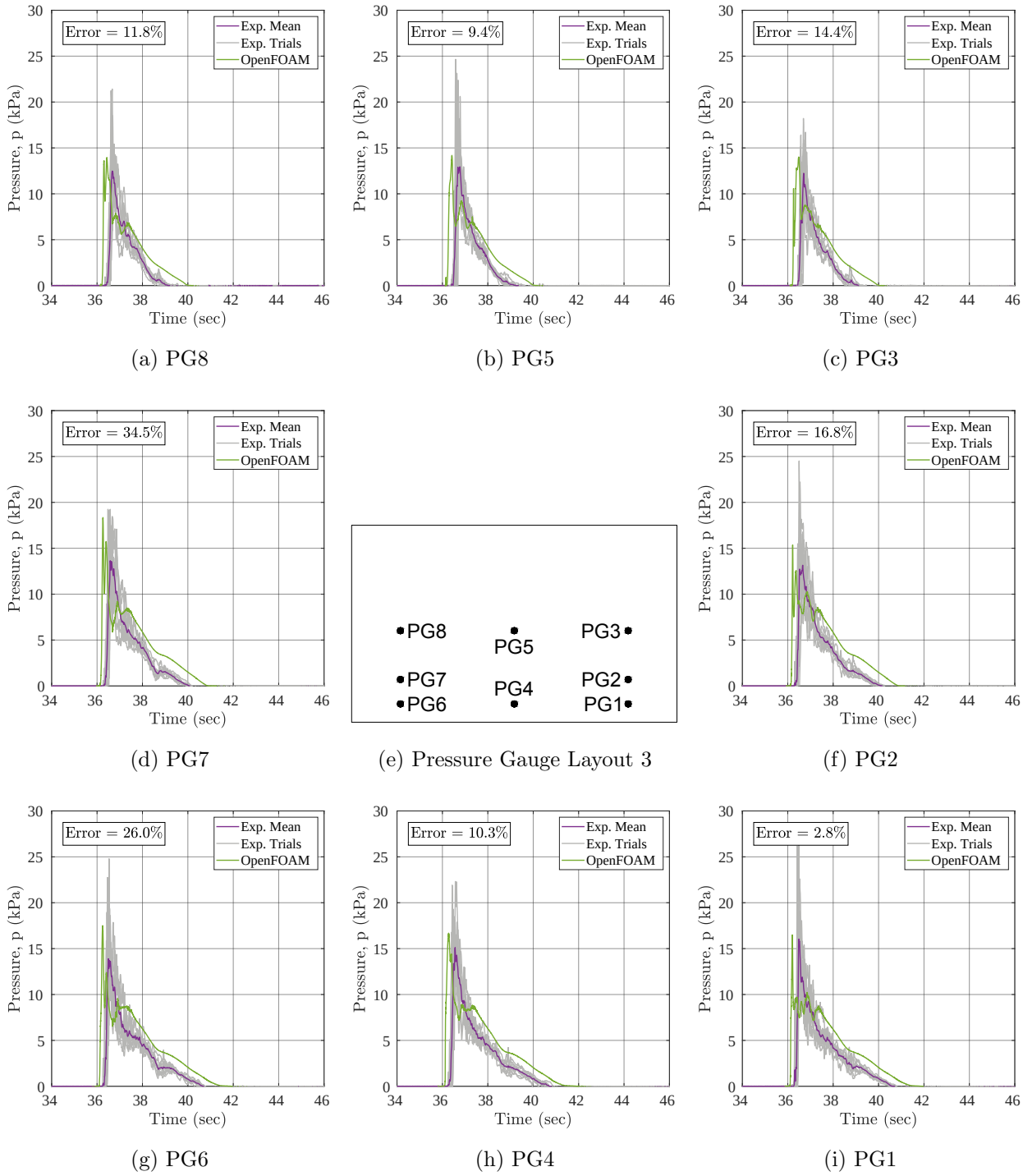

(a) PG8 (b) PG5 (c) PG3

(d) PG7 (e) Pressure Gauge Layout 3 (f) PG2

(g) PG6 (h) PG4 (i) PG1

Figure 7.10: Pressure Gauge Measurements Versus OpenFOAM Time Histories on the Offshore Test Structure Face for the Broken Wave using the Non-linear Realizable k-ε Model

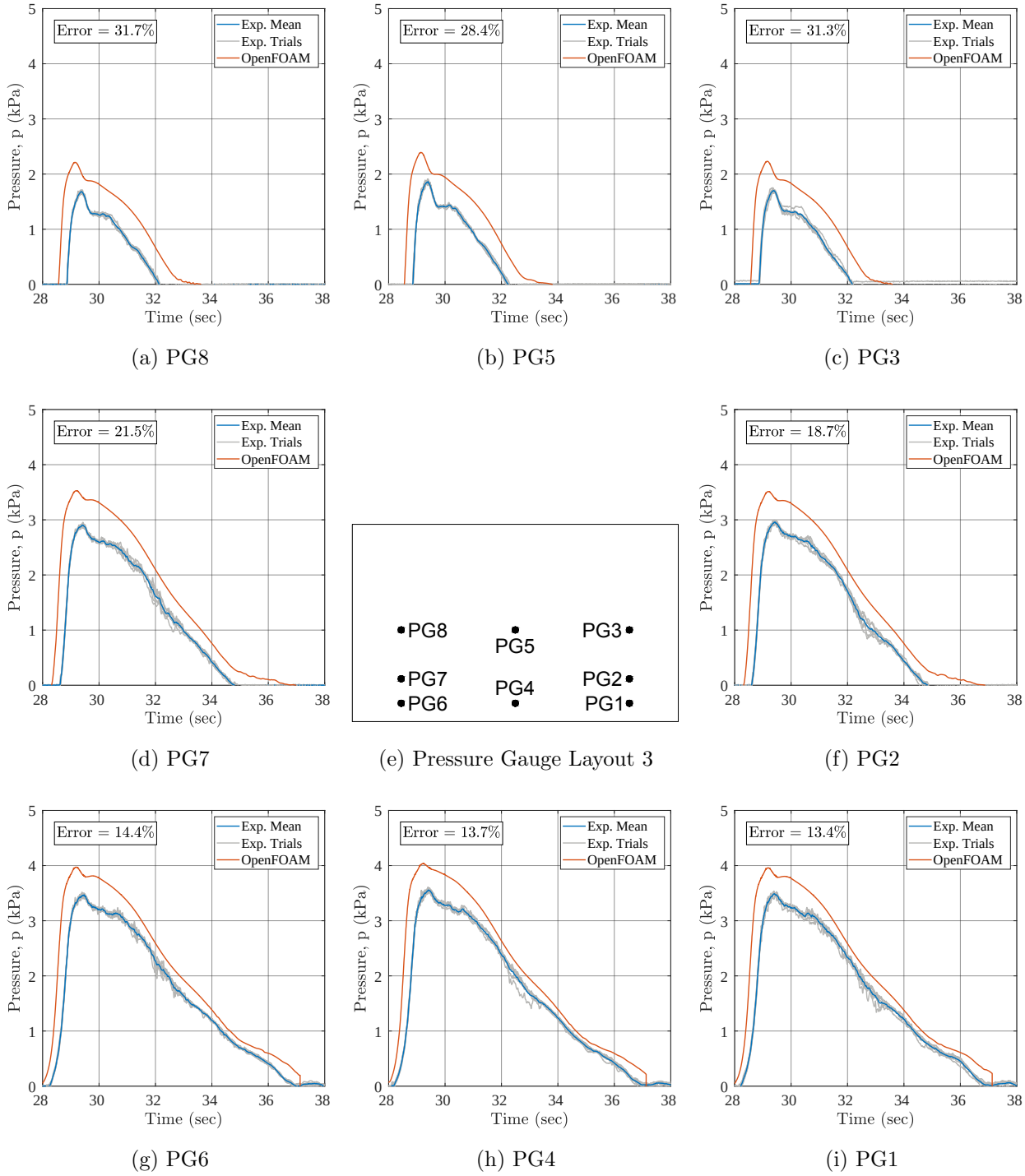

Figure 7.11: Pressure Gauge Measurements Versus OpenFOAM Time Histories on the Offshore Test Structure Face for the Unbroken Wave using the LRR Turbulence Model

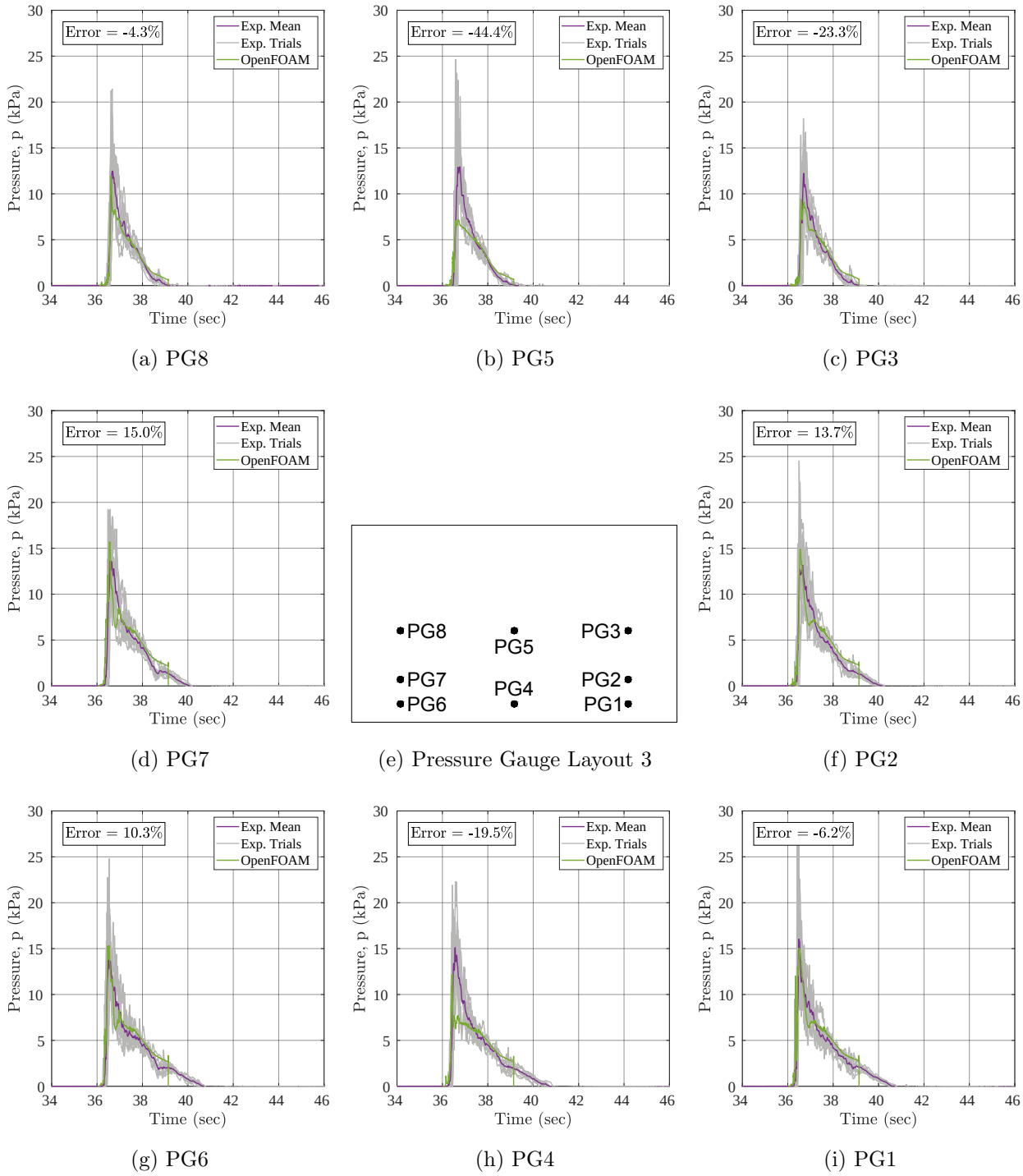

Figure 7.12: Pressure Gauge Measurements Versus OpenFOAM Time Histories on the Offshore Test Structure Face for the Broken Wave using the LRR Turbulence Model

the model still suffered significantly from overly long loading durations in the same manner as the others. Additionally, the worst region of error in peak pressures for all of the turbulence models was near the top of the test structure, which indicates that OpenFOAM may be over-predicting the wave run-up on the test structure offshore face.

For the broken wave, each turbulence model matched the experimental results well during the post-impact phase of the wave loading; however, the peak pressures showed significant variability. For instance the k-ε model, showed the most variability and largest percent errors in peak pressures, which ranged from 120.7% to 305.5% with the largest error occurring near the bottom of the test structure. The LRR model gave the next best results in terms of percent error in peak pressure, which ranged from 4.3% to 44.4% with the largest errors occurring along the middle of the test structure. The k-ω SST and Non-linear Realizable k-ε models gave very similar results in terms of the percent error in peak pressures ranging from 2.8% to 34.5% and 0.2% to 18.8%, respectively. Based on these ranges alone, the k-ω SST model is plainly the best model for reproducing accurate forces and pressures, but also the Non-linear Realizable k-ε model that performed second best showed incorrect timing of the wave impact with the numerical pressure histories beginning roughly a quarter of a second ahead of the experimental pressure histories as was observed with the force histories too, further solidifying the k-ω SST model as the clear choice for modeling the turbulent broken wave.

7.1.3 Free-Surface Elevations

To provide a final level of model validation and investigate the inaccuracy of the OpenFOAM force and pressure results for the unbroken wave, the empirical and numerical free-surface elevation (i.e. the displacement of free-surface relative to the still water level) histories that were recorded along the length of the unobstructed flume as well as near the test structure are compared in this sub-section. As shown in Figure 4.13, there were four wave gauges (*wg1*-*wg3* and *uswg1*) used along the flume in the flat-bottomed deep region near

the wavemaker and in the sloped bottom region, where wave shoaling took place, whereas the remaining five wave gauges (*uswg2-uswg6*) were positioned near the test structure to measure free-surface changes caused by the test structure. The first group of wave gauges always successfully recorded the free-surface elevation of the waves propagating along the flume; however, the second group of wave gauges near the test structure recorded erroneous free-surface time histories due to large splashes that made recording an accurate free-surface nearly impossible in most cases, particularly in front of the test structure near its offshore face where the wave run-up height is a crucial measurement to be made. In these cases, only the OpenFOAM free-surface histories have been provided. The free-surface time histories recorded at the gauge locations along the flume for the unbroken and broken waves using the same 5 cm transverse cell size mesh are compared to empirical results for the k-ε model in Figures 7.13 and 7.14, the k-ω SST model in Figures 7.15 and 7.16, the Non-linear Realizable k-ε model in Figures 7.17 and 7.18, and the Launder-Reece-Rodi model in Figures 7.19 and 7.20.

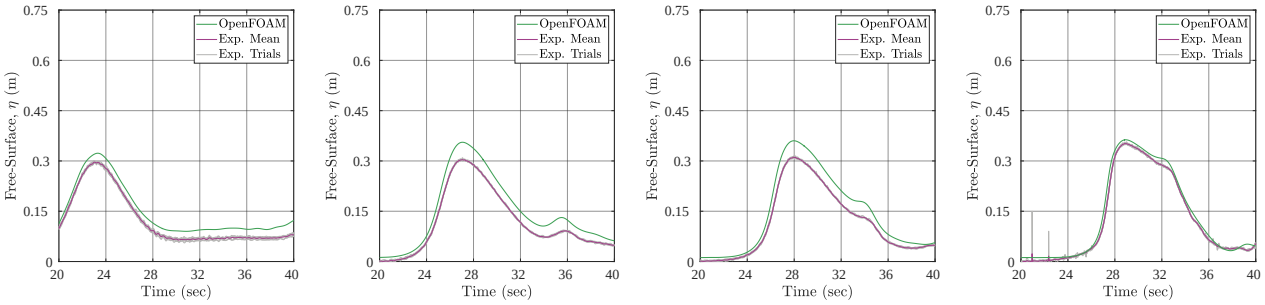

(a) *wg1* (b) *wg2* (c) *wg3* (d) *uswg1*

Figure 7.13: Unbroken Wave Free-Surface Elevation Time Histories of Wave Propagation along the Wave Flume for the Standard k-ε Model

For both wave types, the OpenFOAM numerically modeled free-surface histories matched the experimental results very well with small, consistent deviations of a slightly different nature for each wave type. For the unbroken wave, the experimental recordings of *wg1* and *uswg1* were matched closely for all turbulence models, but *wg2* and *wg3*, which were placed

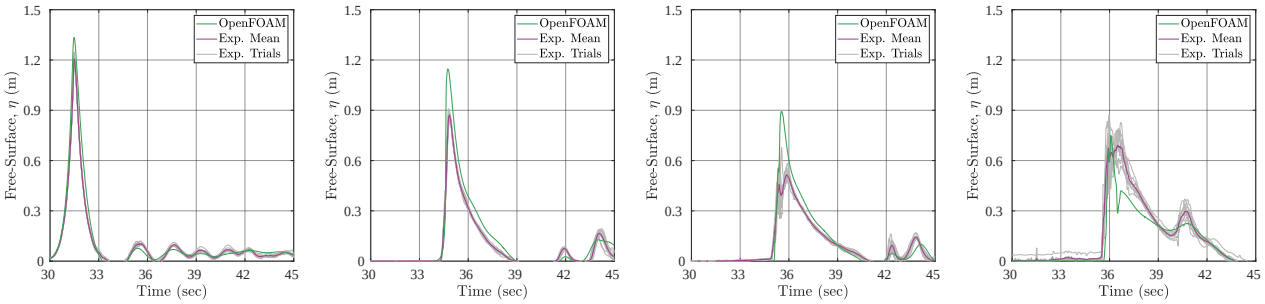

(a) *wg1* (b) *wg2* (c) *wg3* (d) *uswg1*

Figure 7.14: Broken Wave Free-Surface Elevation Time Histories of Wave Propagation along the Wave Flume for the Standard k-ε Model

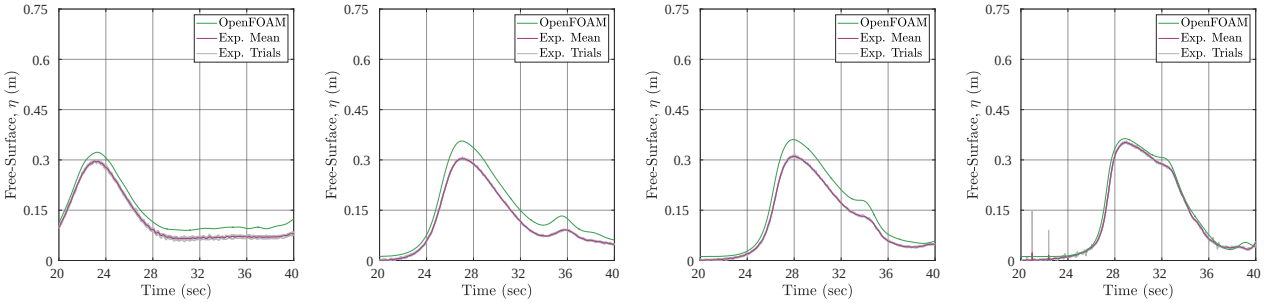

(a) *wg1* (b) *wg2* (c) *wg3* (d) *uswg1*

Figure 7.15: Unbroken Wave Free-Surface Elevation Time Histories of Wave Propagation along the Wave Flume for the k-ω SST Model

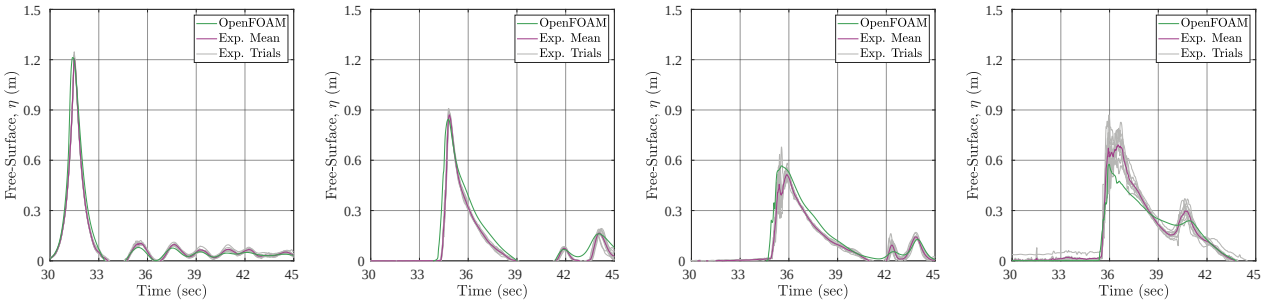

(a) *wg1* (b) *wg2* (c) *wg3* (d) *uswg1*

Figure 7.16: Broken Wave Free-Surface Elevation Time Histories of Wave Propagation along the Wave Flume for the k-ω SST Model

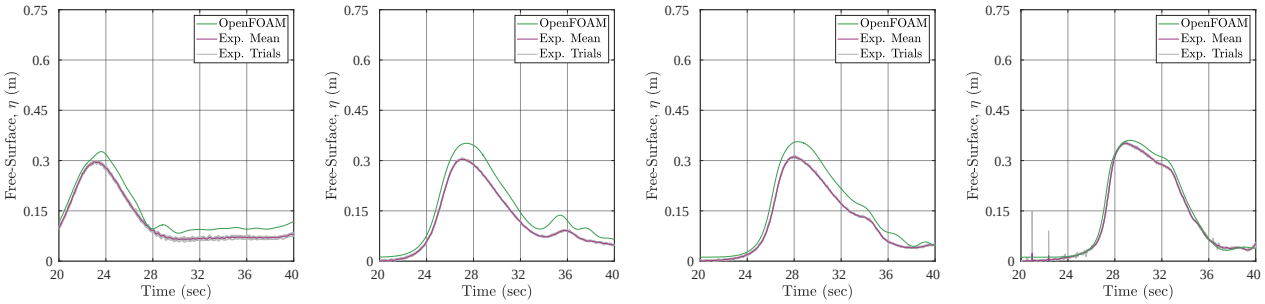

(a) *wg1* (b) *wg2* (c) *wg3* (d) *uswg1*

Figure 7.17: Unbroken Wave Free-Surface Elevation Time Histories of Wave Propagation along the Wave Flume for the Non-linear Realizable k-ε Model

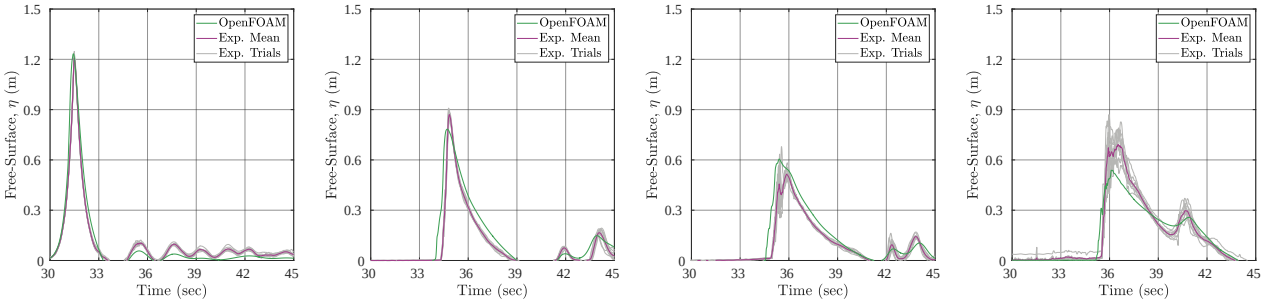

(a) *wg1* (b) *wg2* (c) *wg3* (d) *uswg1*

Figure 7.18: Broken Wave Free-Surface Elevation Time Histories of Wave Propagation along the Wave Flume for the Non-linear Realizable k-ε Model

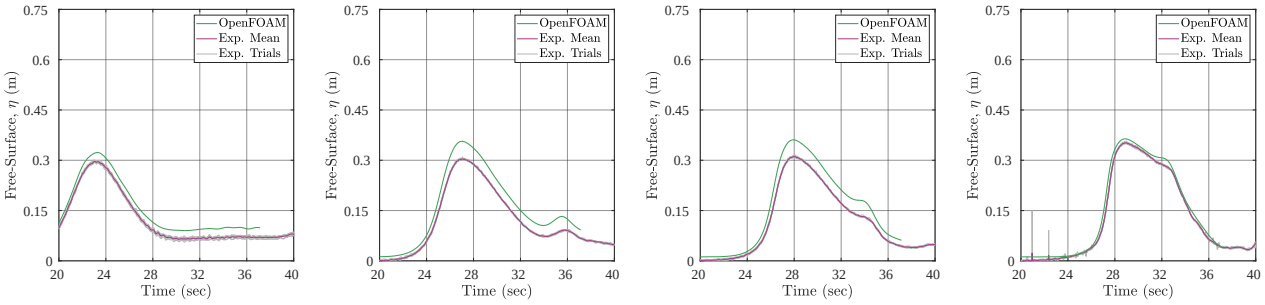

(a) *wg1* (b) *wg2* (c) *wg3* (d) *uswg1*

Figure 7.19: Unbroken Wave Free-Surface Elevation Time Histories of Wave Propagation along the Wave Flume for the Launder-Reece-Rodi Model

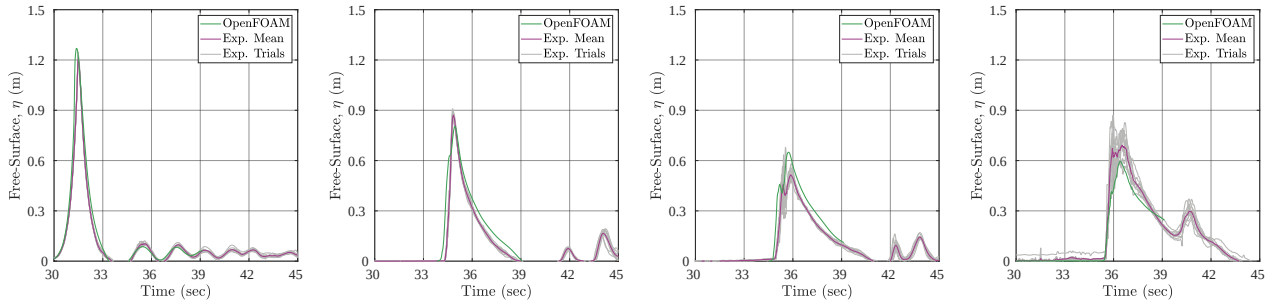

(a) *wg1* (b) *wg2* (c) *wg3* (d) *uswg1*

Figure 7.20: Broken Wave Free-Surface Elevation Time Histories of Wave Propagation along the Wave Flume for the Launder-Reece-Rodi Model

over the second 1:24 slope of the wave flume bottom, repeatedly gave over-predictions of the peak free-surface elevation for all turbulence models. Similarly, the OpenFOAM results for the broken wave consistently over-estimated of the peak free-surface elevation at *wg3*, but tended to under-estimate the peak free-surface elevation at *uswg1*.

These observations highlight the fact that the experimental free-surface elevation near the wavemaker was accurately reproduced by OpenFOAM simulations regardless of the wave type or turbulence model, but notable discrepancies arose far from the wavemaker along the sloped flume bottom, where wave shoaling took place during the experiments. In this region of the flume, the unbroken wave was steepening rapidly, whereas the broken wave was approaching a fully-formed bore-like condition. When trying to replicate these behaviors accurately in OpenFOAM, difficulties arise due to the fact that a distinct, discrete location of the free-surface is not a well-defined concept due to the reliance on the Volume-of-Fluid (VoF) method. To estimate the free-surface elevation using the VoF method, a volume fraction of $\alpha = 0.5$ is used as a target value to define the free-surface for the OpenFOAM free-surface recording function. In turbulent flow regions such as over the sloped flume bottom and near the test structure, swirling eddies and foamy splashes are smeared out unless the finite volume mesh cell size is refined small enough to fully resolve these behaviors at an appropriate scale. As was discussed in the OpenFOAM Mesh Generation section, the mesh used for all models was uniformly graded in the z-direction such that cell size decreased

from the global cell size of 10 cm at the atmosphere and flume bottom boundaries to 2.5 cm at the still water level and in the x-direction from the global cell size of 10 cm at the intersection of the 1:12 and 1:24 sloped flume bottom sections to 2.5 cm by the end of the 1:24 slope in order to better capture turbulent flow characteristics. However, the reduced cell size upstream of the test structure over the 1:24 sloped flume bottom may not have been sufficiently small enough to accurately capture significant, local fluctuations in the free-surface elevation for both wave types.

For the wave gauges located near the test structure, the free-surface time histories have been compared to empirical results for the k-ε model in Figures 7.21 and 7.22, the k-ω SST model in Figures 7.23 and 7.24, the Non-linear Realizable k-ε model in Figures 7.25 and 7.26, and the Launder-Reece-Rodi model in Figures 7.27 and 7.28. Focusing on the unbroken wave results, all of the turbulence models accurately reproduced the experimental free-surface elevation histories to the side of and behind the test structure (*uswg2* and *uswg4*-*uswg6*); however, they all failed to match the experimentally-measured peak run-up on the offshore face of the test structure. This is a curious result since a lesser run-up would correspond to a lesser hydrostatic pressure due to gravity, yet the pressures were consistently over-predicted by OpenFOAM instead of being under-predicted due to lesser run-up elevations.

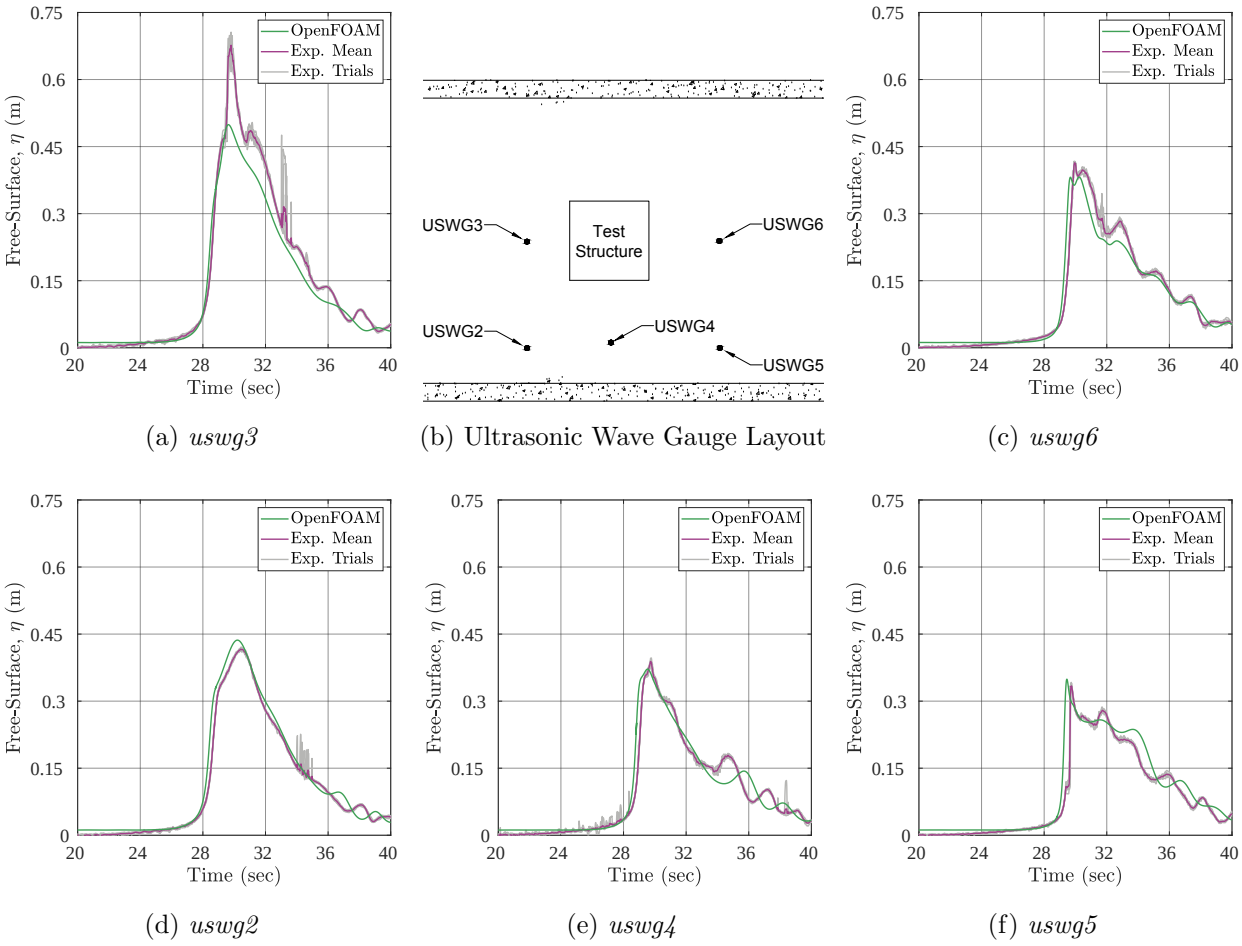

(a) *uswg3* (b) Ultrasonic Wave Gauge Layout (c) *uswg6*

(d) *uswg2* (e) *uswg4* (f) *uswg5*

Figure 7.21: Unbroken Wave Free-Surface Elevation Time Histories near the Test Structure for the Standard k-ε Model

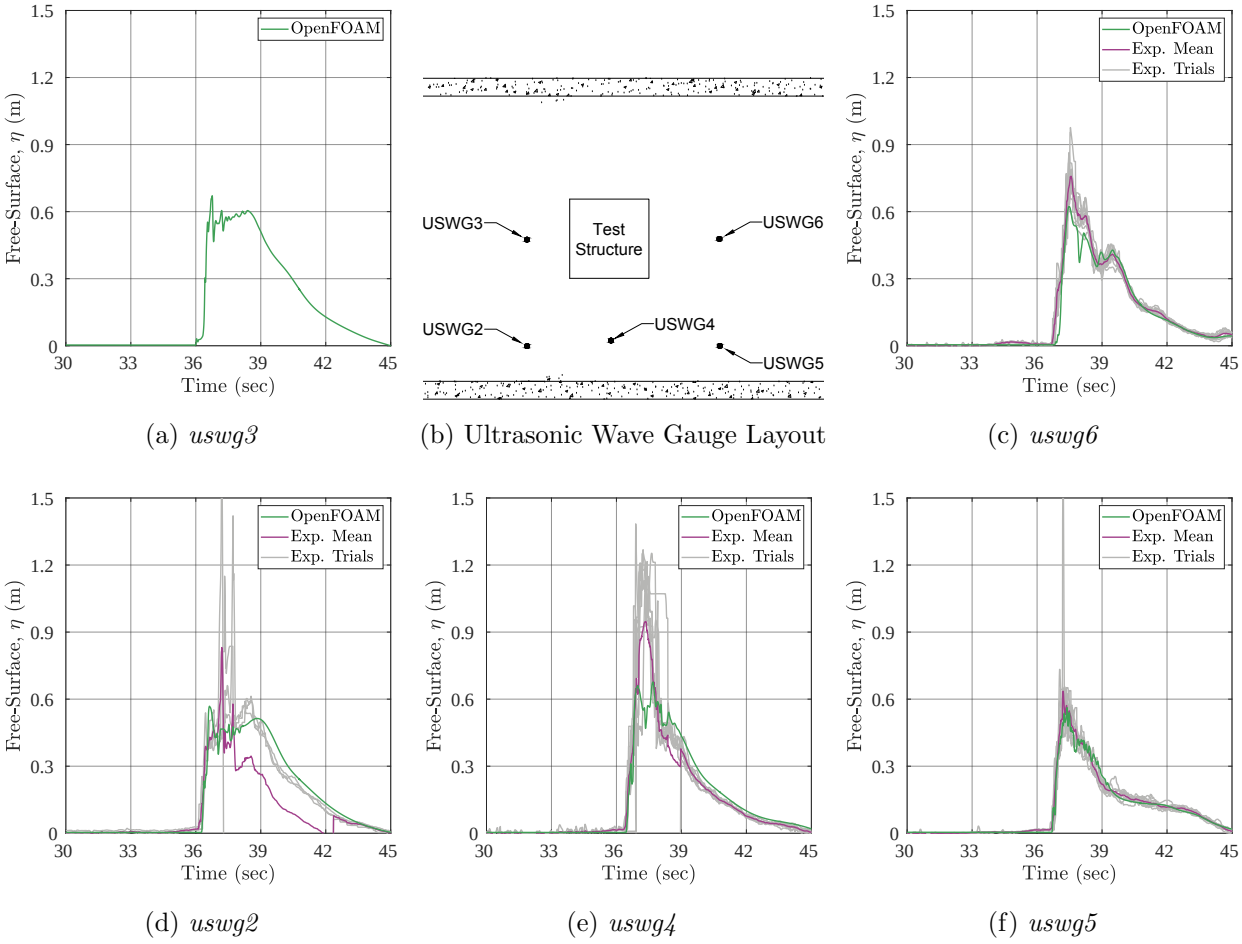

(a) *uswg3* (b) Ultrasonic Wave Gauge Layout (c) *uswg6*

(d) *uswg2* (e) *uswg4* (f) *uswg5*

Figure 7.22: Broken Wave Free-Surface Elevation Time Histories near the Test Structure for the Standard k-ε Model

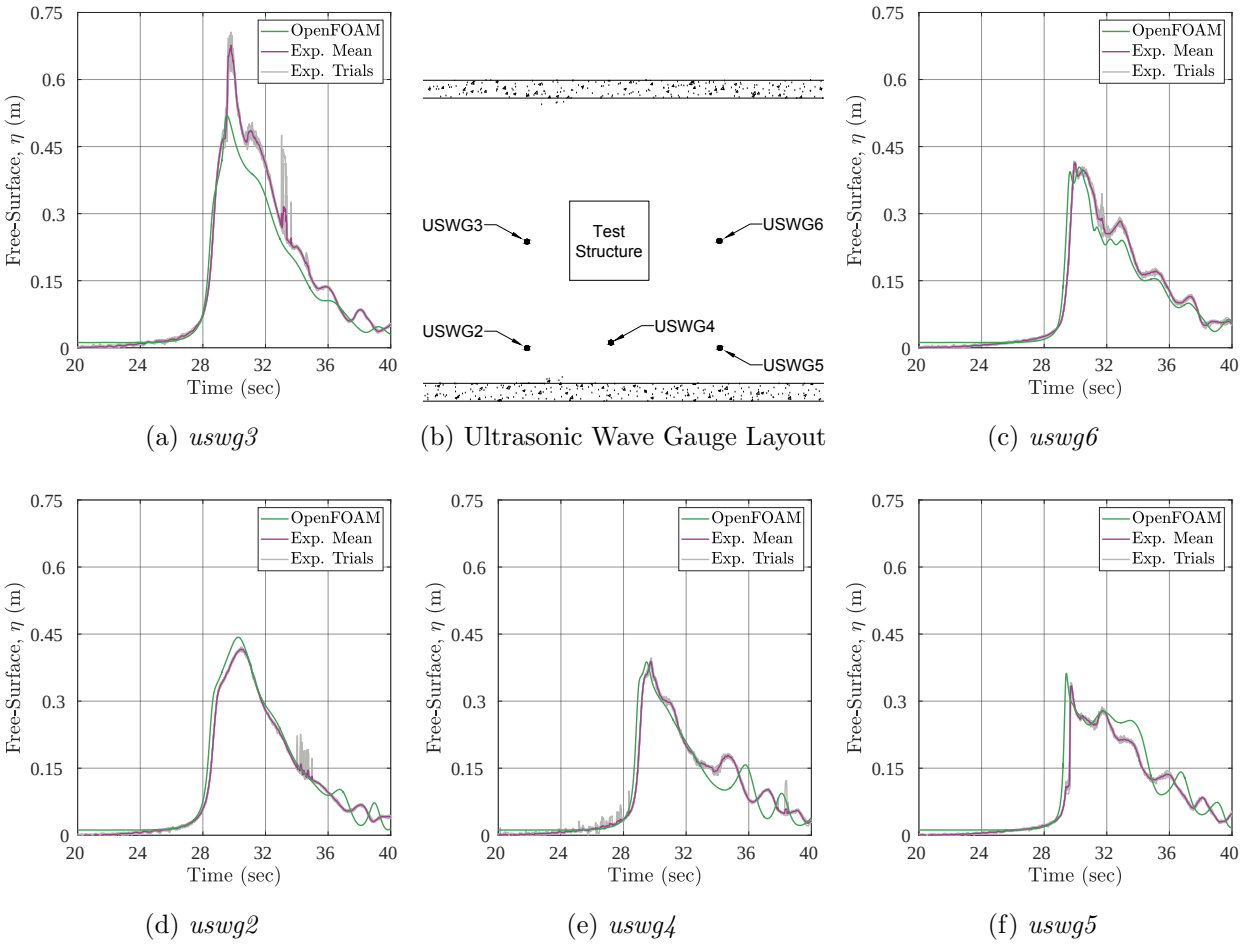

(a) *uswg3* (b) Ultrasonic Wave Gauge Layout (c) *uswg6*

(d) *uswg2* (e) *uswg4* (f) *uswg5*

Figure 7.23: Unbroken Wave Free-Surface Elevation Time Histories near the Test Structure for the k-ω SST Model

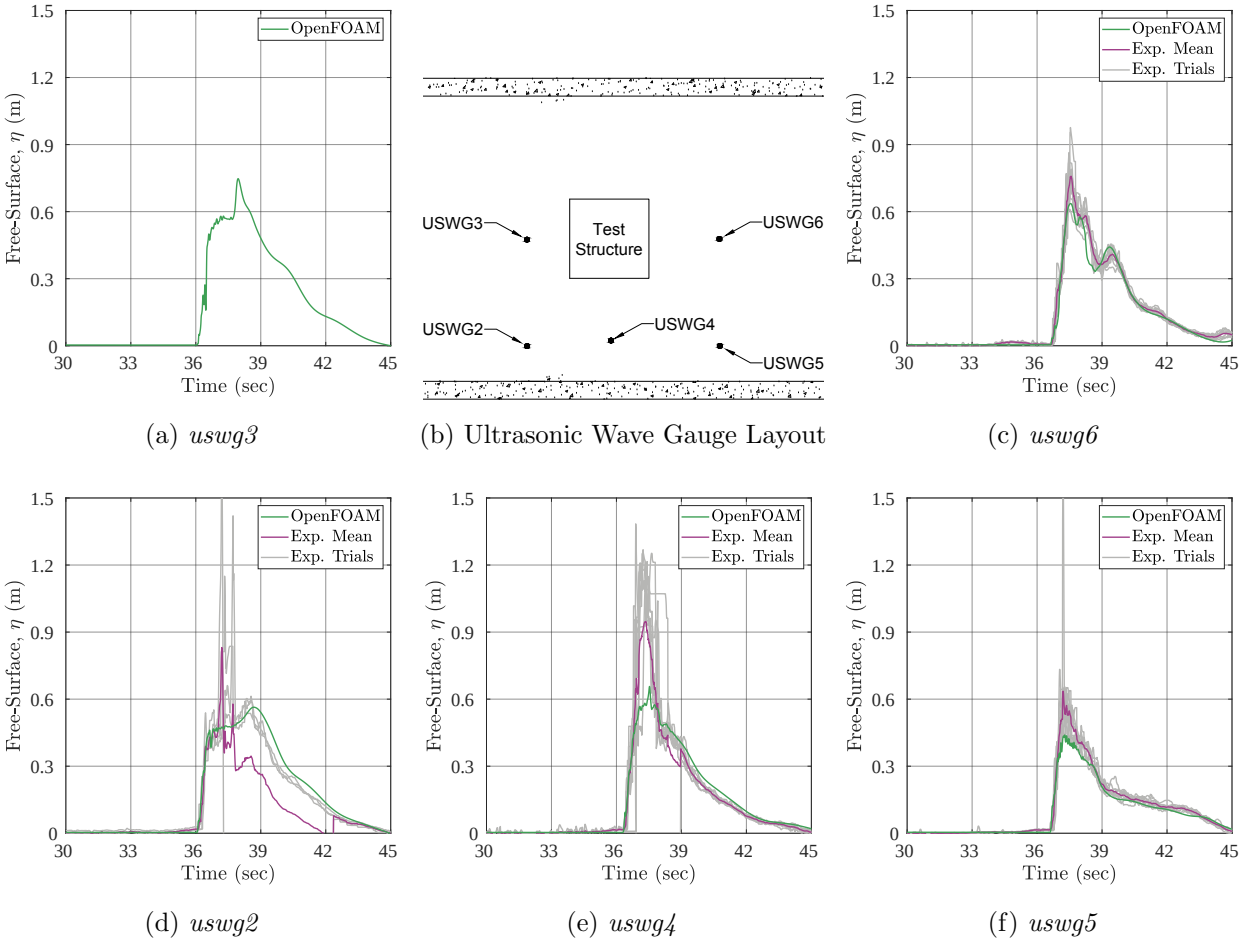

(a) *uswg3* (b) Ultrasonic Wave Gauge Layout (c) *uswg6*

(d) *uswg2* (e) *uswg4* (f) *uswg5*

Figure 7.24: Broken Wave Free-Surface Elevation Time Histories near the Test Structure for the k-ω SST Model

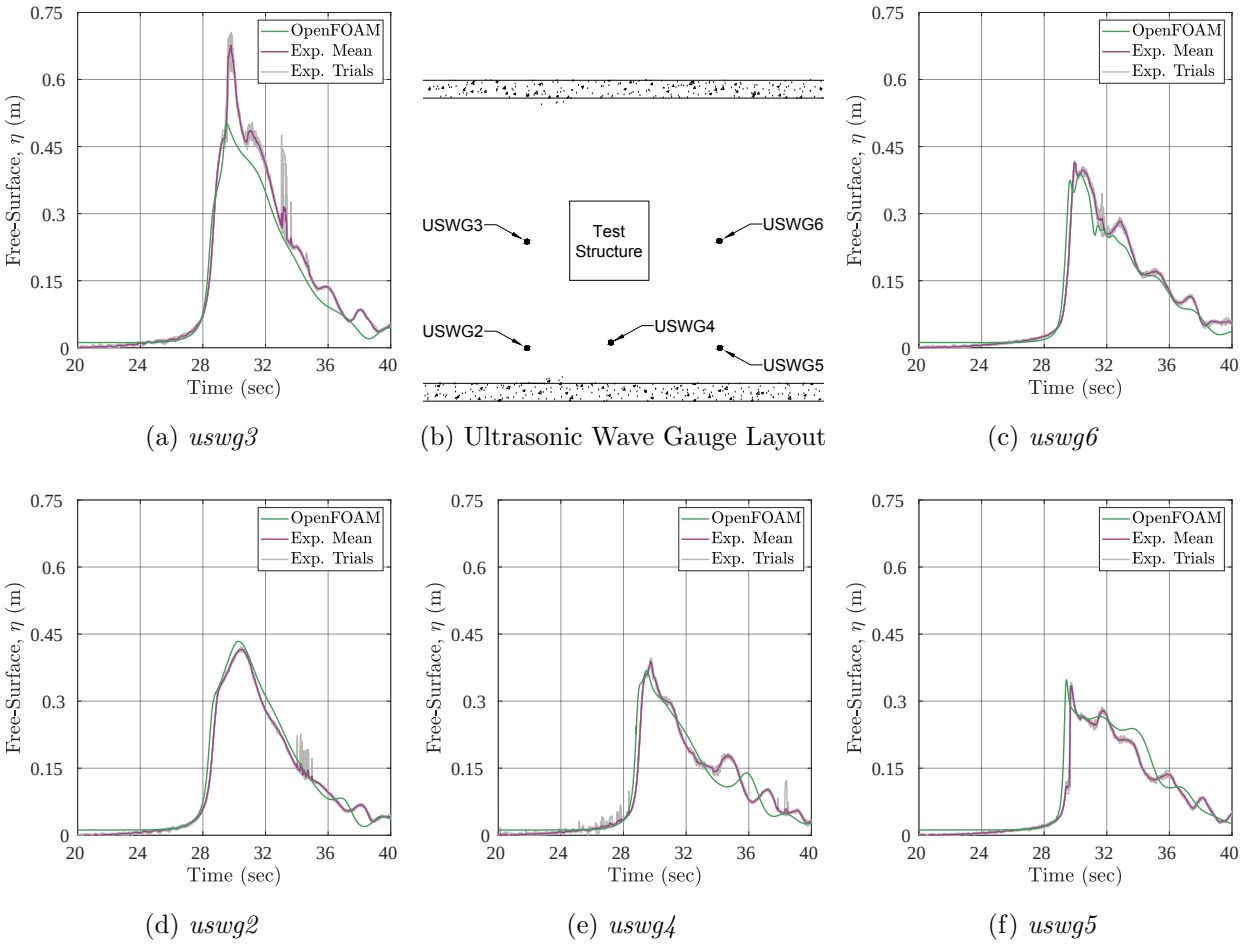

(a) *uswg3* (b) Ultrasonic Wave Gauge Layout (c) *uswg6*

(d) *uswg2* (e) *uswg4* (f) *uswg5*

Figure 7.25: Unbroken Wave Free-Surface Elevation Time Histories near the Test Structure for the Non-linear Realizable k-ε Model

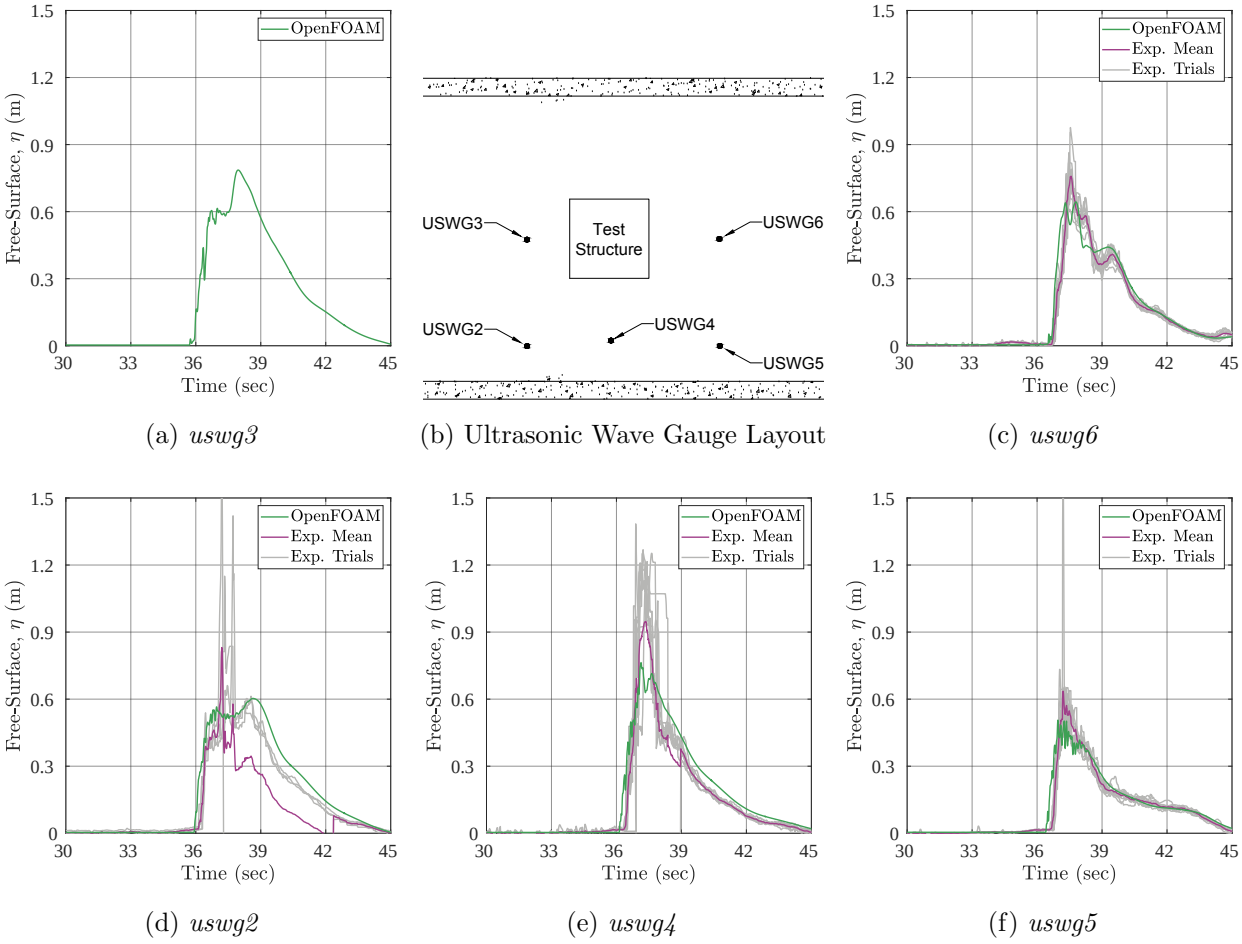

(a) *uswg3* (b) Ultrasonic Wave Gauge Layout (c) *uswg6*

(d) *uswg2* (e) *uswg4* (f) *uswg5*

Figure 7.26: Broken Wave Free-Surface Elevation Time Histories near the Test Structure for the Non-linear Realizable k-ε Model

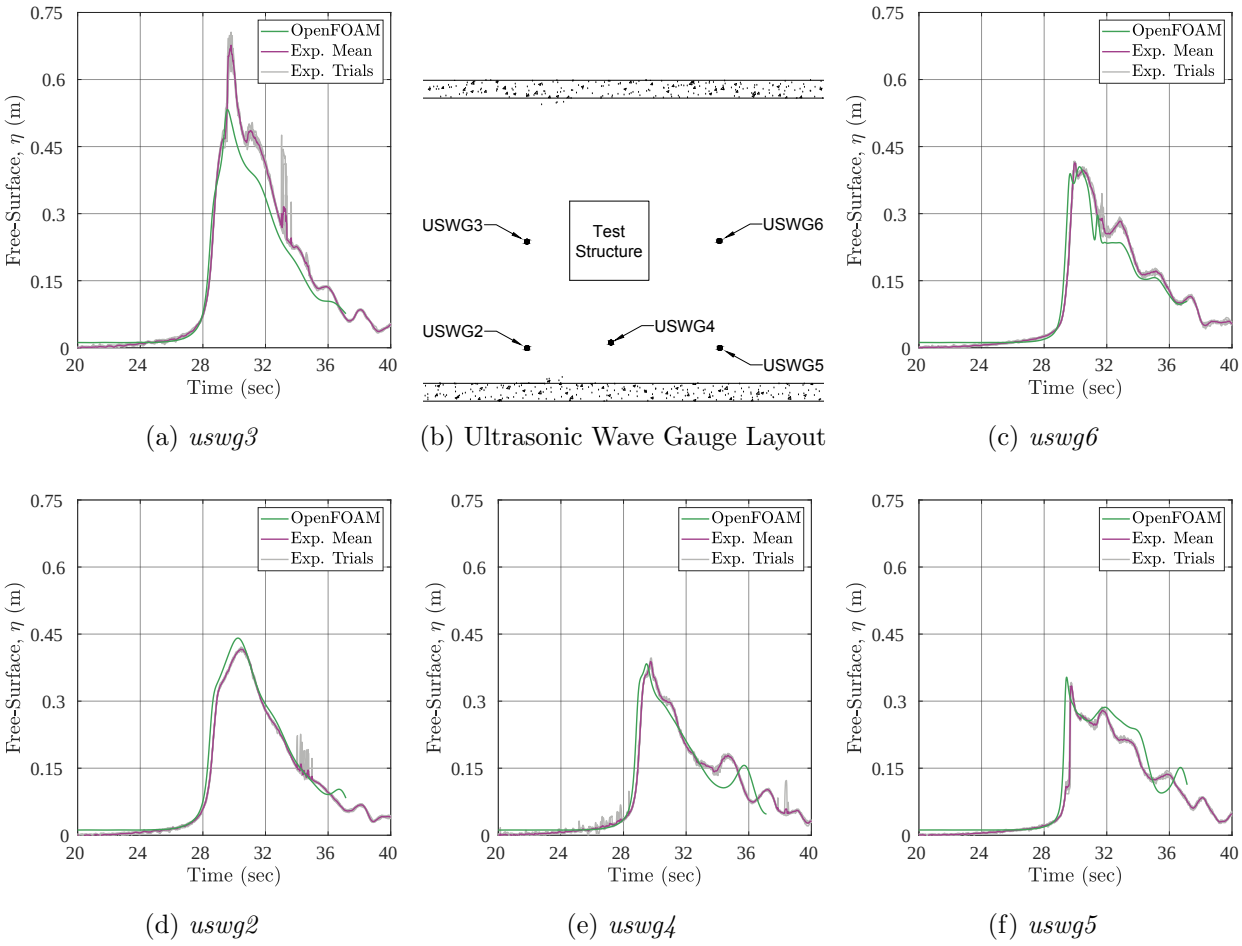

(a) *uswg3* (b) Ultrasonic Wave Gauge Layout (c) *uswg6*

(d) *uswg2* (e) *uswg4* (f) *uswg5*

Figure 7.27: Unbroken Wave Free-Surface Elevation Time Histories near the Test Structure for the Launder-Reece-Rodi Model

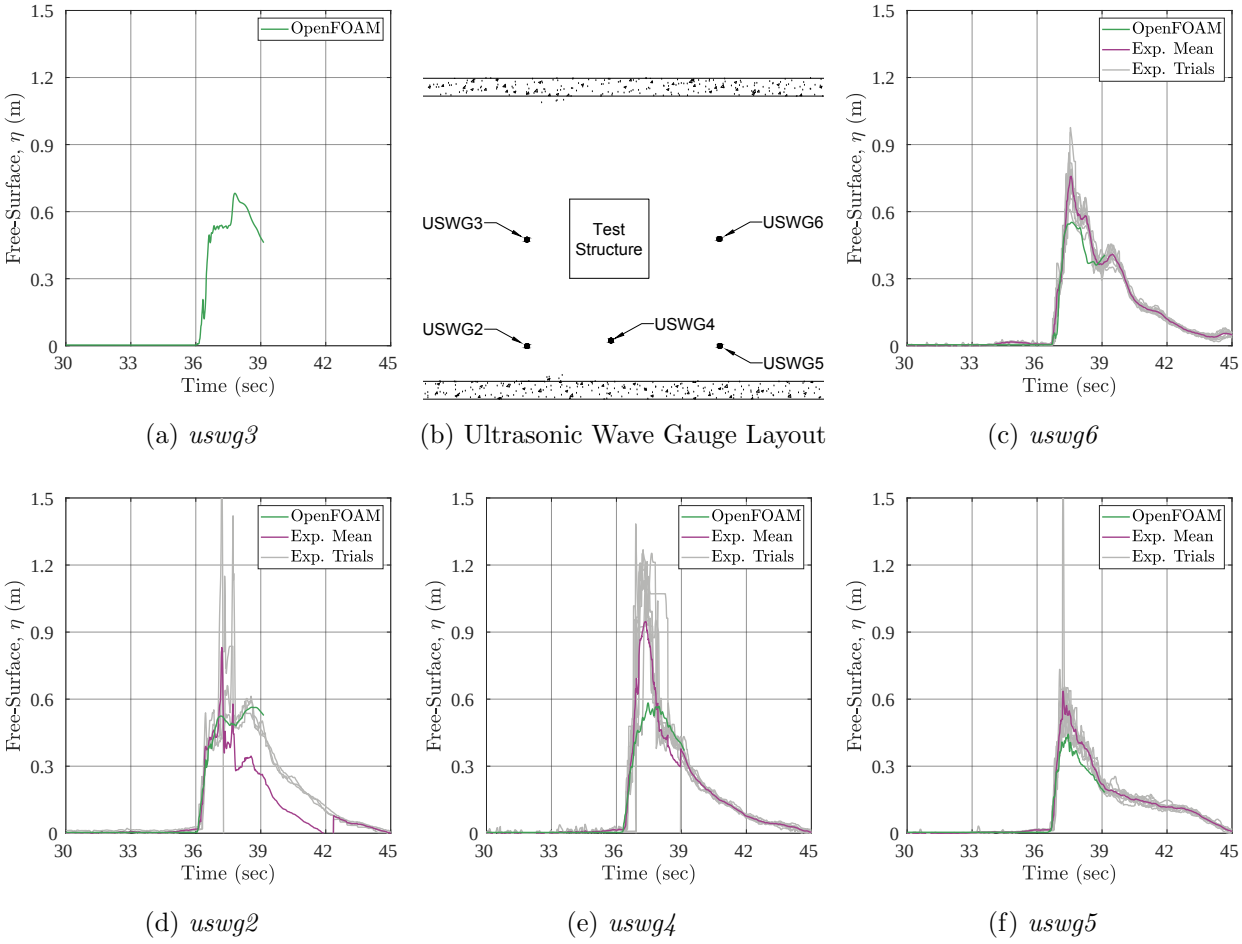

(a) *uswg3* (b) Ultrasonic Wave Gauge Layout (c) *uswg6*

(d) *uswg2* (e) *uswg4* (f) *uswg5*

Figure 7.28: Broken Wave Free-Surface Elevation Time Histories near the Test Structure for the Launder-Reece-Rodi Model

A similar assessment of the peak run-up on the offshore face of the test structure, was not possible for the broken wave due to the large, roughly 3 to 6 m high splashes that occurred during each broken wave test. The ultrasonic wave gauges to the side of the test structure (*uswg2*, *uswg4*, *uswg5*) experienced significant splashing as well, which resulted in erroneous peak free-surface values, but just before and after the peaks parts of the recordings were still physically realistic and useful for comparison to the OpenFOAM results for validation purposes. In particular, the post-peak broken wave free-surface elevations matched experimental data well for all turbulence models without significant variations from model

to model. However, the wave gauge placed behind the test structure was not affected by the broken wave impact splashing, which allowed it to accurately record the free-surface elevation there. The OpenFOAM simulations under-estimated these results to a similar degree with roughly 10% to 20% error in the peak free-surface elevation values for all of the turbulence models. Despite the issues with spurious measurements and minor under- and over-estimations of the peak free-surface values to the side of and behind the test structure, the OpenFOAM simulations for all four turbulence models resulted in excellent qualitative matches with the empirical data in terms of the time history shapes as well as quantitative matches in terms of the peak values except directly in front of the test structure.

7.2 Validation of Macroscale Roughness Cases

Based on the turbulence model study results, the k-ω SST model was selected for further validation of the cases with macroscale roughness elements (Cases B through F) due to its ability to accurately replicate the broken wave results. Additionally, only the broken wave will be considered hereafter due to its direct comparability to an overland tsunami inundation where turbulent, bore-like flows impact coastal regions as opposed to the unbroken wave, which is more representative of a tsunami that has not yet fully shoaled in an offshore region. Using the same finite volume mesh and turbulence model setup as was used for the reference case (Case A) validation, OpenFOAM simulations were run for each of the MRE configurations depicted in Figure 4.4, for which the streamwise force histories are shown in Figure 7.29.

For each MRE configuration, the OpenFOAM streamwise force histories lie mostly if not entirely within the range of experimental variability shown by the load cell trials, which were each plotted individually in addition to the mean load cell and integrated pressure time histories. In particular, Case D where the test structure was 100% shielded was initially under-predicted by OpenFOAM; however, the mean peak experimental value was reached part-way through the extended peak load duration for this case, resulting in an equally good match as for the other MRE configurations. Case F presented the only case with a notable

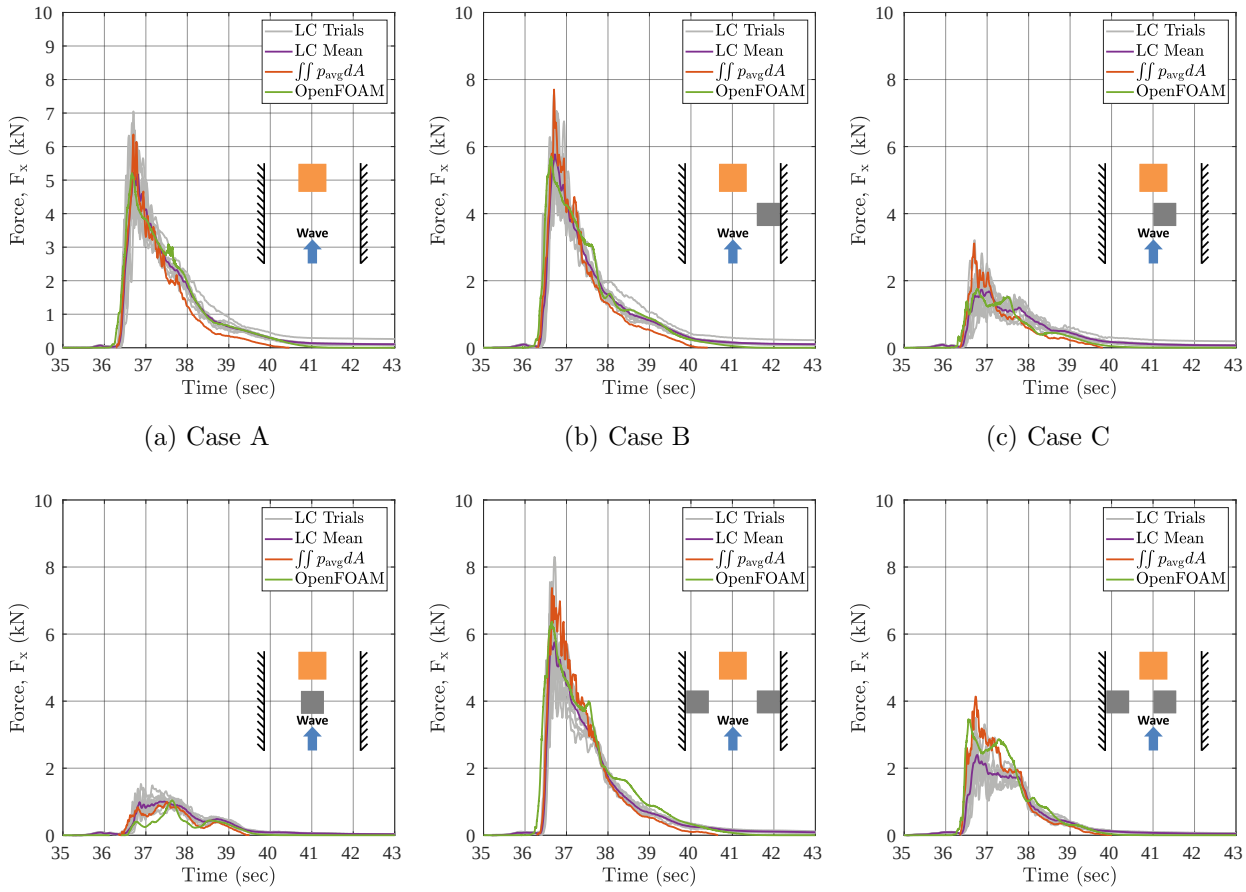

(a) Case A (b) Case B (c) Case C

(d) Case D (e) Case E (f) Case F

Figure 7.29: OpenFOAM Model Validation of Streamwise Force Histories Against Experimental Measurements for Macroscale Roughness Configurations A to F

over-estimation of the peak streamwise force relative to the mean load cell history; however, when compared to the load cell trial range of results as well as the integrated pressure time history, the OpenFOAM force history fits within the expected range of experimental variability, giving an acceptable validation result.

Chapter 8

FORCE-PREDICTION DESIGN EQUATION DEVELOPMENT

In order to achieve the goal of expanding upon the range of applicability of the design recommendations provided by ASCE 7-16 Chapter 6 for streamwise force amplification due to flow channeling effects, an extensive parametric study was conducted using the OpenFOAM model with the k-ω SST turbulence model, which was chosen for its exceptional performance in replicating the experimental streamwise force histories for all of the macroscale roughness element (MRE) configurations as was discussed in the Validation of Macroscale Roughness Cases section. The goal of this study was to generate a large dataset of peak streamwise force values using the validated OpenFOAM model in order to develop a force-prediction equation for a design structure surrounded by adjacent structures that function as MREs during a tsunami inundation. Using a single MRE, 187 total configurations were chosen to not only provide a large number of results near the test structure, but also to determine far-field results in order to ensure that the resulting design equation does not over or under-estimate the peak streamwise force when applied for structures separated by large distances.

8.1 Macro-Roughness Element Configurations

In order to define MRE coordinates for use in developing a streamwise force-prediction equation, the position of the MRE relative to the bottom, center of the offshore face of the test structure (in global coordinates, $(x, y) = (43.76, 0)$ m) was selected as the MRE coordinate origin as shown in Figure 8.1. A summary of the positions of the neighboring structures using this coordinate system for each of the one- and two-structure configurations has been provided in Table 8.1. With the development of a streamwise force-prediction design equation in mind, the terminology of neighboring structure (NS) for the MREs and design

structure (DS) for the test structure have been adopted. These structures were assumed to be square for the sake of simplicity and to match the experimental configurations, but the important dimensions for using the streamwise force-prediction model are the widths of the neighboring structures and design structure, D_{NS} and D_{DS}, respectively.

Table 8.1: Neighboring Structure (NS) Positions

Case #	x **[in]**	y **[in]**	W_F **[ft]**		**Case #**	x **[in]**	y **[in]**	W_F **[ft]**
000	N.A.	N.A.	12, 24		094	48	-64	12, 24
001	0	0	12, 24		095	48	-72	24
002	0	-8	12, 24		096	48	-80	24
003	0	-16	12, 24		097	48	-88	24
004	0	-24	12, 24		098	48	-96	24
005	0	-32	12, 24		099	48	-104	24
006	0	-40	12, 24		100	48	-112	24
007	0	-48	12, 24		101	48	-120	24
008	0	-56	12, 24		102	48	-128	24
009	0	-64	24		103	64	0	12, 24
010	0	-72	24		104	64	-8	12, 24
011	0	-80	24		105	64	-16	12, 24
012	0	-88	24		106	64	-24	12, 24
013	0	-96	24		107	64	-32	12, 24
014	0	-104	24		108	64	-40	12, 24
015	0	-112	24		109	64	-48	12, 24
016	0	-120	24		110	64	-56	12, 24
017	0	-128	24		111	64	-64	12, 24
018	8	0	12, 24		112	64	-72	24
019	8	-8	12, 24		113	64	-80	24

020	8	-16	12, 24		114	64	-88	24
021	8	-24	12, 24		115	64	-96	24
022	8	-32	12, 24		116	64	-104	24
023	8	-40	12, 24		117	64	-112	24
024	8	-48	12, 24		118	64	-120	24
025	8	-56	12, 24		119	64	-128	24
026	8	-64	12, 24		120	96	0	12, 24
027	8	-72	24		121	96	-8	12, 24
028	8	-80	24		122	96	-16	12, 24
029	8	-88	24		123	96	-24	12, 24
030	8	-96	24		124	96	-32	12, 24
031	8	-104	24		125	96	-40	12, 24
032	8	-112	24		126	96	-48	12, 24
033	8	-120	24		127	96	-56	12, 24
034	8	-128	24		128	96	-64	12, 24
035	16	0	12, 24		129	96	-72	24
036	16	-8	12, 24		130	96	-80	24
037	16	-16	12, 24		131	96	-88	24
038	16	-24	12, 24		132	96	-96	24
039	16	-32	12, 24		133	96	-104	24
040	16	-40	12, 24		134	96	-112	24
041	16	-48	12, 24		135	96	-120	24
042	16	-56	12, 24		136	96	-128	24
043	16	-64	12, 24		137	128	0	12, 24
044	16	-72	24		138	128	-8	12, 24

045	16	-80	24		139	128	-16	12, 24
046	16	-88	24		140	128	-24	12, 24
047	16	-96	24		141	128	-32	12, 24
048	16	-104	24		142	128	-40	12, 24
049	16	-112	24		143	128	-48	12, 24
050	16	-120	24		144	128	-56	12, 24
051	16	-128	24		145	128	-64	12, 24
052	24	0	12, 24		146	128	-72	24
053	24	-8	12, 24		147	128	-80	24
054	24	-16	12, 24		148	128	-88	24
055	24	-24	12, 24		149	128	-96	24
056	24	-32	12, 24		150	128	-104	24
057	24	-40	12, 24		151	128	-112	24
058	24	-48	12, 24		152	128	-120	24
059	24	-56	12, 24		153	128	-128	24
060	24	-64	12, 24		154	160	0	12, 24
061	24	-72	24		155	160	-8	12, 24
062	24	-80	24		156	160	-16	12, 24
063	24	-88	24		157	160	-24	12, 24
064	24	-96	24		158	160	-32	12, 24
065	24	-104	24		159	160	-40	12, 24
066	24	-112	24		160	160	-48	12, 24
067	24	-120	24		161	160	-56	12, 24
068	24	-128	24		162	160	-64	12, 24
069	32	0	12, 24		163	160	-72	24

070	32	-8	12, 24		164	160	-80	24
071	32	-16	12, 24		165	160	-88	24
072	32	-24	12, 24		166	160	-96	24
073	32	-32	12, 24		167	160	-104	24
074	32	-40	12, 24		168	160	-112	24
075	32	-48	12, 24		169	160	-120	24
076	32	-56	12, 24		170	160	-128	24
077	32	-64	12, 24		171	160	0	12, 24
078	32	-72	24		172	160	-8	12, 24
079	32	-80	24		173	160	-16	12, 24
080	32	-88	24		174	160	-24	12, 24
081	32	-96	24		175	160	-32	12, 24
082	32	-104	24		176	160	-40	12, 24
083	32	-112	24		177	160	-48	12, 24
084	32	-120	24		178	160	-56	12, 24
085	32	-128	24		179	160	-64	12, 24
086	48	0	12, 24		180	160	-72	24
087	48	-8	12, 24		181	160	-80	24
088	48	-16	12, 24		182	160	-88	24
089	48	-24	12, 24		183	160	-96	24
090	48	-32	12, 24		184	160	-104	24
091	48	-40	12, 24		185	160	-112	24
092	48	-48	12, 24		186	160	-120	24
093	48	-56	12, 24		187	160	-128	24

Furthermore, the idealized, triangular wake region shown behind the neighboring struc-

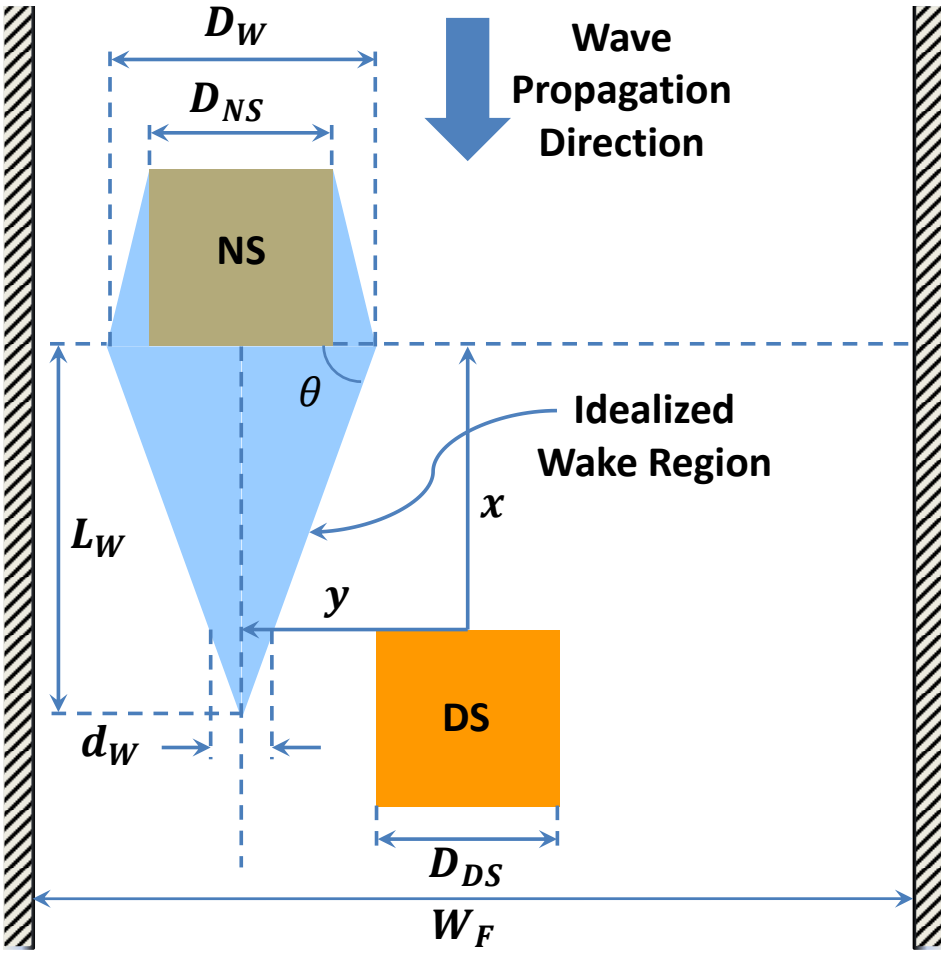

Figure 8.1: Streamwise Force-Prediction Equation Geometry Parameter Definitions

ture is a key element of the proposed force-prediction equation. The length and width of the wake at the onshore face of the neighboring structure, L_W and D_W, respectively, define the size of the neighboring structure wake for use in determining shielding effects. The idea behind this idealized wake is based upon recirculatory turbulent flow regions that form behind bluff bodies such as rectangular structures. The length and width of such wake regions vary depending on the flow velocity and size of the structures, which can be completely characterized by the Reynolds number of the flow. However, for the results presented in this dissertation, the broken wave alone was used as an initial wave condition, which would result in similar velocities for each of the neighboring structure configurations, and the neighboring and design structure sizes were kept fixed. This allowed for the development of a streamwise

force-prediction model with a uniform wake size; although, to make the model generally applicable, additional parametric studies of neighboring structure locations using a wide range of initial wave conditions would need to be modeled.

8.2 Streamwise Force-Prediction Equation

To develop a streamwise force-prediction equation, three phenomenological factors were developed, the product of which would give the normalized maximum streamwise force. Each of these factors was designed to characterize a specific physical phenomenon of the broken wave interaction with neighboring structures and the design structure. The factors were also designed to rely entirely upon the geometry defined in Figure 7.29, which reduced the problem of model calibration down to determining the two unknown wake size dimensions, L_{W} and D_{W}.

8.2.1 Momentum Factor

The first of these factors was dubbed the momentum factor, F_{M}, which is intended to model wave momentum loss due to wave impacts on neighboring structures. When a turbulent, bore-like wave suddenly strikes a fixed object, large, noisy splashes and flow redirection dissipate significant proportions of wave energy. This behavior was observed during the broken wave tests conducted in the Large Wave Flume at the HWRL, where the broken wave resulted in 3 to 6 m high splashes on both the test structure and concrete blocks used to model neighboring structures. To account for such losses, the ratio of the neighboring structure width, D_{NS}, to the flume width, W_{F}, was defined as the lost proportion of wave momentum. Subtracting this ratio from 1 gives the momentum factor as shown in Equation 8.1, which defines the remaining wave momentum that can be transferred to the design structure.

$$F_{\mathrm{M}} = 1 - \frac{D_{\mathrm{NS}}}{W_{\mathrm{F}}} \tag{8.1}$$

8.2.2 Shielding Factor

Using a similar approach, the shielding factor, F_S, was derived to define the reduction in the streamwise tsunami force on the design structure due to redirection of an inundation flow caused by neighboring structures. Again, a ratio of a flow obstruction width to the flume width was used to define this factor. Particularly, the ratio of the overlap width of the neighboring structure's wake with the design structure's offshore face, D_O, to the flume width W_F was established as the force reduction ratio due to shielding effects. The remaining proportion of the design structure streamwise force is then defined by Equation 8.2.

$$F_S = 1 - \frac{D_O}{D_{DS}} \tag{8.2}$$

The overlap width D_O as defined by Equation 8.5 captures the interaction of the neighboring structure's assumed triangular wake. This is achieved by first determining the wake width at the same streamwise location as the offshore face of the design structure, which is denoted as d_W. The determination this local wake width at the design structure location requires first calculating the wake angle as defined by Equation 8.3, which is used along with the neighboring structure position x and maximum wake width D_W in Equation 8.4 to calculate the local wake length, d_W. The local wake width must be a strictly positive quantity since a negative wake width does not make physical sense and as such $d_W \geq 0$ must be satisfied. Furthermore, the neighboring structure position, x, must also be ≥ 0 since the parametric study did not extend to $x < 0$.

$$\theta = \tan^{-1}\left(\frac{2L_W}{D_W}\right) \tag{8.3}$$

$$d_W = D_W\big(1 + \cot(\theta)\big) - 2x\cot(\theta) \geq 0 \qquad \text{for } x \geq 0 \tag{8.4}$$

$$D_O = \max\Big(0, \min\Big(y + \frac{d_W}{2}, \frac{D_{DS}}{2}\Big) - \max\Big(y - \frac{d_W}{2}, -\frac{D_{DS}}{2}\Big)\Big) \tag{8.5}$$

8.2.3 Channeling Factor

Whereas both the momentum and shielding factors result in streamwise force reductions for a design structure, the flow channeling factor, F_C, amplifies the reference case (Case A) streamwise force acting on a design structure. This factor attempts to capture Venturi-type effects, where flow constrictions result in locally-increased flow velocities, which result in increase dynamic pressures applied to a design structure. Assuming that the inundation flow depth remains roughly constant in flow constriction regions, the only flow area variations that can occur are in terms of the channel width in the transverse or alongshore direction. Using mass conservation principles for a steady flow, where for a constant density flow the product of the flow area and flow velocity must be equivalent from point-to-point along the flume, the ratio of the unobstructed flow area to the constricted flow area defines the flow channeling factor, F_C. However, since the depth of the flow was assumed constant it cancels out in the area ratio, leaving F_C to be defined only as the ratio of the unobstructed flume width, W_F, to the constricted flume width, $W_F - d_W$, as defined by Equation 8.6. Here the neighboring structure wake width was used to determine the constricted wake width since flow velocities are drastically reduced in wake regions in addition to the fact that the flow is redirected in a circulatory manner in wake regions.

$$F_C = \frac{W_F}{W_F - d_W} \tag{8.6}$$

8.2.4 Normalized Force Ratio

Using these three factors, the combined result of each effect is then determined by computing the product of the three factors, which is defined as the streamwise force ratio, F_X, as shown in Equation 8.7. The resulting equation produces force ratios that tend to F_M when the streamwise separation of the neighboring structure and design struture is large. On the contrary, when the streamwise separation x and the transverse offset distance y of the neighboring structure tend to zero, the design structure force ratio also tends to zero,

providing the neighboring structure's maximum wake width is equivalent to or larger than the design structures width. If the neighboring structure maximum wake width is smaller than the design structure width, then the streamwise force ratio for the design structure cannot reach zero since it will not be fully obstructed. Thus the model is capable of modeling the behaviors it was intended to capture, producing zero force for a perfect overlap while remaining bounded for infinite distance between the structures.

$$F_X = F_M F_S F_C = \left(1 - \frac{D_{NS}}{W_F}\right)\left(1 - \frac{D_O}{D_{DS}}\right)\left(\frac{W_F}{W_F - d_W}\right) \tag{8.7}$$

8.3 Neighboring Structure Wake Size Calibration

Even though the streamwise force factors accounting for the effects of neighboring structures in terms of wave momentum losses, shielding, and flow channeling have been defined, they cannot be calculated without determining an appropriate measure to define the wake size. To produce wake size parameters that are generally applicable, normalized values of the wake length and width were established, which could then be calibrated using the OpenFOAM parametric study results. Due to the neighboring structure being the source of the wake, the neighboring structure width was used to define the normalized wake size as the wake width and wake length ratios, $R_W = D_W/D_{NS}$ and $R_L = L_W/D_{NS}$, respectively.

In order to determine suitable values for the wake size ratios, a least squares type of method was used to minimize the sum of the normalized force ratio errors between the OpenFOAM values and the values predicted by the force ratio equation, F_M. The error minimization was completed separately for the original flume width cases (i.e. $W_F = 3.6576$ m) and for the doubled width cases listed in Table 8.1, the results of which are shown in Figure 8.2. The minimum points shown on each of the sum of squared errors surfaces as red dots represent the optimum wake width and length ratio combinations, (R_W, R_L), for the original and doubled flume width OpenFOAM data sets, which are (1.27,3.93) and (1.08,5.40), respectively.

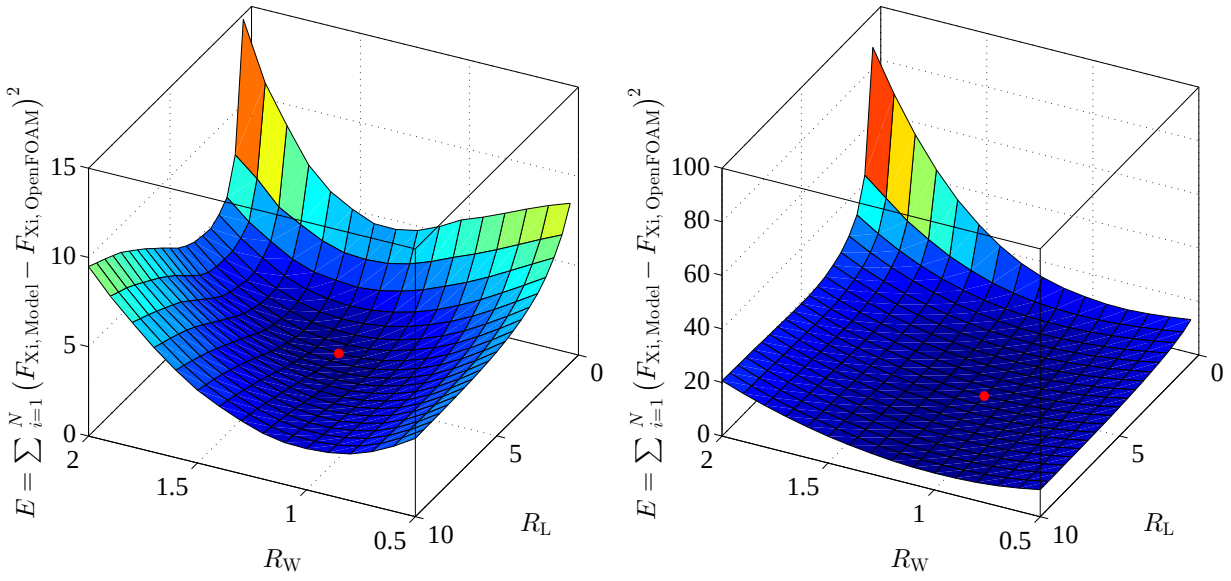

(a) Original Flume Width

(b) Doubled Flume Width

Figure 8.2: Wake Size Optimization in Terms of Minimization of the Sum of Squared Errors between OpenFOAM and Equation 8.7 Results

The optimum wake width ratios for the original and doubled flume are relatively close with a roughly 15% decrease in wake width from the original to the doubled flume width results. However, the wake length ratio increased by over 37% from the original flume width case to the doubled flume width case. Using each set of wake size parameters individually to plot and compare the predicted force ratios versus the OpenFOAM data sets, the results of which are shown in Figures 8.3 and 8.4 for the original and doubled flume width cases, respectively, it may be observed that the OpenFOAM force results tended toward roughly constant values near the flume walls, which were less than the peak force ratios by about 20%. This difference in results as well as the large quantity of results near the flume walls with lesser values than the max value tend to skew the doubled flume width results towards wake size values that are not as representative of strong flow interactions between the neighboring structure and the design structure, but rather are more representative of flows around a single rectangular body.

To make a compromise between these results, a universal set of wake size ratios was

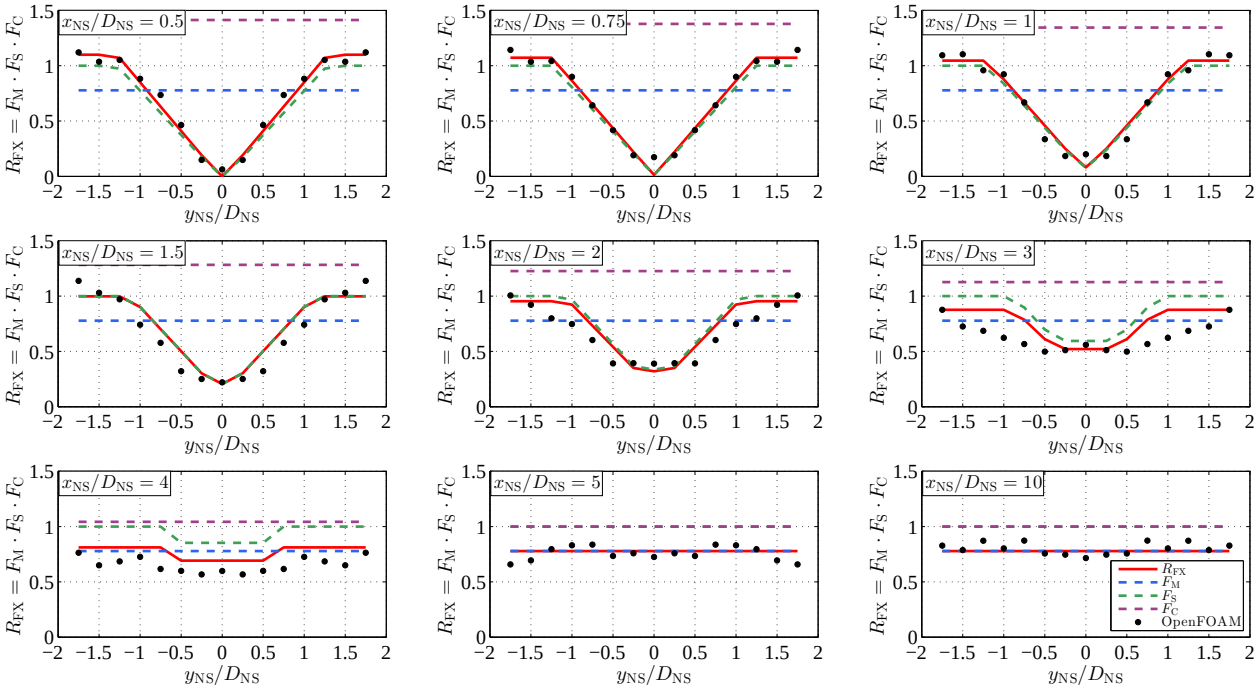

Figure 8.3: Spatial Variation of the Normalized Force Ratio with Force Factors for the Original Flume Width using Optimal Wake Size Ratios $(R_W, R_L) = (1.27, 3.93)$

selected as (1.2,5). The results for each flume width are shown in Figures 8.5 and 8.6, which demonstrate a strong agreement between the normalized force ratio predictions and the OpenFOAM parametric study data sets. The choice of a generalized wake size that gives accurate force predictions with and without nearby flume walls allows for significant variations in flume width to be accounted for by the model.

However, one must approach the use of Equation 8.7 with caution for large flume widths since F_X tends to 1 as W_F increases without bound. To avoid under-predicting the force ratio in situations where flow channeling effects ought to occur for one or more neighboring structures even though flume walls in the form of other structures or topographical features are not in close proximity to the design structure, it is recommended to impose a flume width limit of $W_F \leq 10D_{NS}$. This limit roughly corresponds to the doubled flume width cases, where notable flow channeling on the same order of magnitude as that of the original flume width cases still occurred despite the fact that the flume walls were moved much farther

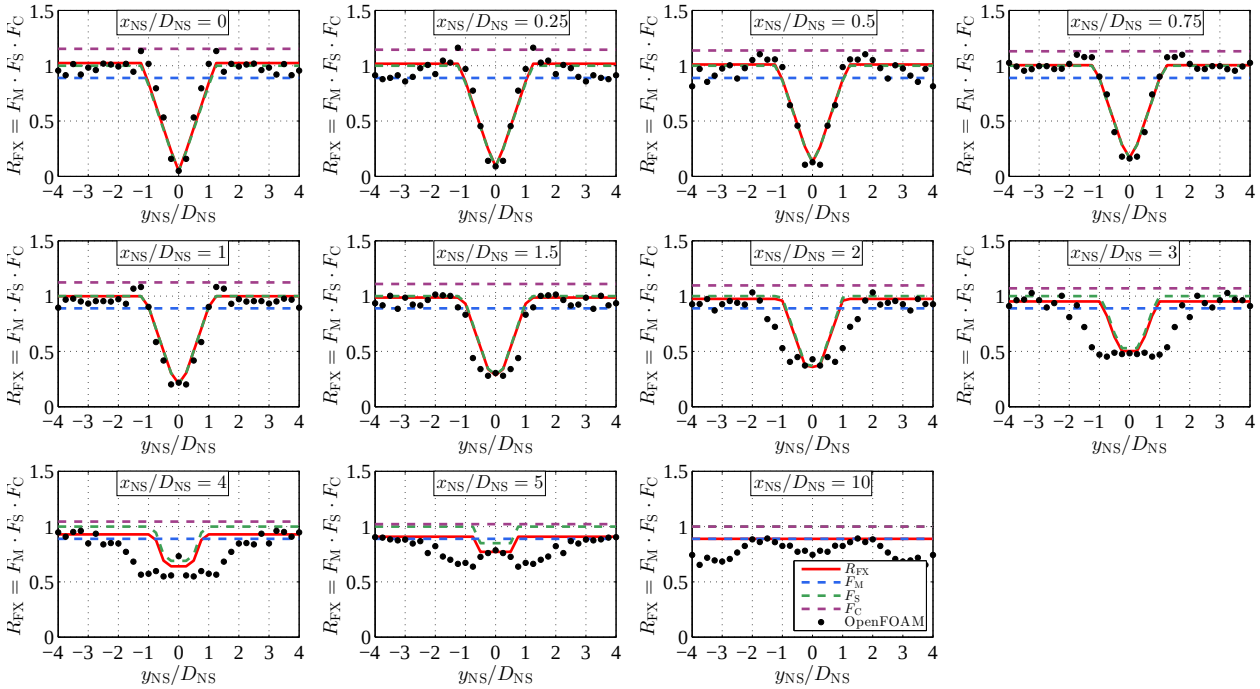

Figure 8.4: Spatial Variation of the Normalized Force Ratio with Force Factors for the Doubled Flume Width using Optimal Wake Size Ratios $(R_W, R_L) = (1.08, 5.40)$

away from the design structure.

8.4 Physical Justification for Fixed Wake Size Ratio

The assumptions made to determine the normalized streamwise force ratio equation, F_X, were in some ways gross simplifications of the flow characteristics. For instance, the assumption that the flow depth remains constant from the unobstructed flume width, W_F, to the constricted flume width, $W_F - d_W$, is a bold claim since significant free-surface elevation changes were observed for the broken wave simulations as was discussed in the Free-Surface Elevations section of the numerical model validation chapter. In order to provide some theoretical, physical justification of the proposed model using a fixed wake size, an investigation was made into the dependence of wakes behind rectangular structures on the Reynolds number of the flow, Re, as defined by Equation 8.8. Here u_1 is the x-direction free-stream or unaffected flow velocity offshore of the neighboring structure, D_{NS} is the neighboring

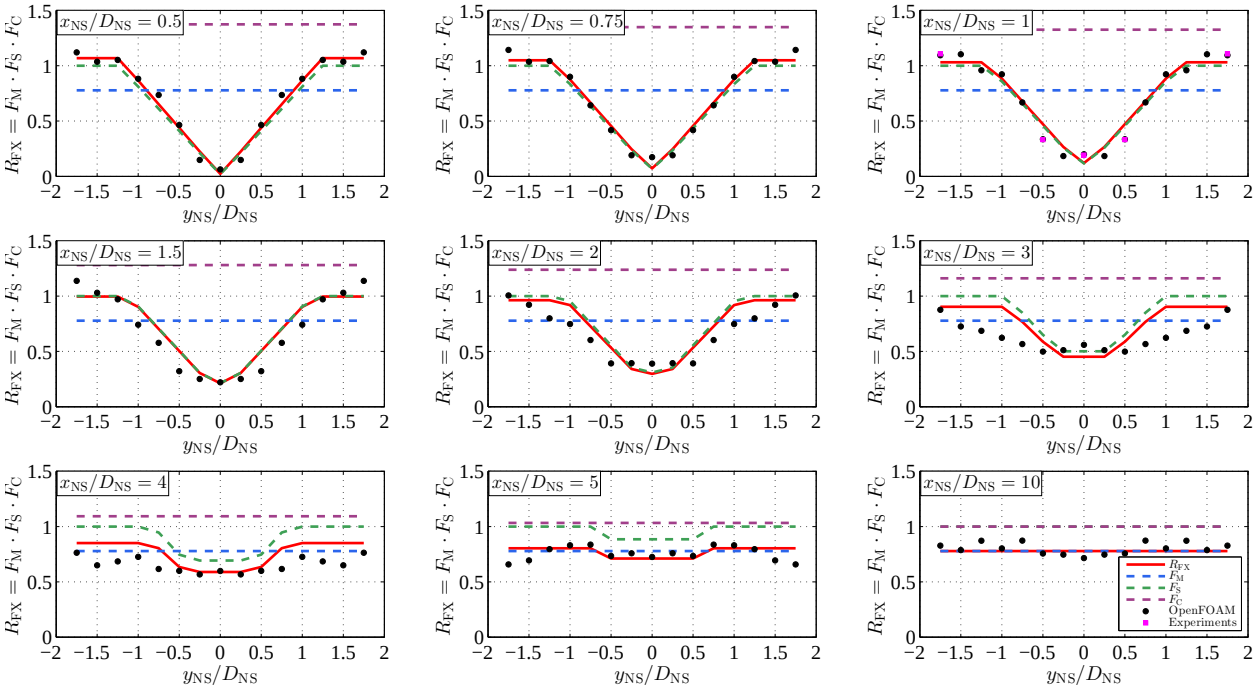

Figure 8.5: Spatial Variation of the Normalized Force Ratio with Force Factors for the Original Flume Width using the Universal Wake Size Ratios $(R_W, R_L) = (1.2, 5.0)$

structure width, and ν is the kinematic viscosity of water.

$$Re = \frac{u_1 D_{NS}}{\nu} \tag{8.8}$$

The study of Bai and Alam (2018) provides an excellent example of a thorough study focusing on flows around rectangular bodies, which also provides piece-wise equations defining the relationship between the wake size and the Reynolds number of the flow. Bai and Alam (2018) characterize the wake length behavior as either steady, where purely recirculatory flow occurs behind the structure, or unsteady, where the degree of turbulent behavior increases with Reynolds number. In addition to providing wake length data, Bai and Alam (2018) also provide curve fit equations of both experimental and numerical data as shown in Figure 8.7. Similarly, wake width curve fit equations were provided along with the corresponding data as shown in Figure 8.8.

For the neighboring structure size used during the experiments, $D_{NS} = 0.8128$ m, an ap-

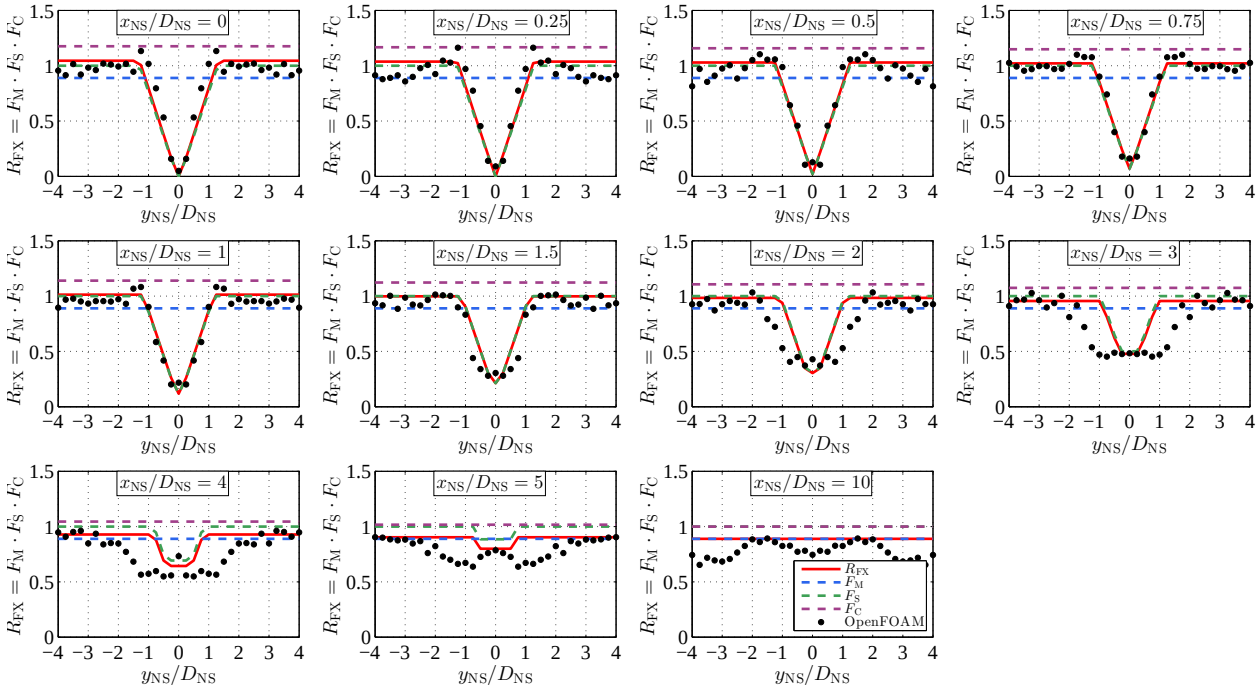

Figure 8.6: Spatial Variation of the Normalized Force Ratio with Force Factors for the Doubled Flume Width using the Universal Wake Size Ratios $(R_W, R_L) = (1.2, 5.0)$

proximate flow velocity of $u_1 = 2$ m/s for the broken wave offshore of the neighboring structure, and the kinematic viscosity of water, which is $8.9(10^{-4})$ Pa $\cdot$ s, the resulting Reynolds number of 1,625,600 gives wake length and width ratios of 1.28 and 1.41, respectively, using the equations of Bai and Alam (2018). The wake width ratio determined using the Reynolds number-based equations matches the optimum value determined using the OpenFOAM parametric study data for the original flume width remarkably well. On the contrary, the wake length is drastically under-estimated by the *Re*-based equations. A comparison of the normalized force ratios calculated using *Re*-based wake size ratios to those determined using the chosen universal wake size ratios for the original flume width is provided in Figure 8.9.

Due to the significantly shorter wake length, the normalized force ratios calculated using the *Re*-based wake size ratios tended to F_M very rapidly with streamwise increasing distance between the neighboring and design structures. However, at a distance of one neighboring structure width or less between the structures, the *Re*-based model force ratios match the

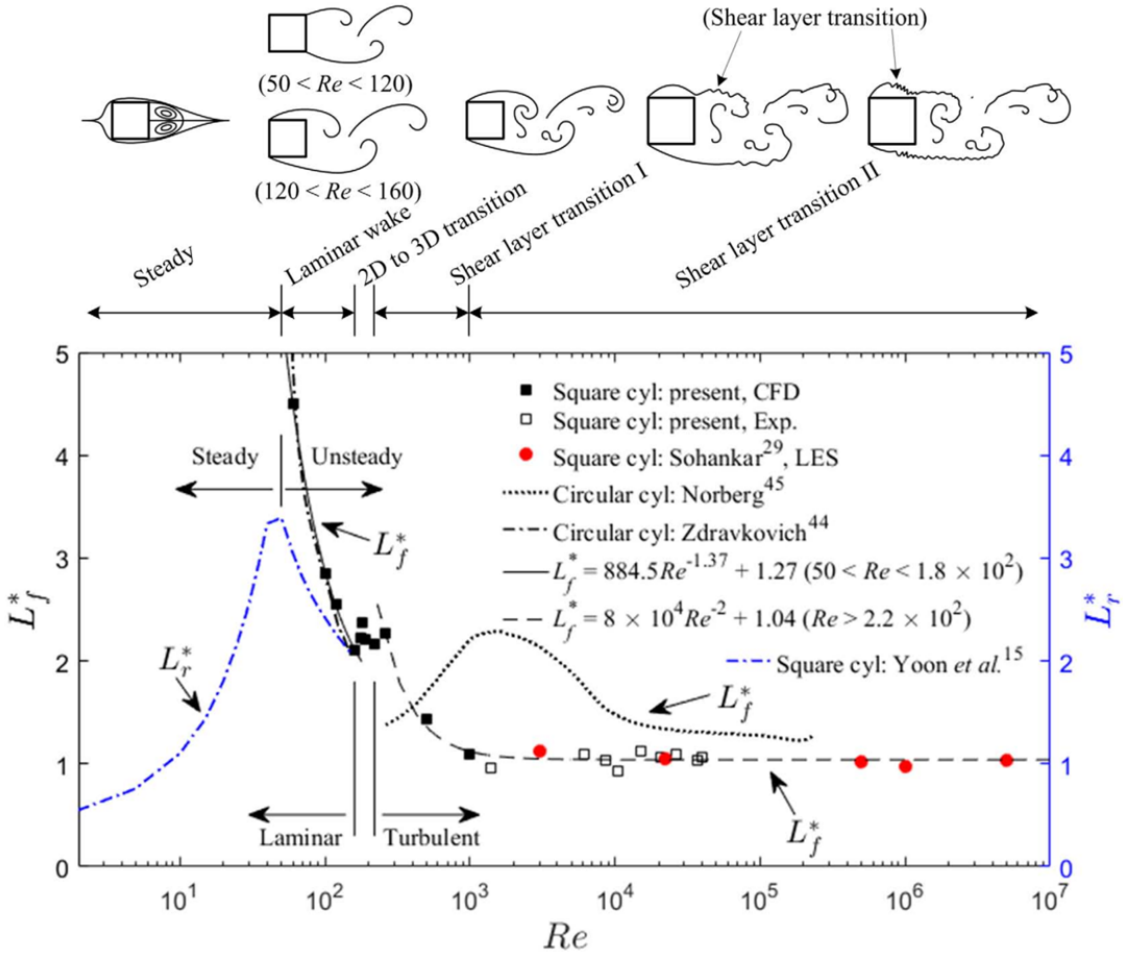

Figure 8.7: Wake Length as a Function of Reynolds Number (Bai and Alam, 2018)

OpenFOAM parametric study data well. The strong agreement in wake width demonstrates that the wake size determined using the OpenFOAM parametric study data provides a realistic estimate that can be backed up by other experimental and numerical data using known relations based on the flow Reynolds number. However, the significant differences in the two flow types led to drastically different wake lengths, which is not surprising considering that uniform inflow towards a rectangular body and a tsunami bore impacting an elevated rectangular structure, are not similar in nature. On the contrary, the success of the wake width comparison is a surprising, but encouraging result. As such, further comparisons of other Reynolds number-based relations for more similar flows ought to be made to further validate the force ratio estimation model for general use.

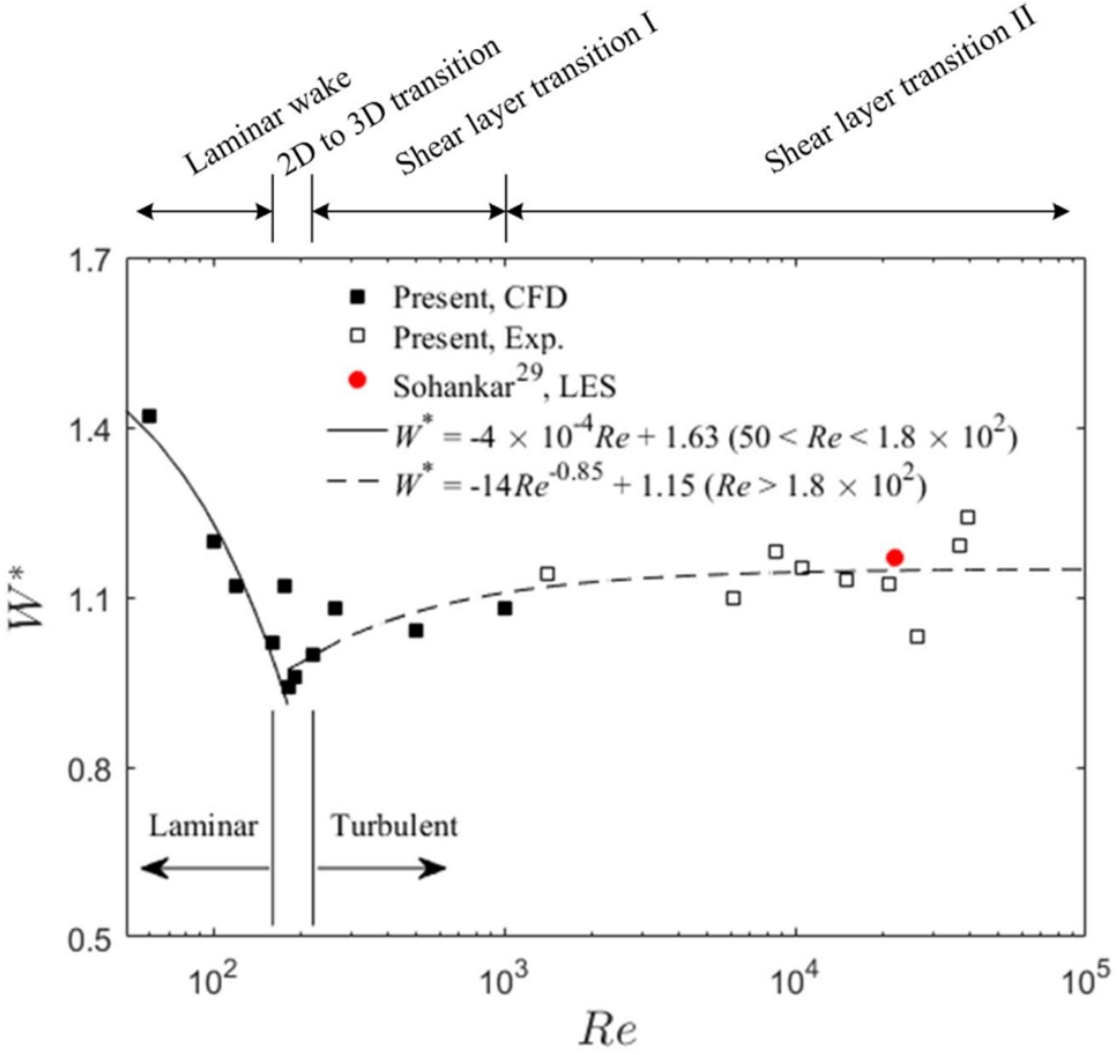

Figure 8.8: Wake Width as a Function of Reynolds Number (Bai and Alam, 2018)

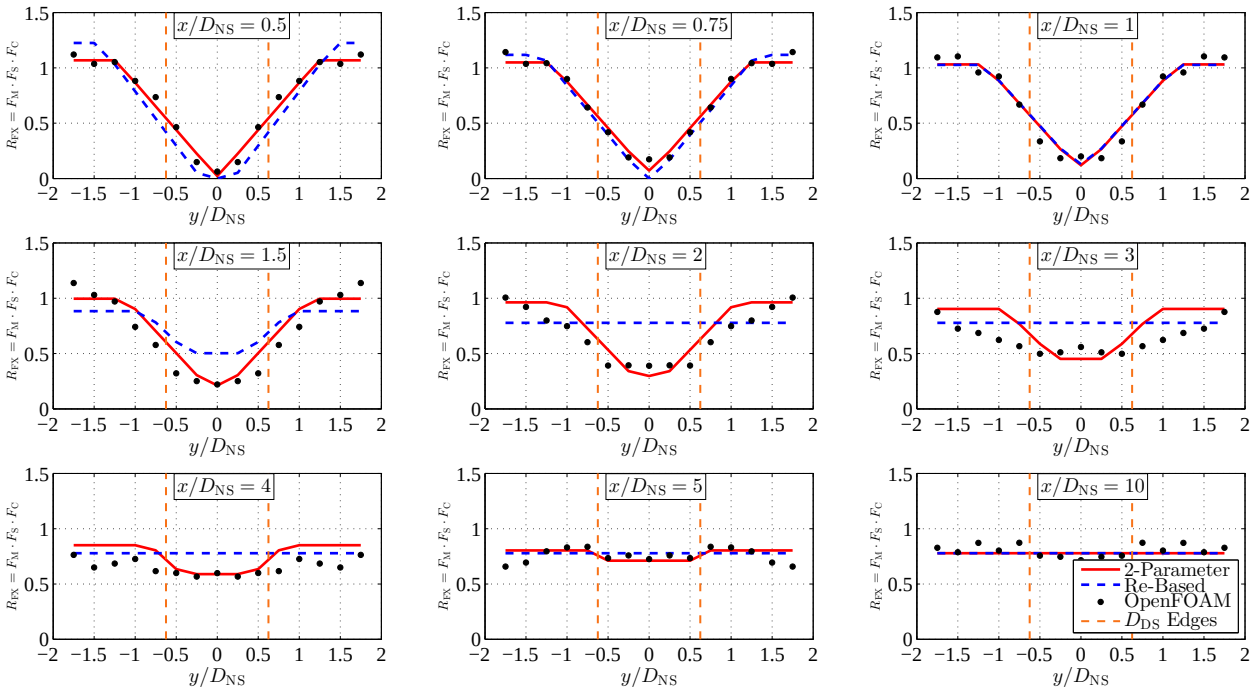

Figure 8.9: Comparison of Predicted Normalized Force Ratios for the Universal and *Re*-Based Wake Size Ratios

Chapter 9

CONCLUSIONS AND FUTURE WORK

Prior to the work conducted during this study, a detailed investigation into the effects of local shielding and flow channeling phenomena of tsunami-like waves due to groups of coastal structures was lacking in the engineering literature. As was discussed in Chapter 3 - Prior Tsunami Impact Research, past numerical modeling of wave-induced fluid-structure interaction (FSI) during tsunami inundations resulted in both over- and under-predictions of forces, pressures, flow velocities, and free-surface elevations, demonstrating highly inconsistent results between different research methods and CFD software. This study aimed to fill the second of these gaps by first developing an experimentally-validated 3D CFD model using the OpenFOAM software that is capable of accurately reproducing force, pressure, and free-surface elevation measurements for a range of multi-structure configurations with both symmetric and antisymmetric arrangements. Following the validation step, the OpenFOAM model was subsequently used to close the first of the identified research gaps by conducting a parameter study that varied structure locations to gather data for the development and calibration of a phenomenological force-prediction equation, which is able to incorporate both shielding and flow channeling effects for a wider range of multi-structure configurations than current ASCE 7-16 Chapter C6 design code provisions.

9.1 Research Findings and Developments

The following conclusions were identified during the experimental and numerical modeling phases of this study.

1. Shielding due to neighboring structures results in reduced structural demands during a tsunami inundation. However, even though the net force may be reduced, regions

of a design structure's offshore face that are not shielded, often experience increased local pressure demands as was discussed in Chapter 5 - Experimental Results. For example, see Figure 5.14, where the 50%-shielded configurations, Cases C and F, show notable pressure increases in unshielded regions of the design structure's offshore face, but experienced reduced overall forces relative to the reference case, Case A, without neighboring structures as shown in Figure 5.16. Thus, unless a structure is 100%-shielded as with Case D, where the pressure reduced uniformly over the offshore face of the design structure, individual structural components will experience locally-increased structural demands.

2. Flow channeling due to neighboring structures produces Venturi-like effects where increased fluid velocities result in increased dynamic pressures and resultant streamwise forces. However, the degree to which such effects matter in terms of causing streamwise force amplifications relies heavily on the alignment of a channelized flow with the offshore face of a design structure. For instance, in Case E the channel between the pair of neighboring structures was aligned with the centerline of the design structure, which resulted in amplifying both local pressures and the total streamwise force acting on the design structure compared to results for the reference case, Case A. On the other hand, in Case F the channel between the pair of neighboring structures was half as large as the channel in Case E and was aligned with the edge of the design structure. The resulting pressure distribution shown in Figure 5.14 for Case F gives larger values near the edge of the design structure than the largest pressures recorded for Case E near the middle of the design structure, which is consistent with a smaller flow channel producing higher flow velocities and consequently larger fluid pressures acting on the design structure. However, since these pressure increases only occurred near the design structure edge instead of over its entire offshore face, the resulting total streamwise force was much less for Case F than Case E, giving a result that was less than 50% of the reference case result as shown in Figure 5.16.

3. Numerical model validation results demonstrated that the k-ω Shear Stress Transport turbulence model most accurately reproduced the experimentally measured forces, pressures, and free-surface elevations compared to the Standard k-ε, Non-linear Realizable k-ε, and Launder-Reece-Rodi models provided in OpenFOAM. This provides evidence that the k-ω SST model is capable of modeling cases with severe flow separation at sharp corners of bodies, for which it was designed.

4. Comparing experimental findings to the ASCE 7-16 Chapter C6 recommended methods for estimating the effect of adjacent structures on tsunami-induced streamwise forces demonstrated that the design provisions provide good estimates of force amplification ratios when flow channeling effects dominated (Cases B and E). However, when shielding alone (Case D) or combined flow channeling and shielding effects occurred (Cases C and F), the ASCE 7-16 force ratios significantly over-predicted the streamwise force.

5. The total streamwise force on a design structure due to neighboring structures was found to depend on three key phenomena, inundation flow momentum loss (F_{M}), shielding (F_{S}), and flow channeling (F_{C}). Factor equations were designed to model the effects each of these phenomena had on the total streamwise design structure force, which are defined by Equation 8.1, Equation 8.2, and Equation 8.6, respectively. The product of these factors gives the force ratio prediction equation defined by Equation 8.7. Additionally, in order to calibrate the size of an idealized triangular wake behind a neighboring structure, a numerical modeling parametric study using a single neighboring structure was conducted to gather peak streamwise force data for 187 neighboring structure locations. This data was used to determine ideal wake size ratios, $(R_{\mathrm{W}}, R_{\mathrm{L}}) = (D_{\mathrm{W}}/D_{\mathrm{NS}}, L_{\mathrm{W}}/D_{\mathrm{NS}}) = (1.2, 5.0)$, as proportions of the neighboring structure size.

9.2 Suggested Future Research

As an extension of these findings and developments, future work should be focused on further development of the normalized force-prediction equation by varying the types of structure configurations further. In particular, three types of cases stand out as needing immediate attention. The first of these is modeling configurations with more than one neighboring structure. At the time of writing this dissertation, parametric study simulations using OpenFOAM have been completed for 341 configurations with two neighboring structures. However, due to time constraints, further analysis of this data will be the subject of future journal articles.

The second category of neighboring structure configurations that deserves attention is staggered arrays, where the structures are not placed at identical streamwise or cross-shore direction positions. Based on findings of Bridges (2011) that were discussed in Chapter 3 - Prior Tsunami Impact Research, such configurations can produce larger degrees of streamwise force amplifications and reductions than configurations were all the structures are placed in a row parallel to a shoreline. In particular, the three-MRE configurations studied by Bridges (2011) demonstrated that the configurations where the middle MRE was closer to and farther from the test structure produced the greatest extremes of both shielding and channeling effects in terms of the most reduced and amplified streamwise forces, respectively.

In addition to varying the arrangement and number of neighboring structures, the type of design structure should be varied as well. In particular, non-elevated structures that extend all the way to the ground need to be modeled. Such a study would result in larger streamwise force demands than for an elevated structure, which would provide a better upper bound estimate of streamwise forces as well as demonstrate the effectiveness of breakwaway walls through a comparison with the elevated structure results.

The most critical topic that was not touched upon during this study was the stochastic nature of tsunami wave generation. In order to account for the variability of initial tsunami wave forms, a probabilistic study of tsunami wave impact forces ought to be conducted.

Such a study would allow for the development of further modifications to the force-prediction equation developed in this dissertation that would amplify estimated streamwise forces to account for the possible variability in tsunami inundation levels and flow velocities that dictate resulting structural demands.

However, conducting a thorough probabilistic numerical simulation program varying the tsunami wave form would require a significant amount of time to complete, potentially taking many months or even several years depending on the amount and availability of the necessary computational resources. An alternative research direction that would achieve the same goal would be to investigate the potential of using physics-based, reduced-order modeling for wave-structure interaction during tsunami inundations, which would employ simplified numerical modeling that would take considerably less time to complete than 3D RANS modeling. This technique has already been successfully applied to many fluid-structure interaction (FSI) problems, including flow around cylinders, haemodynamics (i.e. blood flow interaction with vessel walls), and free-surface flows such as tsunamis, demonstrating that reduced-order modeling presents a viable approach for dealing with the large computational domains and numbers of input variables associated with probabilistic tsunami inundation studies (Walton et al., 2013; Colciago et al., 2014; Xiao et al., 2016, 2017).

BIBLIOGRAPHY

AASHTO (2008). *Guideline Specifications for Bridges Vulnerable to Coastal Storms*. American Association of State Highway and Transportation Officials (AASHTO), 444 North Capitol Street NW, Washington, DC, 20001. Prepared for the Federal Highway Administration (FHWA).

Abukawa, T., Nakamura, Y., and Hasegawa, A. (2013). "Effect of Reducing Tsunami Damage by Installing Fairing in Kesen-Bridge." *The 2013 World Congress on Advances in Structural Engineering and Mechanics (ASEM13)*, Korea Advanced Institute of Science and Technology, International Convention Center, Jeju, South Korea, Techno-Press, 4034 – 4047 (September).

Adams, J. (1990). "Paleoseismicity of the Cascadia Subduction Zone: Evidence from Turbidites off the Oregon-Washington Margin." *Tectonics*, 9(4), 569 – 583.

Adella, S., Nur, M. F., Nisa, N., Putra, A. T., Ramadhana, F. R., Maiyani, F., Munadi, K., and Rahman, A. (2019). "Disaster Risk Communication Issues and Challenges: Lessons Learned From the Disaster Management Agency of Banda Aceh City." *IOP Conference Series: Earth and Environmental Science*, 273, 012041.

Aglipay, M. R. I., Konagai, K., Kyokawa, H., and Keshab, S. (2012). "Road Bridges in Minami-Sanriku Washed Away in the March 11^{th} 2011 Great East Japan Earthquake and Tsunami." *Journal of Japan Society of Civil Engineers, Ser. A1 (Structural Engineering & Earthquake Engineering (SE/EE))*, 68(4), 1307 – 1314.

Akiyama, M., Frangopol, D. M., Arai, M., and Koshimura, S. (2012). "Probabilistic Assessment of Structural Performance of Bridges under Tsunami Hazard." *Structures Congress 2012*, American Society of Civil Engineers, 1919 – 1928.

Akiyama, M., Frangopol, D. M., Arai, M., and Koshimura, S. (2013). "Reliability of Bridges under Tsunami Hazards: Emphasis on the 2011 Tohoku-Oki Earthquake." *Earthquake Spectra*, 29(1), 295 – 314.

Al-Faesly, T., Nistor, I., Palermo, D., and Cornett, A. (2013). "Experimental Study of Structures Impacted by Simulated Tsunami Bore." *Coastal Structures 2011: Proceedings of the 6^{th} International Conference, Yokohama, Japan, September 6-8, 2011*, S. Takahashi, M. Isobe, N. Kobayashi, and K.-I. Shimosako, eds., Vol. 2, World Scientific, 1249–1260 (May).

Al-Faesly, T., Palermo, D., Nistor, I., and Cornett, A. (2012). "Experimental Modeling of Extreme Hydrodynamic Forces on Structural Models." *International Journal of Protective Structures*, 3(4), 477 – 505.

Alam, M. S., Winter, A. O., Galant, G., Shekhar, K., Barbosa, A. R., Motley, M. R., Eberhard, M. O., Cox, D. T., Arduino, P., and Lomonaco, P. (2019). "Tsunami-like Wave Induced Lateral and Uplift Pressures and Forces on an Elevated Coastal Structure." *ASCE Journal of Port, Waterway, Coastal and Ocean Engineering* **Under review**.

Allsop, N. and Calabrese, M. *Impact Loadings on Vertical Walls in Directional Seas*. Chapter 154, 2056 – 2068.

Anderson, D. A., Tannehill, J. C., and Pletcher, R. H. (1997). *Computational Fluid Mechanics and Heat Transfer*. Series in Computational and Physical Processes in Mechanics and Thermal Sciences. Taylor & Francis, 2^{nd} edition.

Andrade, E. C. (1930). "The Viscosity of Liquids." *Nature*, 125, 309 – 310.

Arabi, M. G., Sogut, D. V., Khosronejad, A., and Yalciner, A. C. (2019). "A Numerical and Experimental Study of Local Hydrodynamics due to Interactions between Solitary Wave and an Impervious Structure." *Coastal Engineering*, 147, 43 – 62.

Araki, S. (2015). "Pressure Acting on Underside of Bridge Deck." *Procedia Engineering*, 116, 454 – 461 8^{th} International Conference on Asian and Pacific Coasts (APAC 2015).

Araki, S., Ishino, K., and Deguchi, I. (2011). "Stability of Girder Bridge Against Tsunami Fluid Force." *Proceedings of* 32^{nd} *Conference on Coastal Engineering*, J. M. Smith and P. Lynett, eds., Vol. 1, International Conference on Coastal Engineering, Curran Associates, Inc.

Araki, S., Nakajima, Y., Deguchi, I., and Itoh, S. (2008). "Experimental Study on Tsunami Fluid Force Acting on Bridge Beam near River Mouth." *Proceedings of Coastal Engineering, JSCE*, 55, 866 – 870.

Arikawa, T. (2009). "Structural Behavior under Impulsive Tsunami Loading." *Journal of Disaster Research*, 4(6), 377 – 381.

Arikawa, T., Muhari, A., Okumura, Y., Dohi, Y., Afriyanto, B., Sujatmiko, K. A., and Imamura, F. (2018). "Coastal Subsidence Induced Several Tsunamis during the 2018 Sulawesi Earthquake." *Journal of Disaster Research*, 13 Sci. Comm. sc20181204.

Arikawa, T., Yamano, T., and Akiyama, M. (2007). "Advanced Deformation Method for Breaking Waves by using CADMAS-SURF/3D." *Proceedings of Coastal Engineering, JSCE*, 54, 71 – 75.

Árnason, H. (2005). "Interactions between an Incident Bore and a Free-Standing Coastal Structure." Ph.D. thesis, University of Washington, Seattle, WA (March 17).

Árnason, H., Petroff, C., , and Yeh, H. (2009). "Tsunami Bore Impingement onto a Vertical Column." *Journal of Disaster Research*, 4(6), 391 – 403.

Asakura, R., Iwase, K., Ikeya, T., Takao, M., Kaneto, T., Fujii, N., and Omori, M. (2000). "An Experimental Study on Wave Force Acting on On-shore Structures due to Overflowing Tsunamis." *Proceedings of Coastal Engineering, JSCE*, 47, 911 – 915.

ASCE (2017). *7-16 Minimum Design Loads and Associated Criteria for Buildings and Other Structures*. American Society of Civil Engineers, Reston, VA. U.S.A.

Associated Press Jakarta (2018). "Volcano Three-Quarters Blown Away by Indonesia Tsunami Eruption." *The Guardian* Originally published online Sat 29 Dec 2018 2:49 AM EST.

ATC (2008). *Guidelines for Design of Structures for Vertical Evacuation from Tsunamis*. Federal Emergency Management Agency (FEMA), 201 Redwood Shores Pkwy, Suite 240, Redwood City, CA 94065, 1st edition (June). Prepared by the Applied Technology Council (ATC).

ATC (2012). *Guidelines for Design of Structures for Vertical Evacuation from Tsunamis*. Federal Emergency Management Agency (FEMA), 201 Redwood Shores Pkwy, Suite 240, Redwood City, CA 94065, 2nd edition (June). Prepared by the Applied Technology Council (ATC).

Athukorala, P. and Resosudarmo, B. P. (2005). "The Indian Ocean Tsunami: Economic Impact, Disaster Management, and Lessons." *Asian Economic Papers*, 4(1), 1 – 39.

Attary, N., Unnikrishnan, V. U., van de Lindt, J. W., Cox, D. T., and Barbosa, A. R. (2017). "Performance-Based Tsunami Engineering Methodology for Risk Assessment of Structures." *Engineering Structures*, 141, 676 – 686.

Atwater, B. F. (1987). "Evidence for Great Holocene Earthquakes along the Outer Coast of Washington State." *Science*, 236(4804), 942 – 944.

Atwater, B. F. (1992). "Geologic Evidence for Earthquakes during the Past 2000 Years along the Copalis River, Southern Coastal Washington." *Journal of Geophysical Research: Solid Earth*, 97(B2), 1901 – 1919.

Atwater, B. F. and Griggs, G. B. (2012). "Deep-Sea Turbidites as Guides to Holocene Earthquake History at the Cascadia Subduction Zone–Alternative Views for a Seismic-Hazard Workshop." *Open-File Report 2012-1043*, United States Geological Survey (USGS) (March 12).

Atwater, B. F. and Hemphill-Haley, E. (1997). "Recurrence Intervals for Great Earthquakes of the Past 3500 Years at Northeastern Willapa Bay, Washington." *USGS Professional Paper 1576*, United States Geological Survey (USGS).

Atwater, B. F., Musumi-Rokkaku, S., Satake, K., Tsuji, Y., Ueda, K., and Yamaguchi, D. K. (2015). "The Orphan Tsunami of 1700—Japanese Clues to a Parent Earthquake in North America." *USGS Professional Paper 1707*, U.S. Geological Survey (December). University of Washington Press.

Azadbakht, M. (2013). "Tsunami and Hurricane Wave Loads on Bridge Superstructures." Ph.D. thesis, Oregon State University, Corvalis, OR (December).

Azadbakht, M. and Yim, S. C. (2015a). *Bridge Superstructure Design for Tsunamis: A State-of-the-Art Methodology for Tsunami Modeling, Load Simulation, and Structural Response Assessment*. American Society of Civil Engineers, Chapter 30, 345 – 354.

Azadbakht, M. and Yim, S. C. (2015b). "Simulation and Estimation of Tsunami Loads on Bridge Superstructures." *Journal of Waterway, Port, Coastal, and Ocean Engineering*, 141(2).

Azadbakht, M. and Yim, S. C. (2016a). "Effect of Trapped Air on Wave Forces on Coastal Bridge Superstructures." *Journal of Ocean Engineering and Marine Energy*, 2(2), 139 – 158.

Azadbakht, M. and Yim, S. C. (2016b). "Estimation of Cascadia Local Tsunami Loads on Pacific Northwest Bridge Superstructures." *Journal of Bridge Engineering*, 21(2).

Bagnold, R. (1939). "Interim Report on Wave-Pressure Research." *Report no.*, Institution of Civil Engineers, London, UK (June).

Bai, H. and Alam, M. M. (2018). "Dependence of Square Cylinder Wake on Reynolds Number." *Physics of Fluids*, 30(1), 015102.

Bakker, A. (2006). "Lecture 10 - Turbulence Models. Dartmouth College, ENGS 150 - Applied Computational Fluid Dynamics.

Bandara, J. and Naranpanawa, A. (2005). "The Economic Effects of the Asian Tsunami on the "Tear Drop in the Indian Ocean": A General Equilibrium Analysis." *Presented at the 8th annual conference on global economic analysis, lübeck, germany*, Global Trade Analysis Project (GTAP), Department of Agricultural Economics, Purdue University, West Lafayette, IN.

Baragmage, D., Forouzan, B., Shaloudegi, K., Nakata, N., and Wu, W. (2018). "Hybrid Simulation of Coastal Loading on Structures." *Coastal Engineering Proceedings*, 1(36), 15.

Bardina, J. E., Huang, P. G., and Coakley, T. J. (1997). "Turbulence Modeling Validation, Testing, and Development." *Report no.*, NASA Ames Research Center.

Boussinesq, J. V. (1877). "Essai sur la Théorie des Eaux Courantes." *Mémoires Presentes par Divers Savants à l'Académie des Sciences L'Institut de France*, 23(1), 1 – 680.

Bradner, C. (2008). "Large-Scale Laboratory Observations of Wave Forces on a Highway Bridge Superstructure." M.S. thesis, Oregon State University, Corvalis, OR (December).

Bradner, C., Schumacher, T., Cox, D., , and Higgins, C. (2011a). "Experimental Setup for a Large-Scale Bridge Superstructure Model Subjected to Waves." *Journal of Waterway, Port, Coastal, and Ocean Engineering*, 137(1), 3 – 11.

Bradner, C., Schumacher, T., Cox, D., and Higgins, C. (2011b). "Large-Scale Laboratory Observations of Wave

Forces on a Highway Bridge Superstructure." *Final Report OTREC-RR-11-10*, Oregon Transportation Research and Education Consortium (October).

Bremm, G. C., Goseberg, N., Schlurmann, T., and Nistor, I. (2015). "Long Wave Flow Interaction with a Single Square Structure on a Sloping Beach." *Journal of Marine Science and Engineering*, 3(3), 821 – 844.

Bricker, J. D., Kawashima, K., and Nakayama, A. (2012). "CFD Analysis of Bridge Deck Failure Due to Tsunami." *Proceedings of the International Symposium on Engineering Lessons Learned from the 2011 Great Japan Earthquake*, Japan Association for Earthquake Engineering, 1398 – 1409 (March).

Bricker, J. D. and Nakayama, A. (2014). "Contribution of Trapped Air, Deck Superelevation, and Nearby Structures to Bridge Deck Failure during a Tsunami." *Journal of Hydraulic Engineering*, 140(5).

Bridges, K.-J. (2011). "Influence of Macro-Roughness on Tsunami Runup Forces." M.S. thesis, Department of Civil and Construction Engineering, Oregon State University, Corvalis, OR (March).

Bridges, K.-J., Cox, D., Thomas, S., Shin, S., and Rueben, M. (2013). *Large-Scale Wave Basin Experiments on the Influence of Large Obstacles on Tsunami Inundation Forces*. World Scientific, 1237 – 1248.

Briggs, M. J., Synolakis, C. E., Harkins, G. S., and Green, D. R. (1995). "Laboratory Experiments of Tsunami Runup on a Circular Island." *Pure and Applied Geophysics*, 144(3), 569 – 593.

Briggs, M. J., Synolakis, C. E., Harkins, G. S., and Green, D. R. (1996). "Runup of Solitary Waves on a Vertical Wall." *Long Wave Runup Models: Proceedings of the International Workshop*, Friday Harbor, San Juan Island, WA, 375 – 383.

Brocher, T. M., Filson, J. R., Fuis, G. S., Haeussler, P. J., Holzer, T. L., Plafker, G., and Blair, J. L. (2014). "The 1964 Great Alaska Earthquake and Tsunamis—A Modern Perspective and Enduring Legacies (March 4). U.S. Geological Survey Fact Sheet 2014–3018.

Camus, G. and Vincent, P. M. (1983). "Discussion of a New Hypothesis for the Krakatau Volcanic Eruption in 1883." *Journal of Volcanology and Geothermal Research*, 19(1 - 2), 167 – 173.

Carey, S., Sigurdsson, H., Mandeville, C., and Bronto, S. (1996). "Pyroclastic Flows and Surges over Water - An Example from the 1883 Krakatau Eruption." *Bulletin of Volcanology*, 57(7), 493 – 511.

Carratelli, E. P., Viccione, G., and Bovolin, V. (2016). "Free Surface Flow Impact on a Vertical Wall: A Numerical Assessment." *Theoretical and Computational Fluid Dynamics*, 30(5), 403 – 414.

Carrier, G. F. and Greenspan, H. P. (1958). "Water Waves of Finite Amplitude on a Sloping Beach." *Journal of Fluid Mechanics*, 4(1), 97 – 109.

Chakrabarti, S. K., Kriebel, D., and Berek, E. (1997). "Forces on a Single Pile Caisson in Breaking Waves and Current." *Applied Ocean Research*, 19(2), 113 – 140.

Chang, Y.-H., Hwang, K.-S., and Hwung, H.-H. (2009). "Large-Scale Laboratory Measurements of Solitary Wave Inundation on a 1:20 Slope." *Coastal Engineering*, 56(10), 1022 – 1034.

Charvet, I., Eames, I., and Rossetto, T. (2013). "New Tsunami Runup Relationships Based on Long Wave Experiments." *Ocean Modelling*, 69, 79 – 92.

Chen, X., Hofland, B., Molenaar, W., Capel, A., and Gent, M. R. V. (2019). "Use of Impulses to Determine the Reaction Force of a Hydraulic Structure with an Overhang due to Wave Impact." *Coastal Engineering*, 147, 75 – 88.

Chen, Y., Wu, Y., Stewart, G., Gullman-Strand, J., and Lu, X. (2014). "Numerical Simulation of Wave in Deck Loading on Offshore Structures." *Proceedings of the ASME 2014 33rd International Conference on Ocean, Offshore, and Artic Engineering (OMAE 2014)*, Vol. 2, American Society of Mechanical Engineers (June).

Cheung, V. and Robertson, I. N. (2014). "Evaluating the Effects of Tsunami Loading on Prototypical Steel Structures." *Research Report UHM/CEE/14-02*, Department of Civil and Environmental Engineering, University of Hawaii, Honolulu, HI (December).

Chiocci, F. L., Romagnoli, C., Tommasi, P., and Bosman, A. (2008). "The Stromboli 2002 Tsunamigenic Submarine Slide: Characteristics and Possible Failure Mechanisms." *Journal of Geophysical Research: Solid Earth*, 113(B10102).

Chock, G., Robertson, I., Kriebel, D., Francis, M., and Nistor, I. (2013). *Tohoku, Japan, Earthquake and Tsunami of 2011*. American Society of Civil Engineers.

Choi, B. H., Pelinovsky, E., Kim, K. O., and Lee, J. S. (2003). "Simulation of the Trans-Oceanic Tsunami Propagation due to the 1883 Krakatau Volcanic Eruption." *Natural Hazards and Earth Systems Sciences*, 3(5), 321 – 332.

Chopra, A. K. (2012). *Dynamics of Structures: Theory and Applications to Earthquake Engineering, 4^{th} Edition*. Prentice Hall New Jersey.

Chuang, W.-L., Chang, K.-A., Kaihatu, J., Cienfuegos, R., and Mokrani, C. (2018). "Experimental Modeling of Tsunami Bore Impingement on a Simplified Coastal Building." *Coastal Engineering Proceedings*, 1(36), 43.

City of Richmond (2017). "Tsunamis and Richmond: Tsunami Study (April 28). Richmond, BC, Canada.

Clarke, S. H. and Carver, G. A. (1992). "Late Holocene Tectonics and Paleoseismicity, Southern Cascadia Subduction Zone." *Science*, 255(5041), 188 – 192.

Clawpack Development Team (2019). "Clawpack Software, <http://www.clawpack.org>. Version 5.6.0.

Colciago, C. M., Deparis, S., and Quarteroni, A. (2014). "Comparisons between Reduced Order Models and Full 3D Models for Fluid–Structure Interaction Problems in Haemodynamics." *Journal of Computational and Applied Mathematics*, 265, 120 – 138 Current Trends and Progresses in Scientific Computation.

Cooker, M. J. and Peregrine, D. H. (1990). "A Model for Breaking Wave Impact Pressures." *Coastal Engineering 1990 Proceedings*, B. L. Edge, ed., American Society of Civil Engineers, Delft, Netherlands, 1473–1486 (July 2-6). 22^{nd} International Conference on Coastal Engineering.

Cox, D. T., Tomita, T., Lynett, P. J., and Holman, R. (2008). *Tsunami Inundation with Macro-Roughness in the Constructed Environment*. World Scientific Publishing Company, 1421 – 1432.

L. Cressman, M. Scott, and H. Yeh, eds. (2014). *UJNR Tsunami Modeling Workshop*. Oregon State University (OSU) College of Engineering, Corvalis, OR (December) Prepared in cooperation with the U.S.-Japan Cooperative Program in Natural Resources (UJNR) Panel on Wind and Seismic Effects and the Pacific Earthquake Engineering Research (PEER) Center.

Cross, R. H. (1967). "Tsunami surge forces." *Journal of Waterways and Harbors Division*, 93(4), 201 – 231.

Crowley, R., Robeck, C., and Dompe, P. (2018). "A Three-Dimensional Computational Analysis of Bridges Subjected to Monochromatic Wave Attack." *Journal of Fluids and Structures*, 79, 76 – 93.

Cunningham, L. S., Rogers, B. D., and Pringgana, G. (2014). "Tsunami Wave and Structure Interaction: An Investigation with Smooth-Particle Hydrodynamics." *Proceedings of the Institution of Civil Engineers: Engineering and Computational Mechanics*, Vol. 167, Institution of Civil Engineers, ICE Publishing, 126 – 138 (September).

Cuomo, G., Allsop, W., and Takahashi, S. (2010). "Scaling Wave Impact Pressures on Vertical Walls." *Coastal Engineering*, 57(6), 604 – 609.

Cuomo, G., Piscopia, R., and Allsop, W. (2011). "Evaluation of Wave Impact Loads on Caisson Breakwaters Based on Joint Probability of Impact Maxima and Rise Times." *Coastal Engineering*, 58(1), 9 – 27.

Cuomo, G., Shimosako, K.-I., and Takahashi, S. (2009). "Wave-in-Deck Loads on Coastal Bridges and the Role of Air." *Coastal Engineering*, 56(8), 793 – 809.

Cuomo, G., Tirindelli, M., and Allsop, W. (2007). "Wave-in-Deck Loads on Exposed Jetties." *Coastal Engineering*, 54(9), 657 – 679.

Dalrymple, R. and Derakhti, M. (2018). "Tsunami Generation by Earthquakes: Seabed Topography and Inertial Effects." *Coastal Engineering Proceedings*, 1(36), 58.

Daly, P., Halim, A., Nizamuddin, Ardiansyah, Hundlani, D., Ho, E., and Mahdi, S. (2017). "Rehabilitating Coastal Agriculture and Aquaculture after Inundation Events: Spatial Analysis of Livelihood Recovery in Post-Tsunami Aceh, Indonesia." *Ocean & Coastal Management*, 142, 218 – 232.

Dámian, S. M. (2009). "Description and Utilization of interFOAM Multiphase Solver." *Report no.*, National University of the Littoral.

Darienzo, M. E. and Peterson, C. D. (1995). "Magnitude and Frequency of Subduction-Zone Earthquakes along the Northern Oregon Coast in the Past 3000 Years." *Oregon Geology*, 57(1), 3 – 12.

Dean, R. A. and Dalrymple, R. A. (1991). *Water Wave Mechanics for Engineers and Scientists*, Vol. 2 of *Advanced Series on Ocean Engineering*. World Scientific Publishing Co. Pte. Ltd. (January).

Douglass, S. L., Chen, Q., Olsen, J., Edge, B. L., and Brown, D. (2006). "Wave Forces on Bridge Decks." *Research Report DTFH61-03-C-00015*, U.S. Department of Transportation Federal Highway Administration, Washgington, DC (June).

Dunbar, P. K. and Weaver, C. S. (2015). "United States and Territories National Tsunami Hazard Assessment: Historical Record and Sources for Waves - Update." *Report no.*, National Oceanic and Atmospheric Administration (NOAA), Boulder, CO (December). NOAA Tsunami Program Special Report. Prepared for the ational Tsunami Hazard Mitigation Program (NTHMP) by NOAA and the U.S. Geological Survey (USGS).

Esteban, M., Tsimopoulou, V., Mikami, T., Yun, N., Suppasri, A., and Shibayama, T. (2013). "Recent Tsunamis Events and Preparedness: Development of Tsunami Awareness in Indonesia, Chile and Japan." *International Journal of Disaster Risk Reduction*, 5, 84 – 97.

Foster, A. S. J., Rossetto, T., and Allsop, W. (2017). "An Experimentally Validated Approach for Evaluating Tsunami Inundation Forces on Rectangular Buildings." *Coastal Engineering*, 128, 44 – 57.

Foytong, P., Ruangrassamee, A., Shoji, G., Hiraki, Y., and Ezura, Y. (2013). "Analysis of Tsunami Flow Velocities during the March 2011 Tohoku, Japan, Tsunami." *Earthquake Spectra*, 29(S1), S161 – S181.

Francis, P. W. (1985). "The Origin of the 1883 Krakatau Tsuanmis." *Journal of Volcanology and Geothermal Research*, 5(3), 349 – 363 Elsevier Science Publishers B. V., Amsterdam - Preinted in the Netherlands.

Frandsen, J. B. and Bérubé, F. (2015). "Large Scale Experimental Wave Impact on Walls in the Québec Coastal Physics Laboratory." *Proceedings of the ASME 2015 34th International Conference on Ocean, Offshore and Arctic Engineering*, Vol. 7: Ocean Engineering, Ocean, Offshore and Arctic Engineering Division, St. John's, Newfoundland, Canada, The American Society of Mechanical Engineers, 1 – 10 (May 31 – June 5).

Fritz, H. M., Hager, W. H., and Minor, H.-E. (2001). "Lituya Bay Case: Rockslide Impact and Wave Run-Up." *Science of Tsunami Hazards*, 19(1), 3 – 22.

Fritz, H. M., Hillaire, J. V., Moliére, E., Wei, Y., and Mohammed, F. (2013). "Twin Tsunamis Triggered by the 12 January 2010 Haiti Earthquake." *Pure and Applied Geophysics*, 170(9), 1463 – 1474.

Fritz, H. M., Mohammed, F., and Yoo, J. (2009). "Lituya Bay Landslide Impact Generated Mega-Tsunami 50th Anniversary." *Pure and Applied Geophysics*, 166(1), 153 – 175.

Fryer, G. J., Watts, P., and Pratson, L. F. (2004). "Source of the Great Tsunami of 1 April 1946: A Landslide in the

Upper Aleutian Forearc." *Marine Geology*, 203(3 - 4), 201 – 218.

Fu, L., Kosa, K., and Sasaki, T. (2013). "Tsunami Damage Evaluation of Utatsu Bridge by Video and 2-D Simulation Analyses." *Journal of Structural Engineering, A*, 59A, 428 – 438.

Fujima, K., Achmad, F., Shigihara, Y., , and Mizutani, N. (2009). "Estimation of tsunami force acting on rectangular structures." *Journal of Disaster Research*, 4(6), 404–409.

Gaeta, M. G., Martinelli, L., and Lamberti, A. (2012). "Uplift Forces on Wave Exposed Jetties: Scale Comparison and Effect of Venting." *Coastal Engineering Proceedings*, 1(33), 34.

Garrison-Laney, C. E., Abramson, H. F., and Carver, G. A. (2002). "Late Holocene Tsunamis near the Southern End of the Cascadia Subduction Zone." *Seismological Research Letters*, 73(2), 248.

Gedik, N., Irtem, E., and Kabdasli, S. (2005). "Laboratory Investigation on Tsunami Run-up." *Ocean Engineering*, 32(5), 513 – 528.

Ghobarah, A., Saatcioglu, M., and Nistor, I. (2006). "The Impact of the 26 December 2004 Earthquake and Tsunami on Structures and Infrastructure." *Engineering Structures*, 28(2), 312 – 326.

Gloth, O. (2019). *enGrid Open-Source Mesh Generation*. enGits GmbH Engineering & IT Services, Langenbachstrasse 3 79674 Todtnau, Germany.

Goda, Y. (1973). "A New Method of Wave Pressure Calculation for the Design of Composite Breakwater." *Port and Harbour Research Institute Report, Ministry of Transport, Japan*, 12(3), 31 – 69.

Goda, Y. (1974). "New Wave Pressure Formulae for Composite Breakwaters." *Coastal Engineering Proceedings*, 1(14), 100.

Goldfinger, C., Grijalva, K., Bürgmann, R., Morey, A. E., Johnson, J. E., Nelson, C. H., Gutiérrez-Pastor, J., Ericsson, A., Karabanov, E., Chaytor, J. D., Patton, J., and Gràcia, E. (2008). "Late Holocene Rupture of the Northern San Andreas Fault and Possible Stress Linkage to the Cascadia Subduction Zone." *Bulletin of the Seismological Society of America*, 98(2), 861 – 889.

Goldfinger, C., Nelson, C. H., Johnson, J. E., and The Shipboard Scientific Party (2003). "Holocene Earthquake Records from the Cascadia Subduction Zone and Northern San Andreas Fault Based on Precise Dating of Offshore Turbidites." *Annual Review of Earth and Planetary Sciences*, 31(1), 555–557.

Goldfinger, C., Nelson, C. H., Morey, A. E., Johnson, J. E., Patton, J. R., Karabanov, E., Gutiérez-Pastor, J., Eriksson, A. T., Gràcia, E., Dunhill, G., Enkin, R. J., Dallimore, A., and Vallier, T. (2012). "Turbidite Event History–Methods and Implications for Holocene Paleoseismicity of the Cascadia Subduction Zone." *USGS Professional Paper 1661-F*, United States Geological Survey (USGS) (July 17).

González-Vida, J. M., Macías, J., Castro, M. J., Sánchez-Linares, C., de la Asunción, M., Ortega-Acosta, S., and Arcas, D. (2019). "The Lituya Bay Landslide-Generated Mega-Tsunami - Numerical Simulation and Sensitivity Analysis." *Natural Hazards and Earth System Sciences*, 19(2), 369 – 388.

Goseberg, N. (2011). "The Run-up of Long Waves - Laboratory-scaled Geophysical Reproduction and Onshore Interaction with Macro-Roughness Elements." Ph.d. thesis, Franzius Institute for Hydraulic, Estuarine, and Coastal Engineering, Gottfried Wilhelm Leibniz University, Hannover, DE (January).

Goseberg, N. (2013). "Reduction of Maximum Tsunami Run-Up due to the Interaction with Beachfront Development - Application of Single Sinusoidal Waves." *Natural Hazards and Earth System Sciences*, 13(11), 2991 – 3010.

Goseberg, N. and Schlurmann, T. (2011). "Numerical and Experimental Study on Tsunami Run-Up and Inundation

Influenced by Macro Roughness Elements." *Coastal Engineering Proceedings*, 1(32), 13.

Goseberg, N. and Schlurmann, T. (2014). "Non-Stationary Flow around Buildings during Run-up of Tsunami Waves on a Plain Beach." *Coastal Engineering Proceedings*, 1(34), 21.

Goseberg, N., Wurpts, A., and Schlurmann, T. (2013). "Laboratory-Scale Generation of Tsunami and Long Waves." *Coastal Engineering*, 79, 57 – 74.

Green, G. (1838). "On the Motion of Waves in a Variable Canal of Small Depth and Width." *Transactions of the Cambridge Philosophical Society*, 6, 457 – 462.

Green, G. (2014). *Mathematical Papers of the Late George Green*. Cambridge Library Collection - Mathematics, Cambridge University Press, Chapter On the Motion of Waves in a Variable Canal of Small Depth and Width, 223 – 230.

Grilli, S. T., Losada, M. A., and Martin, F. (1994). "Characteristics of Solitary Wave Breaking Induced by Breakwaters." *Journal of Waterway, Port, Coastal, and Ocean Engineering*, 120(1), 74 – 92.

Grilli, S. T., Svendsen, A., and Subramanya, R. (1997). "Breaking Criterion and Characteristics for Solitary Waves on Slopes." *Journal of Waterway, Port, Coastal, and Ocean Engineering*, 123(3), 102 – 112.

Guerrero, J. (2015). "Introduction to Computational Fluid Dynamics: Governing Equations, Turbulence Modeling Introduction and Finite Volume Discretization Basics (July 5).

Guo, A., Fang, Q., Bai, X., and Li, H. (2015). "Hydrodynamic Experiment of the Wave Force Acting on the Superstructures of Coastal Bridges." *Journal of Bridge Engineering*, 20(12).

Hammack, J. L. (1973). "A Note on Tsunamis: Their Generation and Propagation in an Ocean of Uniform Depth." *Journal of Fluid Mechanics*, 60(4), 769 – 799.

Hansen, W. R., Kachadoorian, R., Coulter, H. W., Migliaccio, R. R., Waller, R. M., Stanley, K. W., Lemke, R. W., Plafker, G., Eckel, E. B., and Mayo, L. R. (1969). "The Alaska Earthquake of March 27, 1964: Effects on Communities." *USGS Professional Paper 542*, United States Geological Survey (USGS), Washington, DC.

Hartana, A., Murakami, K., Yamaguchi, Y., and Maki, D. (2013). "2-Phase Flow Analysis of Tsunami Forces Acting on Bridge Structures." *Journal of Japan Society of Civil Engineers, Ser. B3 (Ocean Engineering)*, 69(2), 347 – 352.

Hattori, M. and Arami, A. (1992). *Impact Breaking Wave Pressures on Vertical Walls*. Chapter 135, 1785–1798.

Hayashi, H., Aoki, K., Shijo, R., Suzuki, T., and Koshimura, S. (2014). "Study on Tsunami Wave Force acting on a Bridge Superstructure." *Kozo Kogaku Ronbunshu. A (Journal of Structural Engineering. A)*, 60A, 45 – 58.

Hayatdavoodi, M., Seiffert, B., and Ertekin, R. C. (2014). "Experiments and Computations of Solitary-Wave Forces on a Coastal-Bridge Deck. Part II: Deck with Girders." *Coastal Engineering*, 88, 210 – 228.

Heidarzadeh, M., Muhari, A., and Wijanarto, A. B. (2019). "Insights on the Source of the 28 September 2018 Sulawesi Tsunami, Indonesia Based on Spectral Analyses and Numerical Simulations." *Pure and Applied Geophysics*, 176(1), 25 – 43.

Heidarzadeh, M. and Satake, K. (2015). "Source Properties of the 1998 July 17 Papua New Guinea Tsunami Based on Tide Gauge Records." *Geophysical Journal International*, 202(1), 361 – 369.

Heinrich, P., Piatanesi, A., and Hébert, H. (2001). "Numerical Modelling of Tsunami Generation and Propagation from Submarine Slumps: The 1998 Papua New Guinea Event." *Geophysical Journal International*.

Heller, V. and Hager, W. H. (2014). "A Universal Parameter to Predict Subaerial Landslide Tsunamis." *Journal of Marine Science and Engineering*, 2(2), 400 – 412.

Higgins, C. C., Cox, D. T., and Lomónaco, P. (2017). "NHERI Experimental Facility for Coastal Waves/Surge and Tsunamis at Oregon State University." *Proceedings of the* 16^{th} *World Conference on Earthquake Engineering*, International Association for Earthquake Engineering, Santiago, Chile, Institute of Theoretical and Applied Mechanics (January).

Higuera, P. (2017). "olaFlow: CFD for Waves.

Hirt, C. and Nichols, B. (1981). "Volume of Fluid (VOF) Method for the Dynamics of Free Boundaries." *Journal of Computational Physics*, 39(1), 201 – 225.

Honda, T., Oda, Y., Ito, K., Watanabe, M., and Takabatake, T. (2014). "An Experimental Study on the Tsunami Pressure Acting on Piloti-Type Buildings." *Coastal Engineering Proceedings*, 1(34).

Hoshikuma, J., Zhang, G., Nakao, H., and Sumimura, T. (2012). "Experimental Researches on Behavior of Bearing Supports in Highway Bridges under Tsunami-Induced Force." •, The United States-Japan Cooperative Program in Natural Resources (October).

Hosoda, A. and Maruyama, K. (2011). "Washed Away of Bridge by the Great East Japan Earthquake." *Disaster Survey Report*, Japan Society of Civil Engineers.

Hu, K., Mingham, C., and Causon, D. (2000). "Numerical Simulation of Wave Overtopping of Coastal Structures using the Non-linear Shallow Water Equations." *Coastal Engineering*, 41(4), 433 – 465.

Hubbard, M. E. and Dodd, N. (2002). "A 2D Numerical Model of Wave Run-up and Overtopping." *Coastal Engineering*, 47(1), 1 – 26.

Iemura, H., Pradono, M. H., and Takahashi, Y. (2005). "Report on the Tsunami Damage of Bridges in Banda Aceh and Some Possible Countermeasures." *Proceedings of the* 28^{th} *JSCE Earthquake Engineering Symposium*, Japan Society of Civil Engineering.

Iemura, H., Pradono, M. H., Yasuda, T., and Tada, T. (2007). "Experiments of Tsunami Force Acting on Bridge Models." *Proceedings of the JSCE Earthquake Engineering Symposium*, 29, 902 – 911.

Imamura, F. (2008). "Devastating Damage due to the 2004 Indian Ocean Tsunami and its Lessons." *Proceedings of the* 14^{th} *World Conference on Earthquake Engineering*, International Association of Earthquake Engineering, Beijing, China, Institute of Engineering Mechanics, CEA (October).

Imamura, F. and Hashi, K. (2003). "Re-examination of the Source Mechanism of the 1998 Papua New Guinea Earthquake and Tsunami." *Pure and Applied Geophysics*, 160(10), 2071 – 2086.

Ismail, N., Okazaki, K., Ochiai, C., and Fernandez, G. (2018). "Livelihood changes in Banda Aceh, Indonesia after the 2004 Indian Ocean Tsunami." *International Journal of Disaster Risk Reduction*, 28, 439 – 449.

Iwasaki, S. (1997). "The Wave Forms and Directivity of a Tsunami Generated by an Earthquake and a Landslide." *Science of Tsunami Hazards*, 15(1), 23 – 40.

Jamin, T., Gordillo, L., Ruiz-Chavarría, G., Berhanu, M., and Falcon, E. (2015). "Experiments on Generation of Surface Waves by an Underwater Moving Bottom." *Proceedings of the Royal Society A: Mathematical, Physical and Engineering Sciences*, 471(2178), 20150069.

R. W. Johnson, ed. (2016a). *Handbook of Fluid Dynamics*. CRC Press, 2^{nd} edition.

Johnson, V. C. T. (2016b). "Wave and Surge Vulnerability of Coastal Residences." Ph.D. thesis, Civil and Environmental Engineering and Earth Sciences, University of Notre Dame, Notre Dame, IN (April).

Jones, W. P. and Launder, B. E. (1972). "The Prediction of Laminarization with a Two-Equation Model of Turbulence." *International Journal of Heat and Mass Transfer*, 15, 301 – 314.

Judge, F. M., Orszaghova, J., Taylor, P. H., and Borthwick, A. G. L. (2018). "A 2DH Hybrid Boussinesq-NSWE Solver for Near-Shore Hydrodynamics." *Coastal Engineering*, 142, 9 – 26.

Kasano, H., Oka, J., Sakurai, J., Kodama, N., and Yoda, T. (2012). "Investigative Research on Bridges Subjected to Tsunami Disaster in 2011 off the Pacific Coast of Tohoku Earthquake." *Australasian Structural Engineering Conference 2012: The Past, Present, and Future of Structural Engineering*, Engineers Australia, 51 – 57.

Kawashima, K. (2012). "Damage of Bridges due to the 2011 Great East Japan Earthquake." *Journal of Japan Association for Earthquake Engineering*, 12(4), 319 – 338.

Kawata, Y., Benson, B. C., Borrero, J. C., Borrero, J. L., Davies, H. L., de Lange, W. P., Imamura, F., Letz, H., Nott, J., and Synolakis, C. E. (1999). "Tsunami in Papua New Guinea Was as Intense as First Thought." *EOS, Transactions, American Geophysical Union*, 80(9), 101 – 112.

Kazama, M. and Noda, T. (2012). "Damage statistics (Summary of the 2011 off the Pacific Coast of Tohoku Earthquake Damage)." *Soils and Foundations*, 52(5), 780 – 792 Special Issue on Geotechnical Aspects of the 2011 off the Pacific Coast of Tohoku Earthquake.

Kelsey, H. M., Nelson, A. R., Hemphill-Haley, E., and Witter, R. C. (2005). "Tsunami History of an Oregon Coastal Lake Reveals a 4600 Yr Record of Great Earthquakes on the Cascadia Subduction Zone." *GSA Bulletin*, 117(7-8), 1009 – 1032.

Kelsey, H. M., Witter, R. C., and Hemphill-Haley, E. (2002). "Plate-Boundary Earthquakes and Tsunamis of the Past 5500 Yr, Sixes River Estuary, Southern Oregon." *GSA Bulletin*, 114(3), 298 – 314.

Kerenyi, K., Sofu, T., and Guo, J. (2009). "Hydrodynamic Forces on Inundated Bridge Decks." *Report No. FHWA-HRT-09-028*, University of Nebraska (May).

Kiersch, G. A. (1965). "Vaiont Reservoir Disaster." *Geotimes*, 9 – 12.

Kihara, N., Niida, Y., Takabatake, D., Kaida, H., Shibayama, A., and Miyagawa, Y. (2015). "Large-Scale Experiments on Tsunami-Induced Pressure on a Vertical Tide Wall." *Coastal Engineering*, 99, 46 – 63.

Kilburn, C. R. J. and Petley, D. N. (2003). "Forecasting Giant, Catastrophic Slope Collapse: Lessons from Vajont Northern Italy." *Geomorphology*, 54(1), 21 – 32.

Kim, J., Moin, P., and Moser, R. (1987). "Turbulence Statistics in Fully developed Channel Flow at Low Reynolds Number." *Journal of Fluid Mechanics*, 177, 133–166.

Kirby, J. T., Wei, G., Chen, Q., Kennedy, A. B., and Dalrymple, R. A. (1998). "FUNWAVE 1.0 Fully Nonlinear Boussinesq Wave Model Documentation and User's Manual." *Research Report CACR-98-06*, Center for Applied Coastal Research, Department of Civil Engineering, University of Delaware, Newark, DE, <https://csdms.colorado.edu/mediawiki/images/Cacr-98-06.pdf> (September).

Ko, H. T.-S. and Yeh, H. (2018). "On the Splash-up of Tsunami Bore Impact." *Coastal Engineering*, 131, 1 – 11.

Kolmogorov, A. N. (1941). "The Local Structure of Turbulence in Incompressible Viscous Fluid for Very Large Reynolds Numbers." *Proceedings: Mathematical and Physical Sciences*, 434(1890), 9 – 13.

Koon, F. S. and Lau, T. L. (2015). "Estimation of Tsunami Forces on Three Different Types of Bridge." *Report no.*, University Sains Malaysia.

Kosa, K. (2014). "Damage Analysis of Bridges Affected by the Tsunami in the Great East Japan Earthquake." *Journal of Japan Society of Civil Engineers*, 2(1), 77 – 93.

Koshimura, S. (2019). "Tsunami." *Encyclopedia of Ocean Sciences*, J. K. Cochran, H. J. Bokuniewicz, and P. L. Yager, eds., Vol. 3, Academic Press, Elsevier Ltd., Cambridge, MA, 3 edition, 692 – 701.

Kulkarni, R., Wong, I., Zachariasen, J., Goldfinger, C., and Lawrence, M. (2013). "Statistical Analyses of Great Earthquake Recurrence along the Cascadia Subduction Zone."

Bulletin of the Seismological Society of America, 103(6), 3205 – 3221.

Kundu, P. K., Cohen, I. M., and Dowling, D. R. (2012). *Fluid Mechanics*. Elsevier, Inc., 5^{th} edition.

Lander, J. F. (1996). "Tsunamis Affecting Alaska 1737-1996." *NGDC Key to Geophysical Research Documentation 31*, U.S. Department of Commerce, National Oceanic and Atmospheric Administration (NOAA), National Environmental Satellite, Data and Information Service, National Geophysical Data Center, Boulder, CO (September).

Lau, T. L., Inoue, S., Ghani, A. A., Zakaria, N. A., Choong, K. K., and Majid, T. A. (2015). "Estimation of Tsunami Force for Onshore Buildings in the Northwest Coast of Peninsular Malaysia." *Modern Civil Engineering in Trend of the Sustainable Infrastructure Development*, Vol. 802 of *Applied Mechanics and Materials*, Trans Tech Publications, 172 – 177 (11).

Lau, T. L., Lukkunaprasit, P., Ruangrassamee, A., and Ohmachi, T. (2010). "Performance of Bridges with Solid and Perforated Parapets in Resisting Tsunami Attacks." *Journal of Earthquake and Tsunami*, 04(02), 95 – 104.

Lau, T. L., Ohmachi, T., Inoue, S., and Lukkunaprasit, P. (2011). "Experimental and Numerical Modeling of Tsunami Force on Bridge Decks." *Tsunami - A Growing Disaster*, M. Mokhtari, ed., InTech, Chapter 6, 105 – 130.

Launder, B. E. and Sharma, B. I. (1974). "Application of the Energy Dissipation Model of Turbulence to the Calculation of Flow Near a Spinning Disc." *Letters in Heat and Mass Transfer*, 1(2), 131 – 138.

Leelawat, N., Suppasri, A., Charvet, I., and Imamura, F. (2014). "Building Damage from the 2011 Great East Japan Tsunami: Quantitative Assessment of Influential Factors." *Natural Hazards*, 73(2), 449–471.

Linton, D., Gupta, R., Cox, D., van de Lindt, J., Oshnack, M. E., and Clauson, M. (2013). "Evaluation of Tsunami Loads on Wood-Frame Walls at Full Scale." *Journal of Structural Engineering*, 139(8), 1318 – 1325.

Liu, F. (2017). "A Thorough Description of How Wall Functions Are Implemented in OpenFOAM (January 22). In Proceedings of CFD with OpenSource Softare 2016, Edited by Nilsson, H.

Liu, Y., Li, Y., Teng, B., Jiang, J., and Ma, B. (2008). "Total Horizontal and Vertical Forces of Irregular Waves on Partially Perforated Caisson breakwaters." *Coastal Engineering*, 55(6), 537 – 552.

Lloyd, T., Allsop, W., Charvet, I., Robinson, D., Robinson, T., and Rossetto, T. (2010). "Physical Modelling of Violent Flows and Their Impact Using a New Tsunami Generator." *Proceedings of the 9^{th} International Conference, September 16-18, 2009, Coasts, Marine Structures and Breakwaters: Adapting to Change*, Vol. 2, Institution of Civil Engineers, Edinburgh, Scotland, Thomas Telford Limited, 435 – 445.

Lomonaco, P., Alam, M., Arduino, P., Barbosa, A., Cox, D., Do, T., Eberhard, M., Motley, M., Shekhar, K., Tomiczek, T., Park, H., van de Lindt, J., and Winter, A. (2018). "Experimental Modeling of Wave Forces and Hydrodynamics on Elevated Coastal Structures Subject to Waves, Surge or Tsunamis." *Coastal Engineering Proceedings*, 1(36).

Lomonaco, P., Istratii, D., Maddux, T., Buckle, I., Yim, S., and Xiang, T. (2016). "Large-Scale Testing of Tsunami Impact Forces on Bridges." *Proceedings of the 6^{th} International Conference on the Application of Physical Modeling in Coastal and Port Engineering and Science*, International Association for Hydro-Environment Engineering and Research (May).

Lukkunaprasit, P., Chinnarasri, C., Ruangrassamee, A., Weesakul, S., and Thanasisathit, N. (2008). *Experimental Investigation of Tsunami Wave Forces on Buildings with Openings*. Chapter 8, 82–93.

Lynett, P. J. (2007). "Effect of a Shallow Water Obstruction on Long Wave Runup and Overland Flow Velocity." *Journal of Waterway, Port, Coastal, and Ocean Engineering*, 133(6), 455 – 462.

Lynett, P. J. (2009). *Tsunami Inundation, Modeling of*. Springer, New York, NY, 9618 – 9631.

Lynett, P. J., Liu, P. L.-F., Sitanggang, K. I., and Kim, D.-H. (2008). *Modeling Wave Generation, Evolution, and Interaction with Depth-Integrated, Dispersive Wave Equations COULWAVE Code Manual Cornell University Long and Intermediate Wave Modeling Package v. 2.0*. Inundation Science & Engineering Cooperative (ISEC) (May).

Macabuag, J., Rossetto, T., and Lloyd, T. (2014). "Sensitivity Analysesof a Framed Structure under Several Tsunami Design-Guidance Loading Regimes." *Proceedings of the Second European Conference on Earthquake Engineering and Seismology*, 1 – 12.

Mader, C. L. (1999). "Modeling the 1958 Lituya Bay Mega-Tsunami." *Science of Tsunami Hazards*, 17(1), 57 – 67.

Mader, C. L. and Gittings, M. L. (2002). "Modeling the 1958 Lituya Bay Mega-Tsunami, II." *Science of Tsunami Hazards*, 20(5), 241 – 250.

Mader, C. L. and Gittings, M. L. (2006). "Numerical Modeling for the Krakatoa Hydrovolcanic Explosion an Tsunami." *Science of Tsunami Hazards*, 24(3), 174 – 182.

Maeno, F. and Imamura, F. (2011). "Tsunami Generation by a Rapid Entrance of Pyroclastic Flow into the Sea during the 1883 Krakatau Eruption, Indonesia." *Journal of Geophysical Research: Solid Earth*, 116(B9).

Manawasekara, C., Aoki, S., Lee, K.-H., Mizutani, N., Hirakawa, N., and Ashizawa, A. (2013). "Effect of Three-Dimensionality on Tsunami Force Acting on a Structure." *Journal of Japan Society of Civil Engineers, Ser. B3 (Ocean Engineering)*, 69(2), 407 – 412.

Mandeville, C. W., Carey, S., Sigurdsson, H., and King, J. (1994). "Paleomagnetic Evidence for High-Temperature Emplacement of the 1883 Subaqueous Pyroclastic Flows from Krakatau Volcano, Indonesia." *Journal of Geophysical Research: Solid Earth*, 99(B5), 9487 – 9504.

Mandli, K. T., Ahmadia, A. J., Berger, M., Calhoun, D., George, D. L., Hadjimichael, Y., Ketcheson, D. I., Lemoine, G. I., and LeVeque, R. J. (2016). "Clawpack: Building an Open Source Ecosystem for Solving Hyperbolic PDEs." *PeerJ Computer Science*, 2, e68.

Maramai, A., Graziani, L., and Tinti, S. (2005). "Tsunamis in the Aeolian Islands (Southern Italy): A Review." *Marine Geology*, 215(1), 11 – 21.

Marinski, J. G. and Oumeraci, H. (1992). *Dynamic Response of Vertical Structures to Breaking Wave Forces – Review of the CIS Design Experience*. Chapter 103, 1357 – 1370.

Martinelli, L., Lamberti, A., Gaeta, M., Tirindelli, M., Alderson, J., and Schimmels, S. (2011). "Wave Loads on Exposed Jetties: Description of Large Scale Experiments and Preliminary Results." *Coastal Engineering Proceedings*, 1(32).

Maruyama, K., Tanaka, Y., and Hosoda, A. (2012). "Damage of Bridge Structures by Huge Tsunami and Evaluation of Tsunami Force on Bridges." *Society for Social Management Systems Internet Journal*.

Maruyama, K., Tanaka, Y., Kosa, K., Hosoda, A., and Arikawa, T. (2013). "Evaluation of Tsunami Force Acting on Bridge Girders." *Proceedings of the* 13^{th} *East Asia-Pacific Conference on Structural Engineering and Construction*.

Mase, H., Kimura, Y., Yamakawa, Y., Yasuda, T., Mori, N., and Cox, D. (2013). "Were Coastal Defensive Structures Completely Broken by an Unexpectedly Large Tsunami? A Field Survey." *Earthquake Spectra*, 29(S1), S145 – S160.

Matsumaru, R., Nagami, K., and Takeya, K. (2012). "Reconstruction of the Aceh Region following the 2004 Indian Ocean tsunami disaster: A transportation perspective." *IATSS Research*, 36(1), 11 – 19.

Mazinani, I., Ismail, Z., Hashim, A. M., and Saba, A. (2014). "Experimental Investigation on Tsunami Acting on Bridges." *International Journal of Civil, Environmental, Structural, Construction and Architectural Engineering*, 8(10), 1092 – 1095.

McCowan, J. (1894). "On the Highest Waves of Permanent Type." *The London, Edinburgh, and Dublin Philosophical Magazine and Journal of Science*, 38(233), 351 – 358.

McGovern, D. J., Robinson, T., Chandler, I. D., Allsop, W., and Rossetto, T. (2018). "Pneumatic Long-Wave Generation of Tsunami-Length Waveforms and Their Runup." *Coastal Engineering*, 138, 80 – 97.

Meyers, R. A., Smith, D. G., Jol, H. M., and Peterson, C. D. (1996). "Evidence for Eight Great Earthquake-Subsidence Events Detected with Ground-Penetrating Radar, Willapa Barrier, Washington." *Geology*, 24(2), 99 – 102.

Mimura, N., Yasuhara, K., Kawagoe, S., Yokoki, H., and Kazama, S. (2011). "Damage from the Great East Japan Earthquake and Tsunami - A Quick Report." *Mitigation and Adaptation Strategies for Global Change*, 16(7), 803 – 818.

Mitsuyasu, H. (1966). "Shock Pressure of Breaking Wave." *Coastal Engineering Proceedings*, 1(10), 17.

Mizutani, N., Aoki, S., Manawasekara, C., and Nakamura, T. (2014). "Effect of Space Configuration of Building on Tsunami Force on It." *Coastal Engineering Proceedings*, 1(34), 44.

Mizutani, S. and Imamura, F. (2001). "Dynamic Wave Force of Tsunamis Acting on a Structure." *ITS 2001 Proceedings*, 941 – 948.

MLIT (2011). "Occurrence of the Earthquake and Approaching Tsunami - The situation of the Great East Japan Earthquake." Earthquake Memorial Museum, Tohoku Regional Bureau, Ministry of Land, Industry, Transport, and Tourism.

Moon, W. C., Chiew, L. Q., Cheong, K. W., Tee, Y. C., Chun, J. B., and Lau, T. L. (2015). "Experimental Study on the Effect of Macroroughness on Tsunami Flow and Loading of Building." *Modern Civil Engineering in Trend of the Sustainable Infrastructure Development*, Vol. 802 of *Applied Mechanics and Materials*, Trans Tech Publications, 190 – 195 (11).

Mori, N., Cox, D. T., Yasuda, T., and Mase, H. (2013). "Overview of the 2011 Tohoku Earthquake Tsunami Damage and Its Relation to Coastal Protection along the Sanriku Coast." *Earthquake Spectra*, 29(S1), S127 – S143.

Mori, N. and Takahashi, T. (2012). "Nationwide Post Event Survey and Analysis of the 2011 Tohoku Earthquake Tsunami." *Coastal Engineering Journal*, 54(1).

Motley, M., Eberhard, M., Arduino, P., Barbosa, A., Andrew Winter, M. S. A., Shekhar, K., and Maddux, T. (2019). "Probabilistic Assessment of Tsunami Forces on Coastal Structures (February 23). DesignSafe-CI [publisher], Dataset, doi:10.17603/ds2-q2w5-0t48.

Motley, M. R., Wong, H. K., Qin, X., Winter, A. O., and Eberhard, M. O. (2016). "Tsunami-Induced Forces on Skewed Bridges." *Journal of Waterway, Port, Coastal, and Ocean Engineering*, 142(3), 04015025.

Muhari, A., Imamura, F., Arikawa, T., Hakim, A. R., , and Afriyanto, B. (2018). "Solving the Puzzle of the September 2018 Palu, Indonesia, Tsunami Mystery: Clues from the Tsunami Waveform and the Initial Field Survey Data." *Journal of Disaster Research*, 13, sc20181108.

Murakami, K., Sakamoto, Y., and Nonaka, T. (2012). "Analytical Investigation of Slab Bridge Damages Caused by Tsunami Flow." *Coastal Engineering Proceedings*, 1(33), 42.

Naito, C., Cercone, C., Riggs, H. R., and Cox, D. T. (2014). "Procedure for Site Assessment of the Potential for Tsunami Debris Impact." *Journal of Waterway, Port, Coastal, and Ocean Engineering*, 140(2), 223 – 232.

Nakamura, T., Mizutani, N., and Fujima, K. (2011). "Three-Dimensional Numerical Analysis on Deformation of Run-Up Tsunami and Tsunami Force Acting on Square Structures." *Coastal Engineering Proceedings*, 1(32), 14.

Nakamura, Y., Abukawa, T., and Hasegawa, A. (2013). "Hydraulic Experiment on Kesen-Bridge Outflow by Tsunami." *The 2013 World Congress on Advances in Structural Engineering and Mechanics (ASEM13)*, 4048 – 4055 (September).

Nakao, H., Nozaka, K., Izuno, K., and Kobayashi, H. (2012). "Tsunami Hydrodynamic Force on Various Bridge Sections." *Proceedings of the* 15^{th} *World Conference on Earthquake Engineering*, International Association for Earthquake Engineering.

Nakao, H., Zhang, G., Sumimura, T., and Hoshikuma, J. (2013a). "Effect of Cross-Sectional Configuration of Superstructure on Hydrodynamic Behavior of Bridges Subjected to Tsunami-Induced Loading." *Journal of Japan Society of Civil Engineers*, 4(69), 42 – 54.

Nakao, H., Zhang, G., Sumimura, T., and ichi Hoshikuma, J. (2013b). "Numerical Assessment of Tsunami-Induced Effect on Bridge Behavior." *Proceedings of the* 29^{th} *US-Japan Bridge Engineering Workshop*.

Nanto, D. K., Cooper, W. H., Donnelly, J. M., and Johnson, R. (2011). "Japan's 2011 Earthquake and Tsunami: Economic Effects and Implications for the United States." *Congressional Research Service Reports on Foreign Policy and Regional Affairs R41702*, Congressional Research Service (April).

Nelson, A. R. (1992a). "Discordant ^{14}C Ages from Buried Tidal-Marsh Soils in the Cascadia Subduction Zone, Southern Oregon Coast." *Quaternary Research*, 38(1), 74 – 90.

Nelson, A. R. (1992b). "Holocene Tidal-Marsh Stratigraphy in South-Central Oregon - Evidence for Localized Sudden Submergence in the Cascadia Subduction Zone." *Quaternary Coasts of the United States: Marine and Lacustrine Systems, SEPM Special Publication 48*, SEPM (Society for Sedimentary Geology) (January 1).

Nelson, A. R., Shennan, I., and Long, A. J. (1996). "Identifying Coseismic Subsidence in Tidal-Wetland Stratigraphic Sequences at the Cascadia Subduction Zone of Western North America." *Journal of Geophysical Research: Solid Earth*, 101(B3), 6115 – 6135.

niga, F. A., Jaiswal, M., Sai, J. O., Cox, D. T., Gupta, R., and van de Lindt, J. W. (2013). *Experimental Study of Tsunami Forces on Structures*. Chapter 11, 111–118.

Nistor, I., Palermo, D., Cornett, A., and Al-Faesly, T. (2011). "Experimental and Numerical Modeling of Tsunami Loading on Structures." *Coastal Engineering Proceedings*, 1(32).

NOAA (2006). *Method of Splitting Tsunami (MOST) Software Manual*. Pacific Marine Environmental Laboratory, National Oceanic & Atmospheric Administration, Seattle, WA (July).

NOAA (2017). "Tsunami Sources 1610 B.C. to A.D. 2017 from Earthquakes, Volcanic Eruptions, Landslides, and Other Causes. Published by the National Oceanographic and Atmospheric Administration (NOAA).

NOAA (2019). "Natural Hazards Data, Images and Education: 2018 September 28 Sulawesi, Indonesia Tsunami. Published by the National Centers for Environmental Information run by the National Oceanographic and Atmospheric Administration (NOAA).

Nouri, Y. (2008). "The Impact of Hydraulic Bores and Debris on Free Standing Structures." M.S. thesis, University of Ottawa, Ottawa, Ontario, Canada (May).

Nouri, Y., Nistor, I., Palermo, D., and Cornett, A. (2010). "Experimental Investigation of Tsunami Impact on Free Standing Structures." *Coastal Engineering Journal*, 52(01), 43 – 70.

NTHMP (2019). "NTHMP Tsunami Information Guide." *Report no.*, National Tsunami Hazard Mitigation Program.

NWS (2005). "Plate Tectonics and Earthquakes (March). Produced by the National Weather Service (NWS) run by the National Oceonographic and Atmospheric Administration (NOAA).

Oda, Y., Honda, T., and Omata, T. (2018). "Experimental Study on Tsunami Forces acting on Vertical Seawalls under Overflow." *Coastal Engineering Proceedings*, 1(36), 37.

Okal, E. A., Synolakis, C. E., Fryer, G. J., Heinrich, P., Borrero, J., Ruscher, C., Arcas, D., Guille, G., and Rousseau, D. (2002). "A Field Survey of the 1946 Aleutian Tsunami in the Far Field." *Seismological Research Letters*, 73(4), 490 – 503.

Omira, R., Dogan, G. G., Hidayat, R., Husrin, S., Prasetya, G., Annunziato, A., Proietti, C., Probst, P., Paparo, M. A., Wronna, M., Zaytsev, A., Pronin, P., Giniyatullin, A., Putra, P. S., Hartano, D., Ginanjar, G., Kongko, W., Pelinovsky, E., and Yalciner, A. C. (2019). "The Semptember 28th, 2018, Tsunami in Palu-Sulawesi, Indonesia: A Post-Event Field Survey." *Pure and Applied Geophysics*, 176(4), 1379 – 1395.

Pacheco, K. H. and Robertson, I. N. (2005). "Evaluation of Tsunami Loads and Their Effect on Reinforced Concrete Buildings." *Research Report UHM/CEE/05-06*, Department of Civil and Environmental Engineering, University of Hawaii, Honolulu, HI (May).

Paczkowski, K., Riggs, H. R., and Robertson, I. N. (2011). "Bore Impact upon Vertical Wall and Water-Driven, High-Mass, Low-Velocity Debris Impact." *Research Report UHM/CEE/11-05*, Department of Civil and Environmental Engineering, University of Hawaii, Honolulu, HI (December).

Palermo, D., Nistor, I., Al-Faesly, T., and Cornett, A. (2013). "Imapct of Tsunami Forces on Structures." *Science of Tsunami Hazards*, 32(2), 58 – 76.

Paris, R., Wassmer, P., Lavigne, F., Belousov, A., Belousova, M., Iskandarsyah, Y., Benbakkar, M., Ontowirjo, B., and Mazzoni, N. (2014). "Coupling Eruption and Tsunami Records: The Krakatau 1883 Case Study, Indonesia." *Bulletin of Volcanology*, 76(4), 814 –.

Park, H., Cox, D. T., Lynett, P. J., Wiebe, D. M., and Shin, S. (2013). "Tsunami Inundation Modeling in Constructed Environments: A Physical and Numerical Comparison of Free-Surface Elevation, Velocity, and Momentum Flux." *Coastal Engineering*, 79, 9 – 21.

Park, H., Tomiczek, T., Cox, D. T., van de Lindt, J. W., and Lomonaco, P. (2017). "Experimental Modeling of Horizontal and Vertical Wave Forces on an Elevated Coastal Structure." *Coastal Engineering*, 128, 58 – 74.

Parsons, T., Geist, E. L., Ryan, H. F., Lee, H. J., Haeussler, P. J., Lynet, P., Hart, P. E., Sliter, R., and Roland, E. (2014). "Source and Progression of a Submarine Landslide and Tsunami: The 1964 Great Alaska Earthquake at Valdez." *Journal of Geophysical Research: Solid Earth*, 119(11), 8502 – 8516.

Patankar, S. V. (1980). *Numerical Heat Transfer and Fluid Flow*. Taylor & Francis.

Paulsen, B. T. (2013). "Efficient Computations of Wave Loads on Offshore Structures." Ph.d. thesis, Department of Mechanical Engineering, Technical University of Denmark (DTU), Kongens Lyngby, DK (August).

Pelinovsky, E., Choi, B. H., Stromkov, A., Didenkulova, I., and Kim, H.-S. (2005). *Analysis of Tide-Gauge Records of the 1883 Krakatau Tsunami*. Springer Netherlands, Dordrecht, 57 – 77.

Petersen, M. D., Moschetti, M. P., Powers, P. M., Mueller, C. S., Haller, K. M., Frankel, A. D., Zeng, Y., Rezaeian, S., Harmsen, S. C., Boyd, O. S., Field, N., Chen, R., Rukstales, K. S., Luco, N., Wheeler, R. L., Williams, R. A., and Olsen, A. H. (2014). "Documentation for the 2014 Update of the United States National Seismic Hazard Maps." *Open-File Report 2014-1091*, United States Geological Survey (USGS) (July 17).

Peterson, C. D. and Darienzo, M. E. (1996). "Discrimination of Climatic, Oceanic, and Tectonic Mechanisms of Cyclic Marsh Burial, Alsea Bay, Oregon." *Assessing Earthquake Hazards and Reducing Risk in the Pacific Northwest - Volume 1*, A. M. Rogers, T. J. Walsh, W. J. Kockelman, and G. R. Priest, eds., United States Geological Survey (USGS), USGS Professional Paper 1560, 115 – 146.

Petrone, C., Rossetto, T., and Goda, K. (2017). "Fragility Assessment of a RC Structure under Tsunami Actions Via Nonlinear Static and Dynamic Analyses." *Engineering Structures*, 136, 36 – 53.

Pope, S. B. (2000). *Turbulent Flows*. Cambridge University Press.

Prandtl, L. (1925). "Bericht über die Entstehung der Turbulenz." *Zeitschrift für Angewandte Mathematik und*

Mechanik (Journal of Applied Mathematics and Mechanics), 5, 136 – 139 Tollmien et al. 1961, 2, 714 - 718.

Prandtl, L. (1926a). *Hydraulische Probleme*. VDI-Verlag, Berlin, DE, Chapter Bericht über neuere Turbulenzforschung, 1 – 13. Tollmien et al. 1961, 2, 719 - 730.

Prandtl, L. (1926b). "Über die ausgebildete Turbulenz." *Verhandlungen des II. Internationalen Kongresses für Technische Mechanik (Proceedings of the Second International Congress for Applied Mechanics)*, E. Meissner, ed., Zurich, CH, Orell Füssli, 62 – 75 (September). Tollmien et al. 1961, 2, 736 - 751.

Pringgana, G. (2016). "Improving Resilience of Coastal Structures Subject to Tsunami-like Waves." Ph.d. thesis, School of Mechanical, Aerospace and Civil Engineering, University of Manchester, Manchester, UK.

Putra, P. S., Aswan, A., Maryunani, K. A., Yulianto, E., and Kongko, W. (2019). "Field Survey of the 2018 Sulawesi Tsunami Deposits." *Pure and Applied Geophysics*, 1 – 11.

Qin, X., Motley, M., LeVeque, R., Gonzalez, F., and Mueller, K. (2018a). "A Comparison of a Two-Dimensional Depth Averaged Flow Model and a Three-Dimensional RANS Model for Predicting Tsunami Inundation and Fluid Forces." *Natural Hazards and Earth System Sciences Discussions*, 2018, 1 – 33.

Qin, X., Motley, M. R., and Marafi, N. A. (2018b). "Three-Dimensional Modeling of Tsunami Forces on Coastal Communities." *Coastal Engineering*, 140, 43 – 59.

Rahman, S., Akib, S., Khan, M. T. R., and Triatmadja, R. (2014). "Performance of Bridge Girder with Perforations under Tsunami Wave Loading." *International Journal of Civil, Environmental, Structural, Construction and Architectural Engineering*, 8(2), 139 – 144.

Ramachandran, K., Genzalez, R., Oumeraci, H., Schimmels, S., Kudella, M., Doorslaer, K. V., Rouck, J. D., Versluys, T., and Trouw, K. (2012). "Loading of Vertical Walls by Overtopping Bores using Pressure and Force Sensors - A Large Scale Model Study." *Coastal Engineering Proceedings*, 1(33), 44.

Raman, C. (1923). "A Theory of the Viscosity of Liquids." *Nature*, 111, 532 – 533.

Ramsden, J. D. (1993). "Tsunamis: Forces on a Vertical Wall Caused by Long Waves, Bores, and Surges on a Dry Bed." *Report KH-R-54*, W. M. Keck Laboratory of Hydraulics and Water Resources, Division of Engineering and Applied Science, California Institute of Technology, Pasadena, CA (May).

Ramsden, J. D. (1996). "Forces on a Vertical Wall due to Long Waves, Bores, and Dry-Bed Surges." *Journal of Waterway, Port, Coastal, and Ocean Engineering*, 122(3), 134 – 141.

Ramsden, J. D. and Raichlen, F. (1990). "Forces on Vertical Wall Caused by Incident Bores." *Journal of Waterway, Port, Coastal, and Ocean Engineering*, 116(5), 592 – 613.

Reynolds, O. (1895). "On the Dynamical Theory of Incompressible Viscous Fluids and the Determination of the Criterion." *Philosophical Transactions of the Royal Society of London*, 186, 123 – 164.

Riggs, H. R., Robertson, I. N., Cheung, K. F., Pawlak, G., Young, Y. L., and Yim, S. C. S. (2008). "Experimental Simulation of Tsunami Hazards to Buildings and Bridges." *Proceedings of 2008 NSF Engineering Research and Innovation Conference*, National Science Foundation, Knoxville, TN. NSF GRANT #0530759.

Riggs, R., Chock, G., and Robertson, I. (2011). "Development of Performance-Based Tsunami Engineering (PBTE) (Jan).

Robertson, B., Hall, K., Zytner, R., and Nistor, I. (2013a). "Breaking waves: Review of characteristic relationships." *Coastal Engineering Journal*, 55(1), 1350002–1–1350002–40.

Robertson, I., Riggs, H., and Mohamed, A. (2008). "Experimental Results of Tsunami Bore Forces on Structures." *Proceedings of the International Conference on Offshore Mechanics and Arctic Engineering - OMAE*, 1, 509–517.

Robertson, I. N. (2014). "Development of Tsunami Loading Expressions for Design of Coastal Infrastructure." *Proceedings of the 37th IABSE Symposium*, Vol. 102, International Association for Bridge and Structural Engineering (IABSE), Madrid, ES, 1544 –.

Robertson, I. N. and Mohamed, A. (2009). "Development of Performance Based Tsunami Engineering, PBTE." *IABSE Symposium Report*, 96(15), 16 – 23.

Robertson, I. N., Paczkowski, K., Riggs, H. R., and Mohamed, A. (2011). "Tsunami bore forces on walls." *Proceedings of th ASME 2011 30th International Conference on Ocean, Offshore and Arctic Engineering (OMAE2011)*, number OMAE2011-49487, American Society of Mechanial Engineers (ASME), Rotterdam, The Netherlands, 1– 9 (June 19-24).

Robertson, I. N., Paczkowski, K., Riggs, H. R., and Mohamed, A. (2013b). "Experimental Investigation of Tsunami Bore Forces on Vertical Walls." *Journal of Offshore Mechanics and Arctic Engineering*, 135(2), 021601–1 – 021601–8.

Röbke, B. R. and Vött, A. (2017). "The Tsunami Phenomenon." *Progress in Oceanography*, 159, 296 – 322.

Rossetto, T., Allsop, W., Charvet, I., and Robinson, D. I. (2011). "Physical Modelling of Tsunami Using a New Pneumatic Wave Generator." *Coastal Engineering*, 58(6), 517 – 527.

Rueben, M., Holman, R., Cox, D., Shin, S., Killian, J., and Stanley, J. (2011). "Optical Measurements of Tsunami Inundation through an Urban Waterfront Modeled in a Large-Scale Laboratory Basin." *Coastal Engineering*, 58(3), 229 – 238.

Saatcioglu, M., Ghobarah, A., and Nistor, I. (2005). "Effects of the December 26, 2004 Sumatra Earthquake and Tsunami on Physical Infrastructure." *ISET Journal of Earthquake Technology*, 42(4), 79 – 94.

Sakakiyama, T. (2014). "Tsunami Pressure on Structures due to Tsunami Inundation Flow." *Coastal Engineering Proceedings*, 1(34), 42.

Salem, H., Mohssen, S., Kosa, K., and Hosoda, A. (2014). "Collapse Analysis of Utatsu Ohashi Bridge Damaged by Tohoku Tsunami." *Journal of Advanced Concrete Technology*, 12, 388 – 402.

Santo, J. and Robertson, I. (2010). "Lateral Loading on Vertical Structural Elements due to a Tsunami Bore." *Research Report UHM/CEE/10-02*, Department of Civil and Environmental Engineering, University of Hawaii at Manoa, Honolulu, HI (May).

Sassa, S. and Takagawa, T. (2019). "Liquefied Gravity Flow-Induced Tsunami: First Evidence and Comparison from the 2018 Indonesia Sulawesi Earthquake and Tsunami Disasters." *Landslides*, 16(1), 195 – 200.

Satake, K. and Tanioka, Y. (2003). "The July 1998 Papua New Guinea Earthquake - Mechanism and Quantification of Unusual Tsunami Generation." *Pure and Applied Geophysics*, 160(10), 2087 – 2118.

Scharnke, J. and Hennig, J. (2015). "Vertical Wave Impact Loading on a Fixed Platform Deck." *Proceedings of the ASME 2015* 34th *International Conference on Ocean, Offshore, and Arctic Engineering (OMAE 2015)*, Vol. 3, American Society of Mechanical Engineers (May).

Schmitt, F. G. (2007). "About Boussinesq's Turbulent Viscosity Hypothesis - Historical Remarks and a Direct Evaluation of Its Validity." *Comptes Rendus Mécanique*, 335(9), 617 – 627.

Seiffert, B., Hayatdavoodi, M., and Ertekin, R. C. (2014). "Experiments and Computations of Solitary-Wave Forces on a Coastal-Bridge Deck. Part I: Flat Plate." *Coastal Engineering*, 88, 194 – 209.

Seiffert, B. R., Ertekin, R. C., and Robertson, I. N. (2015). "Wave Loads on a Coastal Bridge Deck and the Role of Entrapped Air." *Applied Ocean Research*, 53, 91 – 106.

Self, S. (1992). "Krakatau Revisited: The Course of Events and Interpretation of the 1883 Eruption." *GeoJournal*, 28(2), 109 – 121.

Self, S. and Rampino, M. R. (1981). "The 1883 Eruption of Krakatau." *Nature*, 294, 699 – 704.

Shafiei, S., Melville, B. W., and Shamseldin, A. Y. (2016). "Experimental Investigation of Tsunami Bore Impact Force and Pressure on a Square Prism." *Coastal Engineering*, 110, 1 – 16.

Shennan, I., Long, A. J., Rutherford, M. M., Green, F. M., Innes, J. B., Lloyd, J. M., Zong, Y., and Walker, K. J. (1996). "Tidal Marsh Stratigraphy, Sea-Level Change and Large Earthquakes, I: A 5000 Year Record in Washington, U.S.A.." *Quaternary Science Reviews*, 15(10), 1023 – 1059.

Sheppard, D. M. and Marin, J. (2009). "Wave Loading on Bridge Decks." *FDOT BD545-58*, Civil and Coastal Engineering Department, University of Florida, Gainesville, FL (December). Submitted To: Florida Department of Transportation Research Office.

Shi, F., Kirby, J. T., Tehranirad, B., Harris, J. C., Choi, Y.-K., and Malej, M. (2016). "FUNWAVE-TVD Fully Nonlinear Boussinesq Wave Model with TVD Solver: Documentation and User's Manual (Version 3.0)." *Research Report CACR-11-03*, Center for Applied Coastal Research, Ocean Engineering Laboratory, University of Delaware, Newark, DE (December).

Shibayama, T., Mikami, T., and Esteban, M. (2016). "Recent Progress of Physical Modeling Based on Field Investigations of Tsunamis and Storm Surges." *Proceedings of the* 6^{th} *International Conference on the Application of Physical Modelling in Coastal and Port Engineering and Science*, International Association for Hydro-Environment Engineering and Research, 1 – 10 (May).

Shin, S., Lee, K.-H., Park, H., Cox, D., and Kim, K. (2012). "Influence of a Infrastructure on Tsunami Inundation in a Coastal City: Laboratory Experiment and Numerical Simulation." *Coastal Engineering Proceedings*, 1(33), 8.

Shoji, G., Ezura, Y., and Hiraki, Y. (2012). "Modeling of Tsunami Fluid Force on a Bridge Deck Subjected to Plunging Breaker Bores and Surging Breaker Bores." *Proceedings of the* 15^{th} *World Conference on Earthquake Engineering*, International Association for Earthquake Engineering.

Shoji, G., Hiraki, Y., Fujima, K., and Shigihara, Y. (2011). "Evaluation of Tsunami Fluid Force Acting on a Bridge Deck Subjected to Breaker Bores." *Procedia Engineering*, 14, 1079 – 1088 The Proceedings of the Twelfth East Asia-Pacific Conference on Structural Engineering and Construction (EASEC12).

Shoji, G. and Moriyama, T. (2008). "Evaluation of a Tsunami Wave Load acting to a Deck of a Road Bridge." *Proceedings of the* 14^{th} *World Conference on Earthquake Engineering*, International Association for Earthquake Engineering (October).

Shoji, G., Shimizu, H., Koshimura, S., Estrada, M., and Jimenez, C. (2014). "Evaluation of Tsunami Wave Loads Acting on Walls of Confined-Masonry-Brick and Concrete-Block Houses." *Journal of Disaster Research*, 9(6), 976 – 983.

Simamora, C., Shigihara, Y., and Fujima, K. (2007). "Experimental Study on Tsunami Forces Acting on Structures." *Proceedings of Coastal Engineering, JSCE*, 54, 831 – 835.

Sondak, D. L. (1992). "Wall Functions for the k-ϵ Turbulence Model in Generalized Nonorthogonal Curvilinear Coordinates." Ph.D. thesis, Iowa State University, Ames, IA 50011.

Suppasri, A., Imamura, F., and Koshimura, S. (2013a). "Tsunami Hazard and Building Damage Assessment in Thailand using Numerical Model and Fragility Curves." *Journal of Earthquake and Tsunami*, 7(5), 1250028.

Suppasri, A., Koshimura, S., Imai, K., Mas, E., Gokon, H., Muhari, A., and Imamura, F. (2012a). "Damage Characteristic and Field Survey of the 2011 Great East Japan Tsunami in Miyagi Prefecture." *Coastal Engineering Journal*, 54(1), 1250005.

Suppasri, A., Koshimura, S., Imamura, F., Ruangrassamee, A., and Foytong, P. (2013b). "A Review of Tsunami Dam-

age Assesment Methods and Building Performance in Thailand." *Journal of Earthquake and Tsunami*, 7(5).

Suppasri, A., Mas, E., Koshimura, S., Imai, K., Harada, K., and Imamura, F. (2012b). "Developing Tsunami Fragility Curves from the Surveyed Data of the 2011 Great East Japan Tsunami in Sendai and Ishinomaki Plains." *Coastal Engineering Journal*, 54(1), 1250008.

Suppasri, A., Muhari, A., Ranasinghe, P., Mas, E., Shuto, N., Imamura, F., and Koshimura, S. (2012c). "Damage and Reconstruction after the 2004 Indian Ocean Tsunami and the 2011 Great East Japan Tsunami." *Journal of Natural Disaster Science*, 34(1), 19 – 39.

Suppasri, A., Shuto, N., Imamura, F., Koshimura, S., Mas, E., and Yalciner, A. C. (2013c). "Lessons Learned from the 2011 Great East Japan Tsunami: Performance of Tsunami Countermeasures, Coastal Buildings, and Tsunami Evacuation in Japan." *Pure and Applied Geophysics*, 170(6), 993 – 1018.

Sutherland, W. (1893). "The Viscosity of Gases and Molecular Force." *Philosophical Magazine Series 5*, 36(223), 507 – 531.

Sweet, S. and Silver, E. A. (2003). "Tectonics and Slumping in the Source Region of the 1998 Papua New Guinea Tsunami from Seismic Reflection Images." *Pure and Applied Geophysics*, 160(10), 1945 – 1968.

Swigler, D. T. (2009). "Laboratory Study Investigating the Three-Dimensional Turbulence and Kinematic Properties Associated with a Breaking Solitary Wave." Masters thesis, Texas A&M University, College Station, TX (August).

Syamsidik, Fahmi, M., Fatimah, E., and Fitrayansyah, A. (2018). "Coastal Land Use Changes around the Ulee Lheue Bay of Aceh during the 10-year 2004 Indian Ocean Tsunami Recovery Process." *International Journal of Disaster Risk Reduction*, 29, 24 – 36 Tsunami Recovery Processes after the 2004 Indian Ocean Tsunami and the 2011 Great East Japan Earthquake and Tsunami: Lessons Learned and Challenges.

G. J. Symons, ed. (1888). *The Eruption of Krakatoa and Subsequent Phenomena: Report of the Krakatoa Committee of the Royal Society*. Tr ubner & Co., London.

Synolakis, C. E. (1987). "The Runup of Solitary Waves." *Journal of Fluid Mechanics*, 185, 523 – 545.

Synolakis, C. E., Bardet, J.-P., Borrero, J. C., Davies, H. L., Okal, E. A., Silver, E. A., Sweet, S., and Tappin, D. R. (2002). "The Slump Origin of the 1998 Papua New Guinea Tsunami." *Proceedings: Mathematical, Physical and Engineering Sciences*, 458(2020), 763 – 789 The Royal Society.

Tadmor, E. B., Miller, R. E., and Elliott, R. S. (2012). *Continuum Mechanics and Thermodynamics: From Fundamental Concepts to Governing Equations*. Cambridge University Press.

Takabatake, T., St-Germain, P., Nistor, I., Stolle, J., and Shibayama, T. (2019). "Numerical Modelling of Coastal Inundation from Cascadia Subduction Zone Tsunamis and Implications for Coastal Communities on Western Vancouver Island, Canada." *Natural Hazards*.

Takagi, H., Pratama, M. B., Kurobe, S., Esteban, M., Aránguiz, R., and Ke, B. (2019). "Analysis of Generation and Arrival Time of Landslide Tsunami to Palu City Due to the 2018 Sulawesi Earthquake." *Landslides*, 16(5), 983 – 991.

Tanimoto, K., Takahashi, S., Kaneko, T., and Shiota, K. *Impulsive Breaking Wave Forces on an Inclined Pile Exerted by Random Waves*. Chapter 168, 2288–2302.

Tanioka, Y. and Satake, K. (1996). "Tsunami Generation by Horizontal Displacement of Ocean Bottom." *Geophysical Research Letters*, 23(8), 861 – 864.

Tappin, D. R., Matsumoto, T., Watts, P., Satake, K., McMurtry, G. M., Matsuyama, M., Lafoy, Y., Tsuji, Y., Kanamatsu, T., Lus, W., Iwabuchi, Y., Matsumotu, H. Y. Y., Nakamura, M., Hill, M. M. P., Crook, K., Anton, L., and Walsh, J. P. (1999). "Sediment Slump Likely Caused by 1998 Papua New Guinea Tsunami." *EOS, Transactions, American Geophysical Union*, 80(309), 329 – 344.

Tappin, D. R., Watts, P., and Grilli, S. T. (2008). "The Papua New Guinea Tsunami of 17 July 1998: Anatomy of a Catastrophic Event." *Natural Hazards and Earth System Sciences*, 8(2), 243 – 266.

Tavakkol, S. and Lynett, P. (2017). "Celeris: A GPU-accelerated open source software with a Boussinesq-type wave solver for real-time interactive simulation and visualization." *Computer Physics Communications*, 217, 117 – 127.

The OpenFOAM Foundation (2019). *OpenFOAM v7 User Guide*. OpenFOAM Foundation Ltd. (June).

The Star (2018). "Number of Injured in Indonesia Tsunami Surges to over 14,000." *The Star Online* Originally published online Monday, 31 Dec 2018 7:46 PM MYT.

Thio, H. K., Somerville, P., and Polet, J. (2010). "Probabilistic Tsunami Hazard in California." *Report No. 2010/108*, Pacific Earthquake Engineering Research Center (PEER), University of California, Berkeley (October). Prepared for Caltrans/Peer by URS Corporation and California State Polytechnic University.

Thomas, S. and Cox, D. (2012). "Influence of Finite-Length Seawalls for Tsunami Loading on Coastal Structures." *Journal of Waterway, Port, Coastal, and Ocean Engineering*, 138(3), 203 – 214.

Thomas, S., Killian, J., and Bridges, K.-J. (2015). "Influence of Macroroughness on Tsunami Loading of Coastal Structures." *Journal of Waterway, Port, Coastal, and Ocean Engineering*, 141(1).

Tinti, S., Manucci, A., Pagnoni, G., Armigliato, A., and Zaniboni, F. (2005). "The 30 December 2002 Landslide-Induced Tsunamis in Stromboli: Sequence of the Events Reconstructed from the Eyewitness Accounts." *Natural Hazards and Earth System Sciences*, 5(6), 763 – 775.

Tirindelli, M., Cuomo, G., Allsop, W., and Lamberti, A. (2003). "Wave-in-Deck Forces on Jetties and Related Structures." *Proceedings of the International Offshore and Polar Engineering Conference*, 2812 – 2819.

Tirindelli, M., Cuomo, G., Allsop, W., and McConnell, K. (2004). *Physical Model Studies of Wave-Induced Loading on Exposed Jetties: Towards New Prediction Formulae*. Chapter 31, 382 – 393.

Titov, V. V. and Gonzalez, F. I. (1997). "Implementation and Testing of the Method of Splitting Tsunami (MOST) Model." *Technical Memorandum ERL PMEL-112*, Pacific Marine Environmental Laboratory, National Oceanic & Atmospheric Administration (NOAA), Seattle, WA (November).

Titov, V. V., Moore, C. W., Greenslade, D. J. M., Pattiaratchi, C., Badal, R., Synolakis, C. E., and Kânoğlu, U. (2011). "A New Tool for Inundation Modeling: Community Modeling Interface for Tsunamis (ComMIT)." *Pure and Applied Geophysics*, 168(11), 2121 – 2131.

Titov, V. V. and Synolakis, C. E. (1995). "Modeling of Breaking and Nonbreaking Long-Wave Evolution and Runup using VTCS-2." *Journal of Waterway, Port, Coastal, and Ocean Engineering*, 121(6), 308 – 316.

Tollmien, W., Schlichting, H., Görtler, H., and Riegels, F. W. (1961). *Bericht über neuere Turbulenzforschung*. Springer Berlin Heidelberg, Berlin, Heidelberg, 719 – 730.

Tomiczek, T., Prasetyo, A., Mori, N., Yasuda, T., and Kennedy, A. (2016). "Physical Modelling of Tsunami Onshore Propagation, Peak Pressures, and Shielding Effects in an Urban Building Array." *Coastal Engineering*, 117, 97 – 112.

Tomiczek, T., Prasetyo, A., Mori, N., Yasuda, T., and Kennedy, A. (2017). "Effects of a Macro-Roughness Element on Tsunami Wave Amplification, Pressures, and Loads: Physical Model and Comparison to Japanese and US Design Equations." *Coastal Engineering Journal*, 59(1).

Tomita, T. and Honda, K. (2007). *Tsunami Estimation Including Effect of Coastal Structures and Buildings by 3D Model*. World Scientific Publishing Company, 681 – 692.

Tonelli, M. and Petti, M. (2013). "Numerical Simulation of Wave Overtopping at Coastal Dikes and Low-Crested Structures by Means of a Shock-Capturing Boussinesq Model." *Coastal Engineering*, 79, 75 – 88.

Toshimitsu (2014). "Clarification of Behavior of Huge Tsunami Action on Bridges - Hydraulic Model Experiment and Simulation Technology." *Mitsubishi Heavy Industries Technical Review*, 51(3), 21 – 26.

Tremblay, O. G. and Frandsen, J. (2015). "2D Numerical Viscous Predictions of Wave Impact Effects on an Idealized Seawall Rooted in Large Scale Experiments (1:4)." *Proceedings of the ASME 2015 34th International Conference on Ocean, Offshore and Arctic Engineering (OMAE 2015)*, Vol. 7: Ocean Engineering, Ocean, Offshore and Arctic Engineering Division, St. John's, Newfoundland, Canada, The American Society of Mechanical Engineers, 1 – 12 (May 31 – June 5).

Trofimovs, J., Sparks, R. S. J., and Talling, P. J. (2008). "Anatomy of a Submarine Pyroclastic Flow and Associated Turbidity Current - July 2003 Dome Collapse, Soufriere Hills Volcano, Montserrat, West Indies." *Sedimentology*, 55(3), 617 – 634.

Tsai, C.-P. and Jeng, D.-S. (1990). *Forces on Vertical Walls Due to Obliquely-Incident Waves*. Chapter 132, 1742–1754.

Umeda, S., Saitoh, T., and Furumichi, H. (2017). "Mitigation Effects of Onshore Perforated Barriers on Inundation and Forces Induced by Tsunami and Tsunami-Driven Objects." *Ocean Engineering*, 152, 89 – 99.

Unjoh, S. (2012). "Tsunami Damage to Bridge Structures in Rikuzen-Takada City and the Emergency Road Network Recovery Actions." *Proceedings of the International Symposium on Engineering Lessons Learned from the 2011 Great East Japan Earthquake*, Japan Association for Earthquake Engineering, 1429 – 1438.

Unjoh, S. and Endoh, K. (2006). "Damage Investigation and Preliminary Analyses of Bridge Damage Caused by the 2004 Indian Ocean Tsunami." *UJNR WSE Joint Panel Meeting*, number 38, Public Works Research Institute (May).

USGS (2013). "Earthquake Information by Region: Seismicity of the Earth Maps 1900-2013. United States Geological Survey (USGS) Earthquake Hazards Program.

USGS (2016). "20 Largest Earthquakes in the World. United States Geological Survey (USGS) Earthquake Hazards Program.

van de Lindt, J. W., Gupta, R., Garcia, R. A., and Wilson, J. (2009). "Tsunami Bore Forces on a Compliant Residential Building Model." *Engineering Structures*, 31(11), 2534 – 2539.

Verbeek, R. D. M. (1884). "The Krakatoa Eruption." *Nature*, 30, 10 – 15.

Verbeek, R. D. M. (1886). *Krakatau*. Imprimerie de l'état, Batavia (i.e. Jakarta), Indonesia.

Šepić, J., Vilibić, I., Rabinovich, A. B., and Monserrat, S. (2015). "Widespread Tsunami-like Waves of 23-27 June in the Mediterranean and Black Seas Generated by High-Altitude Atmospheric Forcing." *Scientific Reports*, 5(11682) Published by Nature Research.

Walton, S., Hassan, O., and Morgan, K. (2013). "Reduced Order Modelling for Unsteady Fluid Flow using Proper Orthogonal Decomposition and Radial Basis Functions." *Applied Mathematical Modelling*, 37(20), 8930 – 8945.

Weggel, J. R. (1972). "Maximum Breaker Height for Design." *Coastal Engineering Proceedings*, 1(13), 21.

Wei, G. and Kirby, J. T. (1998). "Simulation of Water Waves by Boussinesq Models." *Research Report CACR-98-02*, Center for Applied Ocean Research, Ocean Engineering Laboratory, University of Delaware, Newark, DE (March).

Widiyanto, W., Santoso, P. B., Hsiao, S.-C., and Imananta, R. T. (2019). "Post-Event Field Survey of 28 September 2018 Sulawesi Earthquake and Tsunami." *Natural Hazards and Earth System Sciences Discussions* In review.

Wiebe, D. M., Park, H., and Cox, D. T. (2014). "Application of the Goda Pressure Formulae for Horizontal Wave Loads on

Elevated Structures." *KSCE Journal of Civil Engineering*, 18(6), 1573 – 1579.

Wilcox, D. C. (1988). "Reassessment of the Scale-Determining Equation for Advanced Turbulence Models." *AIAA Journal*, 26(11), 1299 – 1310.

Willan, P. (2003). "Stromboli Eruption Unleashes Tidal Wave." *The Guardian* Originally published online Sunday January 5, 2003 7:37 EST.

Winter, A. O., Motley, M. R., and Eberhard, M. O. (2018). "Tsunami-Like Wave Loading of Individual Bridge Components." *Journal of Bridge Engineering*, 23(2), 04017137.

Witter, R. C., Kelsey, H. M., and Hemphill-Haley, E. (2003). "Great Cascadia Earthquakes and Tsunamis of the Past 6700 Years, Coquille River Estuary, Southern Coastal Oregon." *GSA Bulletin*, 115(10), 1289 – 1306.

Wong, H. K. (2015). "Three-Dimensional Effects of Tsunami Impact on Bridges." M.S. thesis, University of Washington, Seattle, WA 98195.

Wüthrich, D., Pfister, M., Nistor, I., and Schleiss, A. J. (2018). "Experimental Study on Forces Exerted on Buildings with Openings due to Extreme Hydrodynamic Events." *Coastal Engineering*, 140, 72 – 86.

Xiao, D., Fang, F., Pain, C. C., and Navon, I. M. (2017). "Towards Non-Intrusive Reduced Order 3D Free Surface Flow Modelling." *Ocean Engineering*, 140, 155 – 168.

Xiao, D., Yang, P., Fang, F., Xiang, J., Pain, C. C., and Navon, I. (2016). "Non-Intrusive Reduced Order Modelling of Fluid–Structure Interactions." *Computer Methods in Applied Mechanics and Engineering*, 303, 35 – 54.

Xu, G., Cai, C. S., and Chen, Q. (2017). "Countermeasure of Air Venting Holes in the Bridge Deck-Wave Interaction under Solitary Waves." *Journal of Performance of Constructed Facilities*, 31(1), 04016071.

Xu, G., Cai, C. S., Hu, P., and Dong, Z. (2016). "Component Level-Based Assessment of the Solitary Wave Forces on a Typical Coastal Bridge Deck and the Countermeasure of Air Venting Holes." *Practice Periodical on Structural Design and Construction*, 04016012.

Yang, W., Wen, Z., Li, F., and Li, Q. (2018). "Study on Tsunami Force Mitigation of the Rear House Protected by the Front House." *Ocean Engineering*, 159, 268 – 279.

Yeh, H. (2007). "Design Tsunami Forces for Onshore Structures." *Journal of Disaster Research*, 2(6), 531 – 536.

Yeh, H., Francis, M., Peterson, C., Katada, T., Latha, G., Chadha, R. K., Singh, J. P., and Raghuraman, G. (2007). "Effects of the 2004 Great Sumatra Tsunami: Southeast Indian Coast." *Journal of Waterway, Port, Coastal, and Ocean Engineering*, 133(6), 382 – 400.

Yim, S. C. and Azadbakht, M. (2013). "Tsunami Forces on Selected California Coastal Bridges." *Final Report CA13-1983*, California Department of Transportation (June).

Yim, S. C., Boon-intra, S., Nimmala, S. B., Winston, H. M., Azadbakht, M., and Cheung, K. F. (2011). "Development of a Guideline for Estimating Tsunami Forces on Bridge Superstructures." *Report No. OR-RD-12-03*, Oregon Department of Transportation, 200 Hawthorne Ave. SE, Suite B-240, Salem, OR 97301 (October). Prepared by Oregon State University, Corvalis, OR.

Yim, S. C. and Cheung, K. F. (2006). "Experimental and Numerical Modeling of Storm Surge and Tsunami Effects on Structures." *Proceedings of the 38*[38] *Joint Meeting of the Panel on Wind and Seismic Effects*, United States-Japan Cooperative Program in Natural Resources (UJNR) (May 15-20).

Yim, S. C., Wei, Y., Azadbakht, M., Nimmala, S., and Potisuk, T. (2015). "Case Study for Tsunami Design of Coastal Infrastructure: Spencer Creek Bridge, Oregon." *Journal of Bridge Engineering*, 20(1), 05014008.

Yokoyama, I. (1981). "A Geophysical Interpretation of the 1883 Krakatau Eruption." *Journal of Volcanology and Geothermal Research*, 9(4), 359 – 378.

Yokoyama, J. and Robertson, I. N. (2014). "Evaluation of Reinforced Concrete Buildings when Subjected to Tsunami Loads." *Research Report UHM/CEE/14-01*, Department of Civil and Environmental Engineering, University of Hawaii, Honolulu, HI (December).

Zhang, G., ichi Hoshikuma, J., and Usui, T. (2012). "An Experimental Study on Countermeasure for Mitigating Tsunami Effect on Highway Bridge." *Proceedings of the* 15^{th} *World Conference on Earthquake Engineering*, International Association for Earthquake Engineering.

Zheng, Y., Kosa, K., and Sasaki, T. (2013). "Evaluation of Bridge Outflows due to Great Tsunami." *Proceedings of the Japan Concrete Institute*, Vol. 35, Japan Concrete Institute (JCI), Nagoya, Aichi Prefecture, 841 – 846 (July).

Zijlema, M., Stelling, G., and Smit, P. (2011). "SWASH: An Operational Public Domain Code for Simulating Wave Fields and Rapidly Varied Flows in Coastal Waters." *Coastal Engineering*, 58(10), 992 – 1012.

Appendix A

OPENFOAM SCRIPTS: 0 DIRECTORY

alpha:

```
FoamFile
{
    version     2.0;
    format      ascii;
    class       volScalarField;
    object      alpha.water;
}
dimensions      [0 0 0 0 0 0 0];
internalField   uniform 0;
boundaryField
{
    paddle
    {
        type            zeroGradient;
    }
    comprLeft
    {
        type            zeroGradient;
    }
    comprRight
    {
        type            zeroGradient;
    }
    comprBottom
    {
```

```
26          type            zeroGradient;
27      }
28      comprAtmosphere
29      {
30          type            inletOutlet;
31          inletValue      uniform 0;
32          value           uniform 0;
33      }
34      fixedEnd
35      {
36          type            zeroGradient;
37      }
38      fixedLeft
39      {
40          type            zeroGradient;
41      }
42      fixedRight
43      {
44          type            zeroGradient;
45      }
46      fixedBottom
47      {
48          type            zeroGradient;
49      }
50      fixedAtmosphere
51      {
52          type            inletOutlet;
53          inletValue      uniform 0;
54          value           uniform 0;
55      }
56      TSfront
57      {
58          type            zeroGradient;
```

```
    }
    TSback
    {
        type            zeroGradient;
    }
    TSleft
    {
        type            zeroGradient;
    }
    TSright
    {
        type            zeroGradient;
    }
    TSbottom
    {
        type            zeroGradient;
    }
    TStop
    {
        type            zeroGradient;
    }
    concBlock1
    {
        type            zeroGradient;
    }
}
```

epsilon:

```
FoamFile
{
    version     2.0;
    format      ascii;
    class       volScalarField;
    location    "0";
```

```
7       object      epsilon;
8   }
9   dimensions      [0 2 -3 0 0 0 0];
10  epsilonADV1     0.000594018; // epsilon = C_mu^p*k^1.5/l_t m^2/s^3, k =
        0.00953392 m^2/s^2, C_mu = 0.09, p = 0.75, and l_t = 0.07*d_h, where d_h =
        2*SWL+W, SWL = still water level, and W = flume width
11  internalField   uniform $epsilonADV1;
12  boundaryField
13  {
14      paddle
15      {
16          type            epsilonWallFunction;
17          value           uniform $epsilonADV1;
18      }
19      comprLeft
20      {
21          type            epsilonWallFunction;
22          value           uniform $epsilonADV1;
23      }
24      comprRight
25      {
26          type            epsilonWallFunction;
27          value           uniform $epsilonADV1;
28      }
29      comprBottom
30      {
31          type            epsilonWallFunction;
32          value           uniform $epsilonADV1;
33      }
34      comprAtmosphere
35      {
36          type            inletOutlet;
37          inletValue      uniform $epsilonADV1;
```

```
38          value           uniform $epsilonADV1;
39      }
40      fixedEnd
41      {
42          type            epsilonWallFunction;
43          value           uniform $epsilonADV1;
44      }
45      fixedLeft
46      {
47          type            epsilonWallFunction;
48          value           uniform $epsilonADV1;
49      }
50      fixedRight
51      {
52          type            epsilonWallFunction;
53          value           uniform $epsilonADV1;
54      }
55      fixedBottom
56      {
57          type            epsilonWallFunction;
58          value           uniform $epsilonADV1;
59      }
60      fixedAtmosphere
61      {
62          type            inletOutlet;
63          inletValue      uniform $epsilonADV1;
64          value           uniform $epsilonADV1;
65      }
66      TSfront
67      {
68          type            epsilonWallFunction;
69          value           uniform $epsilonADV1;
70      }
```

```
    TSback
    {
        type            epsilonWallFunction;
        value           uniform $epsilonADV1;
    }
    TSleft
    {
        type            epsilonWallFunction;
        value           uniform $epsilonADV1;
    }
    TSright
    {
        type            epsilonWallFunction;
        value           uniform $epsilonADV1;
    }
    TSbottom
    {
        type            epsilonWallFunction;
        value           uniform $epsilonADV1;
    }
    TStop
    {
        type            epsilonWallFunction;
        value           uniform $epsilonADV1;
    }
    concBlock1
    {
        type            epsilonWallFunction;
        value           uniform $epsilonADV1;
    }
}
```

k:

```
FoamFile
```

```
{
    version     2.0;
    format      ascii;
    class       volScalarField;
    location    "0";
    object      k;
}
dimensions      [0 2 -2 0 0 0 0];
kADV1           0.00953392; // k = (u'^2+v'^2+w'^2)/2 m^2/s^2, (u',v',w') =
    (0.04527,-0.01247,0) m/s
internalField   uniform $kADV1;
boundaryField
{
    paddle
    {
        type            kqRWallFunction;
        value           uniform $kADV1;
    }
    comprLeft
    {
        type            kqRWallFunction;
        value           uniform $kADV1;
    }
    comprRight
    {
        type            kqRWallFunction;
        value           uniform $kADV1;
    }
    comprBottom
    {
        type            kqRWallFunction;
        value           uniform $kADV1;
    }
```

```
34      comprAtmosphere
35      {
36          type            inletOutlet;
37          inletValue      uniform $kADV1;
38          value           uniform $kADV1;
39      }
40      fixedEnd
41      {
42          type            kqRWallFunction;
43          value           uniform $kADV1;
44      }
45      fixedLeft
46      {
47          type            kqRWallFunction;
48          value           uniform $kADV1;
49      }
50      fixedRight
51      {
52          type            kqRWallFunction;
53          value           uniform $kADV1;
54      }
55      fixedBottom
56      {
57          type            kqRWallFunction;
58          value           uniform $kADV1;
59      }
60      fixedAtmosphere
61      {
62          type            inletOutlet;
63          inletValue      uniform $kADV1;
64          value           uniform $kADV1;
65      }
66      TSfront
```

```
67      {
68          type            kqRWallFunction;
69          value           uniform $kADV1;
70      }
71      TSback
72      {
73          type            kqRWallFunction;
74          value           uniform $kADV1;
75      }
76      TSleft
77      {
78          type            kqRWallFunction;
79          value           uniform $kADV1;
80      }
81      TSright
82      {
83          type            kqRWallFunction;
84          value           uniform $kADV1;
85      }
86      TSbottom
87      {
88          type            kqRWallFunction;
89          value           uniform $kADV1;
90      }
91      TStop
92      {
93          type            kqRWallFunction;
94          value           uniform $kADV1;
95      }
96      concBlock1
97      {
98          type            kqRWallFunction;
99          value           uniform $kADV1;
```

```
    }
}
```

nut:

```
FoamFile
{
    version     2.0;
    format      ascii;
    class       volScalarField;
    location    "0";
    object      nut;
}
dimensions      [0 2 -1 0 0 0 0];
internalField   uniform 0;
boundaryField
{
    paddle
    {
        type            nutkWallFunction;
        value           uniform 0;
    }
    comprLeft
    {
        type            nutkWallFunction;
        value           uniform 0;
    }
    comprRight
    {
        type            nutkWallFunction;
        value           uniform 0;
    }
    comprBottom
    {
        type            nutkWallFunction;
```

```
31          value           uniform 0;
32      }
33      comprAtmosphere
34      {
35          type            calculated;
36          value           uniform 0;
37      }
38      fixedEnd
39      {
40          type            nutkWallFunction;
41          value           uniform 0;
42      }
43      fixedLeft
44      {
45          type            nutkWallFunction;
46          value           uniform 0;
47      }
48      fixedRight
49      {
50          type            nutkWallFunction;
51          value           uniform 0;
52      }
53      fixedBottom
54      {
55          type            nutkWallFunction;
56          value           uniform 0;
57      }
58      fixedAtmosphere
59      {
60          type            calculated;
61          value           uniform 0;
62      }
63      TSfront
```

```
64      {
65          type            nutkWallFunction;
66          value           uniform 0;
67      }
68      TSback
69      {
70          type            nutkWallFunction;
71          value           uniform 0;
72      }
73      TSleft
74      {
75          type            nutkWallFunction;
76          value           uniform 0;
77      }
78      TSright
79      {
80          type            nutkWallFunction;
81          value           uniform 0;
82      }
83      TSbottom
84      {
85          type            nutkWallFunction;
86          value           uniform 0;
87      }
88      TStop
89      {
90          type            nutkWallFunction;
91          value           uniform 0;
92      }
93      concBlock1
94      {
95          type            nutkWallFunction;
96          value           uniform 0;
```

```
    }
}
```

omega:

```
FoamFile
{
    version     2.0;
    format      ascii;
    class       volScalarField;
    location    "0";
    object      omega;
}
dimensions      [0 0 -1 0 0 0 0];
omegaADV1               0.692285666; // omega = epsilon/(beta*k) s^-1, epsilon = 0.000594018 m^2/s^3, k =  0.00953392 m^2/s^2, beta* = C_mu = 0.09
internalField   uniform $omegaADV1;
boundaryField
{
    paddle
    {
        type            omegaWallFunction;
        value           uniform $omegaADV1;
    }
    comprRight
    {
        type            omegaWallFunction;
        value           uniform $omegaADV1;
    }
    comprLeft
    {
        type            omegaWallFunction;
        value           uniform $omegaADV1;
    }
    comprBottom
```

```
30      {
31          type            omegaWallFunction;
32          value           uniform $omegaADV1;
33      }
34      comprAtmosphere
35      {
36          type            inletOutlet;
37          inletValue      uniform $omegaADV1;
38          value           uniform $omegaADV1;
39      }
40      fixedEnd
41      {
42          type            omegaWallFunction;
43          value           uniform $omegaADV1;
44      }
45      fixedLeft
46      {
47          type            omegaWallFunction;
48          value           uniform $omegaADV1;
49      }
50      fixedRight
51      {
52          type            omegaWallFunction;
53          value           uniform $omegaADV1;
54      }
55      fixedBottom
56      {
57          type            omegaWallFunction;
58          value           uniform $omegaADV1;
59      }
60      fixedAtmosphere
61      {
62          type            inletOutlet;
```

```
63          inletValue      uniform $omegaADV1;
64          value           uniform $omegaADV1;
65      }
66      TSfront
67      {
68          type            omegaWallFunction;
69          value           uniform $omegaADV1;
70      }
71      TSbottom
72      {
73          type            omegaWallFunction;
74          value           uniform $omegaADV1;
75      }
76      TSleft
77      {
78          type            omegaWallFunction;
79          value           uniform $omegaADV1;
80      }
81      TSback
82      {
83          type            omegaWallFunction;
84          value           uniform $omegaADV1;
85      }
86      TSright
87      {
88          type            omegaWallFunction;
89          value           uniform $omegaADV1;
90      }
91      TStop
92      {
93          type            omegaWallFunction;
94          value           uniform $omegaADV1;
95      }
```

```
    concBlock1
    {
        type            omegaWallFunction;
        value           uniform $omegaADV1;
    }
}
```

p_rgh:

```
FoamFile
{
    version     2.0;
    format      ascii;
    class       volScalarField;
    object      p_rgh;
}
dimensions      [1 -1 -2 0 0 0 0];
internalField   uniform 0;
boundaryField
{
    paddle
    {
        type            fixedFluxPressure;
        value           uniform 0;
    }
    comprBottom
    {
        type            fixedFluxPressure;
        value           uniform 0;
    }
    comprLeft
    {
        type            fixedFluxPressure;
        value           uniform 0;
    }
```

```
27      comprRight
28      {
29          type            fixedFluxPressure;
30          value           uniform 0;
31      }
32      comprAtmosphere
33      {
34          type            totalPressure;
35          U               U;
36          phi             phi;
37          rho             rho;
38          psi             none;
39          gamma           1;
40          p0              uniform 0;
41          value           uniform 0;
42      }
43      fixedEnd
44      {
45          type            fixedFluxPressure;
46          value           uniform 0;
47      }
48      fixedLeft
49      {
50          type            fixedFluxPressure;
51          value           uniform 0;
52      }
53      fixedRight
54      {
55          type            fixedFluxPressure;
56          value           uniform 0;
57      }
58      fixedBottom
59      {
```

```
60          type            fixedFluxPressure;
61          value           uniform 0;
62      }
63      fixedAtmosphere
64          {
65          type            totalPressure;
66          U               U;
67          phi             phi;
68          rho             rho;
69          psi             none;
70          gamma           1;
71          p0              uniform 0;
72          value           uniform 0;
73      }
74      TSfront
75      {
76          type            fixedFluxPressure;
77                  value           uniform 0;
78      }
79      TSback
80      {
81          type            fixedFluxPressure;
82                  value           uniform 0;
83      }
84      TSleft
85      {
86          type            fixedFluxPressure;
87                  value           uniform 0;
88      }
89      TSright
90      {
91          type            fixedFluxPressure;
92                  value           uniform 0;
```

```
    }
    TSbottom
    {
        type            fixedFluxPressure;
                value           uniform 0;
    }
    TStop
    {
        type            fixedFluxPressure;
                value           uniform 0;
    }
    concBlock1
    {
        type            fixedFluxPressure;
                value           uniform 0;
    }
}
```

pointDisplacement:

```
FoamFile
{
    version     2.0;
    format      ascii;
    class       pointVectorField;
    location    "0.01";
    object      pointDisplacement;
}
dimensions      [0 1 0 0 0 0 0];
internalField   uniform (0 0 0);
boundaryField
{
    paddle
    {
        type                    wavemakerMovement;
```

```
16          wavemakerDictName       wavemakerMovementDict;
17          value                   uniform (0 0 0);
18      }
19      comprLeft
20      {
21          type                    fixedNormalSlip;
22          n                       (0 1 0);
23          value                   uniform (0 0 0);
24      }
25      comprRight
26      {
27          type                    fixedNormalSlip;
28          n                       (0 1 0);
29          value                   uniform (0 0 0);
30      }
31      comprBottom
32      {
33          type                    fixedNormalSlip;
34          n                       (0 0 1);
35          value                   uniform (0 0 0);
36      }
37      comprAtmosphere
38      {
39          type                    fixedNormalSlip;
40          n                       (0 0 1);
41          value                   uniform (0 0 0);
42      }
43      fixedEnd
44      {
45          type                    fixedValue;
46          value                   uniform (0 0 0);
47      }
48      fixedLeft
```

```
49      {
50          type                    fixedValue;
51          value                   uniform (0 0 0);
52      }
53      fixedRight
54      {
55          type                    fixedValue;
56          value                   uniform (0 0 0);
57      }
58      fixedBottom
59      {
60          type                    fixedValue;
61          value                   uniform (0 0 0);
62      }
63      fixedAtmosphere
64      {
65          type                    fixedValue;
66          value                   uniform (0 0 0);
67      }
68      TSfront
69      {
70          type                    fixedValue;
71          value                   uniform (0 0 0);
72      }
73      TSback
74      {
75          type                    fixedValue;
76          value                   uniform (0 0 0);
77      }
78      TSleft
79      {
80          type                    fixedValue;
81          value                   uniform (0 0 0);
```

```
82
83      }
84      TSright
85      {
86          type                    fixedValue;
87          value                   uniform (0 0 0);
88      }
89      TSbottom
90      {
91          type                    fixedValue;
92          value                   uniform (0 0 0);
93      }
94      TStop
95      {
96          type                    fixedValue;
97          value                   uniform (0 0 0);
98      }
99      concBlock1
100     {
101         type                    fixedValue;
102         value                   uniform (0 0 0);
103     }
104 }
```

U:

```
1  FoamFile
2  {
3      version     2.0;
4      format      ascii;
5      class       volVectorField;
6      location    "0";
7      object      U;
8  }
9  dimensions      [0 1 -1 0 0 0 0];
```

```
10 internalField   uniform (0 0 0);
11 boundaryField
12 {
13     paddle
14     {
15         type            movingWallVelocity;
16         value           uniform (0 0 0);
17     }
18     comprLeft
19     {
20         type            noSlip;
21     }
22     comprRight
23     {
24         type            noSlip;
25     }
26     comprBottom
27     {
28         type            noSlip;
29     }
30     comprAtmosphere
31     {
32         type            pressureInletOutletVelocity;
33         value           uniform (0 0 0);
34     }
35     fixedEnd
36     {
37         type            noSlip;
38     }
39     fixedLeft
40     {
41         type            noSlip;
42     }
```

```
43      fixedRight
44      {
45          type            noSlip;
46      }
47      fixedBottom
48      {
49          type            noSlip;
50      }
51      fixedAtmosphere
52      {
53          type            pressureInletOutletVelocity;
54          value           uniform (0 0 0);
55      }
56      TSfront
57      {
58          type            noSlip;
59      }
60      TSback
61      {
62          type            noSlip;
63      }
64      TSleft
65      {
66          type            noSlip;
67      }
68      TSright
69      {
70          type            noSlip;
71      }
72      TSbottom
73      {
74          type            noSlip;
75      }
```

```
76      TStop
77      {
78          type            noSlip;
79      }
80      concBlock1
81      {
82          type            noSlip;
83      }
84  }
```

Appendix B

OPENFOAM SCRIPTS: CONSTANT DIRECTORY

dynamicMeshDict:

```
FoamFile
{
    version     2.0;
    format      ascii;
    class       dictionary;
    location    "constant";
    object      dynamicMeshDict;
}
dynamicFvMesh       dynamicMotionSolverFvMesh;
motionSolverLibs    ("libfvMotionSolvers.so");
solver              displacementLaplacian;
displacementLaplacianCoeffs
{
    diffusivity  uniform;
}
```

g:

```
FoamFile
{
    version     2.0;
    format      ascii;
    class       uniformDimensionedVectorField;
    location    "constant";
    object      g;
}
dimensions      [0 1 -2 0 0 0 0];
```

```
value           ( 0 0 -9.81 );
```

transportProperties:

```
FoamFile
{
    version     2.0;
    format      ascii;
    class       dictionary;
    location    "constant";
    object      transportProperties;
}
phases (water air);
water
{
    transportModel  Newtonian;
    nu              [0 2 -1 0 0 0 0] 1e-06;
    rho             [1 -3 0 0 0 0 0] 1000;
}
air
{
    transportModel  Newtonian;
    nu              [0 2 -1 0 0 0 0] 1.48e-05;
    rho             [1 -3 0 0 0 0 0] 1;
}
sigma               [1 0 -2 0 0 0 0] 0.07;
```

turbulenceProperties:

```
FoamFile
{
    version     2.0;
    format      ascii;
    class       dictionary;
    location    "constant";
    object      turbulenceProperties;
```

```
}
simulationType  RAS;
RAS
{
    RASModel        kOmegaSST;
    turbulence      on;
    printCoeffs     on;
}
```

wavemakerMovementDict: In the script below, N is the number of data points, t_i is the i^{th} time in seconds, x_i is the wavemaker paddle position at time t_i in meters, and η_i is the free-surface elevation at time t_i in meters. The actual data lists have been omitted for the sake of brevity since the lists are over 20,000 values long.

```
FoamFile
{
    version     2.0;
    format      ascii;
    class       dictionary;
    location    "constant";
    object      wavemakerMovementDict;
}
wavemakerType   Piston;
tSmooth         1.5;
genAbs          0;
timeSeries N(t_1
...
t_N);
paddlePosition 1(N(x_1
...
x_N));
paddleEta 1(N(η_1
...
η_N));
```

Appendix C

OPENFOAM SCRIPTS: SYSTEM DIRECTORY

blockMeshDict:

```
FoamFile
{
    version         2.0;
    format          ascii;
    class           dictionary;
    object          blockMeshDict;
}
convertToMeters 1;
// Coordinates [m]
x1 -2.085; // initial paddle position
x2 9.915; // end of 12 m long compressible mesh region used for wave generation
x3 14.2748; // 562 in, start of first 6"-thick concrete slab lain horizontally on the flume bottom
x4 17.9324; // 706 in, end of horizontal slab and start of sloped bathymetry (1st slope = 1:12, 48' long; 2nd slope = 1:24, 36' long)
x5 28.9052; // 1138 in, intersection of beach slopes
x6 43.5356; // 1714 in, end of 2nd slope
x7 48.6048; // 43.76 m + 40 in + 6 ft, extend refined mesh by W/2 = 6' (half of the flume width) past the end of the test structure, which has a 40" sqare base
x8 61.2352; // x7 + x6 - x5, use the same x-direction length for expanding cell sizes past the test structure as was used for contracting cell sizes before the test structure
x9 80.1116; // 3154 in, end of elevated horizontal bottom section
```

```
y1 -1.8288; // -72 in, right flume wall
y2 1.8288; // 72 in, left flume wall
z1 0.0; // flume bottom near wavemaker
z2 0.1524; // 6 in, top of first horizontal slab lain on flume bottom
z3 1.15; // intersection of beach slopes
z4 1.7526; // 69 in, end of 2nd slope and elevated horizontal bottom section
z5 1.85; // still water level (broken wave: 1.85 m, unbroken wave: 2.0 m)
z6 4.572; // 180 in, top of flume walls (i.e. the "atmosphere" elevation)
vertices
(
    // x1
    ($x1 $y1 $z1) // 0
    ($x1 $y1 $z2) // 1
    ($x1 $y1 $z3) // 2
    ($x1 $y1 $z5) // 3
    ($x1 $y1 $z6) // 4
    ($x1 $y2 $z1) // 5
    ($x1 $y2 $z2) // 6
    ($x1 $y2 $z3) // 7
    ($x1 $y2 $z5) // 8
    ($x1 $y2 $z6) // 9
    // x2
    ($x2 $y1 $z1) // 10
    ($x2 $y1 $z2) // 11
    ($x2 $y1 $z3) // 12
    ($x2 $y1 $z5) // 13
    ($x2 $y1 $z6) // 14
    ($x2 $y2 $z1) // 15
    ($x2 $y2 $z2) // 16
    ($x2 $y2 $z3) // 17
    ($x2 $y2 $z5) // 18
    ($x2 $y2 $z6) // 19
    // x3
```

```
52      ($x3 $y1 $z1) // 20
53      ($x3 $y1 $z2) // 21
54      ($x3 $y1 $z3) // 22
55      ($x3 $y1 $z5) // 23
56      ($x3 $y1 $z6) // 24
57      ($x3 $y2 $z1) // 25
58      ($x3 $y2 $z2) // 26
59      ($x3 $y2 $z3) // 27
60      ($x3 $y2 $z5) // 28
61      ($x3 $y2 $z6) // 29
62      // x4
63      ($x4 $y1 $z2) // 30
64      ($x4 $y1 $z3) // 31
65      ($x4 $y1 $z5) // 32
66      ($x4 $y1 $z6) // 33
67      ($x4 $y2 $z2) // 34
68      ($x4 $y2 $z3) // 35
69      ($x4 $y2 $z5) // 36
70      ($x4 $y2 $z6) // 37
71      // x5
72      ($x5 $y1 $z3) // 38
73      ($x5 $y1 $z5) // 39
74      ($x5 $y1 $z6) // 40
75      ($x5 $y2 $z3) // 41
76      ($x5 $y2 $z5) // 42
77      ($x5 $y2 $z6) // 43
78      // x6
79      ($x6 $y1 $z4) // 44
80      ($x6 $y1 $z5) // 45
81      ($x6 $y1 $z6) // 46
82      ($x6 $y2 $z4) // 47
83      ($x6 $y2 $z5) // 48
84      ($x6 $y2 $z6) // 49
```

```
85      // x7
86      ($x7 $y1 $z4) // 50
87      ($x7 $y1 $z5) // 51
88      ($x7 $y1 $z6) // 52
89      ($x7 $y2 $z4) // 53
90      ($x7 $y2 $z5) // 54
91      ($x7 $y2 $z6) // 55
92      // x8
93      ($x8 $y1 $z4) // 56
94      ($x8 $y1 $z5) // 57
95      ($x8 $y1 $z6) // 58
96      ($x8 $y2 $z4) // 59
97      ($x8 $y2 $z5) // 60
98      ($x8 $y2 $z6) // 61
99      // x9
100     ($x9 $y1 $z4) // 62
101     ($x9 $y1 $z5) // 63
102     ($x9 $y1 $z6) // 64
103     ($x9 $y2 $z4) // 65
104     ($x9 $y2 $z5) // 66
105     ($x9 $y2 $z6) // 67
106 );
107 blocks
108 (
109     // Bottom row
110     hex (0  10 15 5  1  11 16 6)  (80  72  2) simpleGrading (1 1 1) // 1
111     hex (10 20 25 15 11 21 26 16) (44  72  2) simpleGrading (1 1 1) // 2
112     // Lower middle row
113     hex (1  11 16 6  2  12 17 7)  (80  72 10) simpleGrading (1 1 1) // 3
114     hex (11 21 26 16 12 22 27 17) (44  72 10) simpleGrading (1 1 1) // 4
115     hex (21 30 34 26 22 31 35 27) (37  72 10) simpleGrading (1 1 1) // 5
116     hex (30 38 41 34 31 38 41 35) (110 72 10) simpleGrading (1 1 1) // 6
117     // Upper middle row
```

```
118     hex (2  12 17 7  3  13 18 8)  (80  72 10) simpleGrading (1   1 0.5) // 7
119     hex (12 22 27 17 13 23 28 18) (44  72 10) simpleGrading (1   1 0.5) // 8
120     hex (22 31 35 27 23 32 36 28) (37  72 10) simpleGrading (1   1 0.5) // 9
121     hex (31 38 41 35 32 39 42 36) (110 72 10) simpleGrading (1   1 0.5) // 10
122     hex (38 44 47 41 39 45 48 42) (203 72 10) simpleGrading (0.5 1 0.5) // 11
123     hex (44 50 53 47 45 51 54 48) (102 72 10) simpleGrading (1   1 0.5) // 12
124     hex (50 56 59 53 51 57 60 54) (203 72 10) simpleGrading (2   1 0.5) // 13
125     hex (56 62 65 59 57 63 66 60) (189 72 10) simpleGrading (1   1 0.5) // 14
126     // Top row
127     hex (3  13 18 8  4  14 19 9)  (80  72 50) simpleGrading (1   1 4) // 15
128     hex (13 23 28 18 14 24 29 19) (44  72 50) simpleGrading (1   1 4) // 16
129     hex (23 32 36 28 24 33 37 29) (37  72 50) simpleGrading (1   1 4) // 17
130     hex (32 39 42 36 33 40 43 37) (110 72 50) simpleGrading (1   1 4) // 18
131     hex (39 45 48 42 40 46 49 43) (203 72 50) simpleGrading (0.5 1 4) // 19
132     hex (45 51 54 48 46 52 55 49) (102 72 50) simpleGrading (1   1 4) // 20
133     hex (51 57 60 54 52 58 61 55) (203 72 50) simpleGrading (2   1 4) // 21
134     hex (57 63 66 60 58 64 67 61) (189 72 50) simpleGrading (1   1 4) // 22
135 );
136 edges
137 (
138 );
139 boundary
140 (
141     // External boundary faces
142     paddle
143     {
144         type wall;
145         faces
146         (
147             (0 1 6 5)
148             (1 2 7 6)
149             (2 3 8 7)
150             (3 4 9 8)
```

```
151         );
152     }
153     comprBottom
154     {
155         type wall;
156         faces
157         (
158             (0 5 15 10)
159         );
160     }
161     comprLeft
162     {
163         type wall;
164         faces
165         (
166             (5 6 16 15)
167             (6 7 17 16)
168             (7 8 18 17)
169             (8 9 19 18)
170         );
171     }
172     comprRight
173     {
174         type wall;
175         faces
176         (
177             (0 10 11 1)
178             (1 11 12 2)
179             (2 12 13 3)
180             (3 13 14 4)
181         );
182     }
183     comprAtmosphere
```

```
184     {
185         type patch;
186         faces
187         (
188             (4 14 19 9)
189         );
190     }
191     fixedEnd
192     {
193         type wall;
194         faces
195         (
196             (62 65 66 63)
197             (63 66 67 64)
198         );
199     }
200     fixedLeft
201     {
202         type wall;
203         faces
204         (
205             (15 16 26 25)
206             (16 17 27 26)
207             (17 18 28 27)
208             (18 19 29 28)
209             (26 27 35 34)
210             (27 28 36 35)
211             (28 29 37 36)
212             (34 35 41 41)
213             (35 36 42 41)
214             (36 37 43 42)
215             (41 42 48 47)
216             (42 43 49 48)
```

```
217             (47 48 54 53)
218             (48 49 55 54)
219             (53 54 60 59)
220             (54 55 61 60)
221             (59 60 66 65)
222             (60 61 67 66)
223         );
224     }
225     fixedRight
226     {
227         type wall;
228         faces
229         (
230             (10 20 21 11)
231             (11 21 22 12)
232             (12 22 23 13)
233             (13 23 24 14)
234             (21 30 31 22)
235             (22 31 32 23)
236             (23 32 33 24)
237             (30 38 38 31)
238             (31 38 39 32)
239             (32 39 40 33)
240             (38 44 45 39)
241             (39 45 46 40)
242             (44 50 51 45)
243             (45 51 52 46)
244             (50 56 57 51)
245             (51 57 58 52)
246             (56 62 63 57)
247             (57 63 64 58)
248         );
249     }
```

```
250     fixedBottom
251     {
252         type wall;
253         faces
254         (
255             (10 15 25 20)
256             (20 25 26 21)
257             (21 26 34 30)
258             (30 34 41 38)
259             (38 41 47 44)
260             (44 47 53 50)
261             (50 53 59 56)
262             (56 59 65 62)
263         );
264     }
265     fixedAtmosphere
266     {
267         type wall;
268         faces
269                 (
270             (14 24 29 19)
271             (24 33 37 29)
272             (33 40 43 37)
273             (40 46 49 43)
274             (46 52 55 49)
275             (52 58 61 55)
276             (58 64 67 61)
277         );
278     }
279 );
280 mergePatchPairs
281 (
282 );
```

controlDict:

```
FoamFile
{
    version         2.0;
    format          ascii;
    location        "system";
    class           dictionary;
    object          controlDict;
}
application             olaDyMFoam;
startFrom               latestTime;
startTime               0.0;
stopAt                  endTime;
endTime                 20.0;
deltaT                  0.001;
writeControl            adjustableRunTime;
writeInterval           0.05;
purgeWrite              0;
writeFormat             ascii;
writePrecision          6;
writeCompression        uncompressed;
timeFormat              general;
timePrecision           6;
runTimeModifiable       yes;
adjustTimeStep          yes;
maxCo                   1;
maxAlphaCo              1;
maxDeltaT               0.025;
libs
(
    "libOpenFOAM.so"
);
functions
```

```
{
    fieldResiduals
    {
        type            residuals;
        libs            ("libutilityFunctionObjects.so");
        writeControl    timeStep;
        writeInterval   1;
        fields          (epsilon k p U);
    }
    frontFaceForce
    {
        type          forces;
        libs          ("libforces.so");
        writeControl  timeStep;
        timeInterval  1;
        log           yes;
        patches       (TSfront);
        rho           rhoInf;     // Indicates incompressible
        log           true;
        rhoInf        1;          // Redundant for incompressible
        CofR          (0 0 0);
        pitchAxis     (0 1 0);
    }
    rightFaceForce
    {
        type          forces;
        libs          ("libforces.so");
        writeControl  timeStep;
        timeInterval  1;
        log           yes;
        patches       (TSright);
        rho           rhoInf;     // Indicates incompressible
        log           true;
```

```
66          rhoInf          1;          // Redundant for incompressible
67          CofR            (0 0 0);
68          pitchAxis       (0 1 0);
69      }
70      leftFaceForce
71      {
72          type            forces;
73          libs            ("libforces.so");
74          writeControl    timeStep;
75          timeInterval    1;
76          log             yes;
77          patches         (TSleft);
78          rho             rhoInf;     // Indicates incompressible
79          log             true;
80          rhoInf          1;          // Redundant for incompressible
81          CofR            (0 0 0);
82          pitchAxis       (0 1 0);
83      }
84      backFaceForce
85      {
86          type            forces;
87          libs            ("libforces.so");
88          writeControl    timeStep;
89          timeInterval    1;
90          log             yes;
91          patches         (TSback);
92          rho             rhoInf;     // Indicates incompressible
93          log             true;
94          rhoInf          1;          // Redundant for incompressible
95          CofR            (0 0 0);
96          pitchAxis       (0 1 0);
97      }
98      bottomFaceForce
```

```
99      {
100         type            forces;
101         libs            ("libforces.so");
102         writeControl    timeStep;
103         timeInterval    1;
104         log             yes;
105         patches         (TSbottom);
106         rho             rhoInf;      // Indicates incompressible
107         log             true;
108         rhoInf          1;           // Redundant for incompressible
109         CofR            (0 0 0);
110         pitchAxis       (0 1 0);
111     }
112     topFaceForce
113     {
114         type            forces;
115         libs            ("libforces.so");
116         writeControl    timeStep;
117         timeInterval    1;
118         log             yes;
119         patches         (TStop);
120         rho             rhoInf;      // Indicates incompressible
121         log             true;
122         rhoInf          1;           // Redundant for incompressible
123         CofR            (0 0 0);
124         pitchAxis       (0 1 0);
125     }
126     freeSurface
127     {
128         type              interfaceHeight;
129         libs              ("libfieldFunctionObjects.so");
130         outputControl     timeStep;
131         outputInterval    1;
```

```
132         locations
133         (
134             (14.169   -1.388   0)
135             (32.443   -1.379   0)
136             (36.099   -1.368   0)
137             (39.7     -1.38    0)
138             (43.214   -1.377   0)
139             (43.212   -0.012   0)
140             (44.29    -1.306   0)
141             (45.685   -1.375   0)
142             (45.68    -0.003   0)
143         );
144         alpha     alpha.water;
145     }
146     pressureProbes
147     {
148         type                probes;
149         functionObjectLibs  ("libsampling.so");
150         writeControl        timeStep;
151         writeInterval       1;
152         probeLocations
153         (
154             (43.755   -0.3556   2.05715)
155             (43.755   -0.3556   2.13335)
156             (43.755   -0.3556   2.20955)
157             (43.755   -0.3556   2.28575)
158             (43.755    0.0      2.01905)
159             (43.755    0.0      2.05715)
160             (43.755    0.0      2.09525)
161             (43.755    0.0      2.13335)
162             (43.755    0.0      2.17145)
163             (43.755    0.0      2.20955)
164             (43.755    0.0      2.24765)
```

```
            (43.755    0.0      2.28575)
            (43.755    0.0      2.32385)
            (43.755    0.3556   2.05715)
            (43.755    0.3556   2.13335)
            (43.755    0.3556   2.20955)
            (43.755    0.3556   2.28575)
            (43.887    0.0      1.997)
            (44.141   -0.511    2.05715)
            (44.141   -0.3556   1.997)
            (44.141    0.0      1.997)
            (44.141    0.3556   1.997)
            (44.141    0.511    2.05715)
            (44.395   -0.511    2.05715)
            (44.395   -0.3556   1.997)
            (44.395    0.0      1.997)
            (44.395    0.3556   1.997)
            (44.395    0.511    2.05715)
            (44.649    0.0      1.997)
            (44.779    0.0      2.08115)
        );
        fields
        (
            p
        );
    }
    surfaces
    {
        type            surfaces;
        libs            ("libsampling.so");
        writeControl    writeTime;
        surfaceFormat   vtk;
        fields          (p U Q);
        interpolationScheme cellPoint;
```

```
198         surfaces
199         (
200             frontBox
201             {
202                 type            patch;
203                 patches         (TSfront);
204                 interpolate     true;
205             }
206         );
207     }
208 }
```

decomposeParDict_runCase:

```
1  FoamFile
2  {
3      version         2.0;
4      format          ascii;
5      location        "system";
6      class           dictionary;
7      object          decomposeParDict;
8  }
9  numberOfSubdomains 64;
10 method          scotch;
11 simpleCoeffs
12 {
13     n               ( 8 2 4 );
14     delta           0.001;
15 }
16 hierarchicalCoeffs
17 {
18     n               ( 8 2 4 );
19     delta           0.001;
20     order           xyz;
21 }
```

```
metisCoeffs
{
    processorWeights ( 1 1 1 1 );
}
manualCoeffs
{
    dataFile        "";
}
distributed     no;
roots     ();
```

decomposeParDict_sHM:

```
FoamFile
{
    version         2.0;
    format          ascii;
    location        "system";
    class           dictionary;
    object          decomposeParDict;
}
numberOfSubdomains 32;
method          hierarchical;
simpleCoeffs
{
    n               ( 8 2 2 );
    delta           0.001;
}
hierarchicalCoeffs
{
    n               ( 8 2 2 );
    delta           0.001;
    order           xyz;
}
metisCoeffs
```

```
{
    processorWeights ( 1 1 1 1 );
}
manualCoeffs
{
    dataFile        "";
}
distributed     no;
roots       ();
```

fvSchemes:

```
FoamFile
{
    version     2.0;
    format      ascii;
    class       dictionary;
    location    "system";
    object      fvSchemes;
}
// Time Derivative Schemes
// ------------------------
// steadyState; does not solve for time derivatives (i.e. sets time
   derivatives to zero)
// Euler;       transient, 1st-order accurate, bounded, implicit
// localEuler;  local-time step, 1st-order accurate, bounded, implicit
// CoEuler;
// backward;    transient, 2nd-order accurate, potentially unbounded, implicit
// bounded;
// SLTS;
// CrankNicolson; transient, 2nd-order accurate, bounded, implicit; requires
   an off-centering coefficient, psi, where psi = 1 is pure CrankNicolson and
   psi = 0 is Euler; in <caseDict>/system/fvSolution, the parameter
   nAlphaSubCycles must be set to 1 to be able to use the Crank-Nicolson
   method
```

```
19
20 ddtSchemes
21 {
22     default     Euler;
23 }
24
25 // ************************************************************************* //
26
27 // Gradient Schemes
28 // ----------------
29 // Gauss <interpolationScheme>; 2nd-order accurate, Gaussian integration
30 // leastSquares;                2nd-order accurate, least squares
31 // fourth;                      fourth-order accurate, least squares
32 // cellLimited <gradScheme>;    cell-limited version of one of the above
       schemes
33 // faceLimited <gradScheme>;    cell-limited version of one of the above
       schemes
34
35 gradSchemes
36 {
37     default     Gauss linear;
38 }
39
40 // ************************************************************************* //
41
42 // Divergence Schemes
43 // ------------------
44 // Syntax:
45 // Gauss <interpolationScheme>;
46
47 divSchemes
48 {
49     div(rhoPhi,U)                           Gauss limitedLinearV 1;
```

```
50      div(U)                                          Gauss linear;
51      div((rhoPhi|interpolate(porosity)),U)           Gauss limitedLinearV 1;
52      div(rhoPhiPor,UPor)                             Gauss limitedLinearV 1;
53      div(rhoPhi,UPor)                                Gauss limitedLinearV 1;
54      div(rhoPhiPor,U)                                Gauss limitedLinearV 1;
55      div(phi,alpha)                                  Gauss vanLeer;
56      div(phirb,alpha)                                Gauss interfaceCompression;
57      div((muEff*dev(T(grad(U)))))                    Gauss linear;
58      div(phi,k)                                      Gauss upwind;
59      div(phi,epsilon)                                Gauss upwind;
60      div((phi|interpolate(porosity)),k)              Gauss upwind;
61      div((phi|interpolate(porosity)),epsilon)        Gauss upwind;
62      div(phi,omega)                                  Gauss upwind;
63      div((phi|interpolate(porosity)),omega)          Gauss upwind;
64  }
65
66  // Laplacian Schemes
67  // ------------------
68  //      Gauss <interpolationScheme> <snGradScheme>
69
70  laplacianSchemes
71  {
72      default     Gauss linear corrected;
73  }
74
75  // ************************************************************************* //
76
77  // Interpolation Schemes
78  // ---------------------
79  // Centered Schemes:
80  //    linear;           2nd-order accurate, unbounded
81  //    cubicCorrection;
82  //    midPoint;         1st/2nd-order accurate,
```

```
83 //    Upwinded Schemes:
84 //    upwind;          1st-order accurate, unbounded, generally too inaccurate
   to be recommended
85 //    LUST;            Linear-Upwind Stabilised Transport, weighted combination
    of linear and linearUpwind with weights 0.75 and 0.25, respectively
86 //    linearUpwind;    Beam-Warming Method, 2nd-order accurate, upwind-biased
   and unbounded, but much less so than the linear scheme
87 //    linearUpwindV;
88 //    skewLinear;
89 //    filteredLinear;  1st-order accurate, attempts to limit the unboundedness
   of the linear scheme, yet it's still unbounded
90 //    filteredLinear2; 2nd-order accurate, attempts to limit the unboundedness
   of the linear scheme, yet it's still unbounded
91 //    filteredLinear3; 3rd-order accurate, attempts to limit the unboundedness
   of the linear scheme, yet it's still unbounded
92 //    QUICK;           Quadratic Upstream Interpolation for Convective
   Kinematics, 2nd-order accurate, unbounded
93 // Total Variation Diminishing (TVD) Schemes:
94 //    limitedCubic;
95 //    limitedCubicV;
96 //    limitedLinear;   linear that limits toward upwind in regions of rapidly-
   changing gradient, which requires a coefficient, where 1 = upwind and 0 =
   linear
97 //    limitedLinearV;  same as above, but calculates a single limiter
   coefficient for all vector components instead of individual limiters for
   each vector component
98 //    limitedVanLeer;
99 //    Minmod;          diffusive and slow to converge
100 //   MUSCL;           Monotone Upstream-centered Schemes for Conservation Laws
    , 2nd-order accurate, unbounded
101 //   OSPRE;
102 //   UMIST;
103 //   SuperBee;        over-compressive
```

```
104 //    vanAlbada;
105 //    vanLeer;
106 //    vanLeerV;
107 // Normalized Variable Formulation/Diagram (NVF/NVD) Schemes:
108 //    SFCD;
109 //    SFCDV;
110 //    Gamma;
111 //    GammaV;
112
113 interpolationSchemes
114 {
115     default     linear;
116 }
117
118 // ************************************************************************* //
119
120 // Surface Normal Gradient Schemes
121 // ------------------------------
122 // orthogonal;
123 // corrected;      explicit non-orthogonal correction, generally recommended,
    but for maximum non-orthogonality above 70 degrees, limiting may be
    required. For non-orthogonality above 80 degrees, convergence is generally
    hard to achieve
124 // uncorrected;    no non-orthogonal correction
125 // limited <psi>; limited non-orthogonal correction, psi = 0 is uncorrected,
    psi = 0.333 offers improved stability, psi = 0.5 offers greater accuracy,
    psi = 1 is corrected
126 // limited corrected <psi>;
127 // bounded;        bounded correction for positive scalars
128 // fourth;         fourth-order accurate
129
130 snGradSchemes
131 {
```

```
132     default     corrected;
133 }
134
135 // ************************************************************************* //
136
137 fluxRequired
138 {
139     default no;
140     p_rgh;
141     pcorr;
142     alpha.water;
143 }
144
145 wallDist
146 {
147     method meshWave;
148 }
```

fvSolution:

```
1  FoamFile
2  {
3      version     2.0;
4      format      ascii;
5      class       dictionary;
6      location    "system";
7      object      fvSolution;
8  }
9  solvers
10 {
11     "alpha.water.*"
12     {
13         nAlphaCorr              2;
14         nAlphaSubCycles         2;
15         alphaOuterCorrectors    yes;
```

```
16          cAlpha                  1;
17          icAlpha                 0;
18          MULESCorr               yes;
19          nLimiterIter            10;
20          applyAlphaPrevCorr      yes;
21          solver                  smoothSolver;
22          smoother                symGaussSeidel;
23          tolerance               1e-8;
24          relTol                  0;
25          minIter                 1;
26      }
27      "pcorr.*"
28      {
29          solver                  PCG;
30          preconditioner
31          {
32              preconditioner      GAMG;
33              smoother            GaussSeidel;
34              tolerance           1e-5;
35              relTol              0;
36          };
37          tolerance               1e-5;
38          relTol                  0;
39      }
40      pcorrFinal
41      {
42          $pcorr;
43          relTol                  0;
44      }
45      p_rgh
46      {
47          solver                  GAMG;
48          smoother                DIC;
```

```
49          tolerance           1e-08;
50          relTol              0.01;
51      }
52      p_rghFinal
53      {
54          $p_rgh;
55          relTol              0;
56      }
57      "(U|k|omega).*"
58      {
59          solver              smoothSolver;
60          smoother            symGaussSeidel;
61          nSweeps             1;
62          tolerance           1e-8;
63          relTol              0.1;
64          minIter             1;
65      }
66      cellDisplacement
67      {
68          solver              GAMG;
69          tolerance           1e-5;
70          relTol              0;
71          smoother            GaussSeidel;
72          cacheAgglomeration  false;
73          nCellsInCoarsestLevel 10;
74          agglomerator        faceAreaPair;
75          mergeLevels         1;
76      }
77      cellDisplacementFinal
78      {
79          $cellDisplacement;
80          relTol              0;
81      }
```

```
}
PIMPLE
{
    momentumPredictor           no;
    nOuterCcorrectors           1;
    nCorrectors                 3;
    nNonOrthogonalCorrectors    0;
}
relaxationFactors
{
    fields
    {
    }
    equations
    {
        ".*" 1;
    }
}
```

meshQualityDict:

```
FoamFile
{
    version     2.0;
    format      ascii;
    class       dictionary;
    object      meshQualityDict;
}
maxNonOrtho          65;
maxBoundarySkewness  15;
maxInternalSkewness  4;
maxConcave           80;
// Minimum cell pyramid volume; case dependent
minVol               1e-13;
//  1e-15 (small positive) to enable tracking
```

```
// -1e+30 (large negative) for best layer insertion
minTetQuality       1e-15;
// if >0 : preserve single cells with all points on the surface if the
// resulting volume after snapping (by approximation) is larger than
// minVolCollapseRatio times old volume (i.e. not collapsed to flat cell).
//  If <0 : delete always.
// minVolCollapseRatio 0.5;
minArea             -1;
minTwist            0.02;
minDeterminant      0.001;
minFaceWeight       0.02;
minVolRatio         0.01;
minTriangleTwist    -1;
nSmoothScale        4;
errorReduction      0.75;
relaxed
{
    maxNonOrtho     65;
}
nSmoothScale        4; // Number of error distribution iterations
errorReduction      0.75; // amount to scale back displacement at error points
```

setFieldsDict:

```
FoamFile
{
    version     2.0;
    format      ascii;
    class       dictionary;
    location    "system";
    object      setFieldsDict;
}
defaultFieldValues
(
    volScalarFieldValue alpha.water 0
```

```
);
regions
(
    boxToCell
    {
        box (-10 -10 -1) (100 10 1.85); // broken: 1.85, unbroken: 2.0
        fieldValues
        (
            volScalarFieldValue alpha.water 1
        );
    }
);
```

snappyHexMeshDict_testStruct:

```
FoamFile
{
    version     2.0;
    format      ascii;
    class       dictionary;
    object      snappyHexMeshDict;
}
// Choose which of the steps to run
castellatedMesh true;
snap            false;
addLayers       false;

// Geometry. Definition of all surfaces. All surfaces are of class
// searchableSurface.
// Surfaces are used
// - to specify refinement for any mesh cell intersecting it
// - to specify refinement for any mesh cell inside/outside/near
// - to 'snap' the mesh boundary to the surface
geometry
{
```

```
    TSfront
    {
        type triSurfaceMesh;
        file "TSfront.stl";
    }
    TSback
    {
        type triSurfaceMesh;
        file "TSback.stl";
    }
    TSleft
    {
        type triSurfaceMesh;
        file "TSleft.stl";
    }
    TSright
    {
        type triSurfaceMesh;
        file "TSright.stl";
    }
    TSbottom
    {
        type triSurfaceMesh;
        file "TSbottom.stl";
    }
    TStop
    {
        type triSurfaceMesh;
        file "TStop.stl";
    }
};

// Settings for the castellatedMesh generation.
```

```
54 castellatedMeshControls
55 {
56     // Refinement parameters
57     // ~~~~~~~~~~~~~~~~~~~~~
58
59     // If local number of cells is >= maxLocalCells on any processor
60     // switches from from refinement followed by balancing
61     // (current method) to (weighted) balancing before refinement.
62     maxLocalCells 1000000;
63
64     // Overall cell limit (approximately). Refinement will stop immediately
65     // upon reaching this number so a refinement level might not complete.
66     // Note that this is the number of cells before removing the part which
67     // is not 'visible' from the keepPoint. The final number of cells might
68     // actually be a lot less.
69     maxGlobalCells 20000000;
70
71     // The surface refinement loop might spend lots of iterations refining
          just a
72     // few cells. This setting will cause refinement to stop if <=
          minimumRefine
73     // are selected for refinement. Note: it will at least do one iteration
74     // (unless the number of cells to refine is 0)
75     minRefinementCells 10;
76
77     // Number of buffer layers between different levels.
78     // 1 means normal 2:1 refinement restriction, larger means slower
79     // refinement.
80     nCellsBetweenLevels 4;
81
82     // Explicit feature edge refinement
83     // ~~~~~~~~~~~~~~~~~~~~~~~~~~~~~~~~
84
```

```
85      // Specifies a level for any cell intersected by its edges.
86      // This is a featureEdgeMesh, read from constant/triSurface for now.
87      features
88      (
89      );
90
91      // Surface based refinement
92      // ~~~~~~~~~~~~~~~~~~~~~~~~
93
94      // Specifies two levels for every surface. The first is the minimum level,
95      // every cell intersecting a surface gets refined up to the minimum level.
96      // The second level is the maximum level. Cells that 'see' multiple
97      // intersections where the intersections make an
98      // angle > resolveFeatureAngle get refined up to the maximum level.
99
100     refinementSurfaces
101     {
102         TSfront
103         {
104             level (2 2); // Surface-wise min and max refinement level
105         }
106         TSbottom
107         {
108             level (2 2);
109         }
110         TSleft
111         {
112             level (2 2);
113         }
114         TSback
115         {
116             level (2 2);
117         }
```

```
118         TSright
119         {
120             level (2 2);
121         }
122         TStop
123         {
124             level (2 2);
125         }
126     }
127
128     // Resolve sharp angles
129     resolveFeatureAngle 30;
130
131     // Region-wise refinement
132     // ~~~~~~~~~~~~~~~~~~~~~~
133
134     // Specifies refinement level for cells in relation to a surface. One of
135     // three modes
136     // - distance. 'levels' specifies per distance to the surface the
137     //   wanted refinement level. The distances need to be specified in
138     //   descending order.
139     // - inside. 'levels' is only one entry and only the level is used. All
140     //   cells inside the surface get refined up to the level. The surface
141     //   needs to be closed for this to be possible.
142     // - outside. Same but cells outside.
143
144     refinementRegions
145     {
146     }
147
148     // Mesh selection
149     // ~~~~~~~~~~~~~~
150
```

```
151     // After refinement patches get added for all refinementSurfaces and
152     // all cells intersecting the surfaces get put into these patches. The
153     // section reachable from the locationInMesh is kept.
154     // NOTE: This point should never be on a face, always inside a cell, even
155     // after refinement.
156     locationInMesh (3.1459 0.31459 3.1459);
157 
158     // Whether any faceZones (as specified in the refinementSurfaces)
159     // are only on the boundary of corresponding cellZones or also allow
160     // free-standing zone faces. Not used if there are no faceZones.
161     allowFreeStandingZoneFaces true;
162 }
163 
164 snapControls
165 {
166     // Number of patch smoothing iterations before finding correspondence
167     // to surface
168     nSmoothPatch 5; // or 15;
169 
170     // Relative distance for points to be attracted by surface feature point
171     // or edge. True distance is this factor times local
172     // maximum edge length.
173     tolerance 2;  // or 0.1;
174 
175     //- Number of mesh displacement relaxation iterations.
176     nSolveIter 30;
177 
178     //- Maximum number of snapping relaxation iterations. Should stop
179     //  before upon reaching a correct mesh.
180     nRelaxIter 5;
181 
182     // Feature snapping
183 
```

```
184         // Number of feature edge snapping iterations.
185         // Leave out altogether to disable.
186         nFeatureSnapIter 10;
187 
188         // Detect (geometric only) features by sampling the surface
189         // (default=false).
190         implicitFeatureSnap false;
191 
192         // Use castellatedMeshControls::features (default = true)
193         explicitFeatureSnap true;
194 
195         // Detect points on multiple surfaces (only for explicitFeatureSnap)
196         multiRegionFeatureSnap false;
197 }
198 
199 // Settings for the layer addition.
200 addLayersControls
201 {
202     // Are the thickness parameters below relative to the undistorted
203     // size of the refined cell outside layer (true) or absolute sizes (false)
        .
204     relativeSizes true;
205 
206     // Per final patch (so not geometry!) the layer information
207     layers
208     {
209         suplat
210         {
211             nSurfaceLayers 2;
212         }
213     }
214 
215     // Expansion factor for layer mesh
```

```
216     expansionRatio 1.0;
217
218     // Wanted thickness of final added cell layer. If multiple layers
219     // is the thickness of the layer furthest away from the wall.
220     // Relative to undistorted size of cell outside layer.
221     // See relativeSizes parameter.
222     finalLayerThickness 0.3;
223
224     // Minimum thickness of cell layer. If for any reason layer
225     // cannot be above minThickness do not add layer.
226     // Relative to undistorted size of cell outside layer.
227     minThickness 0.1;
228
229     // If points get not extruded do nGrow layers of connected faces that are
230     // also not grown. This helps convergence of the layer addition process
231     // close to features.
232     // Note: changed(corrected) w.r.t 17x! (didn't do anything in 17x)
233     nGrow 0;
234
235     // Advanced settings
236
237     // When not to extrude surface. 0 is flat surface, 90 is when two faces
238     // are perpendicular
239     featureAngle 60;
240
241     // At non-patched sides allow mesh to slip if extrusion direction makes
242     // angle larger than slipFeatureAngle.
243     slipFeatureAngle 30;
244
245     // Maximum number of snapping relaxation iterations. Should stop
246     // before upon reaching a correct mesh.
247     nRelaxIter 3;
248
```

```
249     // Number of smoothing iterations of surface normals
250     nSmoothSurfaceNormals 1;
251
252     // Number of smoothing iterations of interior mesh movement direction
253     nSmoothNormals 3;
254
255     // Smooth layer thickness over surface patches
256     nSmoothThickness 10;
257
258     // Stop layer growth on highly warped cells
259     maxFaceThicknessRatio 0.5;
260
261     // Reduce layer growth where ratio thickness to medial
262     // distance is large
263     maxThicknessToMedialRatio 0.3;
264
265     // Angle used to pick up medial axis points
266     // Note: changed(corrected) w.r.t 17x! 90 degrees corresponds to 130 in 17
            x.
267     minMedianAxisAngle 90;
268
269     // Create buffer region for new layer terminations
270     nBufferCellsNoExtrude 0;
271
272     // Overall max number of layer addition iterations. The mesher will exit
273     // if it reaches this number of iterations; possibly with an illegal
274     // mesh.
275     nLayerIter 50;
276 }
277
278 // Generic mesh quality settings. At any undoable phase these determine
279 // where to undo.
280 meshQualityControls
```

```
{
    #include "meshQualityDict"
}

// Settings for the snapping.
// Merge tolerance. Is fraction of overall bounding box of initial mesh.
// Note: the write tolerance needs to be higher than this.
mergeTolerance 1e-6;
```

snappyHexMeshDict_concBlocks:

```
FoamFile
{
    version     2.0;
    format      ascii;
    class       dictionary;
    object      snappyHexMeshDict;
}
castellatedMesh true;
snap            true;
addLayers       false;
geometry
{
    concBlock1
    {
        type triSurfaceMesh;
        file "concBlock1.stl";
    }
};
castellatedMeshControls
{
    maxLocalCells        10000000;
    maxGlobalCells       200000000;
    minRefinementCells   10;
    nCellsBetweenLevels  2;
```

```
25      features
26      (
27      );
28      refinementSurfaces
29      {
30          concBlock1
31          {
32              level (2  2);
33          }
34      }
35      resolveFeatureAngle 30;
36      refinementRegions
37      {
38      }
39      locationInMesh              (3.1416 0.31416 0.31416);
40      allowFreeStandingZoneFaces true;
41  }
42  snapControls
43  {
44      nSmoothPatch            5;
45      tolerance               2;
46      nSolveIter              30;
47      nRelaxIter              5;
48      nFeatureSnapIter        10;
49      implicitFeatureSnap     false;
50      explicitFeatureSnap     true;
51      multiRegionFeatureSnap false;
52  }
53  addLayersControls
54  {
55      relativeSizes true;
56      layers
57      {
```

```
    }
    expansionRatio              1;
    finalLayerThickness         0.3;
    minThickness                0.1;
    nGrow                       0;
    featureAngle                60;
    slipFeatureAngle            30;
    nRelaxIter                  3;
    nSmoothSurfaceNormals       1;
    nSmoothNormals              3;
    nSmoothThickness            10;
    maxFaceThicknessRatio       0.5;
    maxThicknessToMedialRatio   0.3;
    minMedianAxisAngle          90;
    nBufferCellsNoExtrude       0;
    nLayerIter                  50;
}
meshQualityControls
{
    #include "meshQualityDict"
}
mergeTolerance 1e-06;
```

surfaceFeatureExtractDict:

```
FoamFile
{
    version     2.0;
    format      ascii;
    class       dictionary;
    object      surfaceFeatureExtractDict;
}
TSfront.stl
{
    // How to obtain raw features (extractFromFile || extractFromSurface)
```

```
11      extractionMethod      extractFromSurface;
12      extractFromSurfaceCoeffs
13      {
14          includedAngle     150; // Mark edges whose adjacent surface normals are
                at an angle less than included angle as features (0: selects no
               edges, 180: selects all edges)
15      }
16      subsetFeatures
17      {
18          // Keep nonManifold edges (edges with >2 connected faces)
19          nonManifoldEdges yes;
20
21          // Keep open edges (edges with 1 connected face)
22          openEdges        yes;
23      }
24      // Write features to obj format for postprocessing
25      writeObj             yes;
26  }
27  TSback.stl
28  {
29      extractionMethod      extractFromSurface;
30      extractFromSurfaceCoeffs
31      {
32          includedAngle     150;
33      }
34      subsetFeatures
35      {
36          nonManifoldEdges yes;
37          openEdges        yes;
38      }
39      writeObj             yes;
40  }
41  TSleft.stl
```

```
{
    extractionMethod      extractFromSurface;
    extractFromSurfaceCoeffs
    {
        includedAngle     150;
    }
    subsetFeatures
    {
        nonManifoldEdges yes;
        openEdges        yes;
    }
    writeObj             yes;
}
TSright.stl
{
    extractionMethod      extractFromSurface;
    extractFromSurfaceCoeffs
    {
        includedAngle     150;
    }
    subsetFeatures
    {
        nonManifoldEdges yes;
        openEdges        yes;
    }
    writeObj             yes;
}
TSbottom.stl
{
    extractionMethod      extractFromSurface;
    extractFromSurfaceCoeffs
    {
        includedAngle     150;
```

```
    }
    subsetFeatures
    {
        nonManifoldEdges yes;
        openEdges        yes;
    }
    writeObj             yes;
}
TStop.stl
{
    extractionMethod     extractFromSurface;
    extractFromSurfaceCoeffs
    {
        includedAngle    150;
    }
    subsetFeatures
    {
        nonManifoldEdges yes;
        openEdges        yes;
    }
    writeObj             yes;
}
```

Appendix D

BASH SCRIPTS: CASE DIRECTORY

buildCase.sh: This batch script was used to submit OpenFOAM jobs to non-checkpoint (see runCase.sh discussion) high-performance computing (HPC) queues that completed meshing, setting initial conditions, and decomposing cases prior to running them. Note that this example uses multiple `decomposeParDict` files to handle using `snappyHexMesh` and running a case using `olaDyMFlow` with the runCase.sh batch script. Additionally, multiple `snappyHexMeshDict` files were used to handle meshing the test structure and MREs separately.

```
#!/bin/bash
#SBATCH --job-name=build-<case name>
#SBATCH --account=lehman
#SBATCH --partition=lehman
#SBATCH --nodes=2
#SBATCH --time=2:00:00
#SBATCH --mem=58G
#SBATCH --ntasks-per-node=16
#SBATCH --workdir=<case path>
#SBATCH --mail-type=ALL
#SBATCH --mail-user=<email>

echo loading GCC, OpenMPI, and OpenFOAM-5.0...
module load <compiler + mpi module name>
source <OpenFOAM bashrc file path>

echo Preparing 0 folder...
if [ -d 0 ]; then
```

```
19      rm -r 0
20  fi
21  cp -r 0.org 0
22
23  echo blockMesh meshing...
24  blockMesh > log.blockMesh
25
26  echo surfaceFeatureExtract extracting...
27  surfaceFeatureExtract > log.surfFeatExt
28
29  echo decomposePar setting up parallel case...
30  cp ./system/decompParDict_sHM ./system/decomposeParDict
31  decomposePar -copyZero > log.decomp_sHM
32
33  echo snappyHex meshing testStruct...
34  cp ./system/snappyHexMeshDict_testStruct ./system/snappyHexMeshDict
35  mpirun -np 32 snappyHexMesh -parallel -overwrite > log.sHM_testStruct
36
37  echo snappyHex meshing concBlocks...
38  cp ./system/snappyHexMeshDict_concBlocks ./system/snappyHexMeshDict
39  mpirun -np 32 snappyHexMesh -parallel -overwrite > log.sHM_concBlocks
40
41  echo reconstructParMesh rebuilding mesh...
42  reconstructParMesh -constant -mergeTol 1e-6 > log.reconMesh_sHM
43
44  echo reconstructPar rebuilding fields...
45  reconstructPar > log.reconFields_sHM
46  rm -r processor*
47
48  echo checking mesh quality...
49  checkMesh > log.checkMesh
50
51  echo Setting the fields...
```

```
setFields > log.setFields

echo decomposePar setting up parallel case...
cp ./system/decompParDict_runCase ./system/decomposeParDict
decomposePar > log.decomp_runCase

echo Mesh built, ICs set, and parallel decomposition complete
```

runCase.sh: This batch script was used to submit jobs that ran OpenFOAM cases in parallel in a HPC cluster that had checkpointing enabled, which allowed for shared use of computation nodes when owners were not using their nodes (i.e. cases can be stopped and restarted as nodes became available since `startFrom` was set to `latestTime` in the `controlDict` file).

```
#!/bin/bash
#SBATCH --job-name=run-<case name>
#SBATCH --account=lehman-ckpt
#SBATCH --partition=ckpt
#SBATCH --nodes=4
#SBATCH --time=4:30:00 # set over the max run time (4 hrs) to avoid jobs
    ending early
#SBATCH --mem=58G
#SBATCH --ntasks-per-node=16
#SBATCH --constraint="Ivybridge" # options: "Ivybridge", "Sandybridge"
#SBATCH --workdir=<case path>
#SBATCH --mail-type=ALL
#SBATCH --mail-user=<email>

echo loading GCC, OpenMPI, and OpenFOAM-5.0...
module load <compiler + mpi module name>
source <OpenFOAM bashrc file path>

echo running olaDyMFlow in parallel...
mpirun -np 64 olaDyMFlow -parallel > log.olaDyMFlow
```

reconstructCase.sh: This is an example of case reconstruction from parallel to serial after a case has completed running. In this example, a broken wave case was run for 20 seconds of simulated time, which was just enough time to let the wave pass the test structure considering the fact that 10 seconds of time were truncated from the original experimental wavemaker displacement time history. Since a `writeInterval` of 0.05 seconds was specified in the `controlDict` file, there are 400 time steps to reconstruct, which can be done using the `reconstructPar` command. However, this command cannot work in parallel so the script uses the `reconstructPar` command multiple times, letting it run in the background using the & option at the end of each line. The number of times the command is executed was set to be the number of available processors, which was 16 in this example. The number of time steps specified for each command was determined by splitting up the 400 time steps as equally as possible.

```
#!/bin/bash
#SBATCH --job-name=recon-<case name>
#SBATCH --account=motley
#SBATCH --partition=motley
#SBATCH --nodes=1
#SBATCH --time=48:00:00
#SBATCH --mem=58G
#SBATCH --ntasks-per-node=16
#SBATCH --workdir=<case path>
#SBATCH --mail-type=ALL
#SBATCH --mail-user=<email>

echo loading GCC, OpenMPI, and OpenFOAM-5.0...
module load <compiler + mpi module name>
source <OpenFOAM bashrc file path>

echo reconstructPar rebuilding fields...
reconstructPar -time '0.05,0.1,0.15,0.2,0.25,0.3,0.35,0.4,0.45,0.5,0.55,0.6,
                      0.65,0.7,0.75,0.8,0.85,0.9,0.95,1,1.05,1.1,1.15,1.2,
```

```
                        1.25' &
reconstructPar -time '1.3,1.35,1.4,1.45,1.5,1.55,1.6,1.65,1.7,1.75,1.8,1.85,
                        1.9,1.95,2,2.05,2.1,2.15,2.2,2.25,2.3,2.35,2.4,2.45,
                        2.5' &
reconstructPar -time '2.55,2.6,2.65,2.7,2.75,2.8,2.85,2.9,2.95,3,3.05,3.1,
                        3.15,3.2,3.25,3.3,3.35,3.4,3.45,3.5,3.55,3.6,3.65,3.7,
                        3.75' &
reconstructPar -time '3.8,3.85,3.9,3.95,4,4.05,4.1,4.15,4.2,4.25,4.3,4.35,
                        4.4,4.45,4.5,4.55,4.6,4.65,4.7,4.75,4.8,4.85,4.9,4.95,
                        5' &
reconstructPar -time '5.05,5.1,5.15,5.2,5.25,5.3,5.35,5.4,5.45,5.5,5.55,5.6,
                        5.65,5.7,5.75,5.8,5.85,5.9,5.95,6,6.05,6.1,6.15,6.2,
                        6.25' &
reconstructPar -time '6.3,6.35,6.4,6.45,6.5,6.55,6.6,6.65,6.7,6.75,6.8,6.85,
                        6.9,6.95,7,7.05,7.1,7.15,7.2,7.25,7.3,7.35,7.4,7.45,
                        7.5' &
reconstructPar -time '7.55,7.6,7.65,7.7,7.75,7.8,7.85,7.9,7.95,8,8.05,8.1,
                        8.15,8.2,8.25,8.3,8.35,8.4,8.45,8.5,8.55,8.6,8.65,8.7,
                        8.75' &
reconstructPar -time '8.8,8.85,8.9,8.95,9,9.05,9.1,9.15,9.2,9.25,9.3,9.35,
                        9.4,9.45,9.5,9.55,9.6,9.65,9.7,9.75,9.8,9.85,9.9,9.95,
                        10' &
reconstructPar -time '10.05,10.1,10.15,10.2,10.25,10.3,10.35,10.4,10.45,10.5,
                        10.55,10.6,10.65,10.7,10.75,10.8,10.85,10.9,10.95,11,
                        11.05,11.1,11.15,11.2,11.25' &
reconstructPar -time '11.3,11.35,11.4,11.45,11.5,11.55,11.6,11.65,11.7,11.75,
                        11.8,11.85,11.9,11.95,12,12.05,12.1,12.15,12.2,12.25,
                        12.3,12.35,12.4,12.45,12.5' &
reconstructPar -time '12.55,12.6,12.65,12.7,12.75,12.8,12.85,12.9,12.95,13,
                        13.05,13.1,13.15,13.2,13.25,13.3,13.35,13.4,13.45,13.5,
                        13.55,13.6,13.65,13.7,13.75' &
reconstructPar -time '13.8,13.85,13.9,13.95,14,14.05,14.1,14.15,14.2,14.25,
                        14.3,14.35,14.4,14.45,14.5,14.55,14.6,14.65,14.7,14.75,
```

```
53                      14.8,14.85,14.9,14.95,15' &
54  reconstructPar -time '15.05,15.1,15.15,15.2,15.25,15.3,15.35,15.4,15.45,15.5,
55                      15.55,15.6,15.65,15.7,15.75,15.8,15.85,15.9,15.95,16,
56                      16.05,16.1,16.15,16.2,16.25' &
57  reconstructPar -time '16.3,16.35,16.4,16.45,16.5,16.55,16.6,16.65,16.7,16.75,
58                      16.8,16.85,16.9,16.95,17,17.05,17.1,17.15,17.2,17.25,
59                      17.3,17.35,17.4,17.45,17.5' &
60  reconstructPar -time '17.55,17.6,17.65,17.7,17.75,17.8,17.85,17.9,17.95,18,
61                      18.05,18.1,18.15,18.2,18.25,18.3,18.35,18.4,18.45,18.5,
62                      18.55,18.6,18.65,18.7,18.75' &
63  reconstructPar -time '18.8,18.85,18.9,18.95,19,19.05,19.1,19.15,19.2,19.25,
64                      19.3,19.35,19.4,19.45,19.5,19.55,19.6,19.65,19.7,19.75,
65                      19.8,19.85,19.9,19.95,20' &
66  wait # wait until the last time directory has been reconstructed
67
68  if [ -d 20 ]; then
69      echo field reconstruction complete
70      echo removing processor time directories...
71      com='nProc=$(ls -1 processor* | wc -l'
72      eval $com
73      for proc in 'processor'*; do
74          com='nObj=$(ls -1 '$proc' | wc -l)'
75          eval $com
76          objCount=0
77          for obj in $proc'/'*; do
78              objCount=$((objCount+1))
79              if [ $objCount -eq 1 ]; then
80                  com='rm -r '$obj
81              elif [ $objCount -lt $nObj ]; then
82                  com=$com' '$obj
83              else
84                  com=$com' '$obj' &'
85              fi
```

```
86          done
87          eval $com
88      done
89      wait # wait until all decomposed time directories have been deleted
90      rm -r processor* # remove the now empty processor directories
91      echo processor time directories removed
92  else
93      echo incomplete field reconstruction detected
94      echo keeping processor time directories
95  fi
```

cleanCaseAll.sh: This script may be used to reset a case to its default condition, but without deleting the `postProcessing` directory, where data recorded using OpenFOAM function objects in the `controlDict` file is stored.

```
1  #!/bin/bash
2
3  # Remove processor directories
4  com='nProc=$(ls -1 processor* | wc -l)'
5  eval $com
6  procCount=0
7  for proc in 'processor'*; do
8          procCount=$((procCount+1))
9          com='nObj=$(ls -1 '$proc' | wc -l)'
10         eval $com
11         objCount=0
12         for obj in $proc'/'*; do
13                 objCount=$((objCount+1))
14                 if [ $objCount -eq 1 ]; then
15                         com='rm -r '$obj
16                 elif [ $objCount -lt $nObj ]; then
17                         com=$com' '$obj
18                 else
19                         com=$com' '$obj' &'
```

```
20                  fi
21          done
22          eval $com
23          if [ $procCount -eq $nProc ]; then
24                  lastPID=$! # identify the last command that was executed
25          fi
26  done
27  wait $lastPID # wait until the last processor directory has been emptied
28  rm -r processor* ## remove empty folders
29
30  # Remove reconstructed time directories
31  rm -r 0 & # exclude 0 from the loop below to avoid deleting 0.org
32  for object in [1-9]*; do
33          if [ -d $object ]; then
34                  com='rm -r '$object' &'
35                  eval $com
36          fi
37  done
38
39  # Remove mesh files and their storage directory
40  if [ -d 'constant/polyMesh' ]; then
41          rm -r constant/polyMesh &
42  fi
43
44  # Remove .stl edge mesh files and their storage directory
45  if [ -d 'constant/extendedFeatureEdgeMesh' ]; then
46          rm -r constant/extendedFeatureEdgeMesh &
47          rm constant/triSurface/*.eMesh &
48  fi
49
50  # Remove job log files
51  for object in 'log.'*; do
52          if [ -f $object ]; then
```

```
53                com='rm '$object' &'
54                eval $com
55        fi
56 done
57
58 # Remove batch script output files
59 for object in 'slurm-'*; do
60        if [ -f $object ]; then
61                com='rm '$object' &'
62                eval $com
63        fi
64 done
65
66 # Remove core dump files
67 for object in 'core.'*; do
68        if [ -f $object ]; then
69                com='rm '$object' &'
70                eval $com
71        fi
72 done
```